



Warning and Mitigation Technologies for Travelling Ionospheric Disturbances Effects

TechTIDE

D5.2

Statistical Analysis of the Results

Version 1.3

Grant agreement no: 776011

The TechTIDE has received funding from the European Commission Horizon 2020 research and innovation programme (2017 – 2020)



Table of Contents

Document Information.....	4
Abstract	5
Document history.....	6
Disclaimer	6
1. Service Degradation on EGNOS performance.....	7
1.1 SBAS Overview.....	7
1.2 Impact of Space Weather Events in EGNOS.....	9
1.2.1 Data.....	10
1.2.2 Methodology.....	12
1.2.3 Analysis for 7-8/09/2017	14
1.2.4. AATR Analysis.....	25
1.4 Conclusions.....	30
2. Service Degradation on HF.....	31
2.1 Azimuth Variations in Digisonde-to-Digisonde measurements	31
2.2.1 Data set.....	32
2.1.2 The Digisonde-to-Digisonde Azimuth Performance Index	35
2.1.3 Analysis – Results	36
2.1.3 Summary/Conclusions	38
2.1.4 Outlook	39
2.2 Direction finding	39
2.2.1 TID databases.....	40
2.2.2 Measurement and Analysis process of GFP.....	41
2.2.3 Statistical Analysis.....	42
2.2.4 Statistical Results	44
3. Service Degradation on high accuracy services.	48
3.1 The CATNET NRTK service	49
3.2 Establishing reference unambiguous measurements in the CATNET NRTK service	50
3.2.1 Fixing carrier phase ambiguities in the CATNET NRTK service.	50
3.3 Obtaining the ionosphere free navigation solution.	54
3.4 Obtaining the navigation solution using a single frequency receiver	56



3.5 Degradation of the single frequency solution with respect to the two frequency solution (IF).....	59
3.4 Effect of MSTIDs in position degradation.....	62
3.4.1 Degradation during 2008-2009.....	68
3.5 Conclusions.....	70
Bibliography.....	71
Annex A EGNOS SCENARIOS ANALYSIS	72
A.1 DOY 31 and 32	72
A.2 DOY 60 and 61	78
A.3 DOY 86 and 87	83
A.4 DOY 110 and 113	88
A.5 DOY 139 and 140.....	93
A.6 DOY 148.....	98
A.7 DOY 197.....	102
A.8 DOY 234 and 235.....	106
A.9 DOY 255 to 259.....	111
A.10 DOY 270 and 271.....	121
A.11 DOY 285 and 286.....	126
A.12 DOY 311 and 312.....	131
A.13 DOY 328.....	136
A.14 DOY 346.....	140
A.15 DOY 351.....	144
A.16 DOY 360.....	148
Annex B AATR Scenarios Figures.....	152
B.1 RIMS EGI average xPL values.....	152
B.2 RIMS RKK average xPL values	153
B.3 RIMS KIR average xPL values	155
B.4 RIMS TRO average xPL values.....	159
Annex C: Network Stations' Distances	161



Document Information

Deliverable number: D5.2
Deliverable title: Statistical Analysis of the Results
Date of Delivery: XX/XX/XXXX
Author(s): José Miguel Juan, Jaume Sanz, Cristhian Timoté, Jens Tölle
Sergio Magdaleno, Joanna Rupiewicz, Jens Mielich.
Work Package no.: 5
Work Package title: Assessment of the impact on aerospace and ground systems
Work Package leader: José Miguel Juan (UPC)
Dissemination level:
Nature:



Abstract

The aim of this WP5 is to specify the impact of TID in EGNOS, N-RTK and HF systems through statistical correlation of the performance data recorded from system operators and of TID detection results.

Within the HF-TID-method in TechTIDE WP2 we use Digisonde-to-Digisonde measurements to determine characteristics of TIDs appearing in the region of the ionospheric reflection area between a transmitting and a receiving Digisonde. One of the TID characteristics is the Angle of Arrival (AoA) of the received radio signal, which can be divided into azimuth and elevation. In this analysis, we look for a correlation between TIDs and the variation of the azimuth of the received radio signal.

In N-RTK, statistical tests have been applied over the entire data tests showing NRTK solutions are close to the solutions implementing a dual frequency solution methodology. Additionally, it was possible to correlate presence of MSTID with the degradation in the NRTK solutions.

Document history

Version	Date	Edited by	Reason for modification / Remarks
1.0	28/02/2019	José Miguel Juan, Jaume Sanz, Cristhian Timoté.	Document creation. Added Chapter 3 Service degradation in high accuracy services.
1.1	03/04/2019	Jens Tölle.	Added 2.2 Direction finding on Chapter 2 Service degradation on HF
1.2	03/04/2019	Sergio Magdaleno and Joanna Rupiewicz.	Added Chapter 1 Service Degradation on EGNOS performance
1.3	05/04/2019	Jens Mielich.	Added section 2.1 on Chapter 2 Azimuth Variations in Digisonde-to-Digisonde measurements

Disclaimer

This document contains description of the TechTIDE project findings, work and products. Certain parts of it might be under partner Intellectual Property Right (IPR) rules so, prior to using its content please contact the Project Coordinator (Dr Anna Belehaki, belehaki@noa.gr) for approval.

In case you believe that this document harms in any way IPR held by you as a person or as a representative of an entity, please do notify us immediately.

The authors of this document have taken all reasonable measures in order for its content to be accurate, consistent and lawful. However, neither the project consortium as a whole nor the individual partners that implicitly or explicitly participated in the creation and publication of this document hold any sort of responsibility that might occur as a result of using its content.

This publication has been produced with the assistance of the European Union. The content of this publication is the sole responsibility of the TechTIDE consortium and can in no way be taken to reflect the views of the European Union.

1. Service Degradation on EGNOS performance

This section of the report is devoted on the scales indicating the severity of TID effects in EGNOS, N-RTK and HF communication and geolocation which is part of the ESSP contribution to Task 5.3 of WP5 – Assessment of the impact on aerospace and ground systems in the frame of TechTIDE project.

The document contents the results and conclusions obtained from the analysis of the scenarios defined in the frame of the TechTIDE project where EGNOS degradations related to Space Weather events were identified.

1.1 SBAS Overview

The European Geostationary Navigation Overlay Service (EGNOS) is Europe's regional satellite-based augmentation system (SBAS). It provides an augmentation service to the Global Positioning System (GPS) Standard Positioning Service (SPS). EGNOS uses GNSS measurements taken by accurately located reference stations deployed mainly across Europe and North Africa. All measurements are transferred to a central computing centre where differential corrections and integrity messages are calculated. These calculations are then broadcast over the covered area using geostationary satellites that serve as an augmentation, or overlay, to the original GNSS message.

EGNOS augments the GPS L1 (1575.42 MHz) Coarse/ Acquisition (C/A) civilian signal by providing corrections and integrity information for GPS space vehicles (ephemeris, clock errors) and most importantly, information to estimate the ionosphere delays affecting the user. EGNOS messages are broadcast through two geostationary satellites in compliance with applicable standards ([RD-2] and [RD-3]). The information provided by EGNOS improves the accuracy and reliability of GNSS positioning information while also providing a crucial integrity message. In addition, EGNOS also transmits an accurate time signal.

Similar SBAS systems, designed according to the same standard have already been commissioned by the US (Wide Area Augmentation System – WAAS), Japan (Satellite based Augmentation System – MSAS) and India (GPS Aided GEO Augmented Navigation – GAGAN in India). Analogous systems are under commissioning or deployment in other regions of the world (e.g. System of Differential Correction and Monitoring – SDCM in Russia) or under investigation (e.g. Korea Augmentation Satellite System – KASS in South Korea). Existing and planned SBAS systems are shown in Figure 1.

EGNOS used a network of 40 Ranging Integrity Monitoring Stations (RIMS) distributed along Europe and surrounding countries to collect measurements from GPS satellites and to transmit these raw data every second to each Mission Control Centres (MCC). EGNOS has 2 MCC that computes satellite and ionospheric differential corrections to improve satellite signal accuracy and provides information on the status of the satellites and the ionosphere (integrity). Both differential corrections and integrity information are codified and sent to the Navigation Land Earth Stations (NLES) which are in charge of transmitting the EGNOS message received from the MCC to the GEO satellites for broadcasting to users. Figure 2 depicts a scheme of EGNOS system infrastructure.

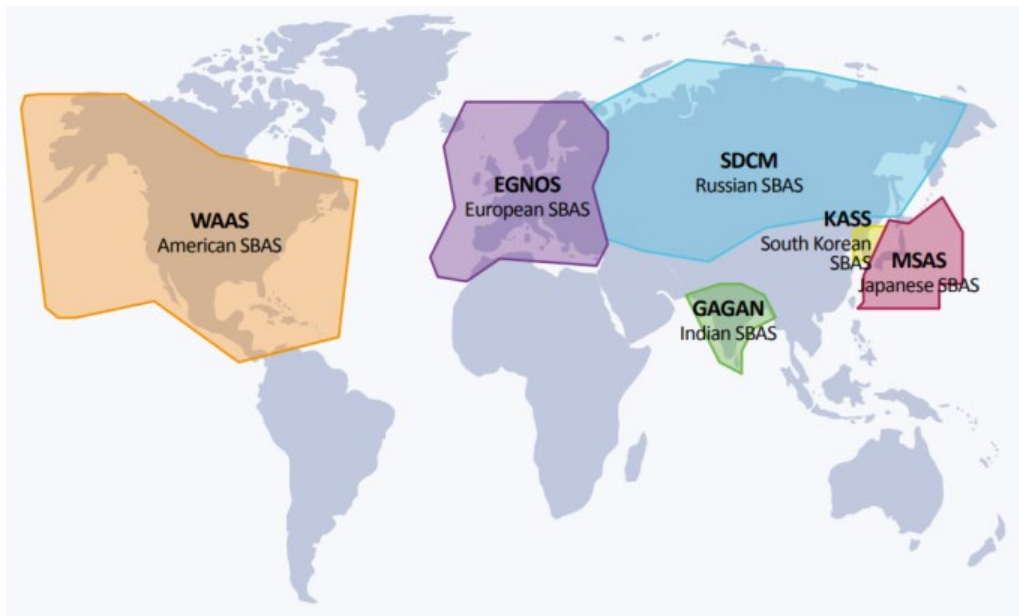


Figure 1 Existing and planned SBAS systems in the world [RD-1]

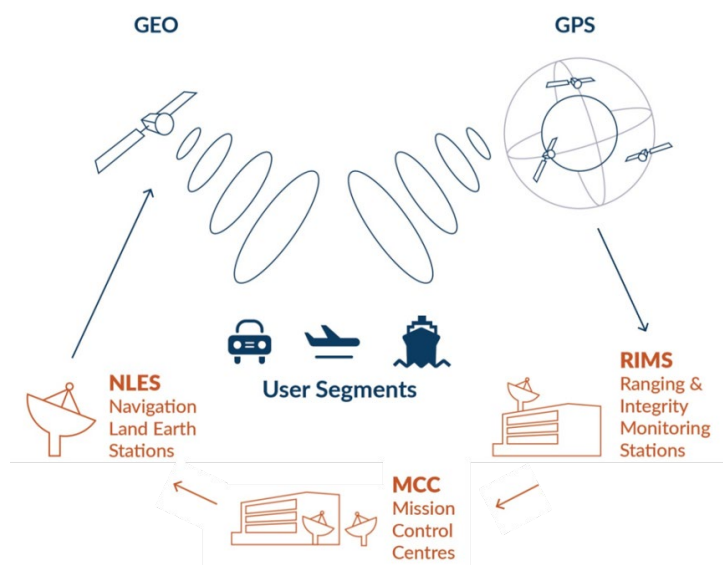


Figure 2 EGNOS infrastructure scheme

EGNOS computes the ionospheric information distributed in a grid of pierce points, called Ionospheric Grid Points (IGP), located at an altitude of 350 Km over the WGS 84 ellipsoid. The map of IGP where EGNOS computes the ionospheric corrections is shown in Figure 3.

The ionospheric information provided for EGNOS is:

- **Grid Ionospheric vertical delay (GIVD):** Ionospheric vertical delay at the IGP for L1 frequency.
- **Grid Ionospheric vertical Error (GIVE):** Ionospheric Vertical Error at the IGP.

The GIVD is related with the TEC value. This parameter indicates the delay (in meters) of the signal due to the cross of the ionosphere. On the other hand, the GIVE is the bounding of the GIVD estimation, that is, is the sigma (at 99.99999%) of the ionospheric delay. Due to the GIVE value must be very confident; any disturbance in the ionosphere would increase the width of the distribution error around the IGP and, therefore, would lead to an increase of this value

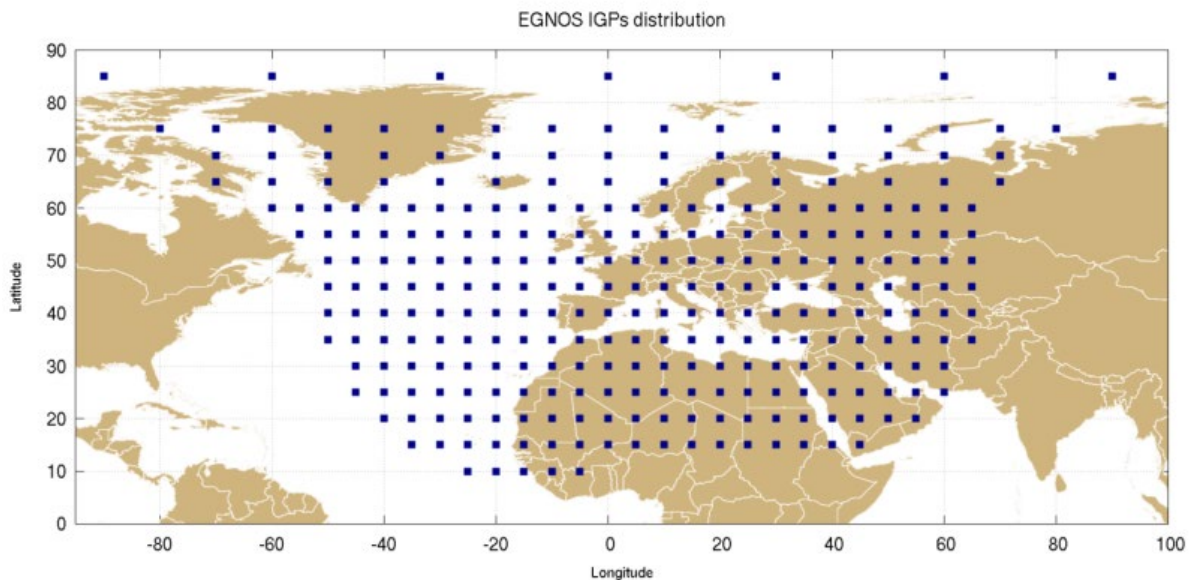


Figure 3 EGNOS IGP mask.

All this information is broadcasted through two SBAS messages:

- Message Type 18, which provides the list of IGPs considered by the system.
- Message Type 26, which provides the ionospheric delay and error.

The Message Type 26 has a nominal broadcast rate of 30 seconds. However, due to the limited number of IGPs that can be included in each Message Type 26, the updating of the ionospheric corrections at all IGPs takes about 5 minutes.

1.2 Impact of Space Weather Events in EGNOS

This section presents analysis results obtained during the assessment of the impact of Space Weather events in EGNOS performance as well as the data and methodology used for each analysis.

The following analyses are presented in the hereafter subsections:

- EGNOS APV-I availability
- Horizontal and Vertical Protection Levels
- EGNOS ionospheric information

1.2.1 Data

In this study, the following data sources were used:

- EGNOS: EGNOS broadcasts its data through EGNOS GEOs which is received by the users for the computation of differential corrections, protection levels, integrity alerts, etc. The data used is:
 - EGNOS APV-I availability maps.
 - Grid Ionospheric Vertical Error Indicator (GIVEI).
- RIMS: performance at EGNOS ground stations (RIMS) is computed as representative of user performance. The data used from the RIMS is:
 - EGNOS APV-I availability at RIMS.
 - Horizontal and Vertical Protection Levels (HPL and VPL, respectively).
- IGS stations: dual-frequency multi-constellation receivers used for the computation of the AATR values.

Table 1 lists the RIMS and IGS stations and their coordinates used in this study.

Table 1 RIMS and IGS stations selection

RIMS station	IGS station
EGI (65.1°N, 14.4°W)	ARGI (61.8°N, 6.8°W)
RKK (64.0°N, 22.0°W)	REYK (64.0°N, 22.0°W)
KIR (69.6°N, 29.9°E)	KIRU (67.7°N, 21.0°E)
	ARJ6 (66.2°N, 18.1°E)
TRO (69.0°N, 18.9°E)	OUL2 (64.9°N, 25.9°E)
	SOD3 (67.3°N, 26.4°E)

Figure 4 presents the location of RIMS (red stars) and IGS stations (blue pentagons) divided in West region (left) and East region (right).

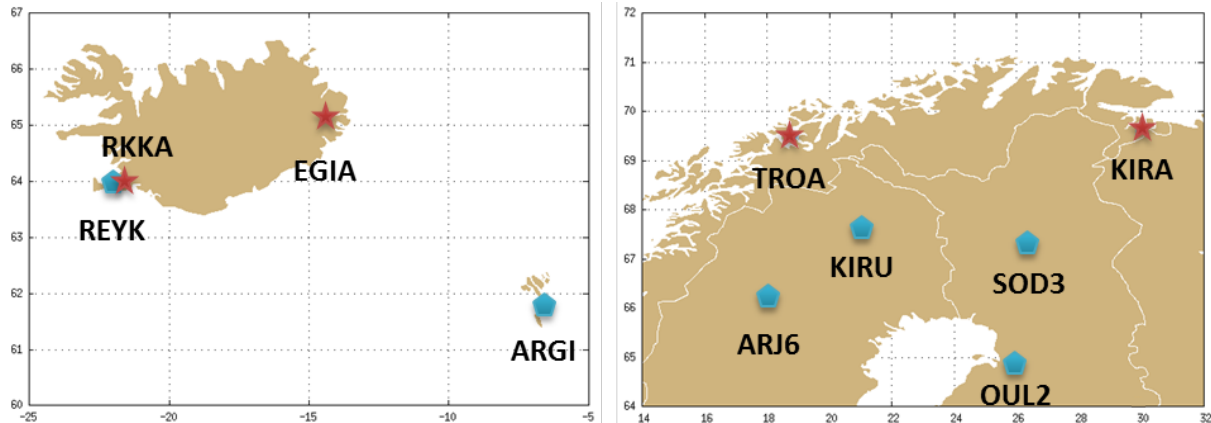


Figure 4 EGNOS RIMS and IGS stations location.

For the study, the following list of scenarios was used. These scenarios were selected due to the identification of EGNOS APV-I availability degradation linked to ionospheric effects. The Availability degradation is classified as follows:

- black – low degradation.
- brown – moderate degradation.
- red – high degradation.

Table 2 List of scenarios analyzed.

Date	APV-I 99% Availability Degraded Area ¹
31/01/2017	12.8%
01/02/2017	9.5%
01/03/2017	6.2%
02/03/2017	6.1%
27/03/2017	10.5%
28/03/2017	4.1%
20/04/2017	7.4%
23/04/2017	7.1%
19/05/2017	6.8%
20/05/2017	7.2%
28/05/2017	21.7%
16/07/2017	1.8%
22/08/2017	6.6%
23/08/2017	5.9%

¹ Degraded area with respect to the Safety of Life SDD v3.1 (Error! Reference source not found.)

Date	APV-I 99% Availability Degraded Area ¹
07/09/2017	12.0%
08/09/2017	33.9%
12/09/2017	10.9%
13/09/2017	8.7%
14/09/2017	6.0%
15/09/2017	15.7%
16/09/2017	7.6%
27/09/2017	6.3%
28/09/2017	8.1%
12/10/2017	5.4%
13/10/2017	5.6%
07/11/2017	4.3%
08/11/2017	11.2%
24/11/2017	8.8%
12/12/2017	6.8%
17/12/2017	13.6%
26/12/2017	6.0%

1.2.2 Methodology

1.2.2.1 EGNOS availability

The first parameter assessed in this study is the EGNOS APV-I availability. The availability of GNSS is characterized by the proportion of time during which reliable navigation information is presented to the crew, autopilot, or other system managing the flight of the aircraft. (ICAO SARPS).

The EGNOS APV-I availability is computed for each day, considering the system available when operational requirements defined in ICAO SARPS ([RD-2]) are met. In this case, EGNOS is considered available when the Protection Levels are lower than the Alarm limits defined by ICAO for the APV-I operation. These Alarm Limits are provided in Table 3.

It is noted that these maps are computed in a 1x1 (degree) grid and per day. That is a limitation if the evolution of the availability along the day is considered. Due to the limitation of daily performance maps, hourly APV-I availability is computed at each RIMS position, where xPL values are computed according to [RD-3]. The hourly availability is calculated computing the number of epochs that EGNOS is available divided by 60 minutes.

Table 3 Signal-in-space performance requirements for APV-I defined in [RD-2].

Operation	Horizontal alert limit	Vertical alert limit
Approach operations with vertical guidance (APV-I)	40 m	50 m

1.2.2.2 Protection levels variability

The Horizontal and Vertical Protection Levels are computed for each RIMS and scenario defined. Instead of using the instantaneous Protection levels, the maximum value of each Protection Level (Horizontal and Vertical) in a 5 minutes' window is computed. It is noted that maximum HPL and VPL could take place in different epochs. That is done to align the protection level rate to the AATR values rate.

1.2.2.3 GIVE indicator estimation within surrounding IGPs

The methodology of this assessment was based on the selection of four IGPs which surrounds the following RIMS stations: RIMS EGI, RIMS KIR, RIMS RKK and RIMS TRO. Table 4 presents the position of chosen IGPs for each corresponding RIMS station.

Table 4 IGPs selection per each RIMS.

RIMS station	IGP location	RIMS station	IGP location
EGI	65°N 20°W	RKK	70°N 20°W
	65°N 00°		60°N 20°W
	60°N 10°W		65°N 30°W
	70°N 10°W		65°N 10°W
KIR	75°N 30°E	TRO	75°N 20°E
	65°N 30°E		65°N 20°E
	70°N 40°E		70°N 10°E
	70°N 20°E		70°N 30°E

The GIVE indicators will be computed for each IGP within all day. This information, as explained in [RD-1], is coming from SBAS Message Type 26 and related with the ionospheric activity and EGNOS APV-I availability. The AATR values which are computed every 5 minutes are compared with the GIVE indicators. In the following chapter 1.2.3 Analysis for 7-8/09/2017, the analysis of two days will be presented. The analysis of the rest of scenarios listed in 1.2.1 Data are included in Annex A EGNOS SCENARIOS ANALYSIS.

1.2.3 Analysis for 7-8/09/2017

This section presents the analysis results for the degradation of EGNOS APV-I availability observed during days 7th and 8th September 2017. Figure 5 shows the EGNOS APV-I availability for day 7th September 2017 (left) and day 8th September 2017 (right). This performance is computed considering Fault Free conditions, that is, local effects are not taken into account for the computation (e.g. multipath, interferences) and only system information is considered.

EGNOS APV-I availability is computed considering that EGNOS is available when EGNOS performances are compliant with APV-I requirements defined in Table 3, i.e. EGNOS APV-I service is considered available when the Horizontal Protection Level (HPL) is lower than 40 m and the Vertical Protection Level (VPL) is lower than 50 m ($xPL < xAL$).

Figure 6 depicts the daily average value of AATR computed at different IGS stations distributed along Europe for the 7th September 2017 (left) and 8th September 2017 (right). It is noted that AATR represents the ionospheric activity, so the higher the AATR value, the higher the ionospheric activity is in the area. The daily average value of AATR is presented in colour scale and size of the circle. It is observed that, for 7th September 2017, the greatest value is located in Greenland and stations at the North of Europe have slightly higher AATR mean values than in the centre of Europe. That is in line with the EGNOS APV-I availability, which shows a small degradation of the EGNOS APV-I availability in the Northwest of Europe. However, 8th September 2017, shows higher values than the previous day in the North region, both East and West. Comparing this with the EGNOS APV-I availability, it is observed that the EGNOS APV-I availability degradation occurs in the same area where these high daily average value of AATR are located.

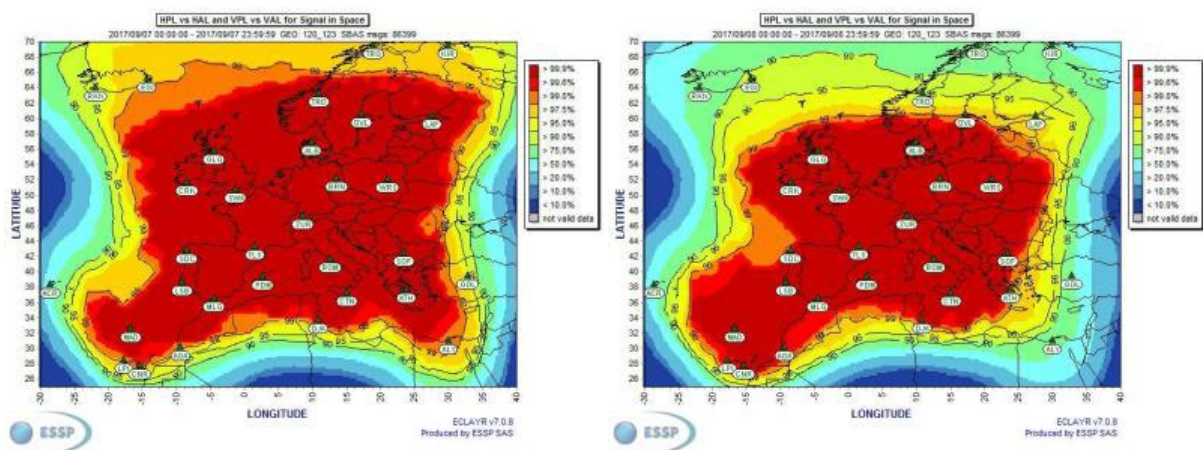


Figure 5 EGNOS APV-I Availability for the 7th September 2017 (left) and 8th September 2017 (right).

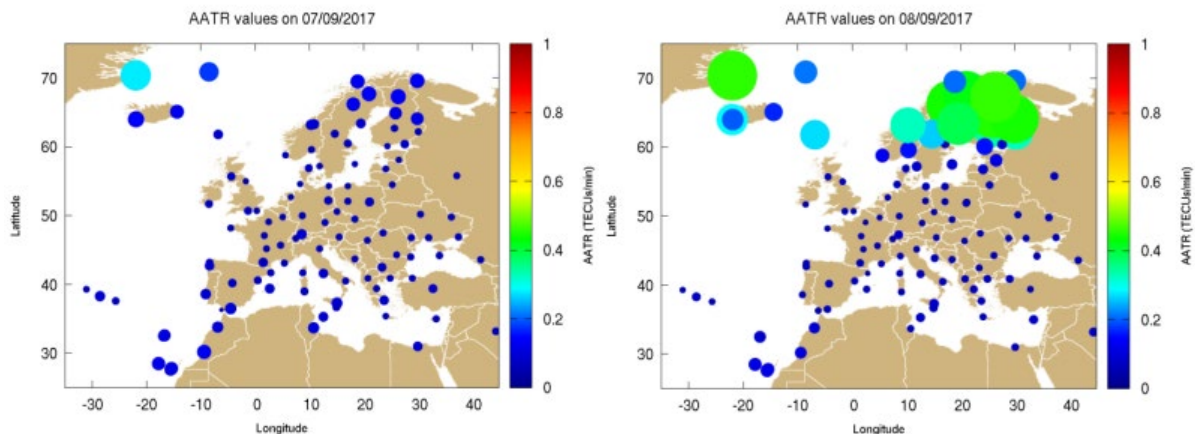


Figure 6 AATR daily mean values at European IGS stations for the 7th September 2017 (left) and 8th September 2017 (right).

1.2.3.1 EGNOS availability analysis

Following the methodology defined in section 1.2.2, first step of the analysis is a cross-check between the hourly availability and the AATR index computed for those IGS stations located close to the RIMS. The list of RIMS analysed as well as the list of IGS stations used for this assessment is provided in section 1.2.1.

Figure 7 shows the temporal evolution of the EGNOS APV-I availability at RIMS EGI (65.1N, 14.4°W) (black line) and AATR values at two IGS stations: ARG1 (61.8°N, 6.8°W) (purple line) and REYK (64.0°N, 22.0°W) (green line) from 7th to 9th September (DOY 250 to 252). The analysis of this availability degradations reveals that all these degradations are linked to ionospheric activity.

Focusing on the 7th September (DOY 250), it is observed an increase of the AATR values at REYK station from epoch 12600 to epoch 20100 with AATR values up to 0.80 TECUs/min but no impact on EGNOS APV-I availability is found. It is noted that AATR values of the other IGS station located close to this RIMS, ARG1 station, are not greater than 0.45 TECU/min during this period. Additionally, the analysis of the other RIMS station located in this area, RKK (64.0°N, 22.0°W) (Figure 8), shows some degradation on the availability performance from epoch 12000 to 13200. These results could be explained placing the ionospheric degradation in the West of REYK station, that is, over Greenland or Canada. In that case, the ionospheric degradation would be located far from ARG1 station and RIMS EGI and so they are not impacted meanwhile RIMS RKK and REYK station would be.

A second slot with great AATR values is observed from epoch 83100 to epoch 6600 of the next day. During this period, AATR values up to 1.33 TECUs/min at REYK station and up to 1.48 TECUs/min at ARG1 station are observed. In this case, a degradation of the EGNOS APV-I availability is observed during this period, doing EGNOS unavailable during some minutes at RIMS EGI and RKK.

Finally, during the second half of the 8th September, a period of ionospheric activity is identified by large AATR values in both REYK (up to 1.48 TECUs/min) and ARG1 (up to 1.10

TECUs/min) stations. During this period, the EGNOS APV-I availability decreases up to 20% in EGI and is unavailable in RKK during some minutes.

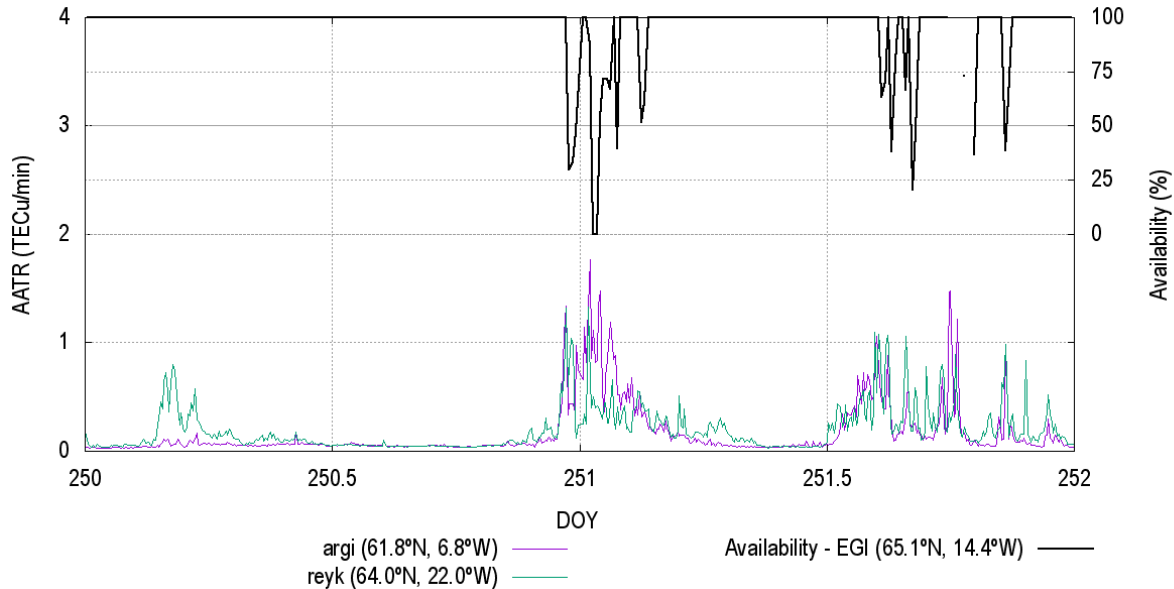


Figure 7 APV-I availability at RIMS EGI (black), AATR values at IGS station ARG1 (purple) and REYK (green) from 7th to 9th September (DOY 250 – 252).

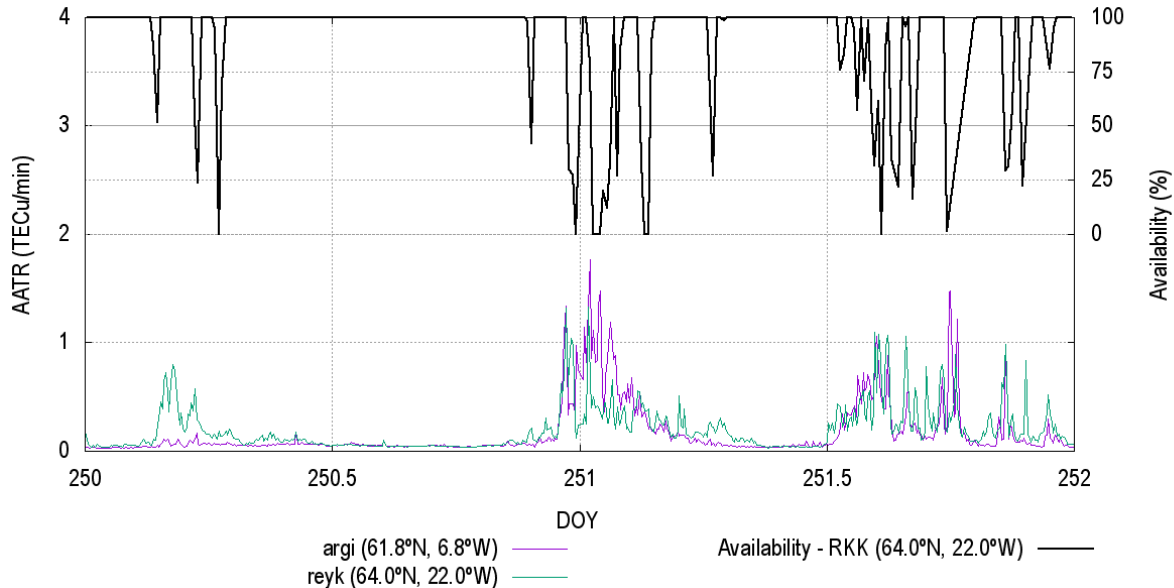


Figure 8 APV-I availability at RIMS RKK (black), AATR values at IGS station ARG1 (purple) and REYK (green) from 7th to 9th September (DOY 250 – 252).

Equivalent behavior is observed between RIMS KIR (69.6°N, 29.9°E), located in Norway, and AATR values from IGS stations KIRU (67.7°N, 21.0°E), ARJ6 (66.2°N, 18.1°E), OUL2 (64.9°N, 25.9°E) and SOD3 (67.3°N, 26.4°E) presented in Figure 9; and RIMS TRO (69°N, 18.9°E), located in Norway, and AATR values from IGS stations KIRU (67.7°N, 21.0°E) and ARJ6 (66.2°N, 18.1°E) presented in Figure 10.

It is noted that some discontinuities in EGNOS APV-I availability (black line) can be observed in RIMS KIR and TRO. They mean data gaps in RIMS information.

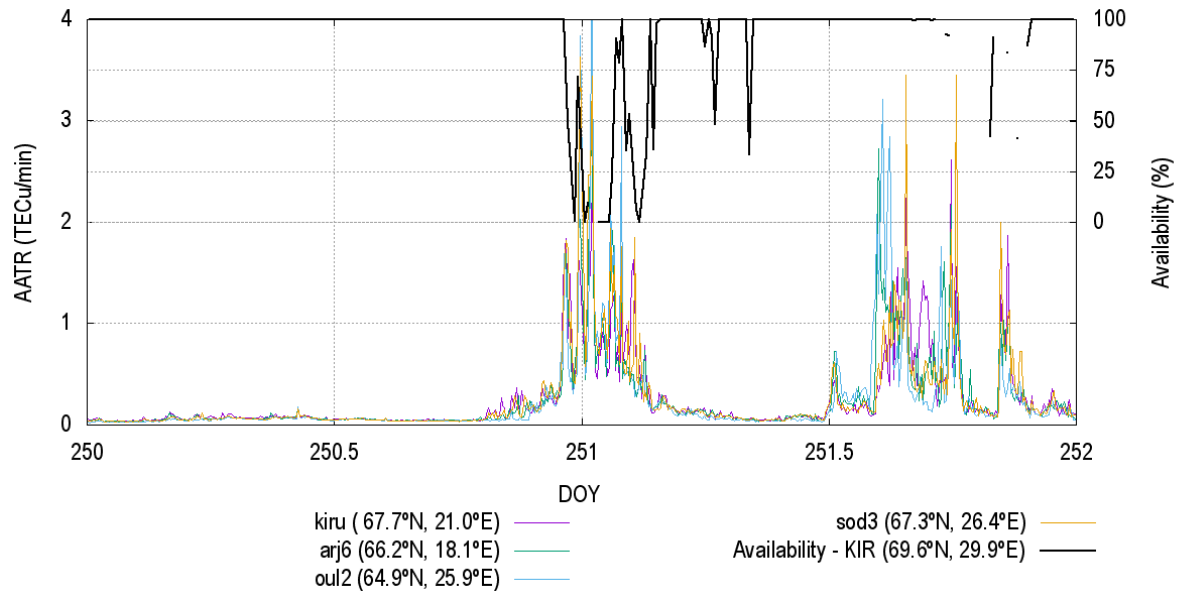


Figure 9 APV-I availability at RIMS KIR (black), AATR values at IGS station KIRU (purple), ARJ6 (green), OUL2 (blue) and SOD3 (orange) from 7th to 9th September (DOY 250 – 252).

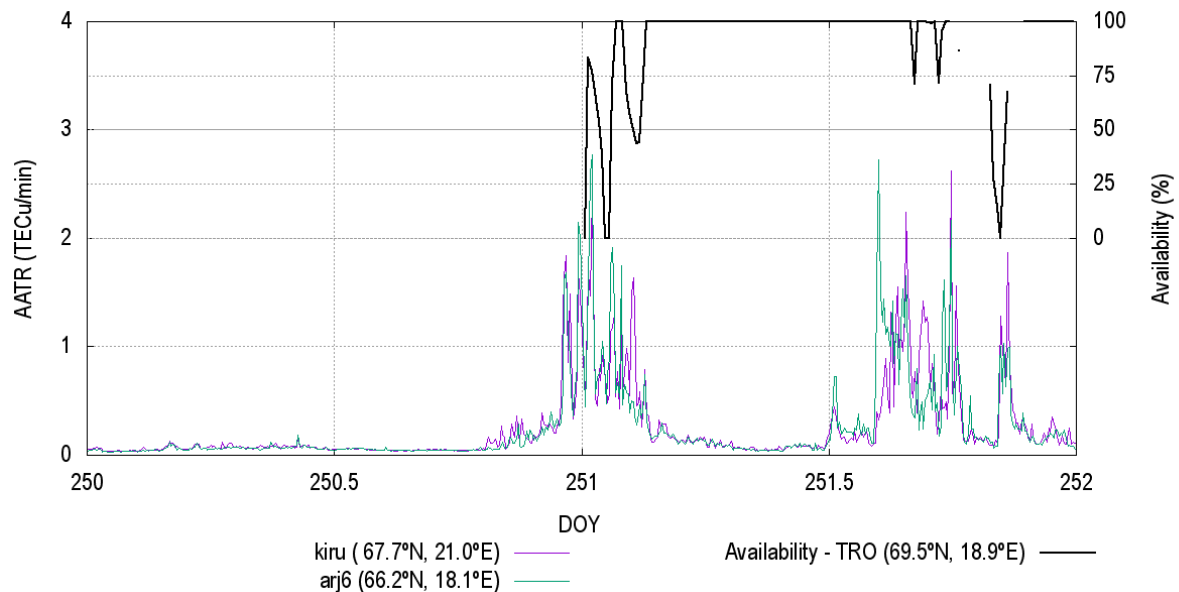


Figure 10 APV-I availability at RIMS TRO (black), AATR values at IGS station KIRU (purple) and ARJ6 (green) from 7th to 9th September (DOY 250 – 252).

1.2.3.2 Protection Level Analysis

After the results obtained from the hourly EGNOS availability and the AATR values comparison, the next step is to find out if there is also a correlation between the AATR and both Horizontal and Vertical Protection Levels, HPL and VPL respectively. For this analysis, the

5-minutes HPL and VPL maximum values have been computed following the methodology defined in section 1.2.2.

Figure 11 shows the 5-minutes HPL (blue) and VPL (red) maximum values at RIMS EGI (65.1°N, 14.4°W) from 7th to 9th September (DOY 250 to 252) and AATR values from IGS stations ARG1 (61.8°N, 6.8°W) (purple line) and REYK (64.0°N, 14.4°W) (green line). It is observed that the behaviour of HPL and VPL is quite similar.

During DOY 250, ARG1 station presents a spike in its AATR values from 0.5 TECUs/min to 1.1 TECUs/min at 83700 seconds of day. REYK station has also an increase of its AATR values from 0.7 to 1.3 at 84000 seconds of day. During this period, HPL and VPL values present some great increases on their values: at epoch 84036, HPL has an increase from 14.1 to 19.5 meters and VPL values from 20.9 to 33.6 meters; also at epoch 84179, HPL values increase from 19.6 to 57.6 meters and VPL values increase from 32.5 to 76.8 meters; it is observed an increase from 65.2 to 145.9 meters in HPL values and from 85.5 to 187.2 meters in VPL values at epoch 84231; finally, an increase from 147.9 to 466.1 meters in HPL values and from 183.9 to 448.0 meters in VPL values is found.

At the beginning of the next day, DOY 251, VPL and HPL values at EGI are still high. This is due to the continuation of high AATR values from the day before. Therefore, these high xPL values are due to the high ionospheric activity started the previous day.

A second degradation period is observed during DOY 251 after noon. This degradation is characterized by increases of AATR values at ARG1 station, reaching values up to 1.06 TECUs/min at epoch 51900, up to 1.48 TECUs/min at epoch 64800 and up to 0.88 TECUs/min at epoch 74400. At REYK station, AATR values present similar behaviour than at ARG1 station, reaching AATR values up to 1.1 TECUs/min at epoch 51600, up to 0.9 TECUs/min at epoch 65700 and up to 1.0 TECUs/min at epoch 74400.

For this second degradation, HPL reach values up to 60.0 meters at epoch 52800, increases from 18.2 meters at epoch 64500 to 96.1 meters at epoch 67200 (data gap between these values) and increases from 18.9 to 43.0 meters at epoch 75000. The same behaviour is observed for VPL values: increases from 35.9 to 158.5 meters at epoch 52500, from 27.6 to 80.9 meters at epoch 67200 and from 38.2 to 82.5 meters at epoch 75000.

Data from the other three RIMS analysed (from Figure 12 to Figure 14) shows the same behaviour: the increase of AATR values at the near IGS stations are followed by an increase of HPL and VPL values in the RIMS.

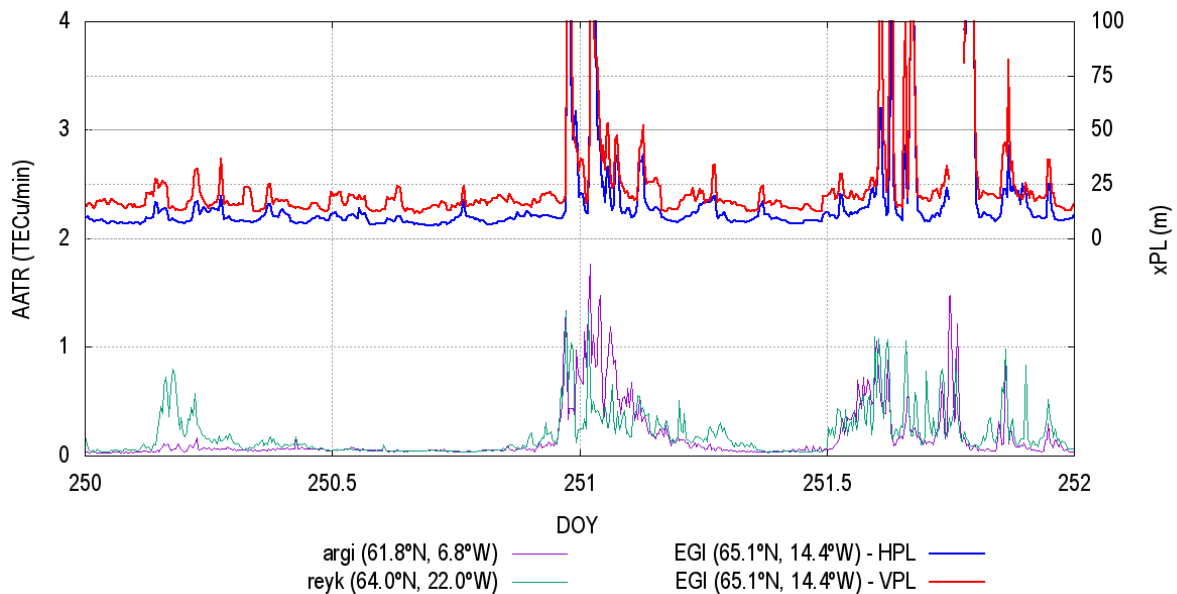


Figure 11 HPL variation (blue), VPL variation (red) and APV-I availability (black) at RIMS EGI, AATR values at IGS station ARG1 (purple) and REYK (green) from 7th to 9th September (DOY 250 – 252).

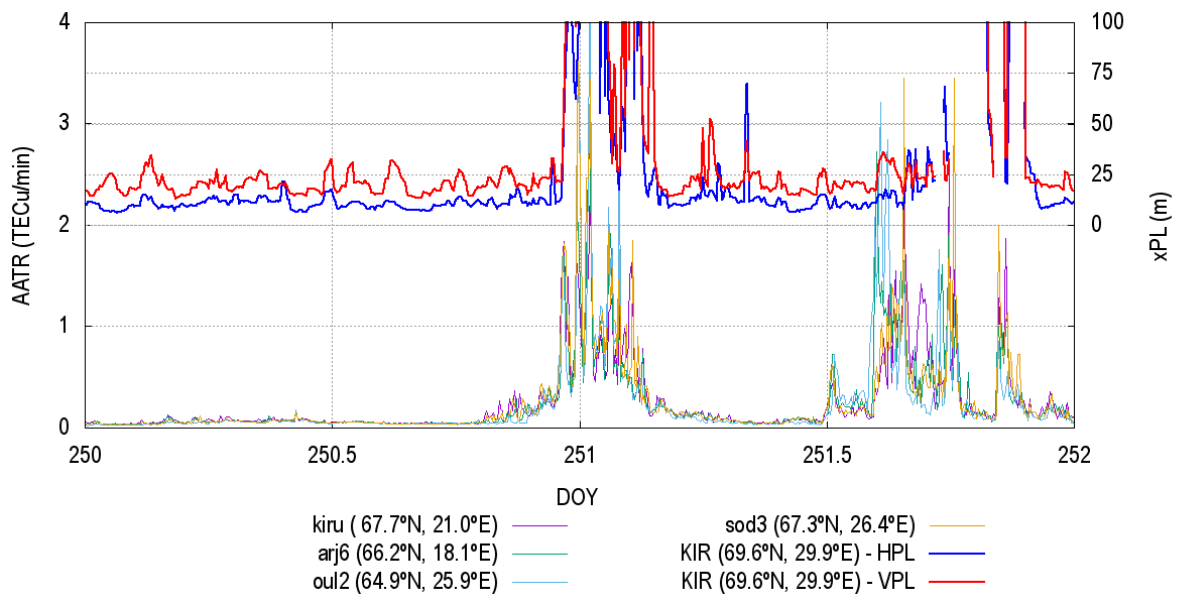


Figure 12 HPL variation (blue), VPL variation (red) and APV-I availability at RIMS KIR (black), AATR values at IGS station KIRU (purple), ARJ6 (green), OUL2 (blue) and SOD3 (orange) from 7th to 9th September (DOY 250 – 252).

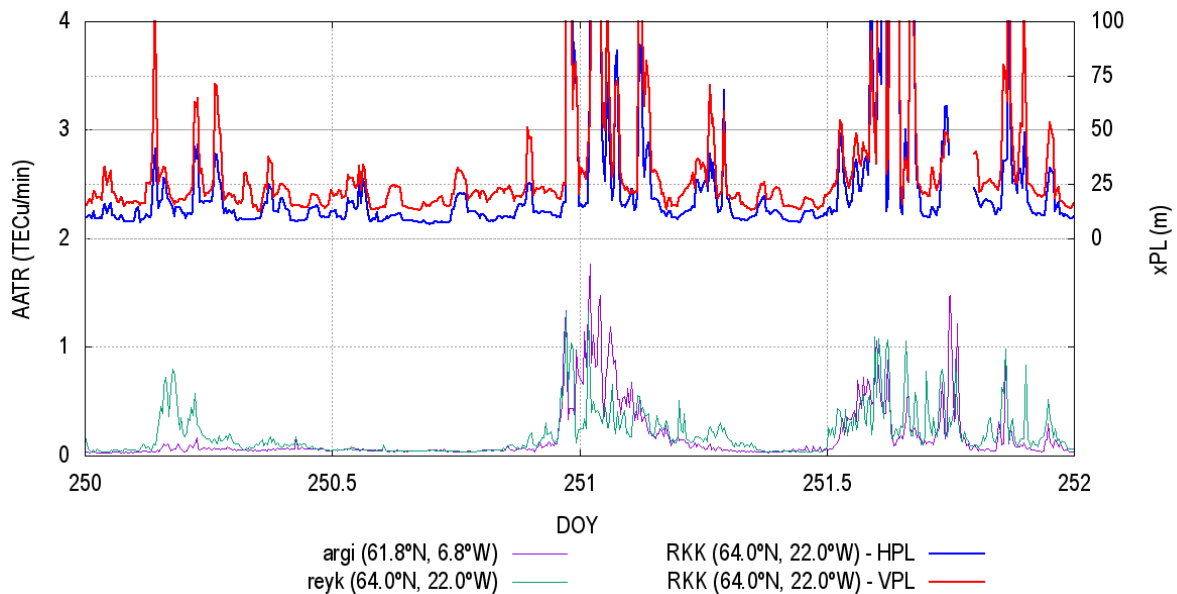


Figure 13 HPL variation (blue), VPL variation (red) and APV-I availability at RIMS RKK (black), AATR values at IGS station ARG1 (purple) and REYK (green) from 7th to 9th September (DOY 250 – 252).

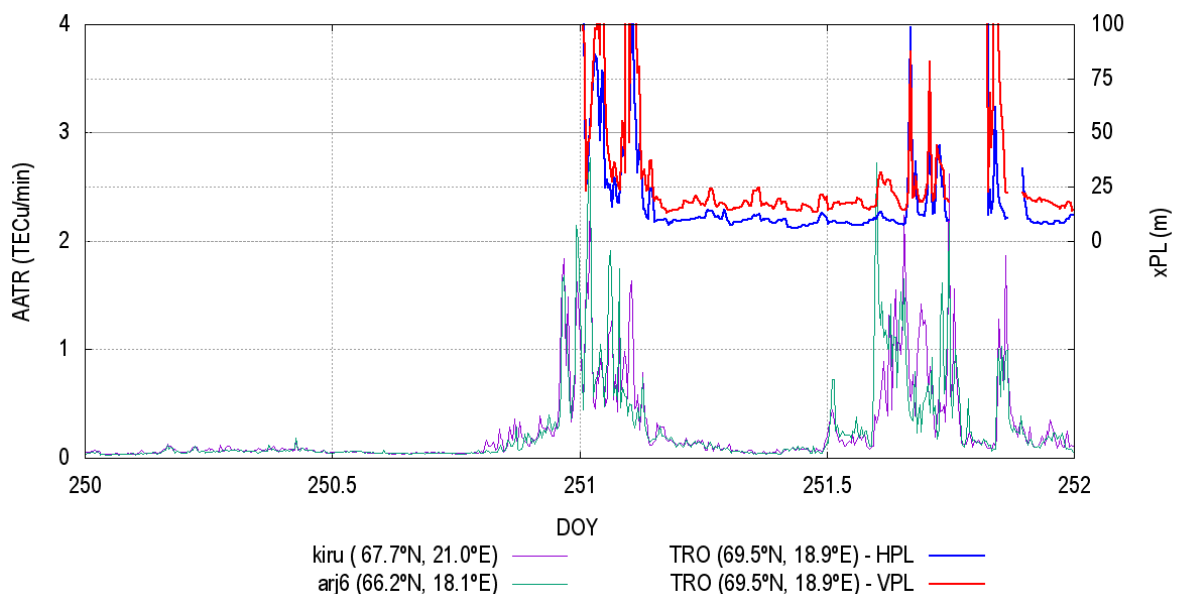


Figure 14 HPL variation (blue), VPL variation (red) and APV-I availability at RIMS TRO (black), AATR values at IGS station KIRU (purple) and ARJ6 (green) from 7th to 9th September (DOY 250 – 252).

3.3.3 SBAS ionospheric information analysis

Following the methodology presented in 1.2.2 Methodology, the next correlation which has been assessed is to cross check how the AATR values behaves with the behaviour of GIVE indices. In this assessment we have analysed the scenarios which are presented in 1.2.1 Data, below the figures contain the correlation of the selected RIMS stations and the IGP which are

located around them, their GIVEI values together with values of AATR from the IGS stations which are located in the neighbourhood. Those correlations are done for the days of 7th and 8th of September 2017.

The Figure 15 below presents the correlation between the AATR values calculated at two IGS stations ARG1 (in bottom blue) and REYK (in bottom red) with respect to GIVE indices which have been estimated at four locations around the RIMS EGI station. It is seen that there is a clear correlation between those two parameters as we can observe a sudden increase in both values at approximately the same time (beginning of the day and end of the day). In the case of 7th of September 2017 there has been a high geomagnetic activity which has been observed by the end of the day and followed the next day. It is seen the increase of the AATR value together with an increase of GIVE indices in all of the IGP's locations. Some of them were set to high values of 14 and some of them to 15 which correspond to discarding them from the calculation of protection levels.

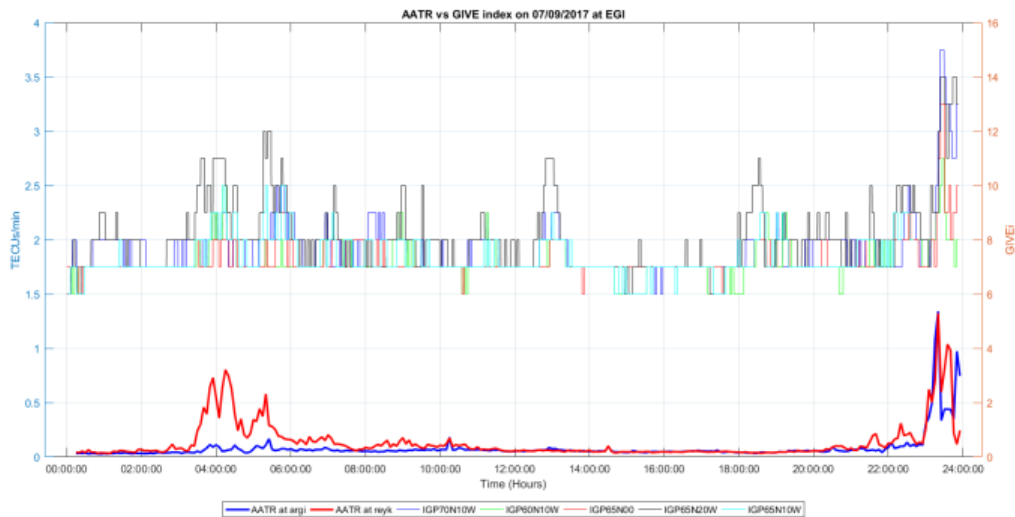


Figure 15 AATR at ARG1 (in bottom blue) and REYK (in bottom red) and the GIVE indices around RIMS EGI (top of the graph) on 7th September 2017.

The following day, on 8th of September 2017 the geomagnetic activity has followed and has been observed during all day. The Figure 16 below presents the behaviour of AATR values at same IGS stations as well as the behaviour of the GIVE indices around the RIMS EGI. As has been seen in the previous day, there is a high correlation between the peaks of AATR values and the time when the GIVEI has been estimated to high values.

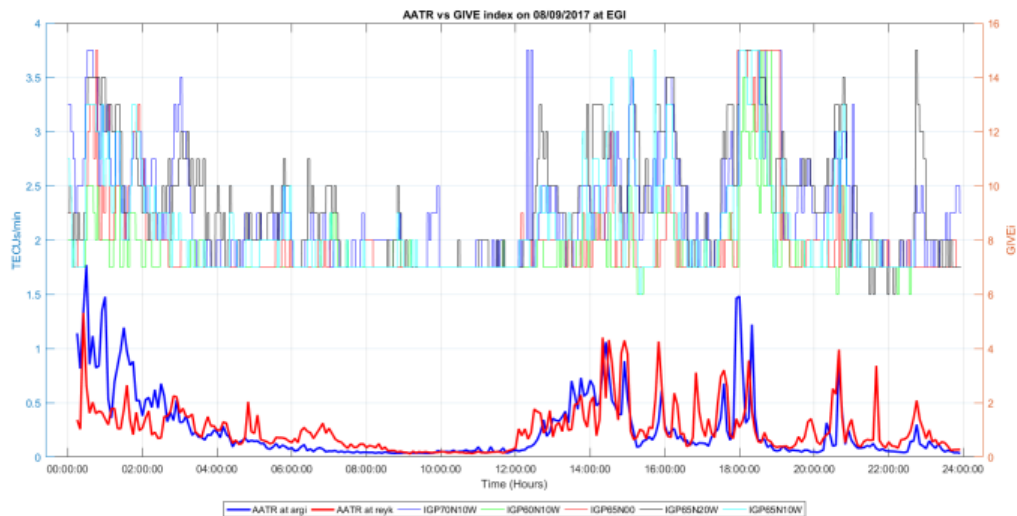


Figure 16 AATR at ARG1 (in bottom blue) and REYK (in bottom red) and the GIVE indices around RIMS EGI (top of the graph) on 8th September 2017.

The two following Figure 17 and Figure 18 present the behaviour of AATR and GIVE indices at the location of RIMS RKK for the two days of 7th and 8th of September 2017. Similar to correlation at RIMS EGI location, it is observed a strong correlation between those two parameters.

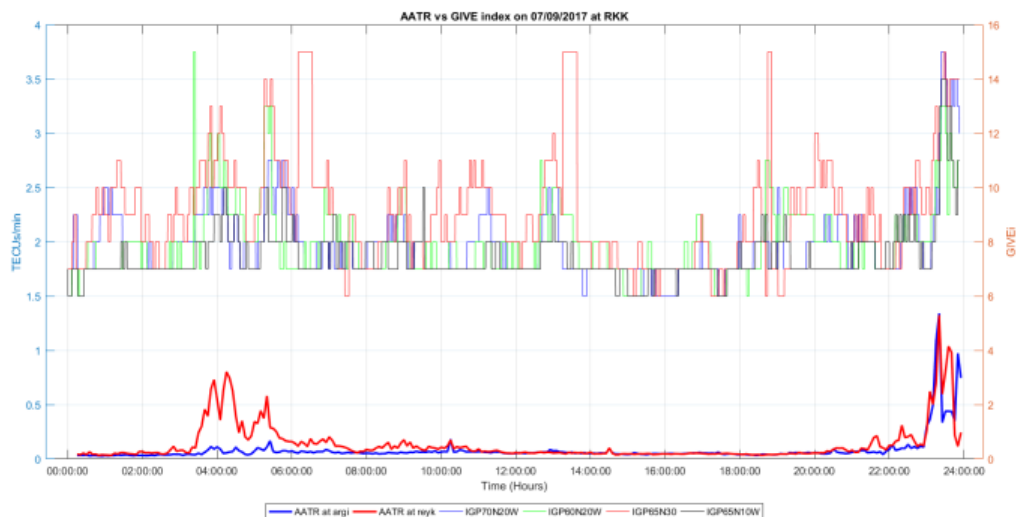


Figure 17 AATR at ARG1 (in bottom blue) and REYK (in bottom red) and the GIVE indices around RIMS RKK (top of the graph) on 7th September 2017.

In the case of 8th of September the geomagnetic activity has been present and impacting the North of ECAC during all day long.

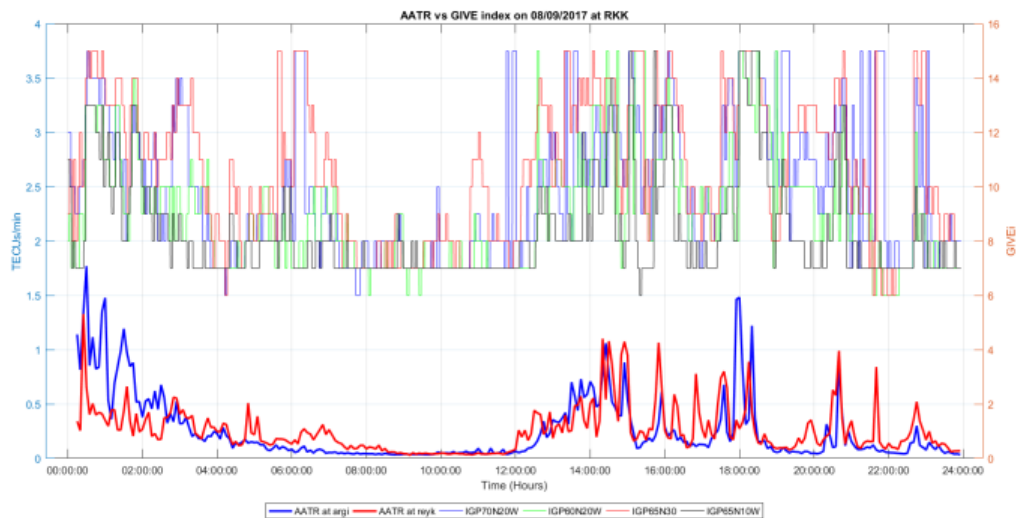


Figure 18 AATR at ARG1 (in bottom blue) and REYK (in bottom red) and the GIVE indices around RIMS RKK (top of the graph) on 8th September 2017.

The two next figures, present the correlation between the parameters in the North East part of ECAC, at the sites of RIMS KIR and RIMS TRO. It is observed that there is a strong correlation between the increases of both parameters by the end of the day when the ionosphere had major impact. In the case of the IGPs which are located around RIMS KIR the Figure 19 below presents the correlation of those two parameters.



Figure 19 AATR at KIRU (in bottom blue), ARJ6 (in bottom red), OUL2 (in bottom green) and at SOD3 (in bottom black) and the GIVE indices around RIMS KIR (top of the graph) on 7th September 2017.

In the case of the correlation at the IGPs stations which are located around RIMS TRO, the Figure 20 below presents the results. It is seen that the AATR has an increase in the values by the end of the day together with an increase of the GIVEI values.



Figure 20 AATR at KIRU (in bottom blue) and ARJ6 (in bottom red) and the GIVE indices around RIMS TRO (top of the graph) on 7th September 2017.

The two following figures present the behavior at those locations on 8th of September. The impact has been seen in the beginning and end of the day setting GIVEI to high values and having AATR peaks.

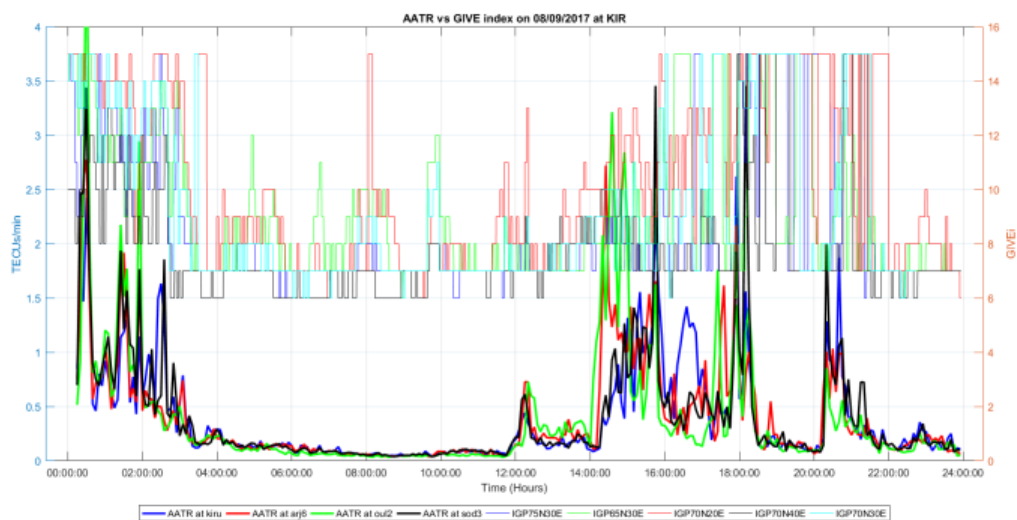


Figure 21 AATR at KIRU (in bottom blue), ARJ6 (in bottom red), OUL2 (in bottom green) and SOD3 (in bottom black) and the GIVE indices around RIMS KIR (top of the graph) on 8th September 2017.

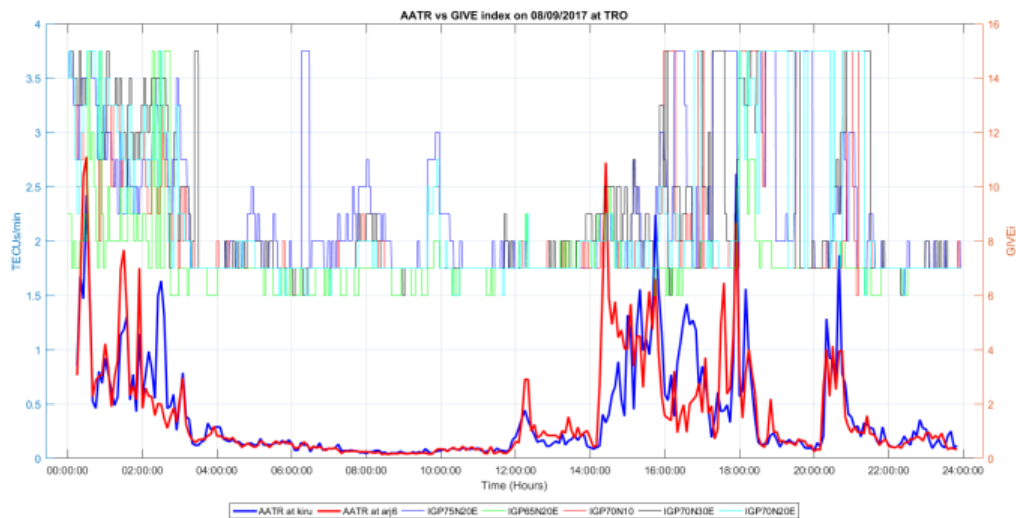


Figure 22 AATR at KIRU (in bottom blue) and ARJ6 (in bottom red) and the GIVE indices around RIMS TRO (top of the graph) on 8th September 2017.

The above figures have presented the correlation between the increase of the AATR values and corresponding increase of GIVEI values at the IGPs located in the North East and North West part of EGNOS service. However, the GIVE indices are set to high values not only due to high ionospheric activities. This can occur also when some of the EGNOS assets are under maintenance activities.

1.2.4. AATR Analysis

This section presents the results of AATR analysis. This analysis considers the AATR values as a trigger of the EGNOS unavailability. For that, the study has considered the Horizontal and Vertical Protection Levels as representative of the EGNOS unavailability. It is clear that the highest AATR values will be registered once the ionospheric disturbance is close (or above) to the monitoring station but the ionospheric disturbance could be monitored earlier, so it is not needed to wait for the highest AATR values but to an increase of the AATR values above from the “nominal” or “quiet” values.

To define which AATR values can be considered as a good trigger of EGNOS performance degradation, first step is to characterize the AATR values at each IGS station. For that, AATR values distribution has been computed. Table 5 shows the AATR distribution for the six IGS stations considered in this study. It is observed that AATR values present different behaviour according to the longitude as those IGS stations located in the East (i.e. ARJ6, KIRU, OUL2 and SOD3) present greater AATR values than those IGS stations located in the West (i.e. ARG1 and REYK).

Table 5 Classification of AATR values per IGS station.

IGS Station	AATR > 1.0 TECUs/min	AATR > 0.8 TECUs/min	AATR > 0.5 TECUs/min	AATR < 0.5 TECUs/min
ARGI	23	45	118	101561
REYK	58	130	655	101265
ARJ6	181	288	693	103143
KIRU	357	612	1541	102837
OUL2	70	93	210	50663
SOD3	181	272	579	45985

For the definition of the AATR threshold, the following steps have been done:

1. AATR threshold is set to identify when the ionospheric event starts.
2. Once AATR threshold is exceeded, Horizontal and Vertical Protection Level values from this epoch to one hour later are selected.
3. For each period the AATR threshold is exceeded a Protection Level dataset is defined. These datasets are reduced considering only those Protection Level values until either Horizontal Protection Level values are greater 40 meters or Vertical Protection Level values are greater than 50 meters. Next Protection Level values are not considered once one of these values is exceeded.
4. Protection Levels values are classified according to the time since the AATR threshold was exceeded.
5. Average value is computed for both Horizontal and Vertical Protection Level according to the first epoch AATR threshold was exceeded.

To clarify the results presented later, the visibility of each RIMS and the IGS stations selected for this study is shown in Figure 23. In this figure, the RIMS location is represented by a red square and the visibility area is plotted in red. The IGS stations visibility area is represented by a coloured ellipse where each colour corresponds to the respective IGS station. The visibility area is computed considering a minimum elevation angle of 5 degrees. This info shows what ionospheric region is used for the computation of the AATR (IGS Station) and what is impacting in EGNOS system (RIMS).

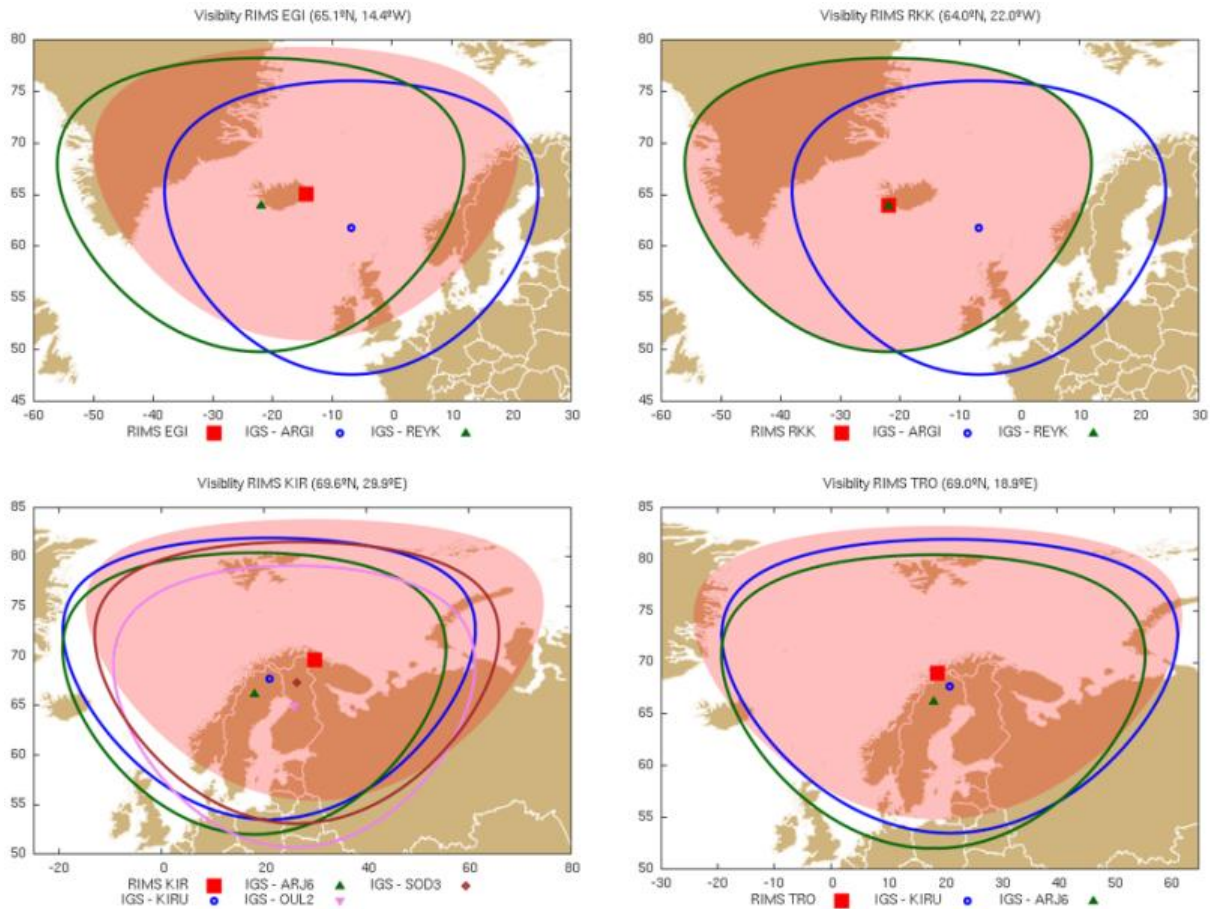


Figure 23 Visibility for RIMS AGI (top left), RKK (top right), KIR (bottom left) and TRO (bottom right) and their respectively IGS stations defined for the analysis.

The AATR thresholds used for this analysis were: 0.5 TECU/min, 0.8 TECU/min, 1.0 TECU/min, 1.2 TECU/min and 1.5 TECU/min. Hereafter it is presented the epochs when either HPL values or VPL values present a clear increase of their values. The information given bellow is a summary of the analyses; all figures are provided in Annex B.

Table 6 presents the offset between the epoch the AATR threshold is exceeded and the epoch when Protection Levels present a clear increase of their values for RIMS EGI. The table shows that offset values from ARG1 IGS Station are greater than from REYK IGS Station. That result is expected as REYK is closer to RIMS EGI than ARG1, so ARG1 will observe the ionospheric event earlier than REYK and earlier the ionospheric event reach the RIMS EGI. Additionally, it is clear that the highest the AATR threshold, the offset between the AATR threshold exceeded and the Protection Level increase will be shorter.

Table 6 Offset between AATR increase and xPL increase at RIMS EGI.

AATR Threshold (TECUs/min)	ARGI (s)	REYK (s)
0.5	1500	600
0.8	1200	600
1.0	1200	600
1.2	600	-

Similar results to those obtained for EGI are observed in RIMS RKK (Table 7). It is noted that those RIMS are quite close and the IGS stations selected are the same. In this case, REYK IGS station is located in the same area and the offset is linked not only to the ionospheric disturbance velocity propagation but also to the EGNOS system responding time and the time for the dissemination of the EGNOS ionospheric information (which is about 5 minutes). As in the previous case, ARG1 IGS station is located further from RIMS RKK and offset values are greater than those from REYK IGS Station.

Table 7 Offset between AATR increase and xPL increase at RIMS RKK.

AATR Threshold (TECUs/min)	ARGI (s)	REYK (s)
0.5	1500	600
0.8	1200	600
1.0	1200	600
1.2	600	300

In the same way, RIMS KIR (Table 8) and TRO (Table 9) present similar results. IGS stations OUL2 and SOD3 are located closer to RIMS KIR and so the offset values are lower than those observed from ARJ6 and KIRU Stations. Offset values from ARJ6 and KIRU are lower for RIMS TRO than RIMS KIR as these stations are located closer to the RIMS TRO.

Table 8 Offset between AATR increase and xPL increase at RIMS KIR.

AATR Threshold (TECUs/min)	ARJ6 (s)	KIRU (s)	OUL2 (s)	SOD3 (s)
0.5	900	-	600	1200
0.8	900	900	600	900
1.0	900	900	-	-
1.2	300	-	-	-
1.5	-	-	-	-

Table 9 Offset between AATR increase and xPL increase at RIMS TRO.

AATR Threshold (TECUs/min)	ARJ6 (s)	KIRU (s)
0.5	900	2700
0.8	600	900
1.0	600	600
1.2	-	600
1.5	-	-

The criteria for the selection of the AATR thresholds are:

1. The AATR value should be as low as possible to identify the ionospheric activity as soon as possible. However, it must be noted that this criterion would increase the probability of false alarms. This must be taken into account.
2. The increase of both HPL and VPL (or at least the increase of one of them) must be clear.
3. The offset should be as great as possible to be able to activate the mitigation procedures as soon as possible.

From Table 5 it is observed that AATR values are greater in those RIMS located in the North-East (TRO, KIR) than those located in the North-West (EGI, RKK). To take this into account, and according to criteria 1, it is proposed to set a different AATR threshold in each region.

Based on the figures from Annex B and offset time from above tables, it is proposed to set an AATR threshold of 0.8 TECUs/min for Western RIMS (EGI and RKK) and 1.0 TECUs/min for the Eastern RIMS (KIR and TRO).

The assessment of IGS stations OUL2 and SOD3 concludes that it is proposed to not use them as part of this study. This proposal is based on the fact that these stations are in the edge of the EGNOS region. Due to the AATR characteristics, all ionospheric information is considered for its computation. That includes ionospheric information outside EGNOS area that may not impact on EGNOS system.

Regarding to GIVE indices, the analysis shows that correlation between AATR and GIVEI is not so clear. That is because selected IGPs are the closest ones to the RIMS stations. Therefore, selected IGPs only provides information about the ionosphere located over the RIMS but not about other areas where ionospheric information may impact on the RIMS positioning estimation (it is noted that RIMS measurements can be placed anywhere in the red area shown in Figure 23). So an ionospheric disturbance located in this red area (Figure 23) can impact in the xPLs and in the APV-I availability but it could be only observed in those IGPs located close to the ionospheric disturbance.

1.4 Conclusions

This study has analyzed the impact of Space Weather events in EGNOS performance. For that, a dataset of 31 days identified with EGNOS APV-I availability degradations due to ionospheric events were chosen.

The AATR analysis has shown the inverse correlation between the AATR values and the EGNOS availability. This correlation is also observed between AATR and HPL and VPL values: an increase of the AATR values leads to an increase of the xPL values.

AATR values present different distribution according to the IGS station. For the scenarios analyzed it is shown that IGS stations located in the North-East of Europe present higher AATR values than those located in the North-West, so for the use of AATR as indicator of ionospheric activity, different AATR values could be defined.

The analysis of the temporal evolution of xPL after an AATR threshold has revealed an offset between the AATR values and the xPL values. The values identified are:

Table 10 Summary of AATR thresholds per RIMS and Offset per IGS station.

EGNOS Area	RIMS	AATR threshold (TECUs/min)	IGS station	Offset (s)
North-West	EGI	0.8	ARGI	1200
			REYK	600
	RKK	0.8	ARGI	1200
			REYK	600
North-East	KIR	1.0	ARJ6	900
			KIRU	900
	TRO	1.0	ARJ6	600
			KIRU	600

The GIVE assessment has not provided relevant results. However, in this WP only a preliminary assessment has been done. GIVE data will be further analyzed for the definition of the macro-models during WP 6.

2. Service Degradation on HF

This section discusses the HF location service degradation caused by Travelling Ionospheric Disturbances (TID). Not only the transmission quality of HF communication links may suffer from TIDs, but analysis of radio transmissions may be affected as well. In order to learn about the potential location of a transmitter of an HF transmission direction finding technology is used. Several approaches to direction finding are in use, e.g. TdoA approaches measuring the time difference between the reception of a signal at different locations or the usage of multiple antennas positioned in a (typically) circular layout, measuring the azimuth of an arriving HF signal. Here we focus on the latter approach.

Service degradation on HF has been assessed by two working groups: The Leibniz Institute of Atmospheric Physics (IAP), contributing with the study of the azimuth variations in digisonde-to-digisonde measurements, and the German Federal Police (GFP), contributing with the study of the direction finder they operate in the western part of Germany, close to the cities of Bonn and Cologne.

2.1 Azimuth Variations in Digisonde-to-Digisonde measurements

The application of locating of a distant HF transmitter (mainly the azimuth) usually is known as HF Direction Finding.

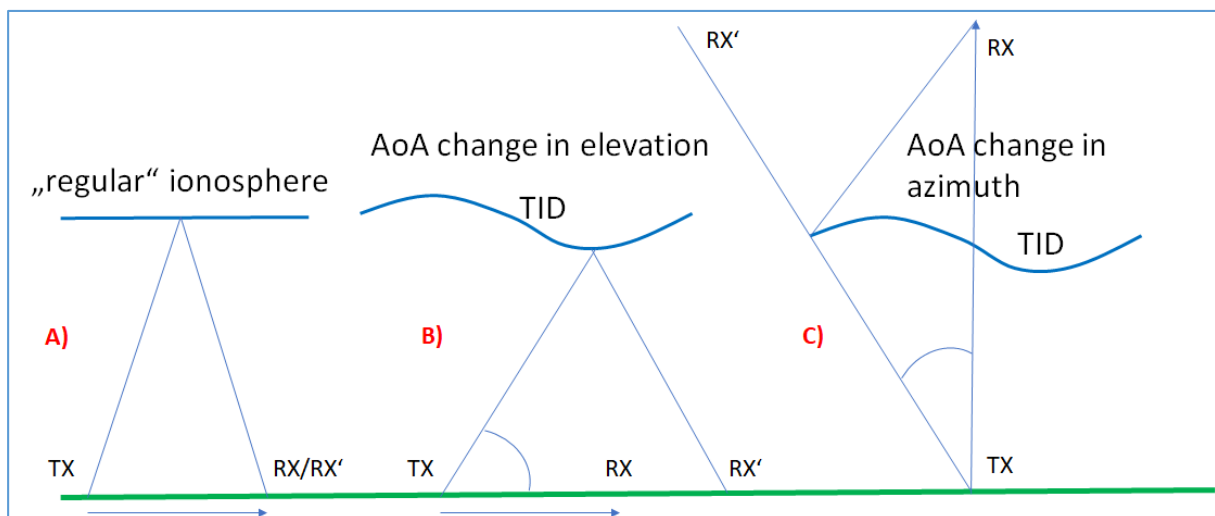


Figure 24 simplified representation of direction finding errors on a radio path between a fixed transmitter TX and a receiver at a fixed, known location RX.

Figure 24 presents three cases for direction finding errors on a radio path between a fixed transmitter TX and a receiver at a fixed, known location RX. *Case A*: Under undisturbed or “normal” or “regular” ionospheric conditions the ionosphere is more or less “flat”, and the measured location RX' is nearby the known location RX. *Case B* represents a TID travelling along the radio path; TID related height changes in the reflection area lead to changes in elevation, which let the measured receiver location RX' be in front or behind the known location RX. In *case C* the TID is travelling crosswise to the radio wave propagation direction; the slightly tilted ionosphere allows the radio signals to be reflected a bit left or right from the

main propagation direction, which leads to changes in azimuth of the measured receiver location RX'.

Because of the known fixed location of the Digisonde-to-Digisonde (D2D)-transmitters, the difference between the measured and the known azimuth could be a marker for: a) the quality of this azimuth estimation or b) a measure of the perturbation of the radio link nearby the ionospheric reflection area (like cases B or C) in Figure 24.

During sunrise and sunset, the ionosphere is tilted at the reflection area. This leads to a strong diurnal variation in the measured azimuth and by that the measured azimuth variations. By subtraction a mean azimuth from the measured single azimuth variations, we define an index, which describes these corrected azimuth variations for each radio path – the Digisonde-to-Digisonde Azimuth Performance Index D2D-APX.

A correlation analysis show that there is nearly no correlation between the Digisonde-to-Digisonde Azimuth Performance Index and TID events.

2.2.1 Data set

For this analysis, we use data from Digisonde-to-Digisonde (D2D) Doppler measurements from four European Digisondes, which are data contributors to the TechTIDE project. Station related information are presented in Table 11.

Table 11 D2D link characteristics

D2D Link	Data Availability	Link Distance	Calculated Azimuth
DB - EB	2015/07 – 2018/09	1082 km	15.7 °
AT – EB	2017/05 – 2018/01	1994 km	91.3 °
PQ - JR	2015/04 – 2019/03*	517 km	170.4 °
DB - JR	2018/03 – 2019/03	778 km	233.3 °

Table 11 provides information about the D2D-Links, data availability per link, their path lengths and the calculated transmitter azimuths seen from the receiver site. The first station code in the D2D Link column represents the transmitting Digisonde station, the second the receiving Digisonde. The abbreviations stand for DB – Dourbes/Belgium DB049, EB – Ebro Observatory/Spain EB040, AT – Athens/Greece AT138, PQ – Pruhonice/CzechRepublic PQ052, JR – Juliusruh/Germany JR055.

From the set of hundreds of Gigabytes of raw Doppler data, we have to extract single measurements with timestamp, signal strength and path geometry data like range delay and Angle of Arrival (Elevation and Azimuth). There is no official or regular analysis software for these purposes. The local processing is done with an old standalone version of TID-Explorer (TID-X v.0.3.0). To perform a first raw data reduction and extraction, we used the TID-X's Skymap Calculator with the following options:

- a) +/- 35° around calculated azimuth.

- b) Minimum 20 dB SNR.
- c) +/-5 Hz Doppler shift.

While preparing the data set for further analysis we have to deal with data gaps and other technical or ionospheric effects, which have negative influence on the data quality or make the data unacceptable to use:

- Regular data gaps due to morning/evening Digisonde Schedule Switching (SST)
- Data gaps on northern link due to ionospheric/geomagnetic conditions:
 - Weak frequency band during summer (increased Lowest Usable Frequency LUF) and low solar activity (decreased Maximum Usable Frequency MUF)
 - F layer splitting into F1 and F2 during summer
 - Blanketing F layer signals due to mainly summer sporadic-E
 - Lowering the already low MUF due to geomagnetic disturbances, which let the MUF be too close to the operational D2D frequency
- Not usable data, which mostly are related to technical issues or the radio link geometry:
 - Strong RF interferer, which saturate all receiver height bins and have too strong signals
 - High azimuthal variation in the near of the MUF (F1/F2)

Furthermore, we had to reduce the azimuths of multiple, so called skymap sources from different height ranges to one single azimuth value per timestamp. Because of our interest to study TID effects on the lower F region, we have to omit the lowest (E region), the highest (multiple F layer) echoes and focus on the so called fast-1F mode, which is the lowest detected signal from the F region corresponding to the shortest one hop radio path over the F layer.

To obtain this, we introduced several data reduction filters like Minimum SNR, Minimum and Maximum F layer range, Minimum and Maximum elevation, Maximum Doppler shift and RMS error. All these filters are set specifically for each D2D radio link.

The D2D link specific operating frequencies are used to distinguish between day and night conditions (see the horizontal dark green lines in the upper part of Figure 25).

Besides the individual transmitter antenna pattern, which describes the TX antenna gain depending on frequency and radiation direction, it is clear, that longer radio path lengths result in a weaker signal strength at the receiving site. The Frequency and Angular Sounding Technique (FAS, see HF-TID method in TechTIDE WP2) expects a minimum SNR of ~50 dB to extract reasonable TID characteristics from the raw D2D Doppler measurements.

At the end of year 2017, all contributing stations performed a hardware upgrade of their Digisonde transmitter card to increase the energy in each transmitted radio pulse during the D2D Doppler measurement. Since 2018 we use this new waveform to increase the signal-to-noise ratio (SNR) of the radio signal at the corresponding receiving station of each D2D radio link by about 10 dB (Figure 25).

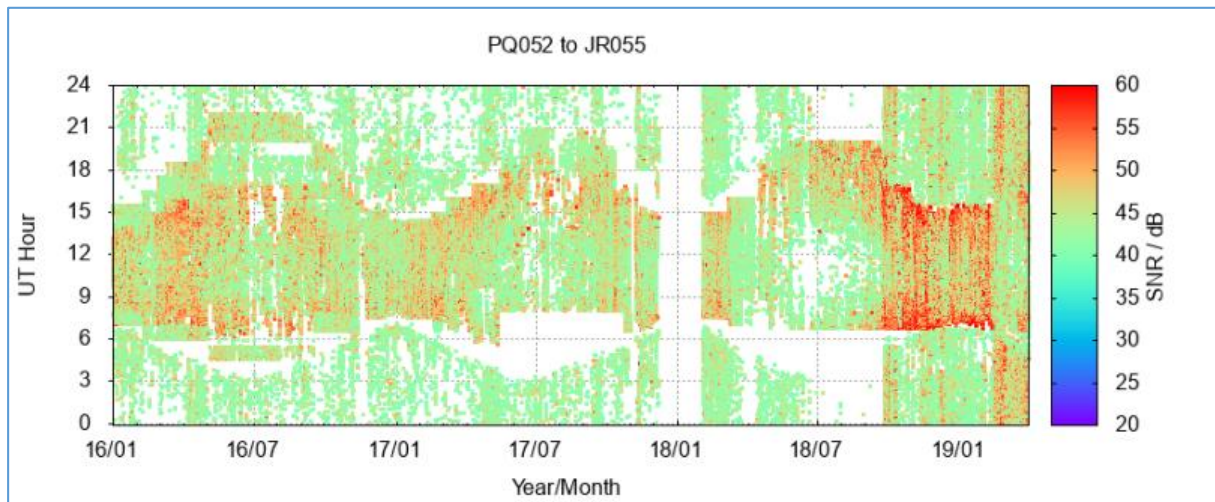


Figure 25 Signal-to-Noise Ratio (SNR) over more than 3 years for the D2D link Pruhonice to Juliusruh for signals with SNR > 40 dB

Figure 25 presents the Signal-to-Noise Ratio (SNR) over more than 3 years for the D2D link Pruhonice to Juliusruh for signals with SNR > 40 dB. Mainly the following effects are seen: a) diurnal variation caused by stronger ionospheric signals during daytime, b) seasonal variation, c) markedly stronger signal after August 2018 due to enhanced signal waveform, d) periods with larger data gaps partly related to technical failures and inappropriate frequency settings and partly related to low signal during nighttime.

The following two plots in Figure 26 clearly show the dependence of the azimuth distribution on the signal strength so, that stronger signals with higher SNR are less scattered around the calculated azimuth. Figure 26 presents example plots for a daily azimuth time series for the D2D link Pruhonice to Juliusruh for the day 09.01.2019. The upper plot is for signals with a SNR > 20 dB, the lower plot for signals with SNR > 40 dB. Mainly two effects are seen: a) stable azimuth at higher signal strength, b) loss of signal during late nighttime hours. - The dark green lines at ~210° azimuth represent the D2D operational frequency in MHz on the right x-axis.

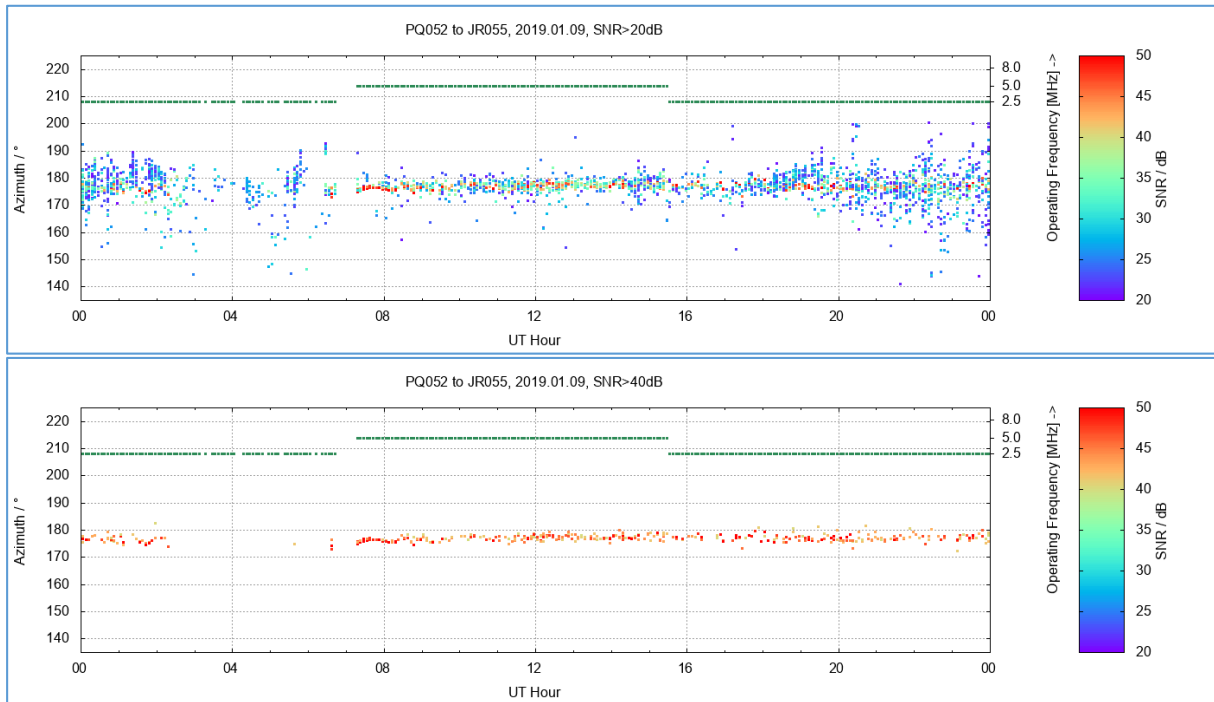


Figure 26 Example plots for a daily azimuth time series for the D2D link Pruhonice to Juliusruh for the day 09.01.2019.

2.1.2 The Digisonde-to-Digisonde Azimuth Performance Index

Depending on the D2D links, the set of single azimuths show a more or less strong diurnal and seasonal variation (see **Error! Reference source not found.**). This effect is noticeable mainly for the Pruhonice-Juliusruh D2D link.

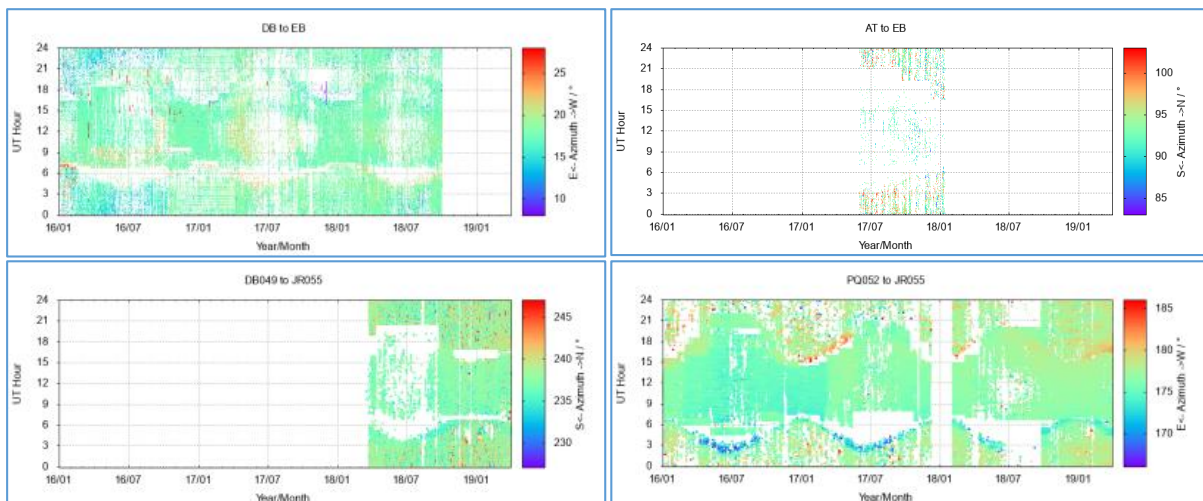


Figure 27 Color-coded azimuths over more than 3 years for all contributing D2D links for signals with SNR > 30 dB receiving at Ebre observatory (DB-EB, AT-EB) and with SNR > 40 dB receiving at Juliusruh (PQ-JR, DB-JR).

Figure 27 presents color-coded azimuths over more than 3 years for all contributing D2D links for signals with SNR > 30 dB receiving at Ebre observatory (DB-EB, AT-EB) and with SNR > 40 dB receiving at Juliusruh (PQ-JR, DB-JR). The color is centered at light green level, which represents the calculated or mean azimuth per each D2D link. For all links a more or less stronger diurnal variation and except the AT-EB link a seasonal variation is seen.

To obtain a time independent azimuth related index, a quiet time smoothed background have to be calculated. 27 days running means and running medians together with their standard deviations were calculated. Here, the 27-day median show more smooth results.

By subtracting the running azimuth median values from the single azimuth, we define the Digisonde-to-Digisonde Azimuth Performance Index D2D-APX according to the simple formula

$$D2D - APX = AzMn - RazMd$$

Where AzMn is the mean of azimuths per single measurement after filtering and RAzMd is the 27-day running median for the UT time of that measurement. Only means and medians with a standard deviation below 10° were taken into account.

In the sense of HF Direction Finding, the D2D-APX represents the deviation of the measured azimuth from the mean or calculated azimuth.

2.1.3 Analysis – Results

First investigations with D2D data with minimum SNR of 20 dB showed, that the spread of azimuth values is too wide and no reasonable results could be expected. Nevertheless, this low signal strength limit allows us to better detect technical failures on the links.

All further investigations were done with different minimum SNRs, 30, 40 or even 50 dB, resulting in smaller final data sets but with better data quality, namely smaller standard deviations.

Mean azimuths and their standard deviations are presented in the following table and figures.

Table 12 Mean azimuths and their standard deviations for all D2D links

D2D Link	AT-EB	DB-EB	DB-JR	PQ-JR
<i>Day</i>	92.1 +/- 2.0	18.0 +/- 2.4	237.3 +/- 1.5	176.3 +/- 1.8
<i>Night</i>	94.2 +/- 3.6	17.8 +/- 1.6	238.2 +/- 2.3	177.6 +/- 3.2
<i>Whole day</i>	93.9 +/- 3.5	17.9 +/- 2.2	237.9 +/- 2.1	176.6 +/- 2.3
<i>Meas. – Calc.</i>	2.6	2.2	4.6	6.2

Table 12 presents mean azimuths and their standard deviations for all contributing D2D links with a minimum SNR of 40 dB and for their available data in the period January 2016 until March 2019. The values are given in angle degrees and separately for daytime, nighttime and the whole day. Remember, the distinction between day and night conditions is given by the

operational frequency. - The last row shows the absolute difference between the mean measured azimuth and the calculated azimuth per each D2D link according to table Table 11.

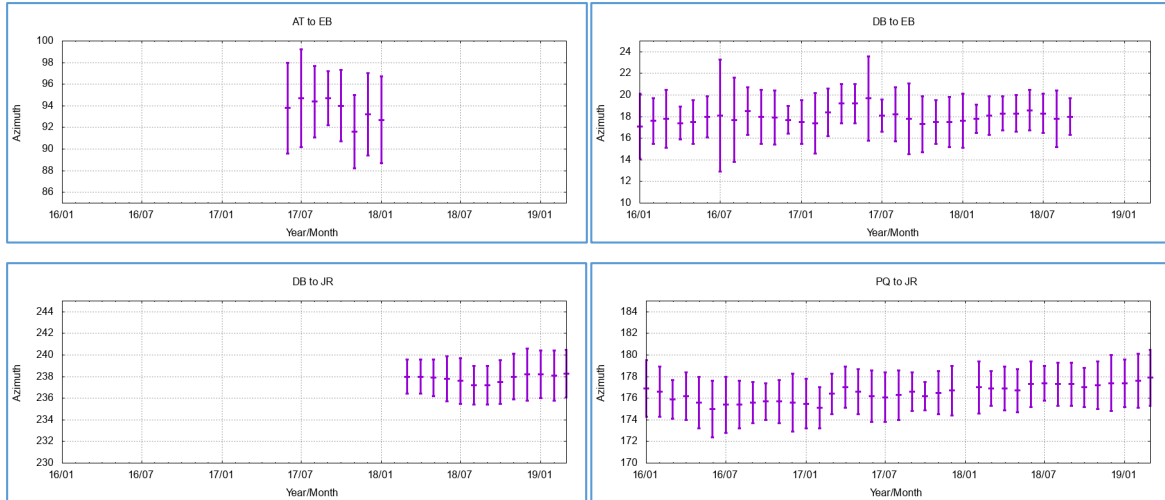


Figure 28 Mean monthly azimuths and their standard deviation for all contributing D2D links with a minimum SNR of 40 dB.

The D2D-APX distributions for the two primary D2D links are represented in Figure 29. Mainly the following effects are seen: a) the natural spreading of D2D-APX is stronger at low signal strengths, b) for a given SNR the spreading of D2D-APX is stronger during night than during day time and reaches up to $\pm 10^\circ$ for DB-EB and even up to 20° for PQ-JR, c) signals with SNR > 55 dB we reach only during daytime.

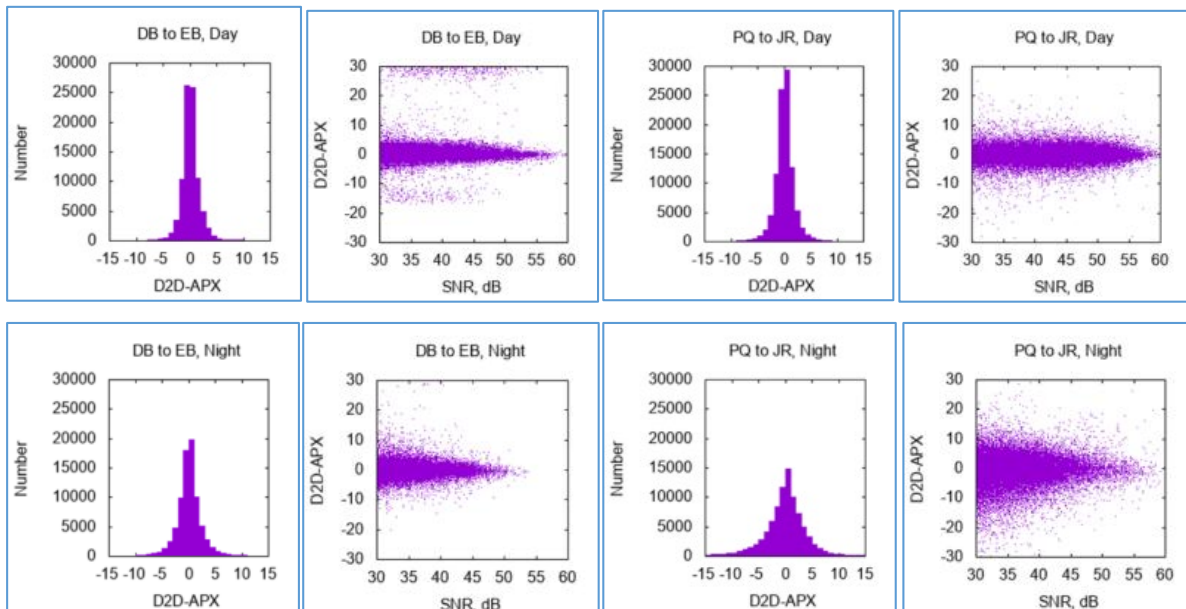


Figure 29 Quantitative distribution of the D2D-APX for the both primary D2D links with the longest data set of more than 4 years, DB-EB and PQ-JR. The minimum SNR is set to 30 dB.

The working group of TechTIDE WP3 collected a list of reference TID events over the last years. While checking and comparing the time periods from that TechTIDE WP3 EventsList, we found no larger D2D-APX values during that TID events.

Otherwise we found larger D2D-APX values, which does not correspond to any TID events.

To analyze a possible correlation between TIDs and larger D2D-APX values, the comparison was done by manual inspection of individual link recordings for each event from the list.

Unfortunately for the time, when high signal data exists (2018-2019) there's only one entry in the *WP3 EventsList* (21-24.01.2019). For this event, we found only some minor enhancements in the D2D-APX values for DB-JR and PQ-JR for signals with SNR > 40 dB. For the link DB-JR for signals with SNR > 50 dB we found one D2D-APX entry (2019 01 21 13 22 -9.1) at the very beginning of the event. We are not sure, if this entry is correct.

Nevertheless, there is a partly agreement of the TechTIDE *WP3 EventsList* with not well defined perturbations in azimuth.

On the other hand, we found single examples of TID or wave like structures in the recordings, where we also can see a significant variation in azimuth and an enhanced D2D-APX.

2.1.3 Summary/Conclusions

There is no general agreement with the TechTIDE WP3 TID *EventsList*!

The D2D-APX is provided for each D2D link separately for timestamps, when the D2D-APX exceeds a link specific threshold of 3 Sigma, 3 times the standard deviation of the D2D-APX.

Table 13 D2D-APX warning threshold limits for signals with SNR > 40 dB. The values given here are 3 Sigma for the while day (see table 2.2.b), but can be calculated for day and night separately.

D2D Link	AT-EB	DB-EB	DB-JR	PQ-JR
Threshold	10.5	6.6	6.3	6.9

With the appropriate software, the D2D-APX could be generated in near real-time. The D2D-APX can be easily adjusted and used as a threshold depending, color coded operational warning indicator for each D2D link separately.

For D2D-APX values greater than +/- 10° exists an ITU reference: A bearing error of +/- 10° (so called classD) of ill-defined bearing indication with very strong fading and interference is based on Recommendation ITU-R SM.854-3 table 1.

For further use of the Digisondes within the HF-TID method (see TechTIDE WP2), we recommend techniques to increase the SNR on the receiving site and a correct frequency selection in D2D measurements.

The receiving station Juliusruh shows an offset of ~5 ° in azimuth detections. That may be related to phase calibration issues in the RX antenna geometry or to local vegetation effects and should be investigated.

The strong summer sunrise effects seen in azimuths on the Pruhonice-Juliusruh link (~10 deg) could not be cleaned up completely.

2.1.4 Outlook

For further analyses on this topic, we suggest to investigate the following key points:

- Understand the quantitative effects of TIDs on the AoA variation. Which theoretical AoA variations we can expect from the radio path geometry?
- Discuss a “digital” classification of the TID-EventsList to better compare with detected TID effects
- Analyze the D2D-APX depending on D2D link direction and TID propagation direction. The primary D2D links are in north-south direction – north-south directed TIDs are mainly seen in elevation, east-west directed TIDs in azimuth.
- Crosscheck the sunrise/sunset effects with ionospheric tilt results from local Digisonde drift measurements
- Use other, shorter than 27 days, time period for the mean background calculation.
- Analyze similar effects on D2D elevation variations

Possibly this could be done within the remaining project period.

2.2 Direction finding

It consists of a highly sensitive antenna system for electromagnetic sky and ground waves with high bearing accuracy for the frequency range from 1 to 30 MHz, which is a set of rod antennas, installed in two 16/8 elements concentric circles and the additional computer equipment to evaluate the signals received by the antennas. It is optimized for the HF frequency range from 1 to 30 MHz. GFP’s direction finder is typically used as a directional antenna and in order to analyze the azimuth of arriving HF signals. Figure 30 and Figure 31 show a close-up and an aerial view photography of the site.



Figure 30 GFP Direction finder: antenna array



Figure 31 GFP Direction Finder aerial photography

Practical experience shows that azimuth measurements of incoming radio transmissions of known transmitters show deviations of different intensity. It may not be able to identify the true reason of a distorted measurement with high reliability. Nevertheless, as a first approach to better understand effects of ionospheric anomalies on HF direction finding we have chosen to correlate knowledge about TIDs with HF direction finding results.

We compared existing knowledge about TIDs in specific areas with the quality of direction finding results. We used HF communication links travelling through areas with ionospheric anomalies caused by TIDs at the same time.

2.2.1 TID databases

In order to gain knowledge about TID events we analyzed two different data sources:

- 1.) The website <http://tid.space.noa.gr/> is a result of a predecessor project of TechTIDE called NetTIDE and presents several measurement values determined by a set of cooperating ionosounders.
- 2.) The website <https://lgdc.uml.edu> is operated by the University of Massachusetts in Lowell and offers a database and the ability to search for specific TID events. It is possible to download TID data with 5-minute granularity.

For our analysis we have chosen to use data source number two. Figure 32 shows a slightly shortened (reduced number of data rows) example of such a data set.


```
# Global Ionosphere Radio Observatory
# Traveling Ionospheric Disturbance Subsystem
# TID Detection Database : Signal Tracking Module
# Generated by Track-Info-Servlet version 0.2 on 2018-05-18T20:18:12.755Z
#
# Requested TID ident: 197749
#
# Reference time (UT) 2017.07.28 21:53:15.000
# Receiver EB040 at 40.80N 0.50E
# Transmitter AT138 at 38.00N 23.50E
# Ground distance 1994 km
# Operating Frequency: 4725.0 kHz
# Polarization: O
#
##      Date      Time  path km  dopp Hz  zen deg  azim deg  SNR dB  Err deg  Amp dB
01,2017.07.28,21:18:15, 2469.0, -1.660,  61.91,  264.96,  24.3,  1.54,  21.3
02,2017.07.28,21:23:15, 2474.0, -1.489,  51.89,  254.90,  22.7,  1.32,  15.7
03,2017.07.28,21:28:15, 2467.3, -0.993,  64.58,  268.23,  22.2,  4.71,  15.9
04,2017.07.28,21:33:15, 2389.0, -0.684,  66.39,  265.71,  24.2,  2.01,  16.2

[...]
```

Figure 32 TID data set

The data set contains a time stamp, an ID, information about sending and receiving ionosounder (here: Sender AT138, an ionosounder installed at National Observatory of Greece in Athens and Receiver EB040 at Observatori de l'Ebre in Roquetes in Spain), their ground distance and some more information. Measurement values describing the state of the ionosphere are given in 5 minute time intervals. These values offer an insight to the TID situation between the positions of transmitter and receiver.

2.2.2 Measurement and Analysis process of GFP

Figures from 4 to 6 show a rough overview of GFP's measurement and analysis process.

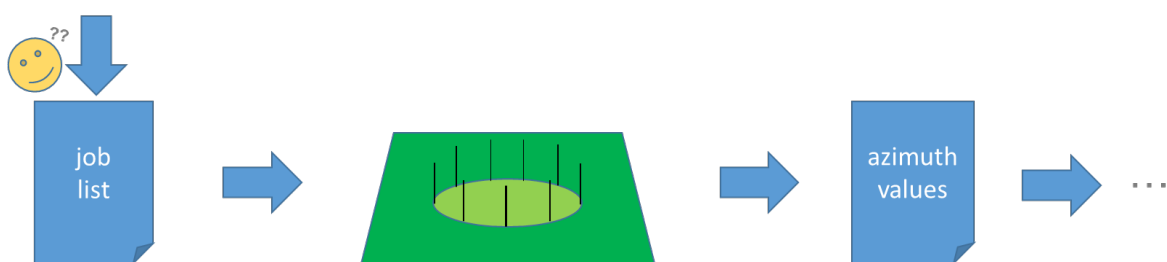


Figure 33 Job list processing.

A job list of transmitting stations is generated. This list is automatically processed by the direction finder control system. Azimuth values for all the senders from the job list are generated on a regular basis and stored in a database.

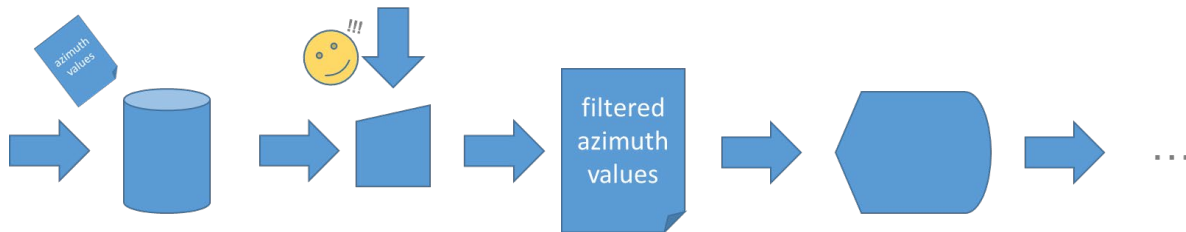


Figure 34 Data manage and filtering

This database offers query capabilities. So filtering the existing data for specific senders, receivers, combination of senders and receivers, date and time, frequencies and so on is possible. Visualization and export of these query results is possible in order to allow further statistical analysis.

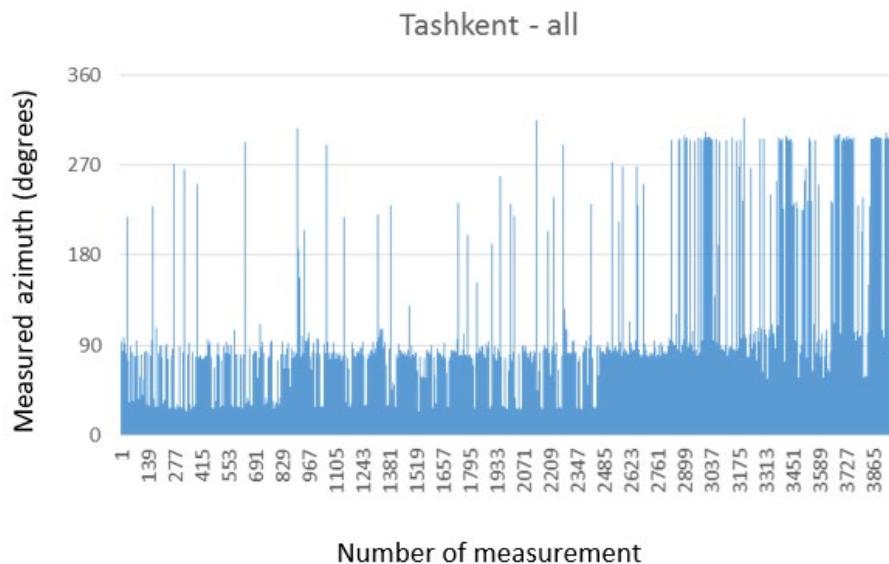


Figure 35 Data visualization.

Due to the fact that a 24/7 logging of direction finding results does not allow a manual online check if really the expected transmitter was sounded a significant number of incorrect measurements occurred. This can easily be seen in the Figure 35, showing measurement results from one transmitter. Obviously at least three to four different transmitters were found by the direction finder. As an easy workaround a filter process was added to remove all results deviating by more than a configurable azimuth value from the known true value. This workaround would obviously fail if two different transmitters are sending from approximately the same azimuth. Random samples did not reveal such problems, but this is not a guarantee that the processed data did not contain this kind of errors.

2.2.3 Statistical Analysis

A quick analysis of the TID database from University of Massachusetts in Lowell reveals that it contains an extensive set of measurements from several transmitter/receiver combinations: The most comprehensive sets are from the connections PQ052 -> JR055 (Pruhonice, Czech to Juliusruh, Germany) and DB049 -> EB040 (Dourbes, Belgium to Ebre, Spain). Thus we focus on

these two connections, especially the first one. Figure 36 shows the location of involved transmitters and receivers and the monitored HF links.



Figure 36 HF receivers/transmitters network.

Concatenating, sorting and separating of the database entries gives insight to presence or absence of TIDs on the monitored links. A clustering operation generates a list of dates and times of TIDs on a given link which can be visualized as follows:



Figure 37 TID presence or absence in the link Athens-Ebre.

Due to the highest amount of available TID information we mainly analyzed HF transmissions close to the PQ052 -> JR055 ionosounder test route.

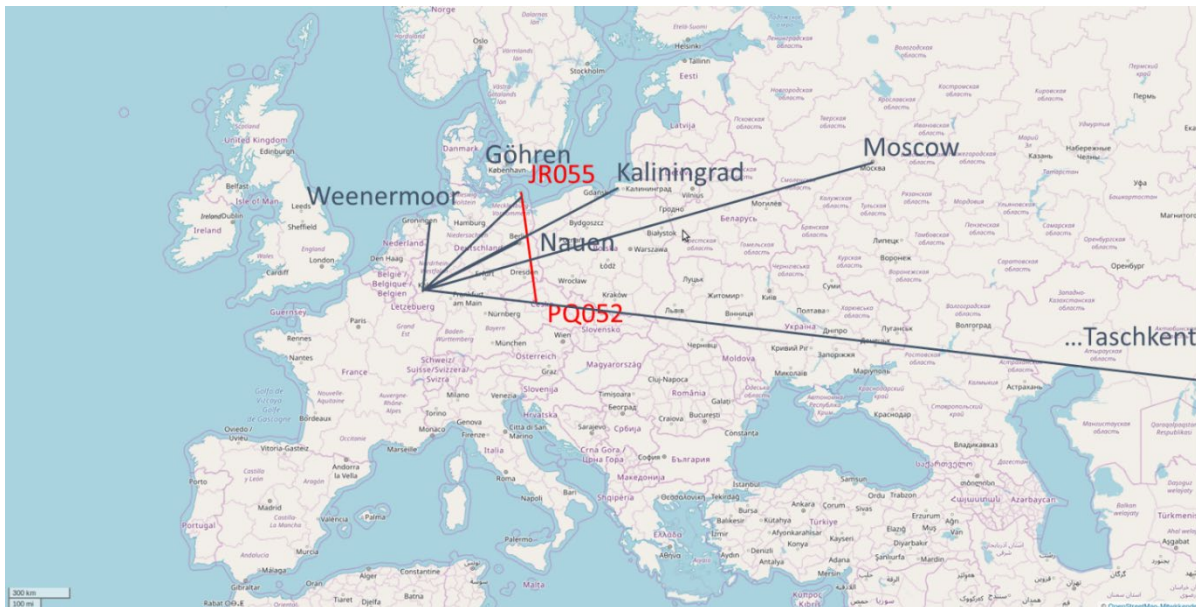


Figure 38 Juliusruh-Pruhonice link

It is easy to see that closest correlation of HF direction finder deviations and occurring TIDs should be observed roughly when there is a crossing of the middle of the ionosounder link and the HF communication link between transmitter and GFP's direction finder. This property can be observed best for the PQ052 -> JR055 ionosounder link and the Kaliningrad -> direction finder link. Here we can assume a reflection of the transmitted signal from the transmitter approximately in the same area which is analyzed by the ionosounders. The comparison of the measurement from the Kaliningrad transmitter with the other transmitters shown in the map of the Figure 38 confirms this assumption.

2.2.4 Statistical Results

Figure 39 shows azimuth values of approx. 5000 measurements. It is easy to see that two strong transmitters and several weaker ones were seen by the direction finder. A histogram of azimuth values shows that more than 3000 values lie in the true azimuthal direction of Kaliningrad.

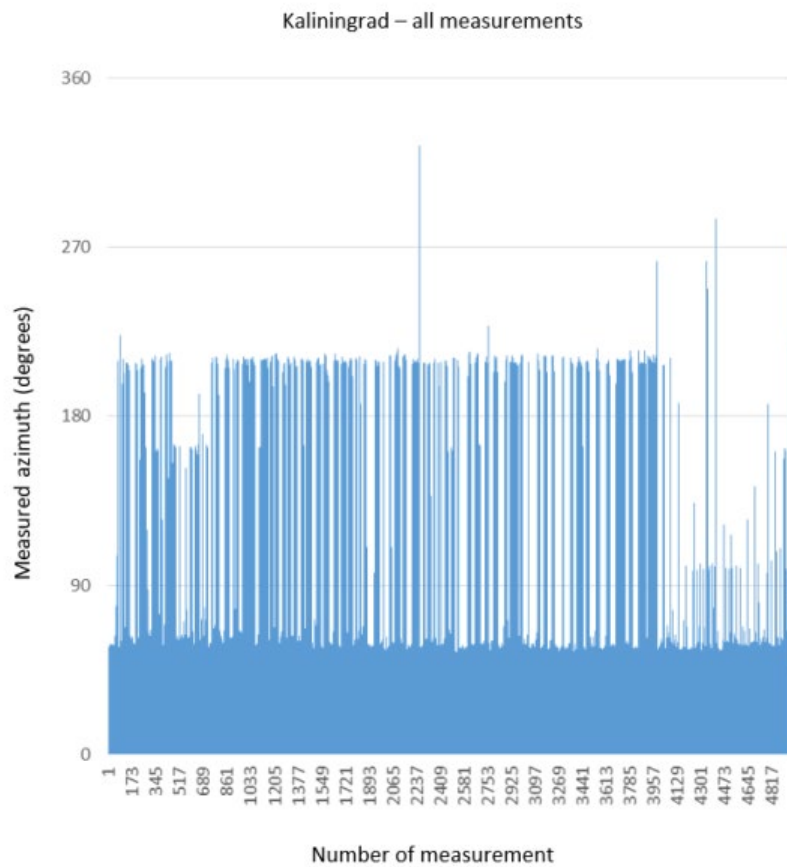


Figure 39 Histogram of measurements Kaliningrad

In this case filtering is easily applicable. The next figure shows the results after removing the measured azimuth values which pointed to completely different directions. Here we removed all values with a deviation of more than 30 degrees.

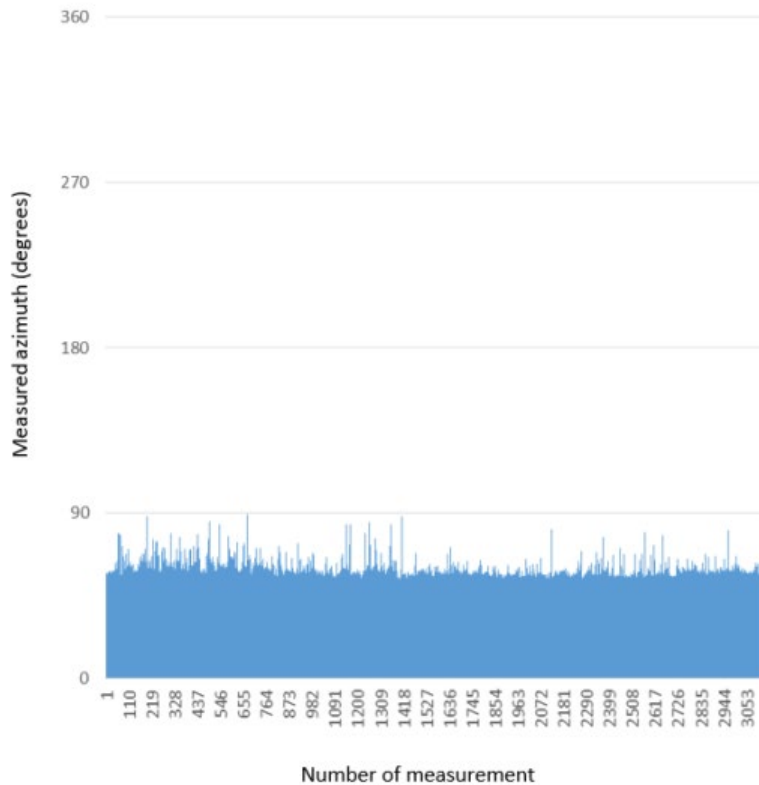


Figure 40 Filtered measurements.

We still observe a significant variation of measured azimuths. Based on the approach described in section *TID databases* we identified for every single measurement whether it was made during a TID period or not. Figure 41 shows the results of this binning. Every bar in this chart represents the mean squared error of azimuth measurements during a (numbered) TID. The rightmost bar represents the mean squared error of all measurements done during times where no TID could be observed. In order to illustrate the deviations this value is added as a dashed line. It can be observed that the quality of azimuth determination is not very good but still quite acceptable. In contrast to this the deviations during TIDs differ significantly: During some TID periods (e.g. #4, #6,...) the quality of measurements is really good, while sometimes (e.g. #35, which is the worst period) we see dramatic deviations between measured and real azimuths.

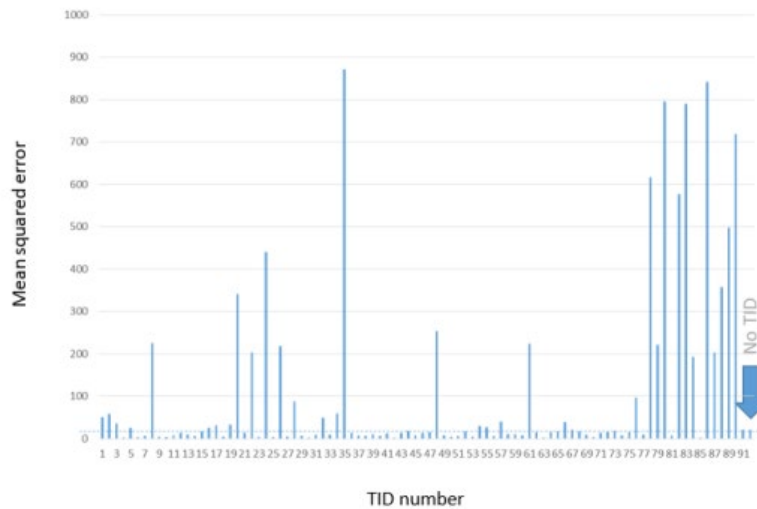


Figure 41 Mean squared error during TIDs – Kaliningrad

The Figure 42 shows the mean squared error for the transmitter location Weenermoor. The PQ050-JR055 ionosounder measurements give information about the state of the ionosphere approximately in the middle of this link, but the ionosphere in this location does not have influence on the link between Weenermoor and our direction finder, thus the mapping between distorted measurements and TID periods does not show clear results. This seems to confirm the expectation that a TID analysis has to be done in a location close to the area where the reflection on the ionosphere happens.

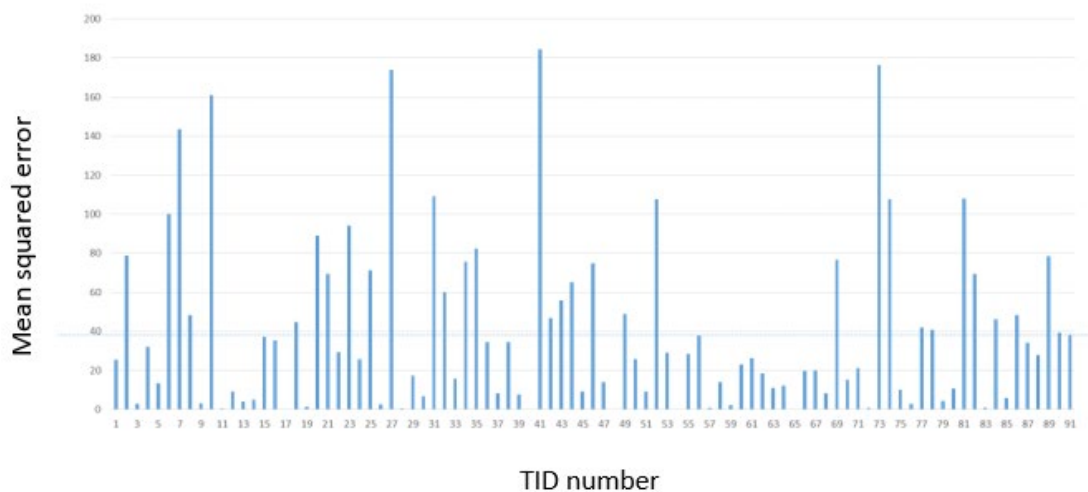


Figure 42 Mean squared error during TIDs – Weenermoor

3. Service Degradation on high accuracy services.

High accuracy services (HAS) are GNSS services using the carrier phase measurements as the fundamental observable. There are two main of HAS:

1.- Precise point positioning (PPP), which uses precise products of the GNSS satellites (orbits and clocks).

2.- Real Time Kinematics (RTK), which works through differentiating the user measurements with respect to the measurements of a near reference receiver.

Usually, PPP works using the ionospheric free combination of carrier phases, which allows the service to be quite unaffected by ionospheric perturbations, such as the Travelling Ionospheric Disturbances (TIDs). However, during the last years, numerous works have been published presenting a mitigation on the ionospheric effect in GNSS signals by using an external ionospheric model, thus they can have a positioning using single frequency signals [RD-4]. These works call such techniques as single frequency (SF) PPP. The problem with SF-PPP is that the accuracy of the external ionospheric models, typically Global Ionospheric Maps (GIMs), are usually at the level of several TECUs (see [RD-5]) which is, at least, one order of magnitude over the accuracy of the precise products used in PPP. Therefore, the quality of the navigation solution is quite degraded with respect to the expected accuracy using the ionospheric free combination of carrier phases (i.e. the standard PPP). Indeed, in [RD-6] it is shown that the typical accuracies of SF-PPP, using standard GIMs, are hardly at the sub-meter level in the 3D positioning error and only the more precise GIM used in Fast PPP [RD-7] provides accuracies at the decimeter level in SF-PPP. Then, in general, SF-PPP should not be considered as HAS.

Moreover, regarding the effect of MSTID in SF-PPP using a GIM as external ionospheric information, it is important to take into account that the typical amplitudes of MSTID are below 1 TECU (see [RD-8]). This is pretty much below the typical accuracies of the external ionospheric models. Therefore, it is worth to focus the study about the impact of TIDs in HAS on those services that requires accurate ionospheric corrections.

In the case of RTK or network RTK (NRTK), the service can work with both dual or single frequency receivers, and its performance depends on the distance between stations (see [RD-9] and [RD-10]). In the case of single frequency receivers, the ionospheric delay of the GNSS signals are corrected by assuming that is the same that the ionospheric delays suffered by the reference receiver (RTK) or a linear combination of the ionospheric effects suffered by the network of reference receivers (NRTK). For the single frequency receivers case, MSTIDs can affect the ionospheric mitigation, this is because:

- a) the required accuracy of the ionospheric corrections is at the level of a tenth of a TECU
- b) the baselines of RTK or NRTK are at the level of tens of kilometers which are comparable to the typical wavelength of MSTIDs.

During the last 10 years the concept of PPP-RTK has been under development. PPP-RTK uses the precise products from PPP and a ionospheric correction similar to NRTK. In spite of PPP-RTK works with the ionospheric free combination of carrier phases, the ionospheric corrections are used for speeding up the convergence time of the PPP solution. So, the

problem is similar to NRTK, this is the reason why we have focused the impact of MSTIDs in HAS in the NRTK service.

For this purpose, we work with a defined network of permanent stations closely located and with access to continuous gathered data.

3.1 The CATNET NRTK service

CATNET NRTK service is composed of 16 receiver stations located in the Catalonian region, Spain, belonging to the Cartographic and Geologic Institute of Catalonia (*Institut Cartogràfic i Geològic de Catalunya* - ICGC). From this 16-stations network, only 9 stations are implemented in this study: 3 receivers are used as *user rover's receiver* (PLAN, MARE, and SBAR), whereas 6 receivers are used as *permanent stations* (SONA, BEUD, BELL, GARR, LLIV and CASE). This decision is mainly due to the performance-distance relationship mentioned before. The location of each station is referenced in Table 14 as well as in Figure 43 NRTK stations . Distances between GARR and rover user stations are provided in Table 15. Distances between stations within the full network are provided in Annex C: Network Stations' Distances.

Table 14 CATNET Receivers specifications

Receiver	Geo-Distance	Latitude	Longitude	Type of receiver	Data Availability	
					From	To
PLAN	6369141.991	41.22769279	1.98695163	User receiver	001 / 2008	212 / 2018
MARE	6368868.186	41.33751032	2.43431900	User receiver	062 / 2011	212 / 2018
SBAR	6369551.946	41.78884865	2.17429311	User receiver	001 / 2008	212 / 2018
BEUD	6369391.625	42.06418880	2.67572687	Permanent receiver	193 / 2013	212 / 2018
BELL	6369608.416	41.40864751	1.40113711	Permanent receiver	001 / 2008	212 / 2018
SONA	6369365.058	41.80096138	1.51682187	Permanent receiver	177 / 2008	212 / 2018
GARR	6369503.026	41.10222500	1.91403558	Permanent receiver	001 / 2008	212 / 2018
LLIV	6369896.966	42.28654708	1.97304827	ICGC receiver	001 / 2008	212 / 2018
CASE	6368901.897	41.69167531	2.90416817	Permanent receiver	001 / 2008	212 / 2018

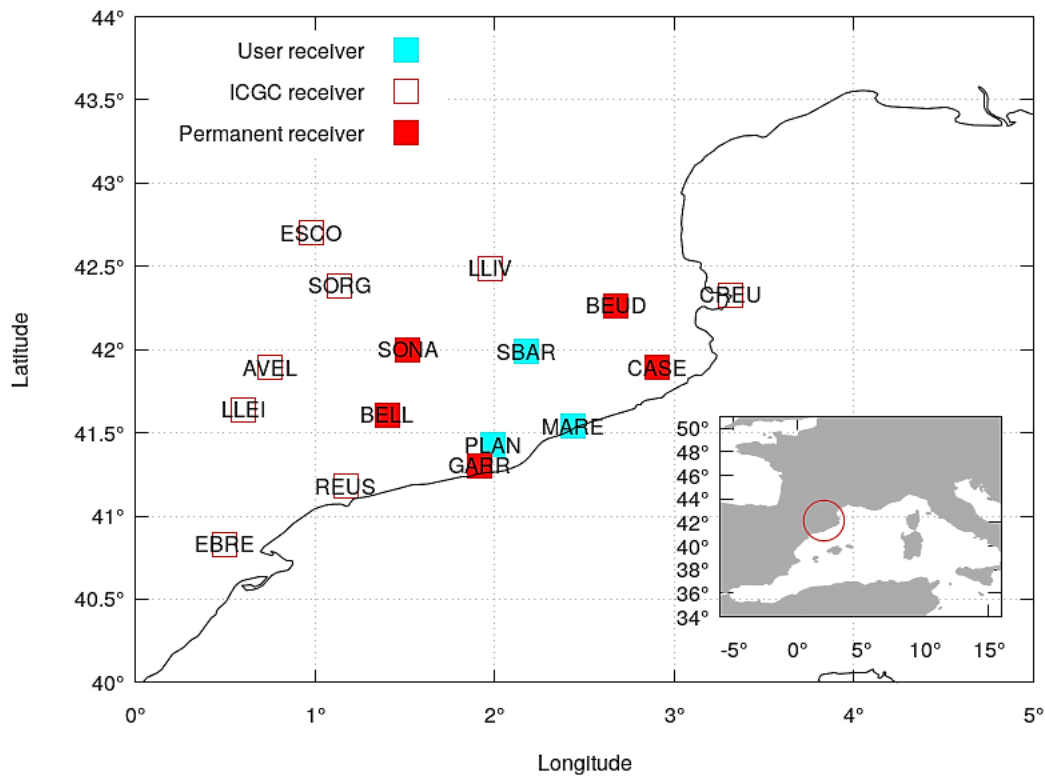


Figure 43 NRTK stations distribution

Table 15 Rover-Permanent receiver distances

	Station name	Station name	Distance (km)
1	GARR	PLAN	15.2248
2	GARR	MARE	50.7652
3	GARR	SBAR	79.3528

3.2 Establishing reference unambiguous measurements in the CATNET NRTK service

Besides the ionospheric effect, the accuracy of a HAS depends on several factors (geometry and quality of the corrections specially), which makes difficult to associate a degradation in the navigation solution to any of these different factors. In this section we will explain how we have selected the set of reference degradation values in the CATNET NRTK service.

3.2.1 Fixing carrier phase ambiguities in the CATNET NRTK service.

NRTK services are based on fixing carrier phase ambiguities and, after the fixing process, the carrier phases can be treated as very precise pseudoranges. Therefore, the accuracy of the solutions should depend on the capability of fixing carrier phase ambiguities which could depend on multiple factors ([RD-11]).

In order to avoid such dependency on the capability of fixing carrier phase ambiguities, we have taken advantage of the well-known positions of the receivers and we have solved the phase biases (fractional part of the carrier phase ambiguities. See for instance [RD-11] and [RD-12]) and estimated the integer part of the carrier phase ambiguities for all the measurements in the network. In this way, after correcting the measurements, we can work with unambiguous and undifferenced carrier phase measurements as very precise pseudorange.

In order to illustrate the fixing ambiguity process, the Figure 44 is presented. It consists of 4 panels, the two at the left side depict the values without fixing the carrier phase ambiguities whilst the two at the right side right depict values after fixing carrier phases ambiguities. In this same figure, the two upper panels represent the geometry-free combination of pseudorange (green) and carrier phases (red). Ionospheric combinations only accounts for the ionospheric delays, the ambiguities and instrumental biases. The two bottom panels depict the residual measurements in L1 (red) and P1 (green) (i.e. direct measurements after subtracting the well-known effects as geometry, clocks). It is worth to mention that, for fixing carrier phase ambiguities, it is necessary an initial estimation of receiver clock biases and the tropospheric delays (these two parameters do not affect to the geometry free combinations). Thanks to this initial estimation, it is possible to correct the measurements from these two parameters. This is the reason why the unambiguous carrier phase measurements (left bottom) presents a noisier behavior in contrast to the measurements with the fixed ambiguities (right bottom).

As commented before, carrier phase ambiguities have been fixed for each one of the 9 receivers (including *user receivers*) of the CATNET network. The initial approach was to continue with this methodology during all the days in 2017. However, we found that during the first half of 2017, the RINEX files were obtained using different convertors (*teqc* or *GPSNet*). These convertors, as they were implemented, treated differently the L2 carrier phase in the modern blocks (IIR-M or IIF). Indeed, it is well known that L2C have a shift of 0.25 cycles with respect to L2W that should be corrected in order to do not have incoherencies between different L2 signals (L2C or L2W) (for further information, regarding the quarter of cycle alignment, reader can consult [RD-13] and [RD-14]).

As it can be seen in Figure 45, the handling of this problem is different with *teqc* or with *GPSNet*. In this way, for those satellites having L2C, one can have non integer single differences (0.25 of cycle, around 21cm in wide lane) depending of the convertor used for generating the RINEX.

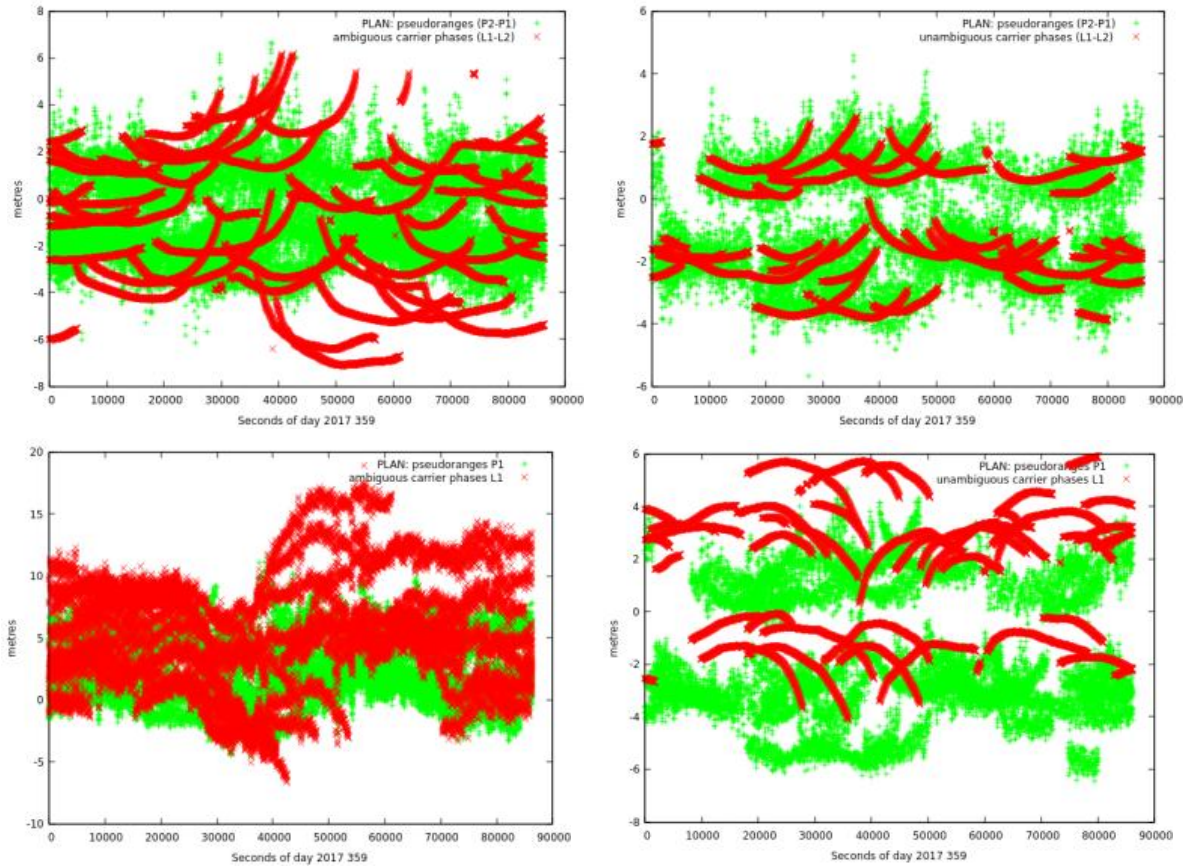


Figure 44 PLAN receiver positioning error

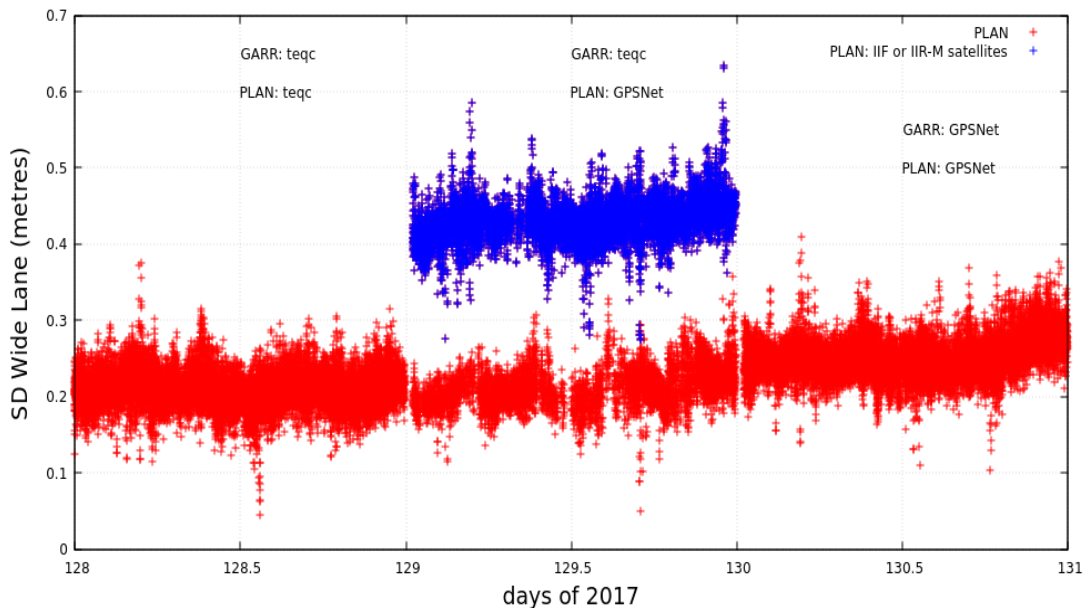


Figure 45 Positioning solution comparison tecq-GPSNet

The Figure 46 depicts the different convertors used for all the receivers in CATNET beginning at the year 2017. As it can be seen since the day 200 generation of the RINEX files has been done using “*teqc*”, this is the reason we have limited the study to a full one-year period, starting from the day 200 of the year 2017 until the day 200 of the year 2018.

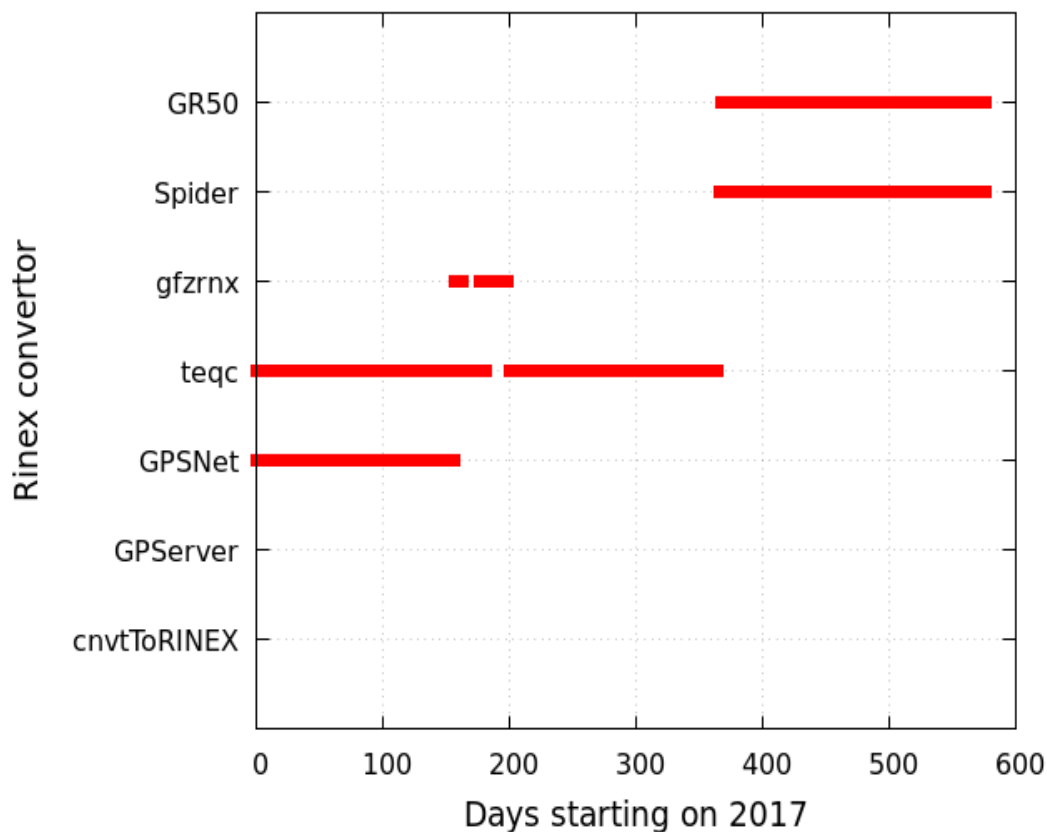


Figure 46 RINEX convertors discrepancies

This issue can be inspected for a longer time of period, covering a full solar cycle, as it is done in Figure 47 where the different RINEX convertors are depicted. In order to perform a more consistent study in terms of time and data, it is analyzed the time period from year 2008 to 2009, taking advantage of having one single convertor (*teqc*) working on the stations. Impact of the convertor *GPSNet* on the receivers is noticeable from 2010. This convertor does not apply the before mentioned 0.25 cycle correction, preventing the computation of carrier phase ambiguities fixing.

In this way, we are able to present results for two periods of time:

- 1) A two-years' period from 2008 to 2009
- 2) A one-year period starting at the day 200 of the year 2017 and ending at the day 200 of the year 2018.

This, in summary, allow us to perform a complete 3-year study.

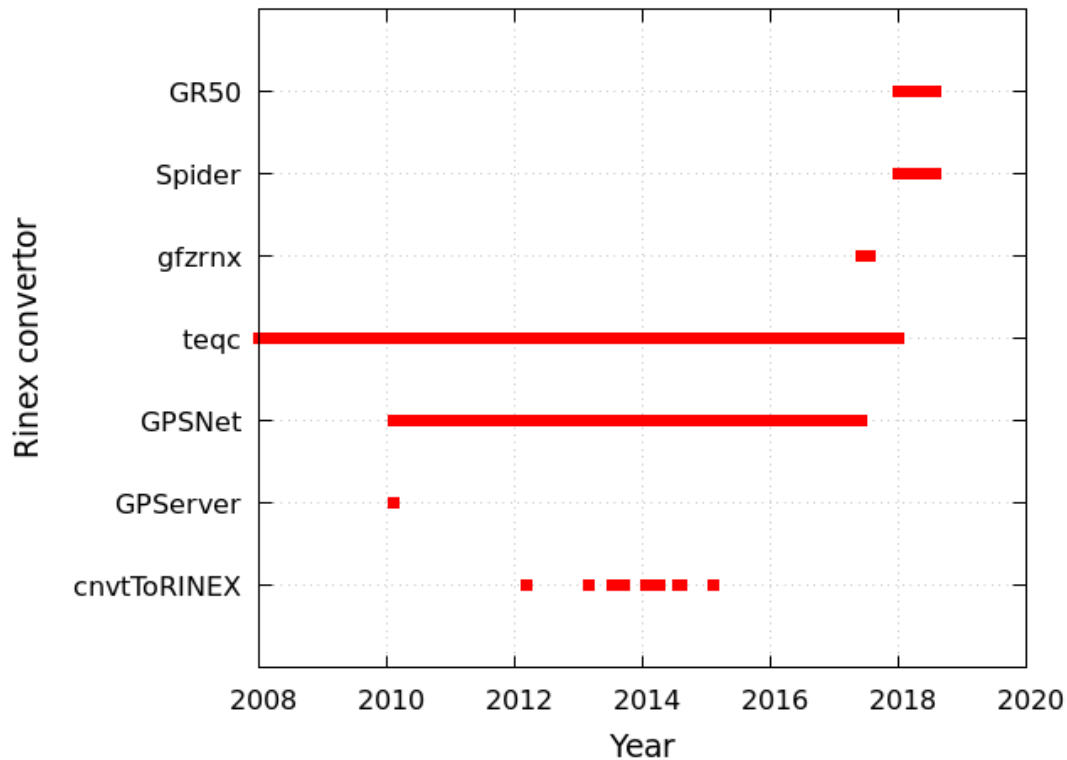


Figure 47 RINEX convertors discrepancies 2008-2018.

3.3 Obtaining the ionosphere free navigation solution.

Treating these unambiguous carrier phase measurements as precise pseudoranges allows to obtain reference position values using the ionosphere free combination (L_{IF}) of such measurements. These position values could be compared with the solutions obtained using L1 (corrected from the ionospheric delays and susceptible for being affected by the presence of TIDs). In this way, the difference between both types of navigation solutions can be attributed to the effect of the ionosphere in the GNSS signal.

The Figure 48 depicts the navigation solution using the ionosphere free combination of carrier phases. As it can be seen, the 3D error in the navigation solution is usually below 5 cm, except during some epochs with bad geometries. The red points correspond to the epochs when the DOP is larger than 4. This is normally the expected performance for a Network RTK (see for instance [RD-15], [RD-16] and [RD-10]).

The Figure 48 also depicts an example during one day for the *rover receiver* PLAN (i.e. the closest *rover receiver* with respect to a *reference receiver*). Because the solution is computed with the ionosphere free combination, one should expect similar results for all the other days and for the other user receivers.

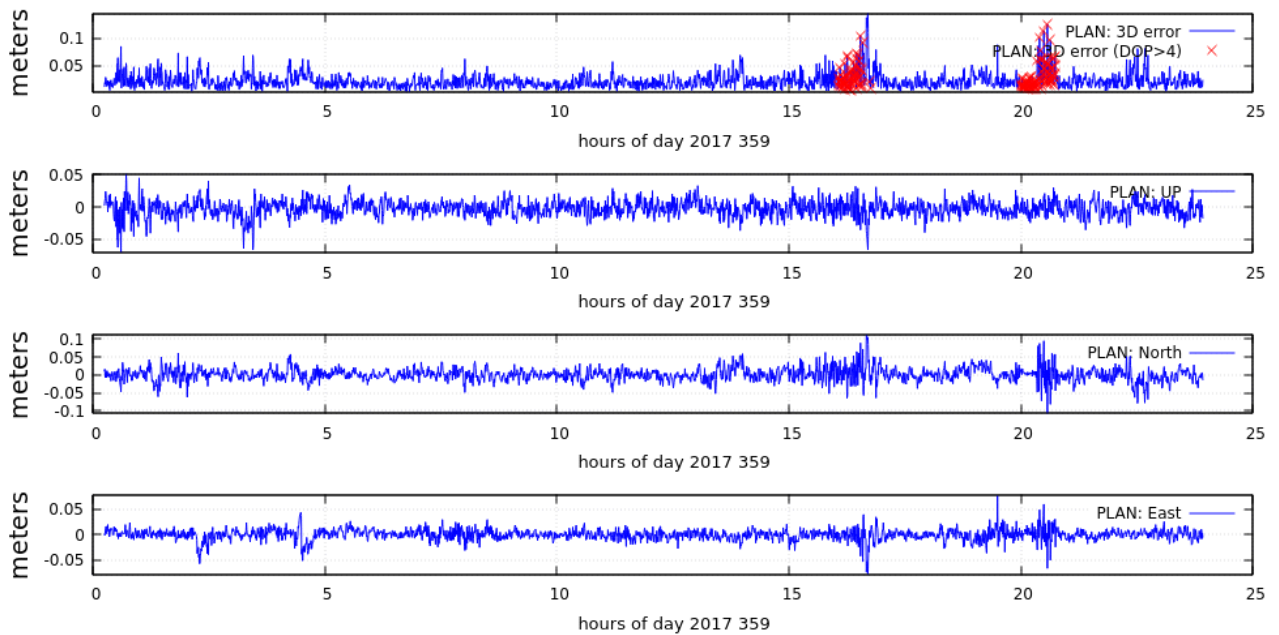


Figure 48 Ionospheric free combination navigation solution

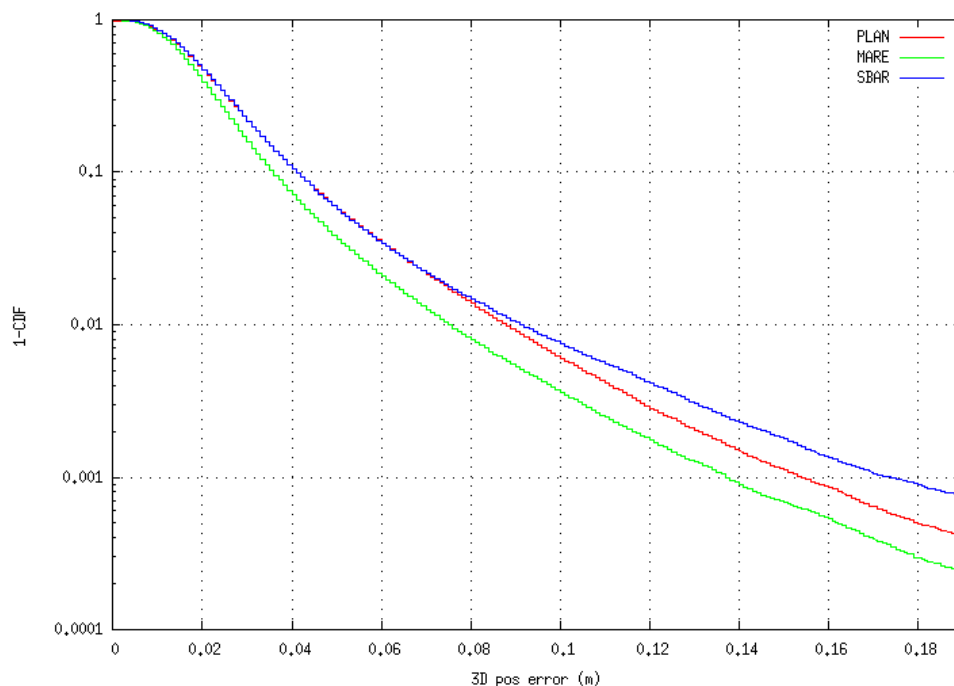


Figure 49 Statistics for the 3D positioning error using IF combination

Figure 49 shows the statistic of the 3D positioning error using the L_{IF} combination of carrier phases for each of the 3 user receivers. The statistic is done by depicting in the Y-axis, for each of the 3 rover receivers, the probability of the error to be greater than the value in the X-axis (i.e., the complementary of the cumulative distribution function), determining the value of 3D position error associated with a specific probability. For instance, for the 3 rover receivers, there are only around a 10% of the cases with a 3D positioning error greater than 4 cm and a

5% of the cases with an error larger than 6 cm. The Figure 49 also depicts the 3 rover receivers presents a similar behavior. We can establish this last value as a nominal reference value (95th percentile) for the 3D positioning error with the L_{IF} combination of carrier phases.

The full data source for the computation of IF navigation results for the 3 rover receivers is located at the internet address 147.83.27.240, within the directory:

http://147.83.27.240/TechTIDE_database/YYYY/DOY/NRTK_performance_CATNET/Data/

Where **YYYY** stands for the year and **DOY** stands for the day of the year. All the files within the folder are referred to the three rover receivers (SBAR, PLAN and MARE). Folder and files formats are the following:

Ionosphere free solution data files: *sd_sol_Lc.name*

This files contains the data for the three rover receivers (SBAR, PLAN and MARE) sorted by time (column 2), and specifying in the first column the reference system with "XYZ:" for the x, y and z position solution (in columns 3, 5 and 7, and with "ENU" for the east, north and up position solution (in columns 3, 4 and 5), as shown in Figure 7.

mare lc										
XYZ:	72030	0.016	.14E+01	-0.011	.77E+00	0.014	.14E+01	-0.002	.28E+00	0.147 .93E+00
ENU:	72030	-0.011	0.000	0.021						
XYZ:	72060	0.014	.14E+01	-0.007	.76E+00	0.011	.14E+01	-0.004	.26E+00	0.154 .92E+00
ENU:	72060	-0.008	-0.001	0.017						

Figure 50 Format of ionosphere free navigation solution data files

3.4 Obtaining the navigation solution using a single frequency receiver

The ionospheric free solution, shown in the previous section, requires a dual frequency receiver and needs a large convergence time (several tens of minutes) for achieving an accuracy at the level of 10 cm (or below). With a single frequency receiver (or in the case it is necessary to reduce the convergence time) ionospheric corrections provided externally by the service has to be used. In this way, the navigation accuracy will depend on the quality of the ionospheric corrections. These ionospheric corrections are computed typically through a linear interpolation from the ionospheric delays in one (RTK) or several (NRTK) reference receivers. In this way, the presence of MSTID with non-linear behavior will degrade the quality of the ionospheric corrections.

Thanks to the ambiguity fixing, we are able to assess the error of the ionospheric corrections used in RTK or NRTK. The 3D error and ionospheric error are presented in the Figure 51 and Figure 52.

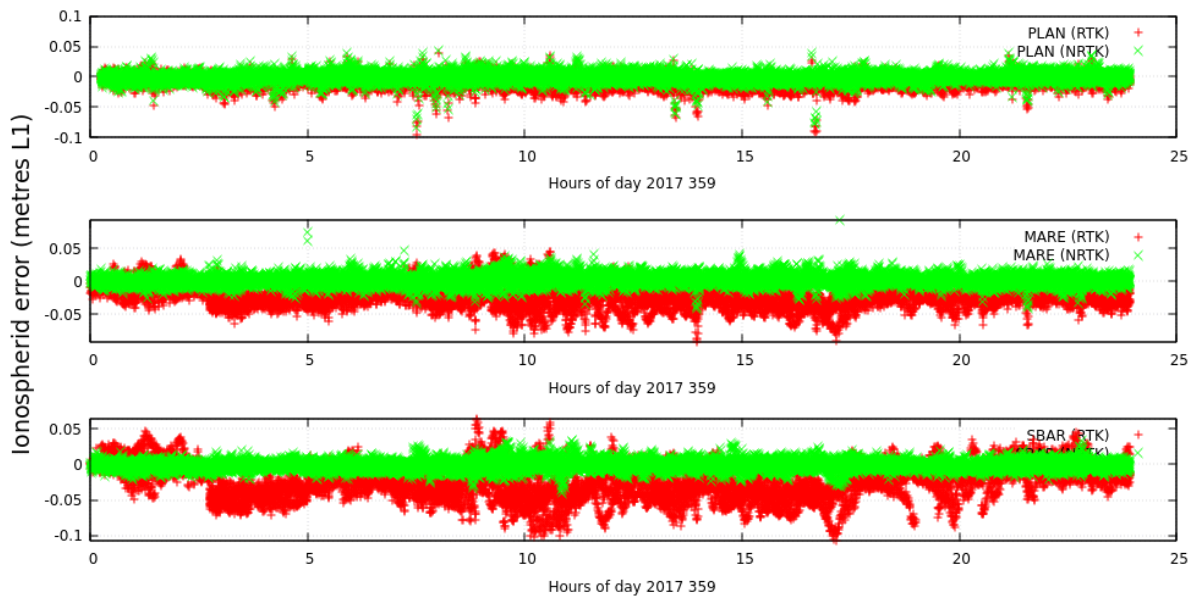


Figure 51 Ionospheric error

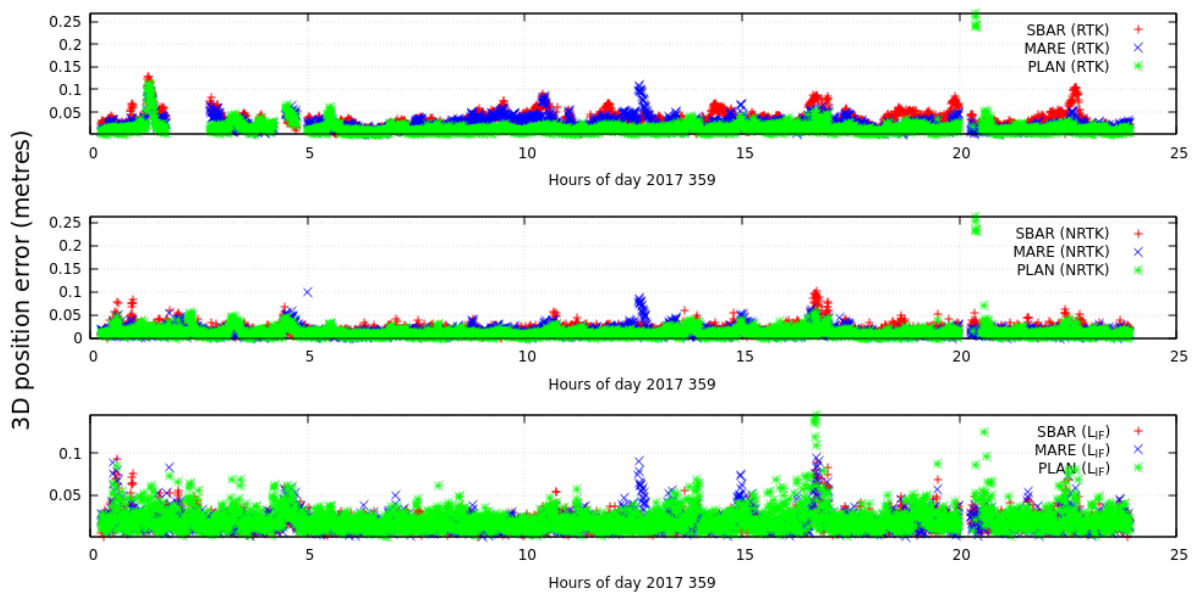


Figure 52 3D positioning error

If we use the same statistic methodology for assessing the positioning error using just the measurements in the L1 frequency, we obtain the results depicted in Figure 53, Figure 54 and Figure 55.

In the case of the nearest *rover receiver* with respect to a *reference station*, PLAN (at 15 km from GARR), it is possible to observe that the position error using L1 can be even smaller than using L_{IF}. This is because the differential ionospheric effects between PLAN and GARR are quite small and the thermal error of the L_{IF}, 3 times the error of L1, can predominate over the ionospheric error.

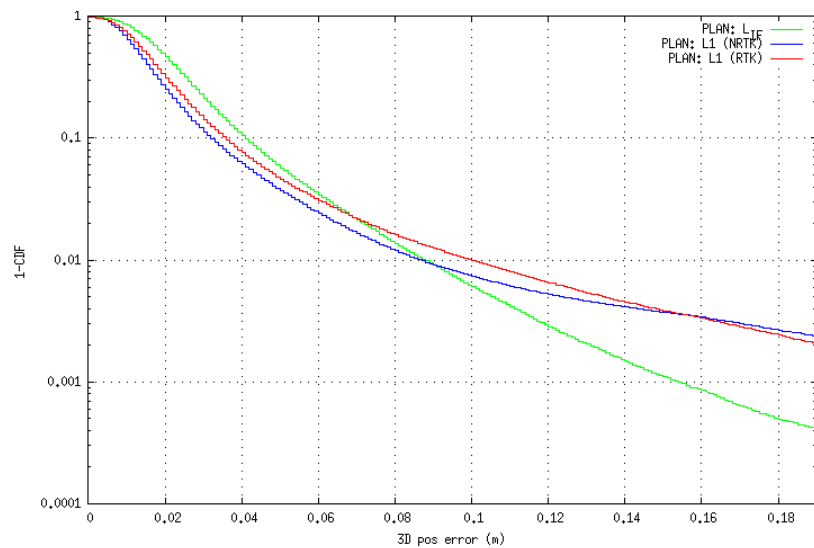


Figure 53 Statistics for PLAN receiver

In the case of MARE (at 50km from GARR) the ionospheric errors become more important than in the case of PLAN and the probability of having position errors larger than 6cm is now more than a 10% of the cases using L1 with RTK. However, if the ionospheric delay is corrected using the data from the network (NRTK) and the probability of having an error larger than 6cm is around a 5%. This is a quite good result which is at the level of the percentage in the case of processing with the L_{IF} (around a 3%).

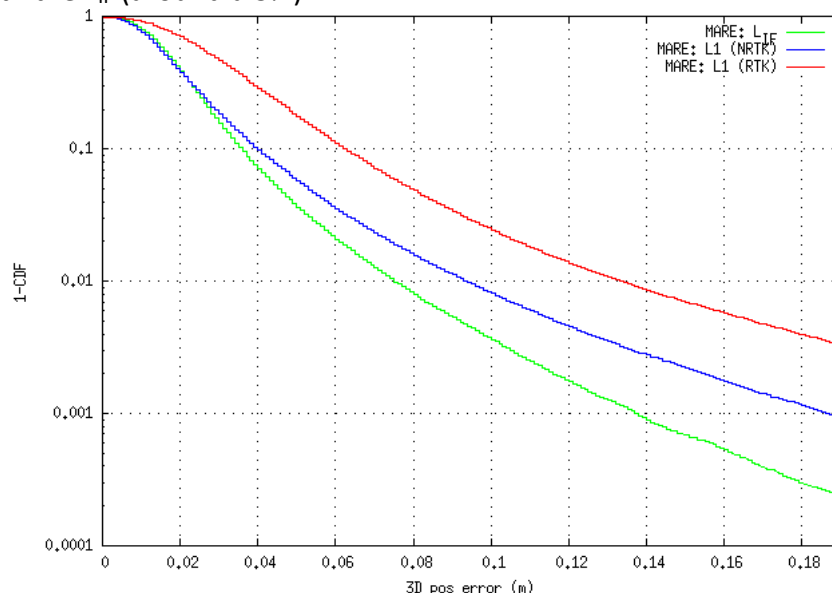


Figure 54 Statistics for MARE receiver

Lastly, for the rover receiver SBAR (at 79 km from GARR) the degradation on RTK increases considerably. Indeed, the probability of having an error larger than 6 cm in the 3D positioning is now close to a 30%, but the error using NRTK is maintained at the same levels than for MARE.

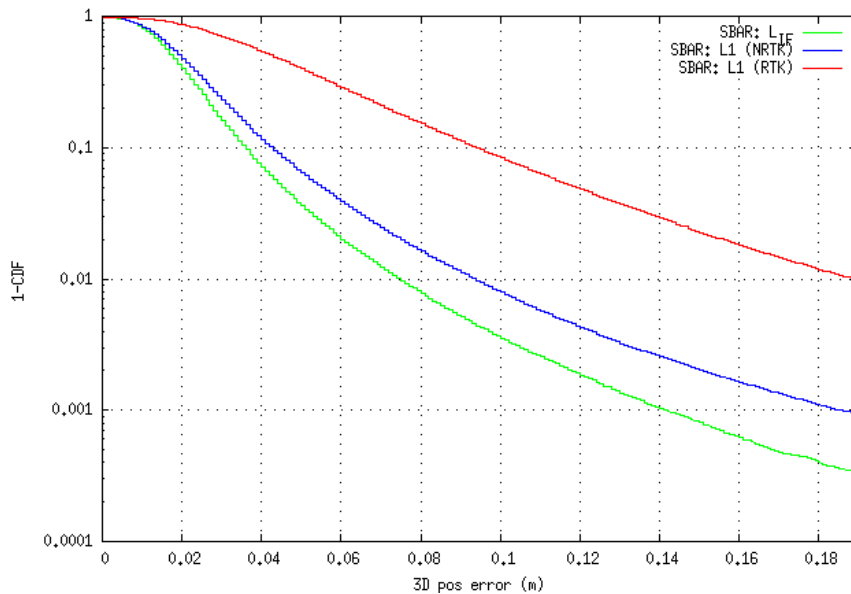


Figure 55 Statistics for SBAR receiver

The full data source used for the computation of the navigation solution using single frequency is located at the internet address 147.83.27.240, within the directory:

http://147.83.27.240/TechTIDE_database/YYYY/DOY/NRTK_performance_CATNET/Data/Solution/

Where **YYYY** stands for the year and **DOY** stands for the day of the year. All the files within the folder are referred to the three rover receivers (SBAR, PLAN and MARE). Folder and files formats are the following:

Single frequency solution data files: *sd_netsol_L1.name* and *sd_sol_L1.name*
This files contains the data for the three rover receivers (SBAR, PLAN and MARE) sorted by time (column 2), and specifying in the first column the reference system with “XYZ:” for the x, y and z position solution (in columns 3, 5 and 7, and with “ENU” for the east, north and up position solution (in columns 3, 4 and 5), as shown in Figure 13.

XYZ:	72030	0.003	.14E+01	-0.022	.77E+00	-0.002	.14E+01	0.002	.28E+00	0.167	.93E+00
ENU:	72030	-0.022	-0.003	0.000							
XYZ:	72060	-0.003	.14E+01	-0.021	.76E+00	-0.004	.14E+01	0.004	.26E+00	0.172	.92E+00
ENU:	72060	-0.021	-0.001	-0.006							
XYZ:	72090	-0.010	.14E+01	-0.020	.76E+00	-0.006	.14E+01	0.006	.24E+00	0.167	.92E+00
ENU:	72090	-0.019	0.002	-0.012							

Figure 56 Single frequency solution data format

3.5 Degradation of the single frequency solution with respect to the two frequency solution (IF).

From the previous study it is clear that the worst case for positioning with a single frequency receiver occurs for the farthest receiver, SBAR. For this reason, SBAR rover receiver is going to be selected to start our study. The same methodology will be applied and presented briefly for the two other rover receivers PLAN and MARE at the end of this section.

Let us define the degradation in positioning as the differences of the position errors using the single frequency navigation solution with respect to the two frequency solution. In order to mitigate the effect of different or bad geometries, we have imposed two requirements for considering the solutions:

1. both solutions shall be computed with the same satellites, ensuring satellite geometry impact is equally to both solutions.
2. the DOP of the solution shall not be larger than 6, limiting the amplification of error due to bad geometries.

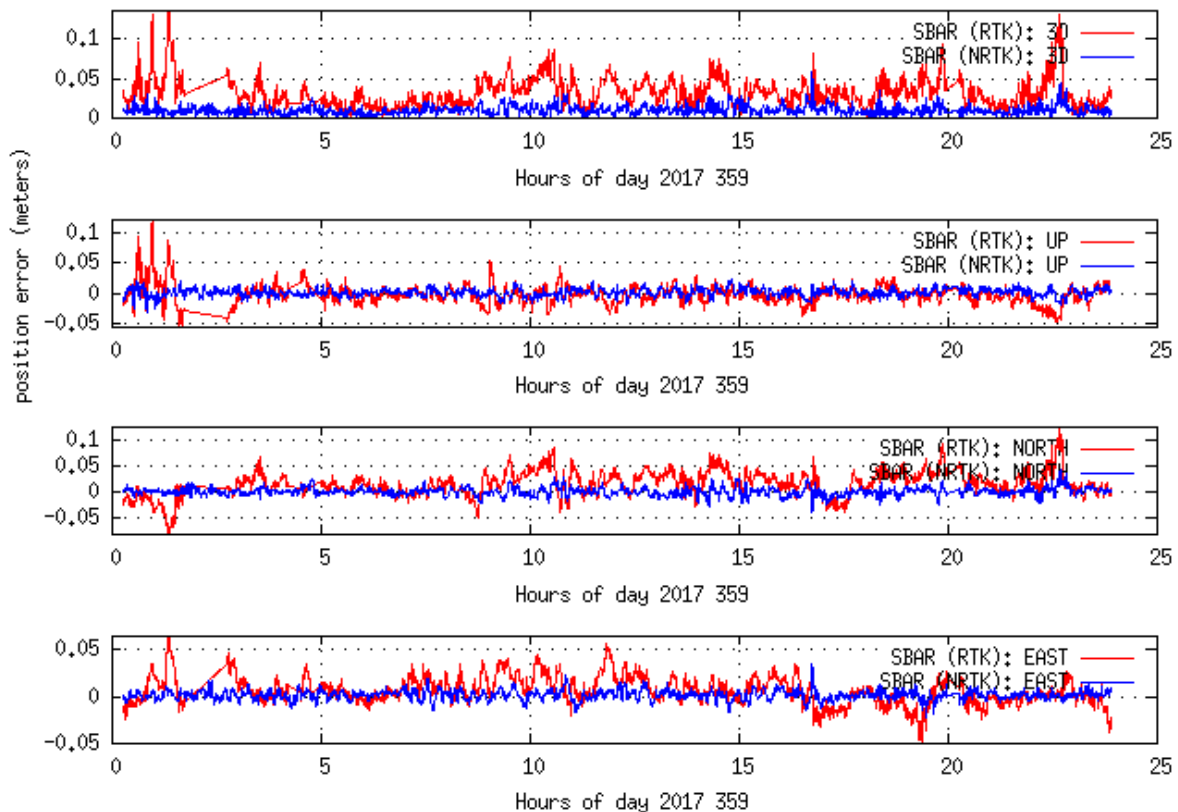


Figure 57 3D error using ionosphere free navigation

Following this approach, it is presented in Figure 57 the degradation vectors during the day 359 of the year 2017. The top panel depicts the 3D position error, while the other panels show, respectively, the degradation in the East, North and Up directions. It can be observed that, while the error of the RTK (red) solution can take values larger than 10 cm, the error of the NRTK solution (blue) is maintained below 5 cm.

The statistical results for the *rover receiver* SBAR regarding the 3D degradation during the days from 200 to 365 in 2017 and from 001 to 119 in 2018, this is a whole year, is presented in Figure 58. This plot confirms the results obtained and presented in the previous plot (Figure 57). Indeed, while in RTK a 10% of the cases present a degradation larger than 10 cm, in NRTK only a 0.2% of the cases present a degradation larger than 10 cm.

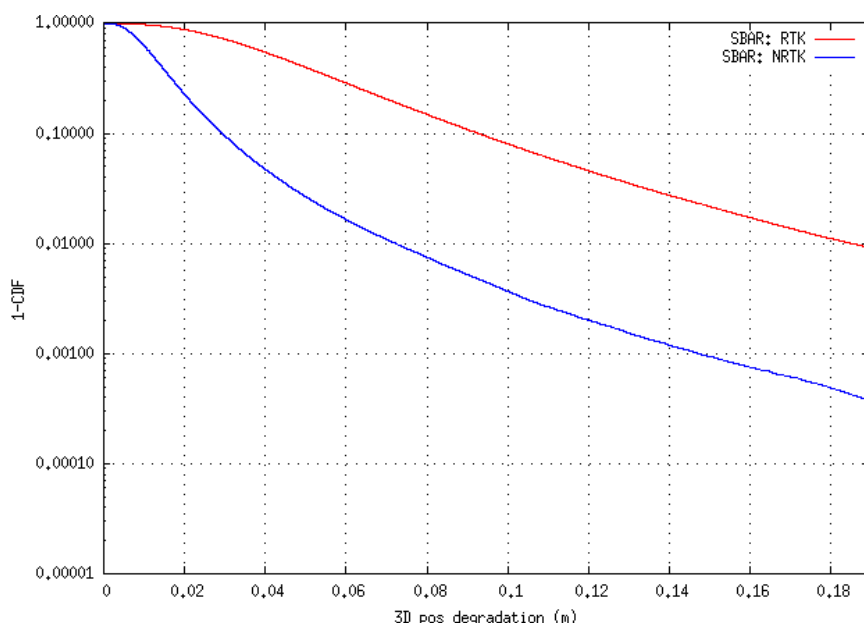


Figure 58 Statistics for SBAR receiver (2017-2018)

The full data source used for the computation of the degradation of the single frequency solution with respect to the two frequency solution is located at the internet address 147.83.27.240, within the directory:

http://147.83.27.240/TechTIDE_database/YYYY/DOY/NRTK_performance_CATNET/Data/Solution/

Where **YYY** stands for the year and **DOY** stands for the day of the year. All the files within the folder are referred to the three rover receivers (SBAR, PLAN and MARE). Folder and files formats are the following:

Positioning error data files: *pos_err.name*

This files contains the positioning error sorted by time (column 1) and if the navigation results were computed as RTK or NTRK (column 11). Columns 2, 3 and 4 corresponds to the error in the x, y and z components in the ionosphere free (IF). Column 5 stands for the 3D_{IF} position error, column 6 refers to the Dilution of Precision (DOP_{IF}), column 7 and 8 are the single frequency error and DOP, respectively. Finally, column 9 and 10 are the maximum instantaneous and averaged (over a 30 minutes' period) MSTID value, respectively. This data and its format is presented in Figure 16.

0	-0.004	0.045	-0.069	0.033	2.33e+00	0.053	2.33e+00	99.0000	99.0000	RTK
30	0.003	0.033	-0.043	0.009	2.33e+00	0.054	2.33e+00	99.0000	99.0000	RTK
60	0.003	0.036	-0.049	0.013	2.33e+00	0.064	2.33e+00	99.0000	99.0000	RTK
90	-0.001	0.045	-0.068	0.022	2.40e+00	0.065	2.40e+00	99.0000	99.0000	RTK
120	-0.007	0.042	-0.074	0.027	2.40e+00	0.063	2.40e+00	99.0000	99.0000	RTK
150	-0.002	0.029	-0.075	0.021	2.40e+00	0.063	2.40e+00	99.0000	99.0000	RTK
0	0.000	0.025	-0.039	0.033	2.33e+00	0.021	2.33e+00	99.0000	99.0000	NET
30	0.006	0.011	-0.017	0.009	2.33e+00	0.023	2.33e+00	99.0000	99.0000	NET
60	0.010	0.011	-0.017	0.013	2.33e+00	0.028	2.33e+00	99.0000	99.0000	NET
90	0.004	0.020	-0.032	0.022	2.40e+00	0.025	2.40e+00	99.0000	99.0000	NET
120	-0.001	0.015	-0.039	0.027	2.40e+00	0.026	2.40e+00	99.0000	99.0000	NET
150	0.002	0.004	-0.040	0.021	2.40e+00	0.024	2.40e+00	99.0000	99.0000	NET
180	0.000	0.005	-0.046	0.021	2.40e+00	0.026	2.40e+00	99.0000	99.0000	NET
210	-0.003	0.009	-0.056	0.040	2.40e+00	0.017	2.40e+00	99.0000	99.0000	NET
240	0.003	0.016	-0.034	0.026	2.41e+00	0.011	2.41e+00	99.0000	99.0000	NET
270	-0.004	0.014	-0.048	0.034	2.41e+00	0.016	2.41e+00	99.0000	99.0000	NET

Figure 59 Positioning error data files

As it was mentioned at the beginning of this section, Figure 60 and Figure 61 are the result of the same methodology applied in the MARE and PLAN receivers.

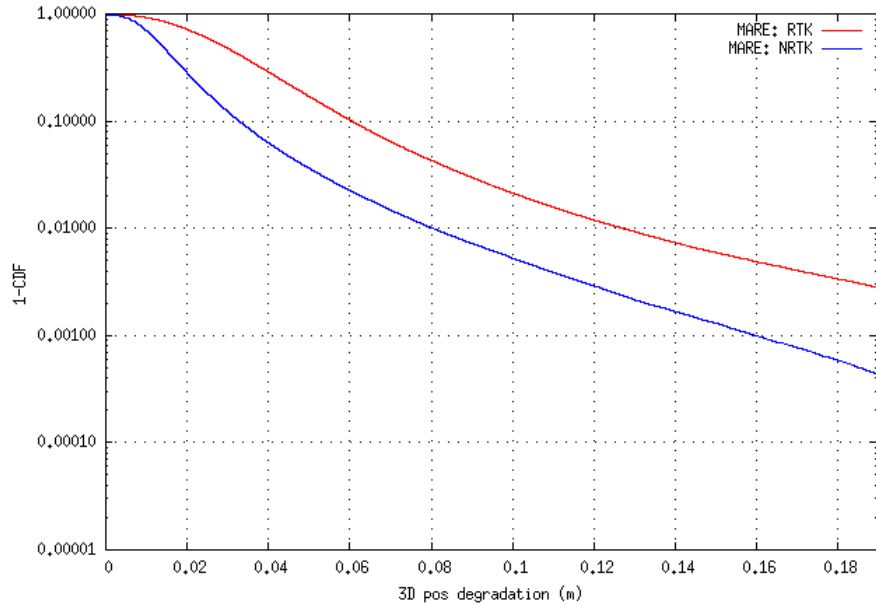


Figure 60 Statistics for MARE receiver (2017-2018)

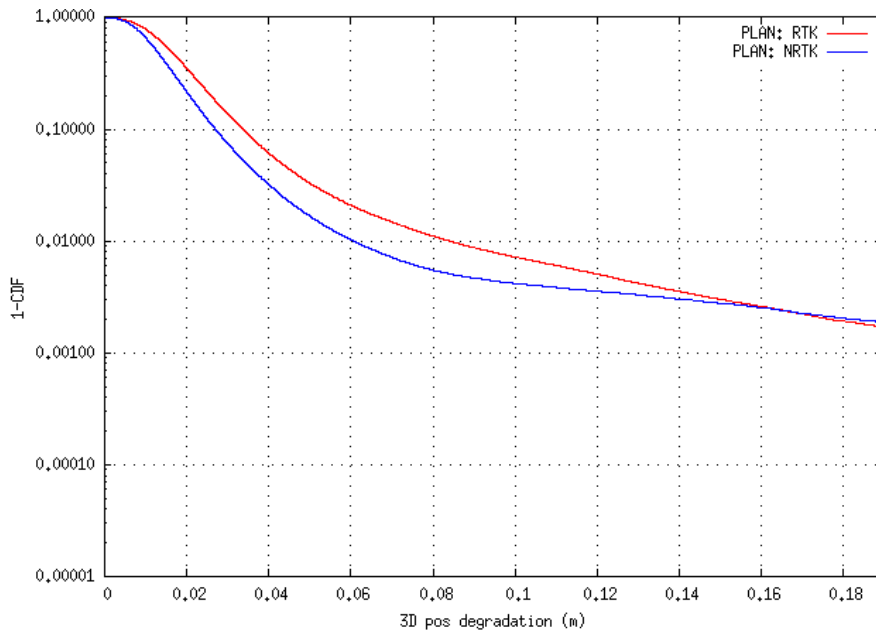


Figure 61 Statistics for PLAN receiver during the days 200-365

3.4 Effect of MSTIDs in position degradation

In the previous sections it was shown that the NRTK solutions are close to the solutions using a dual frequency solution (L_{IF}). In this section we will see that part of the degradation in the NRTK solutions are associated to the presence of MSTID. For instance, in Figure 62 it is depicted the degradation in the 3D positioning and the MSTID index for a 5 days period. It is

clear that for some of the peaks in the degradation occurs around the time when the MSTID index for the receiver SBAR reaches largest values.

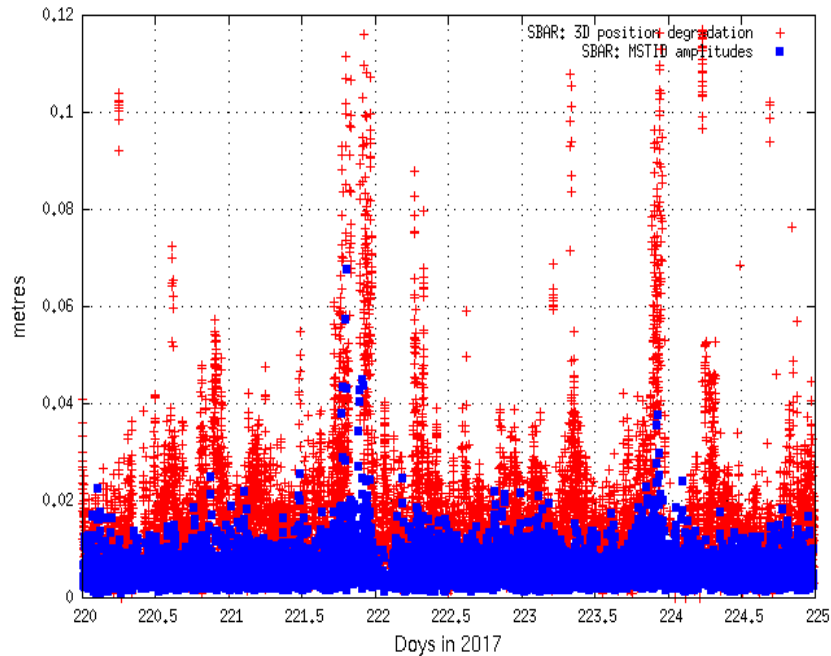


Figure 62 SBAR 3D position degradation and MSTID

Figure 63 presents the degradation of the receiver position for SBAR and the $D^2\text{STEC}$ (this is, the measurement that feeds the MSTID-GNSS index) for the permanent receiver BEUD and the user receiver SBAR. This figure reveals that the degradation in SBAR position is not only related with a MSTID affecting the user measurements, but extends to a MSTID having an impact in any of the receivers in the network. In other words, a MSTID affecting any of the receivers used for the interpolation can affect the computation of the ionospheric correction in the network.

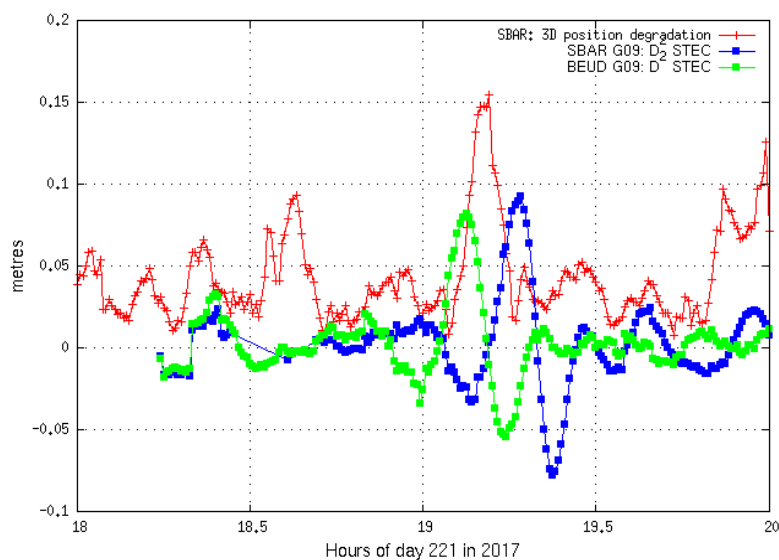


Figure 63 3D position degradation and $D^2\text{STEC}$

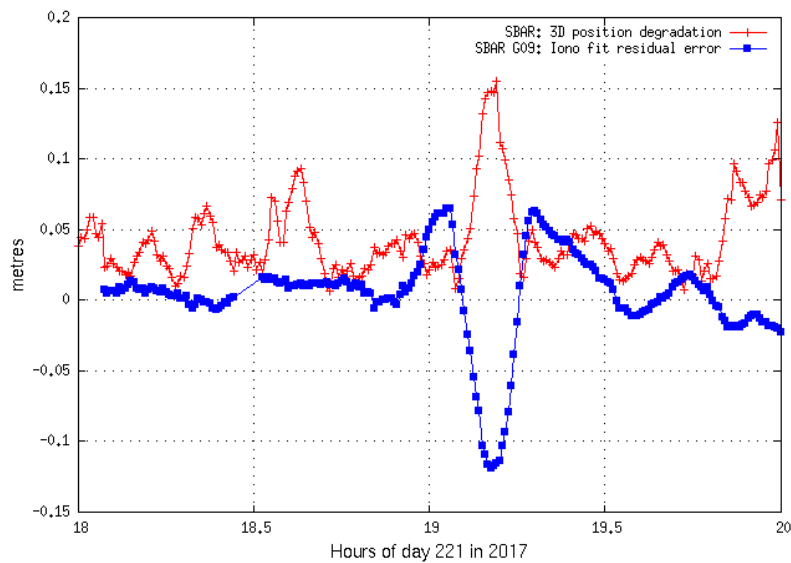


Figure 64 SBAR 3D position degradation and Ionospheric residual error

In contrast, due to the presence of the MSTID, the linear interpolation of the STECs from the reference receivers to the user positions provide larger errors with respect to the actual STEC in the user receiver. This phenomenon can be observed in Figure 64, where the residual error due to the ionosphere is clearly correlated with the 3D positioning error of the SBAR receiver. Figure 65 presents the 3D position error for three stations (MARE, PLAN and SBAR, from left to right) in contrast to the amplitude of the MSTID, during two days (298 and 325) of year 2017. A strong and noticeable relationship exists between the degradation in the position error of the receiver and the maximum detected MSTID amplitude in the NRTK network. For a better representation, MSTID amplitude has been amplified by a factor of 4 its original amplitude.

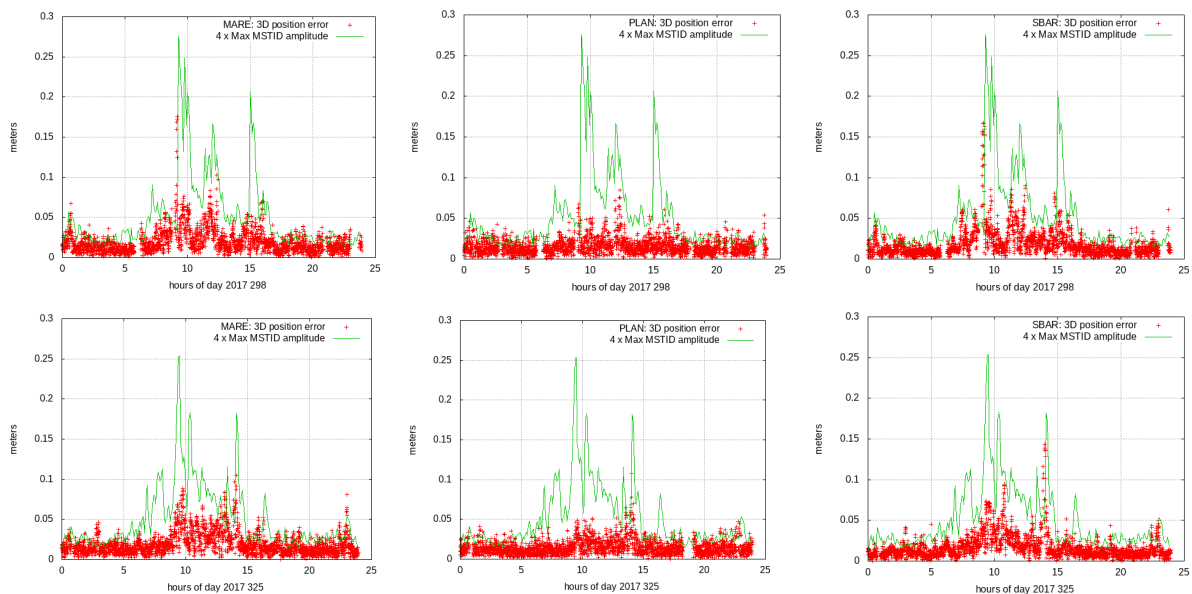


Figure 65 Position error and MSTID amplitude for MARE, SBAR and PLAN receivers.

An analysis for the set of days of the year 2017 from 200 to 365, and the set of days from 001 to 200 of the year 2018 is presented in *Figure 66*, *Figure 67* and *Figure 68*, for the three different rover receivers.

In order to see the relationship between position degradation and MSTID, NRTK solution is computed for MSTID amplitudes lower than 0.01 (LI meters), for which a 0.2% of the cases present a degradation larger than 10 cm, and MSTID amplitudes lower than 0.015 (LI meters), for which only a 0.1% of the cases present a degradation larger than 10 cm.

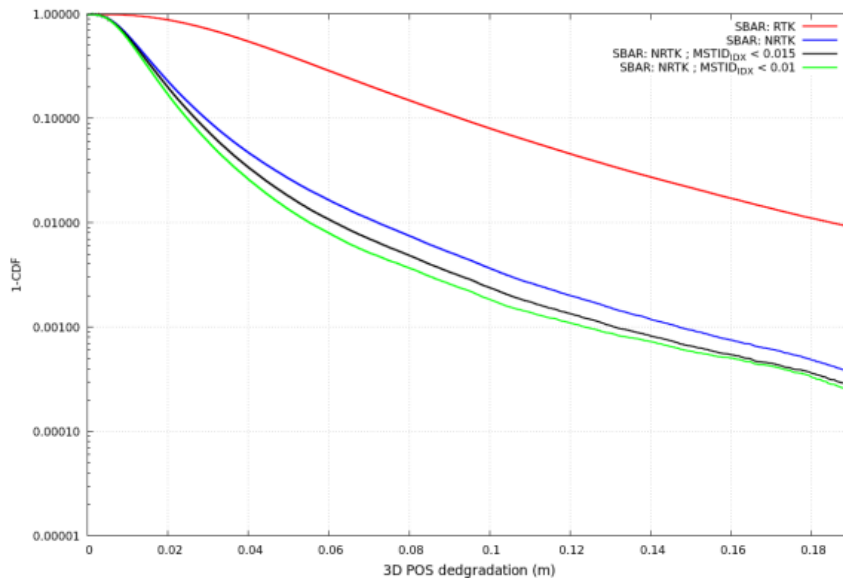


Figure 66 3D Position degradation probability for SBAR (2017 - 2018).

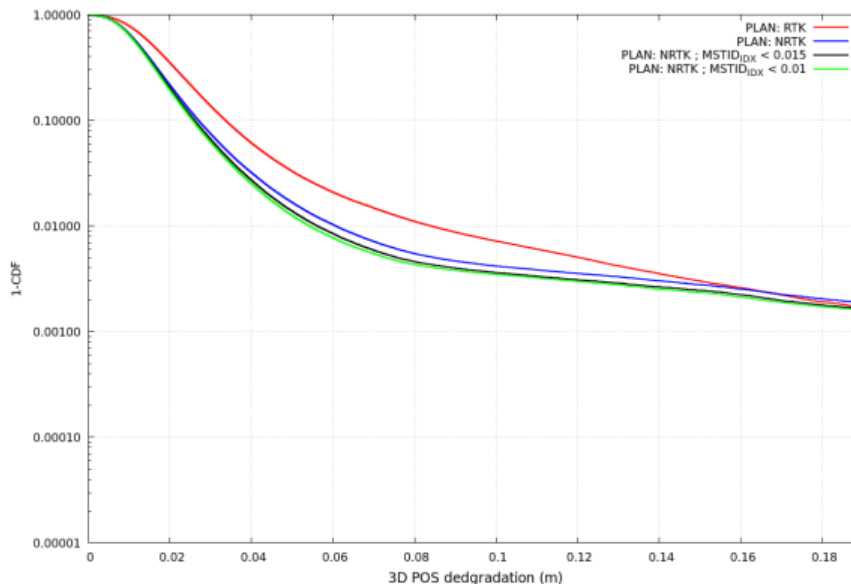


Figure 67 3D position degradation probability for PLAN (2017 - 2018).

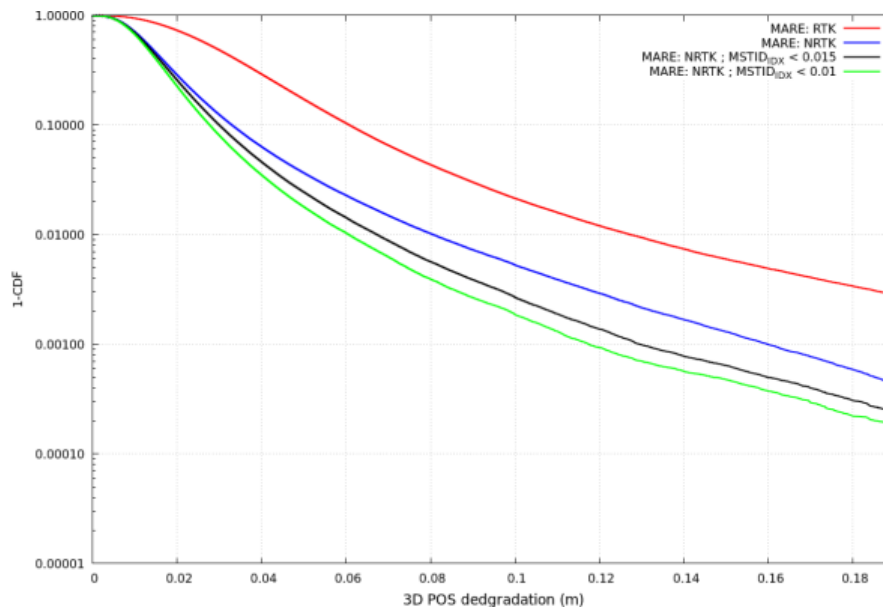


Figure 68 3D Position degradation probability for MARE (2017 - 2018).

It is important to remark there is a noticeable improvement in the positioning solution for rover stations located at long distances, such as MARE or SBAR, with respect to a near rover station such as PLAN. Regarding SBAR receiver and with a threshold in the MSTID index less than 0.01, for instance, there are a 50% of the cases with a 3D positioning degradation error greater 1.1 cm, a 95% of the cases with 3.1 cm and a 99% of the cases having 5.2 cm. This results are at the level of the rover PLAN, where the MSTID effects are quite limited.

The situation with a MSTID index threshold of 0.015 is similar, mitigating the position degradation specially the farthest.

The statistical analysis of figures Figure 66, Figure 67 and Figure 68 is also summarized in Table 16, Table 17 and Table 18, respectively.

Table 16 NRTK Position degradation case 1 (2017-2018).

	NRTK (no threshold for MSTID) position degradation.		
	50%	95%	99%
<i>SBAR</i>	1.2 (cm)	3.9 (cm)	7.2 (cm)
<i>PLAN</i>	1.2 (cm)	3.4 (cm)	6.0 (cm)
<i>MARE</i>	1.4 (cm)	4.4 (cm)	8.0 (cm)

Table 17 NRTK Position degradation case 2 (2017-2018).

	NRTK (MSTID index less than 0.015) position degradation.		
	50%	95%	99%
<i>SBAR</i>	1.1 (cm)	3.4 (cm)	6.1 (cm)
<i>PLAN</i>	1.2 (cm)	3.2 (cm)	5.6 (cm)
<i>MARE</i>	1.3 (cm)	3.8 (cm)	6.7 (cm)

Table 18 NRTK position degradation case 3 (2017-2018).

	NRTK (MSTID index less than 0.01) position degradation.		
	50%	95%	99%
<i>SBAR</i>	1.1 (cm)	3.2 (cm)	5.5 (cm)
<i>PLAN</i>	1.2 (cm)	3.2 (cm)	5.4 (cm)
<i>MARE</i>	1.3 (cm)	3.5 (cm)	6.0 (cm)

It is possible to have access to the computed MSTID indexes through the address 147.83.27.240, within the directory:

http://147.83.27.240/TechTIDE_database/YYYY/DOY/Methodologies/Data

Where **YYYY** stands for the year and **DOY** stands for the day of the year. This index is stored as `mstid_idx.YY.DDY`, where **YY** refers to the year (2 digit) and **DDY** refers to the day of year (DoY, 3 digit). Data format is organized by columns, where the first column is seconds of the day, column two is receiver name, column three is the satellite PRN, column four stand for the arcs and column five is the MSTID amplitude (LI m). Figure 69 shows an example of the MSTID index data format.

1200	acor	2	205	0.0019494	-0.40	46.72	0.013290	0.770940	0.636770	2.1	0
1200	adar	2	205	0.0024290	2.96	54.62	0.045480	0.778620	0.625850	1.8	0
1200	ajac	2	205	0.0017029	14.09	43.81	0.009420	0.743110	0.669110	1.7	0
1200	alac	2	205	0.0015166	6.20	41.47	-0.003980	0.751120	0.660160	2.0	0
1200	alba	2	207	0.0012649	5.05	42.17	-0.002040	0.754440	0.656370	2.0	0
1200	alme	2	205	0.0015166	4.63	40.44	-0.007940	0.751620	0.659550	2.1	0

Figure 69 MSTID index data format

3.4.1 Degradation during 2008-2009

As it was commented, the previous section analyses specifically the statistics for the time period between the day 200 of the year 2017 and the day 200 of the year 2018. The reason of this limitation is the before mentioned problem with the RINEX convertors (see section 3.2.1 Fixing carrier phase ambiguities in the CATNET NRTK service).

Concerning the other period of time, from 2008 to 2009, there was not issue regarding the RINEX convertors. Thus, it was possible to assessed the degradation of positioning, working with the same methodology carried out up to now. However, the 2008-2009 network differs from the network used for 2017-2018, due to BEUD receiver data is available from day 193 of 2013 (see Table 14 CATNET Receivers specificationsTable 14). BEUD is one of the closest receivers to rover receiver "SBAR". This is the reason why this study is performed in a different section. The statistics are presented in Figure 70 and Figure 71.

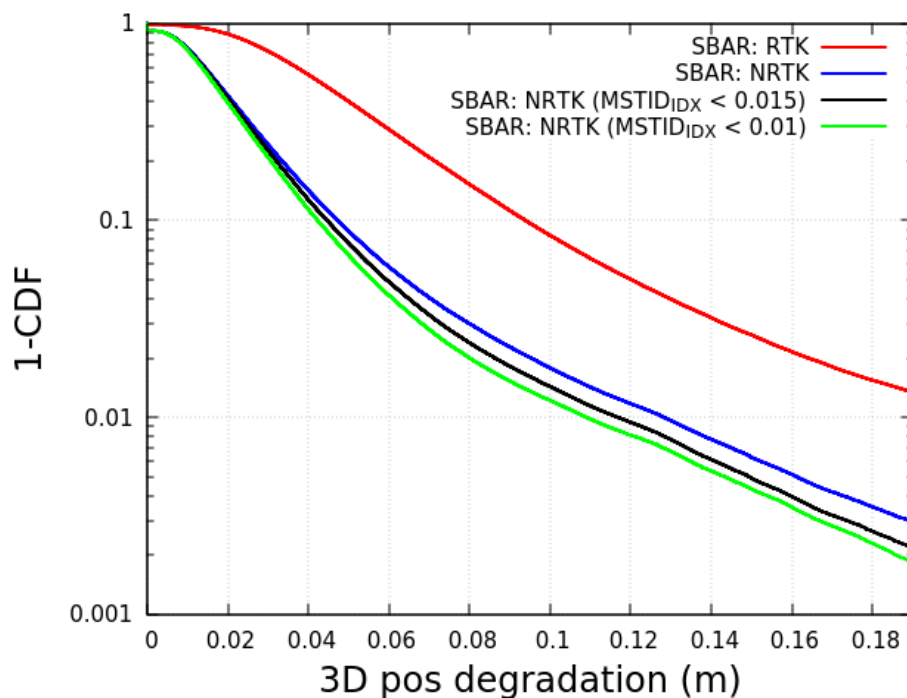


Figure 70 3D Position degradation probability for SBAR (2008 - 2009).

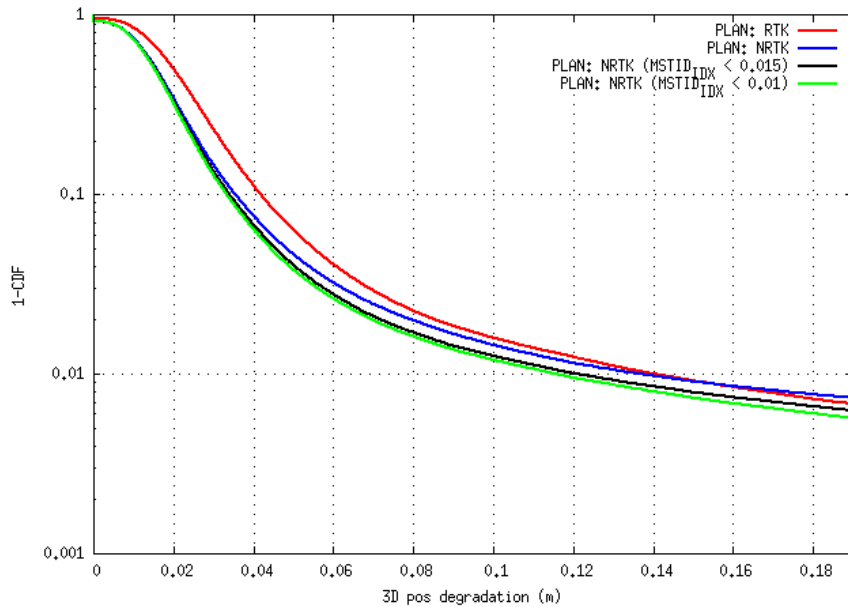


Figure 71 3D Position degradation probability for PLAN (2008 - 2009).

The derived results for the years 2008 and 2009 are consistent with respect to those for the time period 2017-2018, presenting a similar shape behavior for 3D Position degradation probability for both SBAR and PLAN stations.

3.5 Conclusions

The methodology defined and implemented in this work for testing the impact of the MSTID lead into three major achievements:

- A new methodology has been defined in order to obtain reference values:
 - *Reference measurements by fixing carrier phase ambiguities.* Indeed, NRTK is based on fixing carrier phase ambiguities of the double differenced carrier phase measurements. We have solved this point by applying a novel method consisting on fixing carrier phase ambiguities in the undifferenced measurements. In this way we have been able to do the study independently from the ambiguity fixing success rate.
 - *Reference navigation solution using the ionosphere free navigation solution L_{IF} .* In GNSS positioning degradation can be related with multiple effects (satellite clocks, geometry, ionosphere, ...), taking the solution obtained with the ionosphere free combination of carrier phases as the reference solution has allow us to consider just the effect related with the ionosphere.
 - *Reference navigation solution using RTK and NRTK.* Comparing RTK and NRTK solutions we have been able to assess the impact of the ionospheric effects in the RTK positioning and how this impact increase with the distance to the reference receiver. These errors are mitigated in the NRTK solutions.
- Relationship between positioning error and the Medium Scale Traveling Disturbances:

It has been shown that the presence of MSTIDs degrades the user positioning, not only in RTK but also in NRTK. This degradation is not only related with the effect of the TID on the user measurements but in the measurements of any of the reference receivers.
- Definition of a MSTID index for predicting the error in positioning:

It has been show that it is possible to implement a MSTID index as a tool to mitigate positioning degradation. This has been proven working with 3 stations located at 15, 50 and 79 km from the reference receiver. Using this index over a data set covering 3 years, we have shown that is possible to obtain similar accuracies in the three baselines. i.e. mitigating the effect of the TIDs.

Bibliography

- [RD-1] EGNOS Safety of Life (SoL) Service Definition Document
- [RD-2] ICAO International Standards and Recommended Practices (SARPS) - Annex 10- Aeronautical Telecommunications. Volume I Radio Navigation Aids
- [RD-3] RTCA DO 229-E, Minimum Operational Performance Standards for GPS/WAAS Airborne Equipment (MOPS)
- [RD-4] Chen, K. & Gao, Y., 2005. Real-Time Precise Point Positioning Using Single Frequency Data. *Proceedings of the 18th International Technical Meeting of the Satellite Division of The Institute of Navigation*, pp. 1514 - 1523.
- [RD-5] Rovira-Garcia, A. et al., 2016. Accuracy of ionospheric models used in GNSS and SBAS: methodology and analysis. *Journal of Geodesy*, pp. 229-240.
- [RD-6]
- [RD-7] Rovira-Garcia, A. et al., 2016. Fast Precise Point Positioning: A System to Provide Corrections for Single and Multi-Frequency Navigation. *Journal of The Institute of Navigation*, pp. 231-247.
- [RD-8] Hernández-Pajares, M., Juan Zornoza, J. M. & Sanz, J., 2006. Medium Scale Traveling Disturbances Affecting GPS Measurements: Spatial and Temporal Analysis. *Journal of Geophysical Research, Space Physics*, Volume 111.
- [RD-9] Alves, P. et al., 2001. Evaluation of Multiple-Reference DGPS RTK Using a Large Scale Network. *ION NTM-2001*, 22-24 January.
- [RD-10] Lachapelle, G. & Alves, P., 2002. Multiple Reference Station Approach: Overview and Current Research. *Journal of Global Positioning System*, Volume 1, pp. 133-136.
- [RD-11] Lachapelle, G. & Cannon, M., 1992. High-precision GPS navigation with emphasis on carrier-phase ambiguity resolution. *Marine Geodesy*, January, 15(4), pp. 253-269.
- [RD-12] Ge, M., Gendt, G., Rothacher, M.A., Shi, C. and Liu, J., 2008. Resolution of GPS carrier-phase ambiguities in precise point positioning (PPP) with daily observations. *Journal of Geodesy*, 82(7), pp.389-399.
- [RD-13] NAVSTAR GPS space segment/navigation user segment interfaces, 2018. *Global Positioning System Directorate Systems Engineering and Integration interface specification IS-GPS-200*. [Online]
Available at: <https://www.gps.gov/technical/icwg/IS-GPS-200J.pdf> [Accessed 01 02 2019].
- [RD-14] Wanninger, L., 2018. Detection of RINEX-2 Files With Mixed GPS L2P(Y)/L2C Carrier Phase Observations. *Sensor*, 19 December.
- [RD-15] Wielgosz, P., Kashani, I. & Grejner-Brzezinska, D., 2005. Analysis of long-range network RTK during a severe ionospheric storm. *Journal of Geodesy*, 79(9), pp. 524-531.
- [RD-16] Cannon, M. et al., 2001. *GPS RTK Positioning Using a Regional Reference Network: Theory and Results*. Seville, GNSS International Symposium.

Annex A EGNOS SCENARIOS ANALYSIS

This annex contains the analysis results for all periods analyzed but DOY 250 and 251 which were already presented in 1.2.3 Analysis for 7-8/09/2017.

The information provided in this annex is grouped in days and presented as follows:

- Brief description of the EGNOS APV-I availability degradation due to ionospheric event.
- EGNOS APV-I availability daily map.
- AATR daily mean values map.
- Temporal evolution of the hourly EGNOS APV-I availability per RIMS and the 5 minutes AATR values of their associated IGS stations.
- Temporal evolution of the maximum 5-minutes xPL values per RIMS and the 5 minutes AATR values of their associated IGS stations.
- Temporal evolution of the instantaneous GIVE indicator per IGP and the 5 minutes AATR values of their associated IGS stations.

A.1 DOY 31 and 32

On 31/01/2017 the high geomagnetic activity has been observed by the end of the day which leads to degradation in performance of EGNOS in the North East part of Service Area. This day additional degradations have been identified in the North West part at the beginning of the day which were not linked to the ionospheric activities but to assets maintenance.

On 01/02/2017 the high geomagnetic activity has been still presented and continued impacting the EGNOS availability in the North part of Service Area. The impact has been observed at the beginning of the day. The degradation which has been observed in the North West part of EGNOS Service Area has been increased with additional maintenance activities of the EGNOS assets.

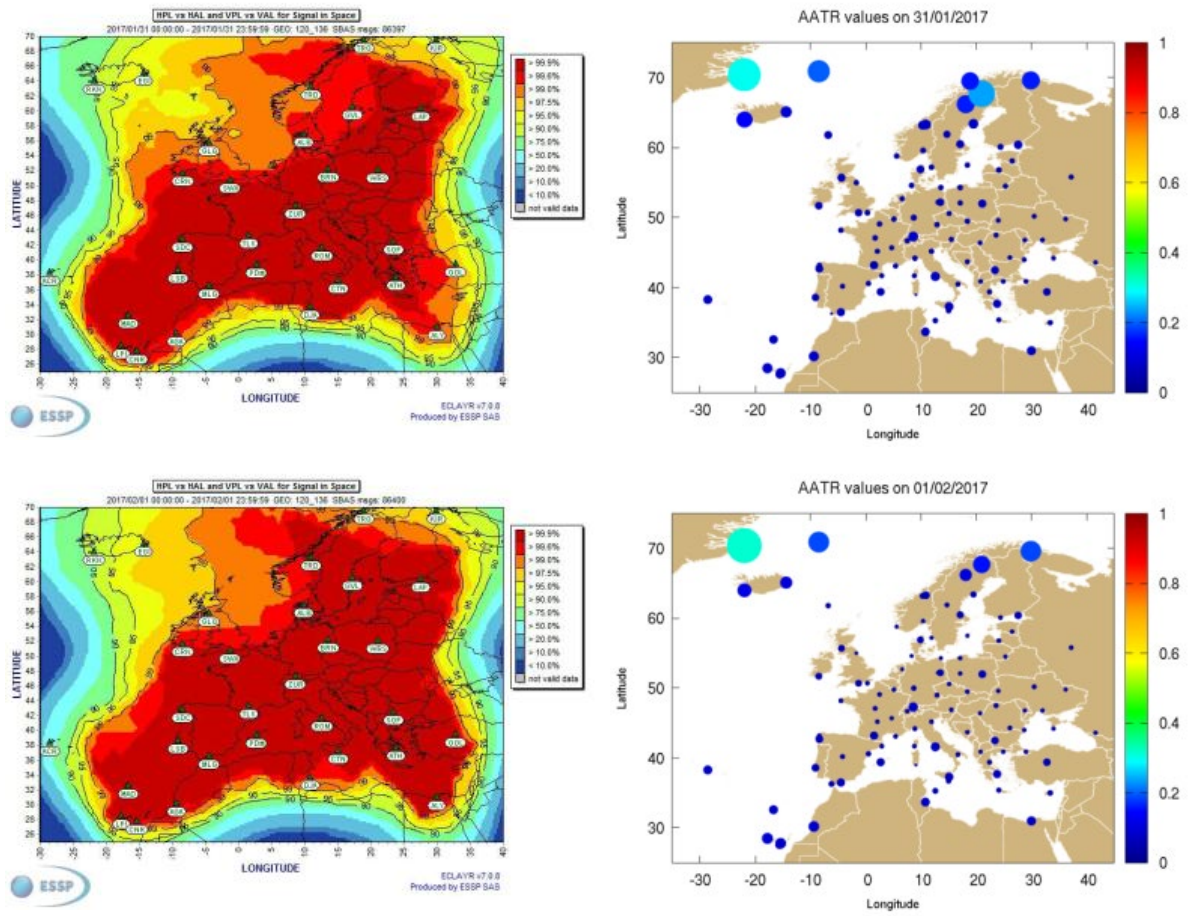


Figure 72. EGNOS APV-I availability maps and AATR daily mean values at IGS stations on DOY 31 and 32.

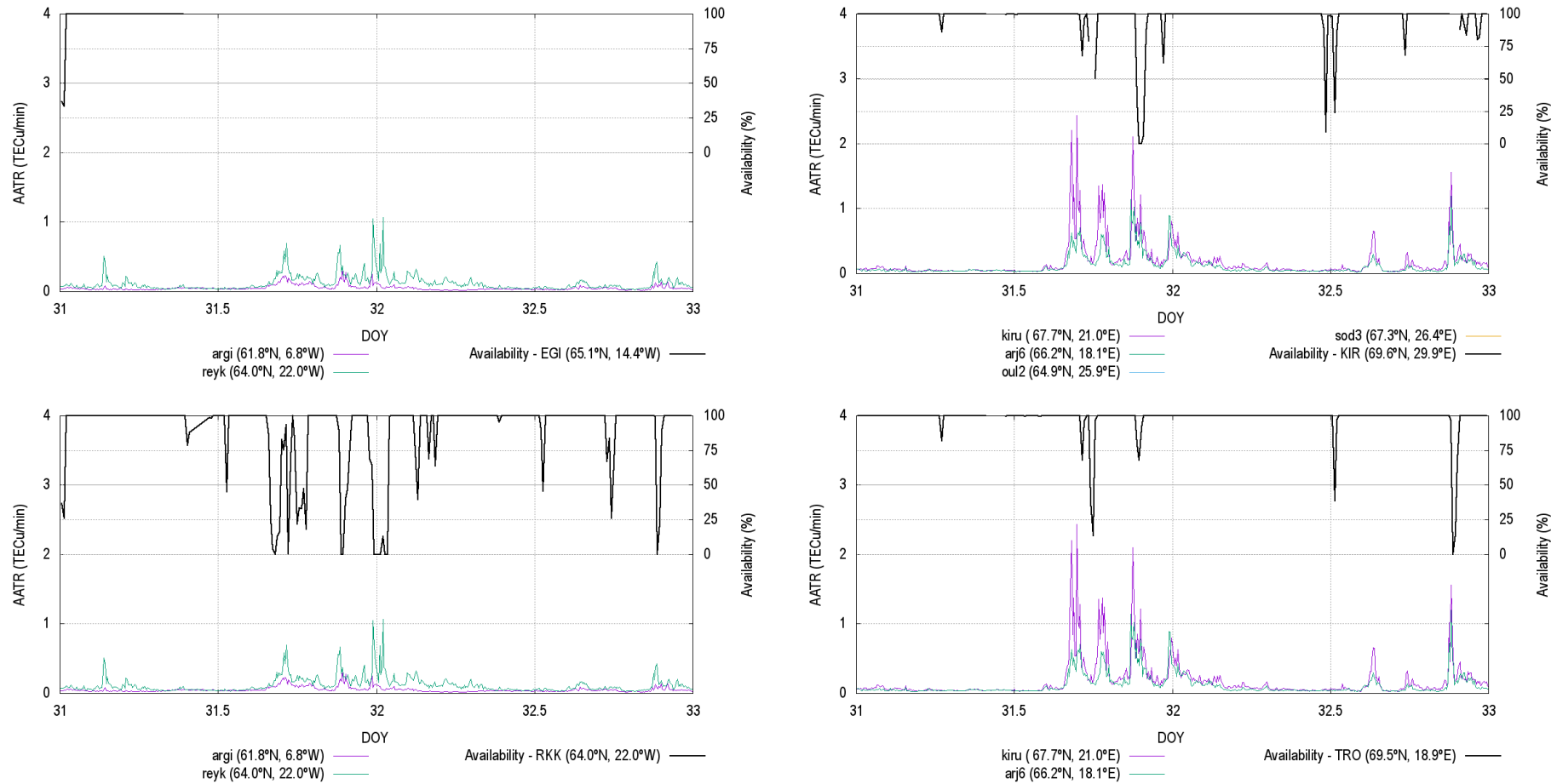


Figure 73. APV-I availability for assessed RIMS and AATR values at IGS station on DOY 31 and 32.

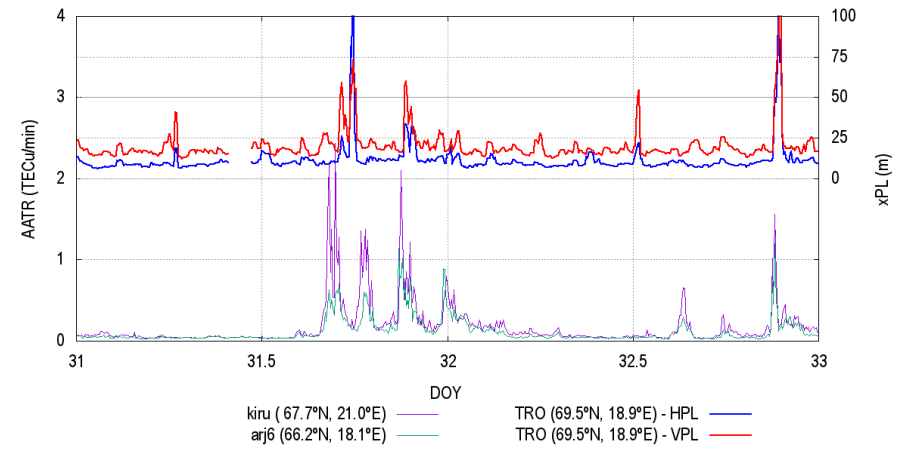
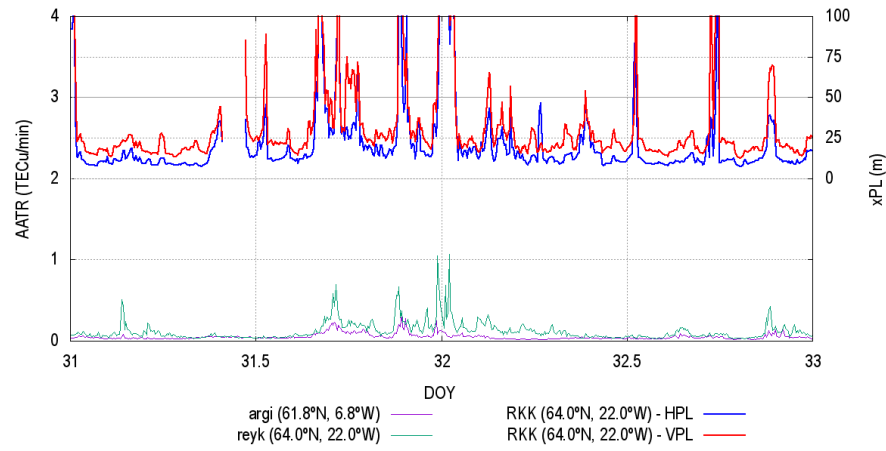
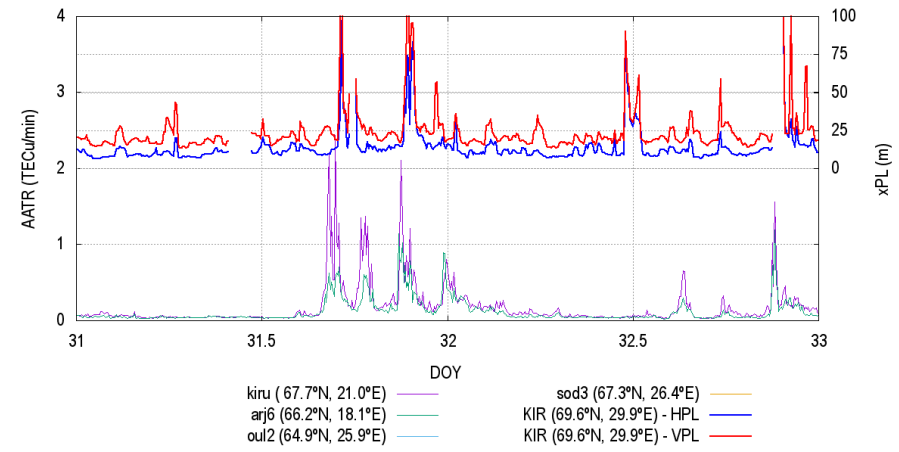
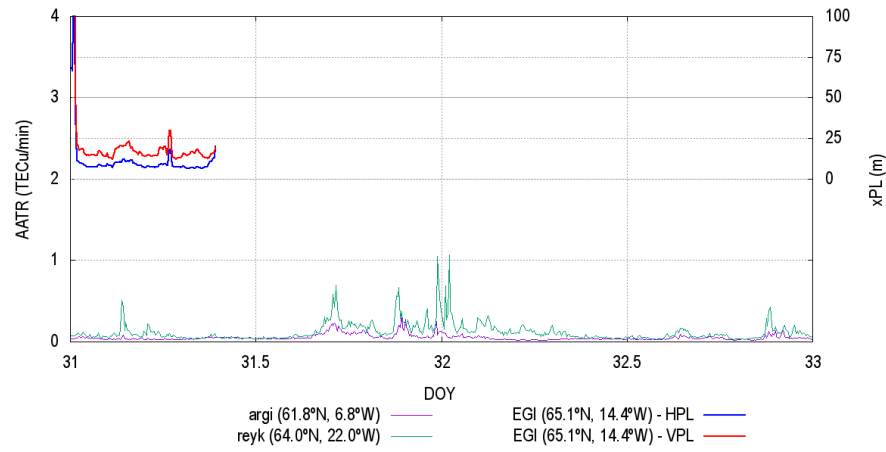


Figure 74. HPL and VPL variation for assessed RIMS and AATR values at IGS station on DOY 31 and 32.

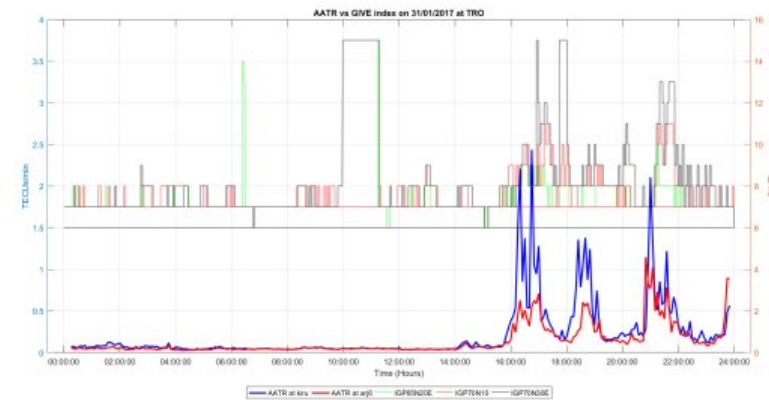
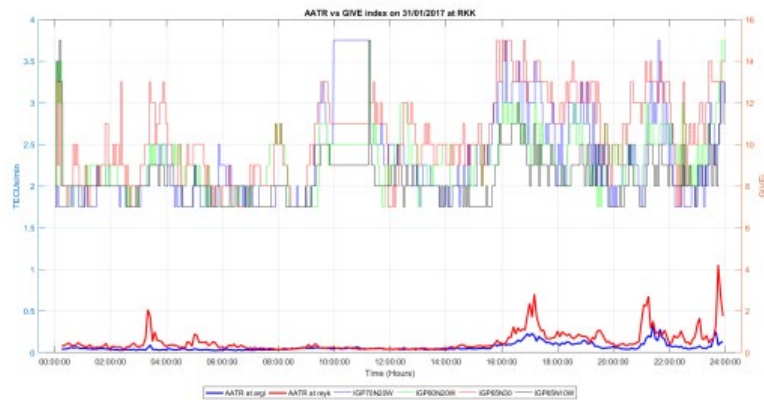
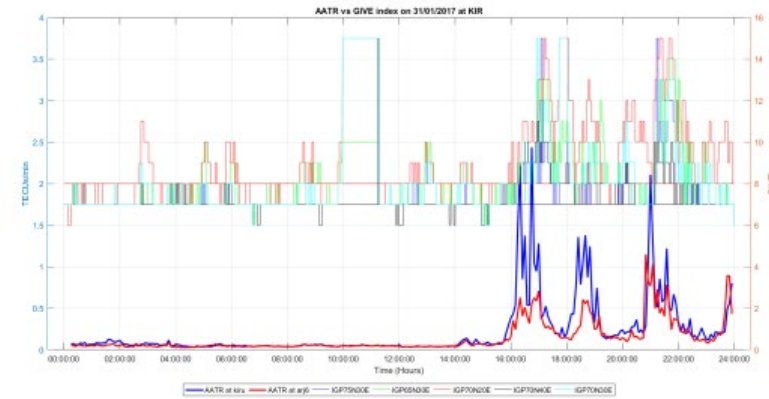
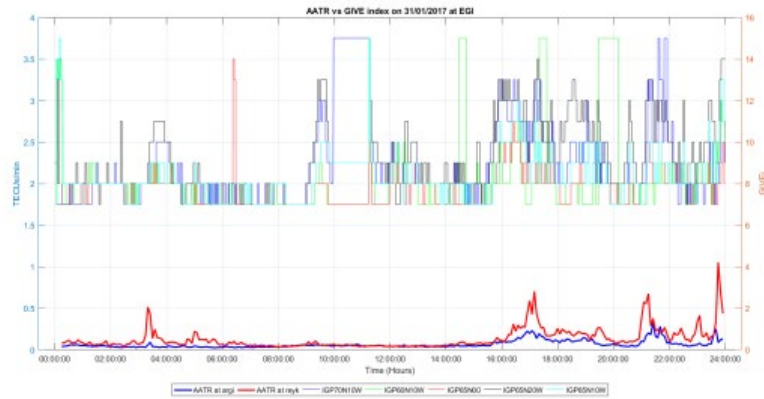


Figure 75. Temporal evolution of GIVE indices at IGPs surrounding assessed RIMS and AATR at IGS stations on DOY 31.

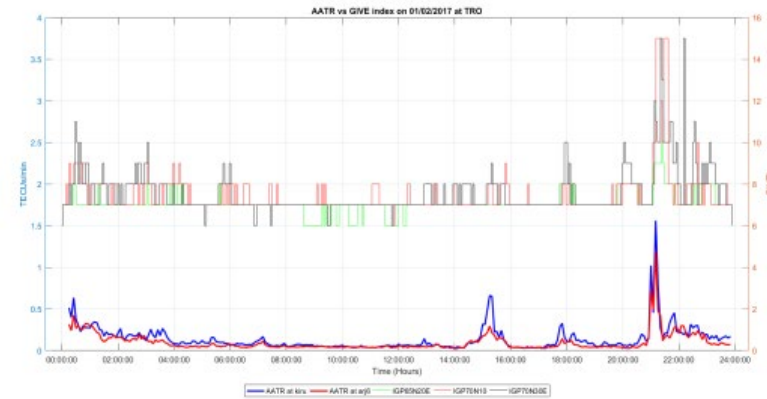
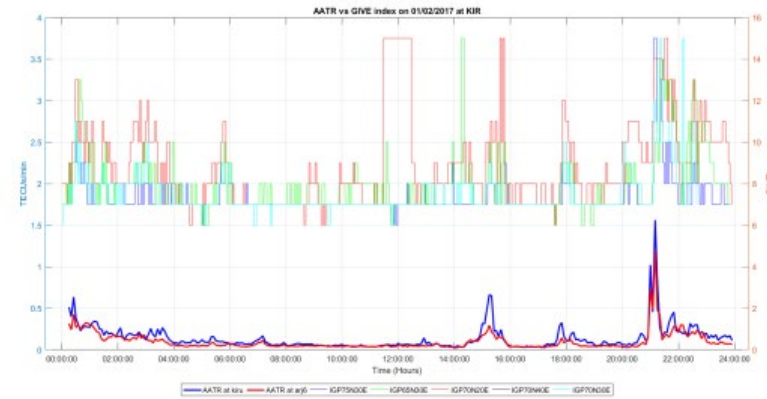
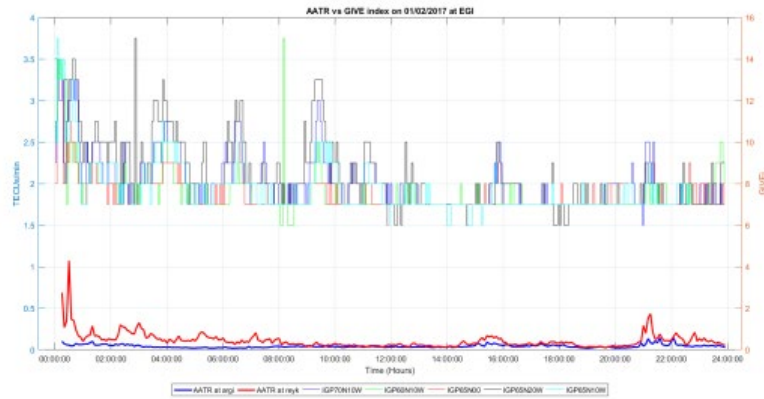


Figure 76. Temporal evolution of GIVE indices at IGPs surrounding assessed RIMS and AATR at IGS stations on DOY 32.

A.2 DOY 60 and 61

On 01/03/2017 the high geomagnetic activity has been observed during all day long. The high spikes of AATR values are observed specially by the end of the day which well correlates with increase of xPL values. It is also observed a correlation with high spikes of AATR and increase in GIVE indicators.

On 02/03/2017 the high geomagnetic activity continued and followed degrading North part of EGNOS Service Area. The correlation between the AATR values and the other parameters is well seen.

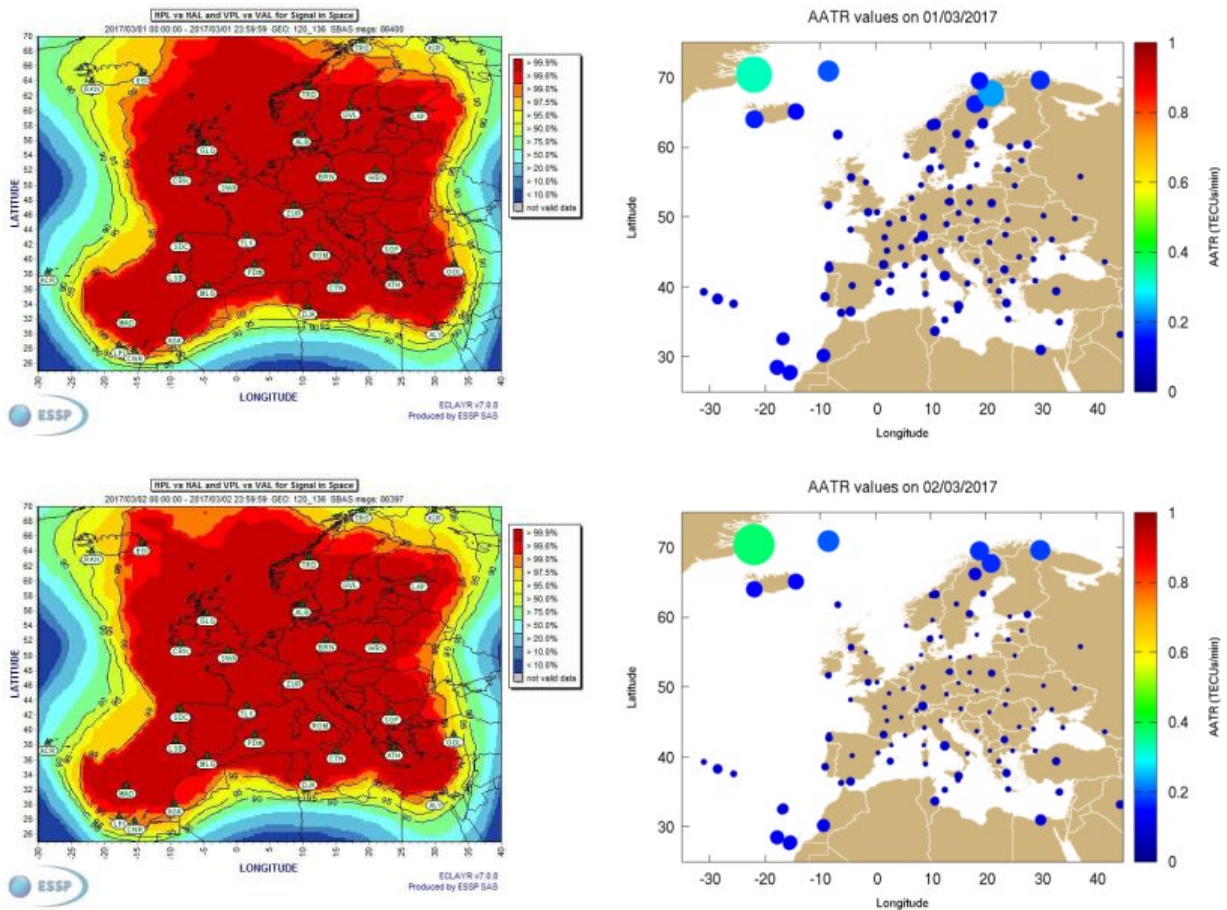


Figure 77. EGNOS APV-I availability maps and AATR daily mean values at IGS stations on DOY 60 and 61.

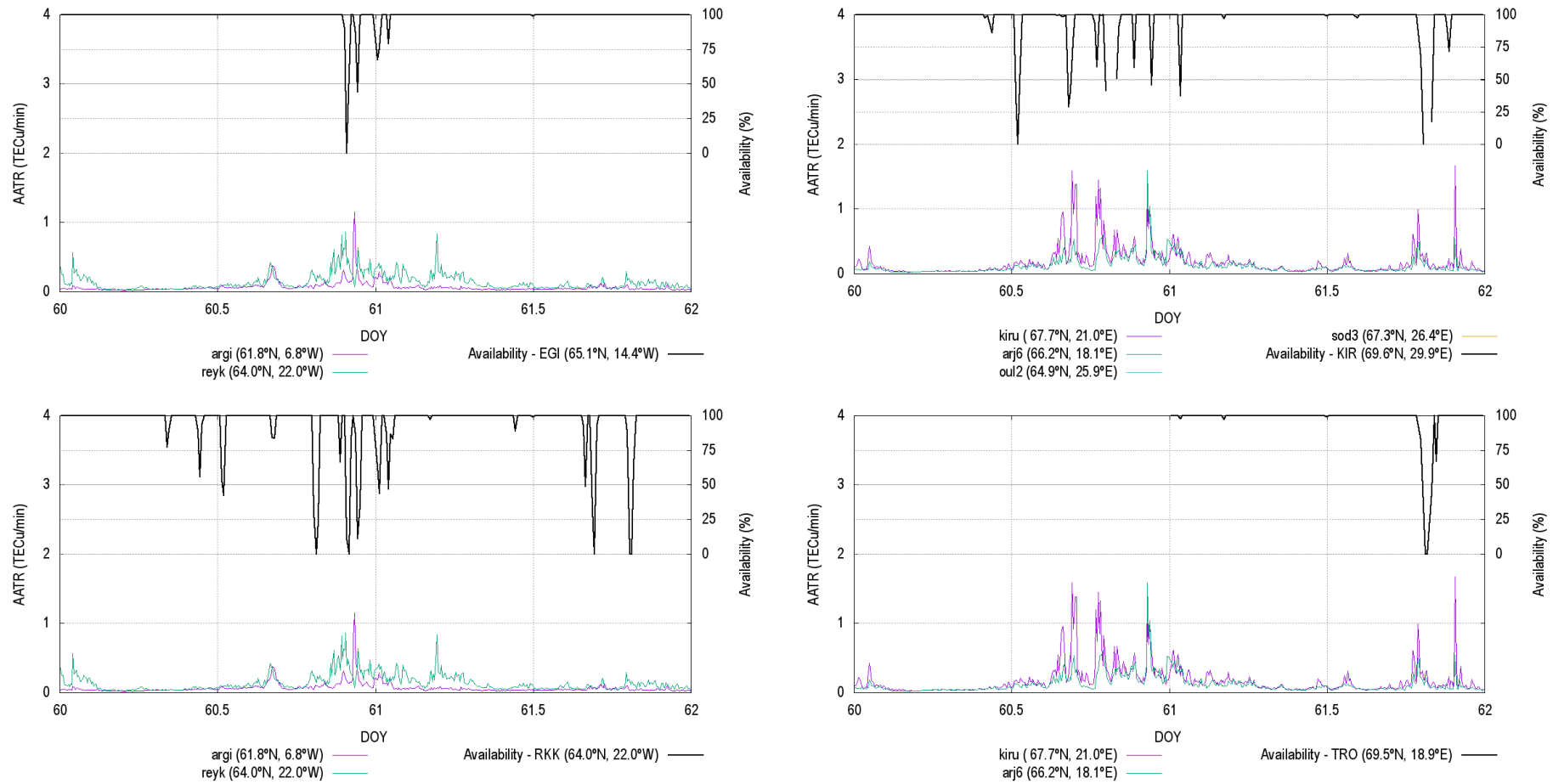


Figure 78. APV-I availability for assessed RIMS and AATR values at IGS station on DOY 60 and 61.

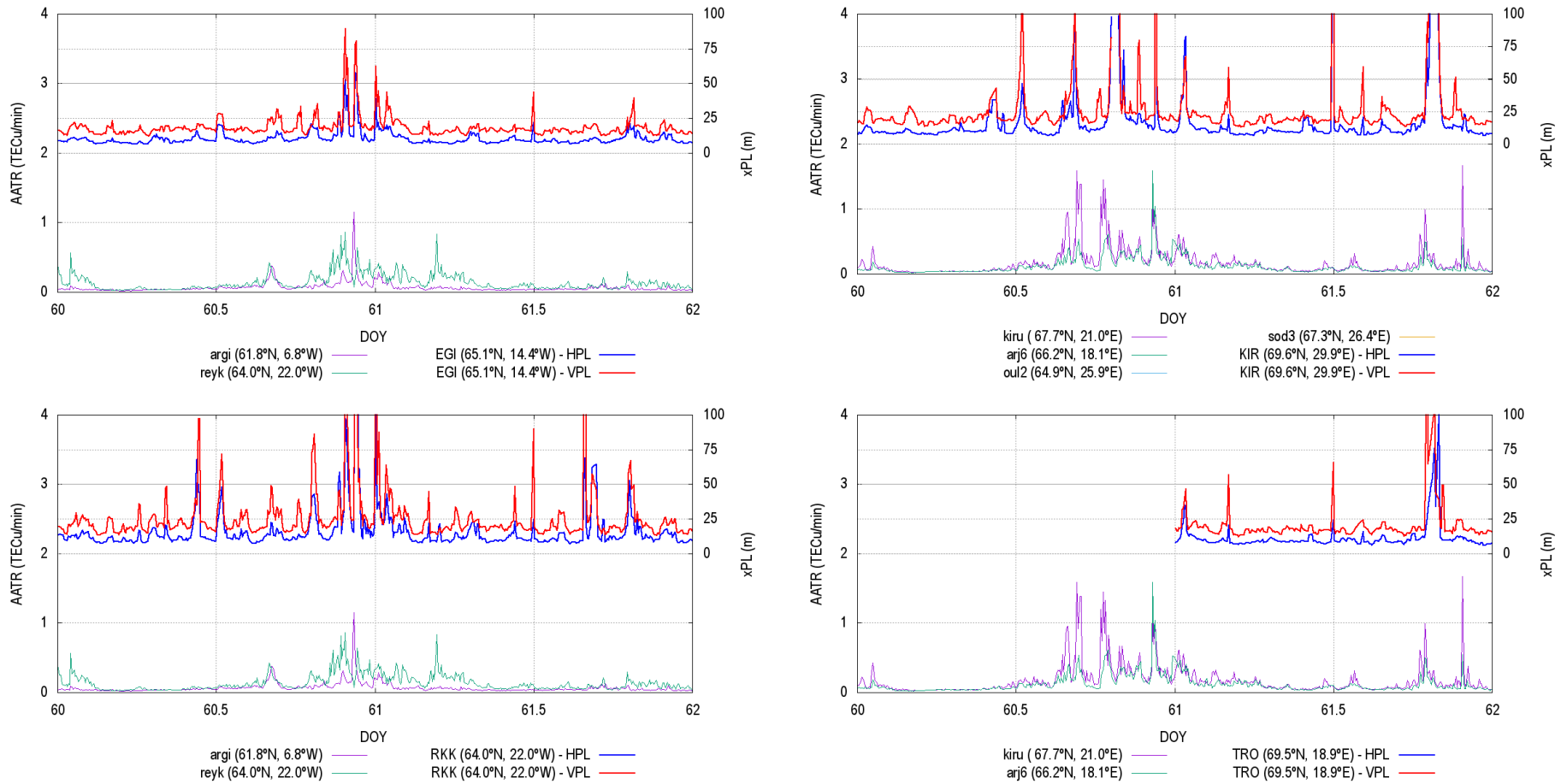


Figure 79. HPL and VPL variation for assessed RIMS and AATR values at IGS station on DOY 60 and 61.

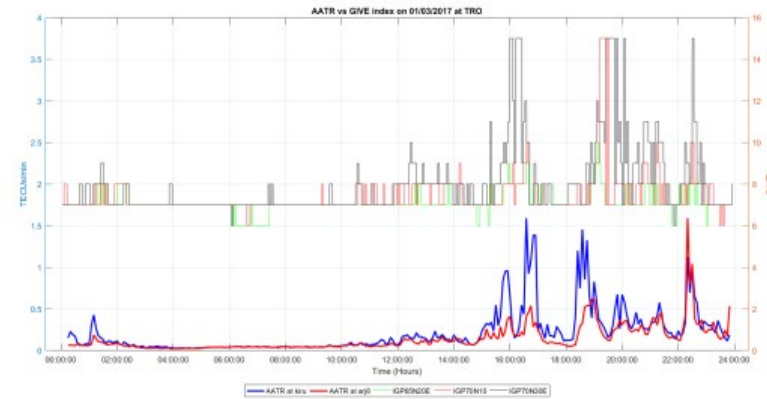
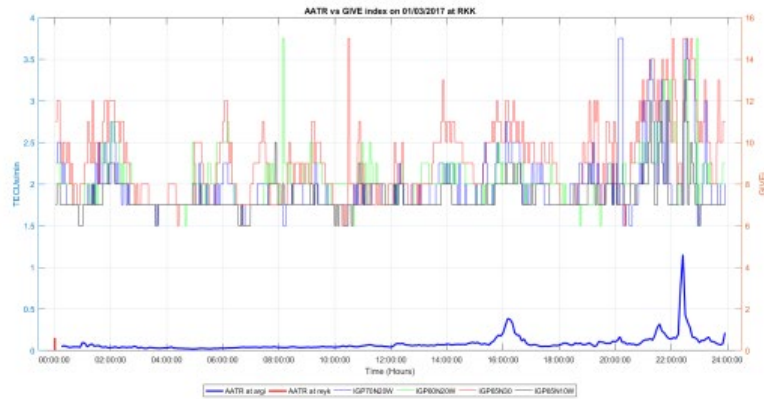
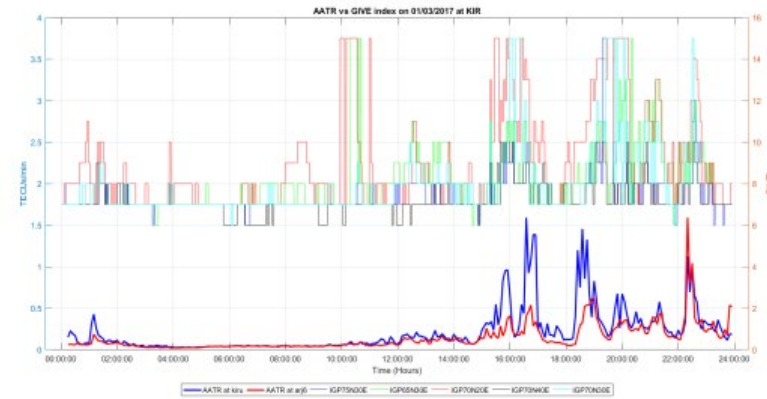
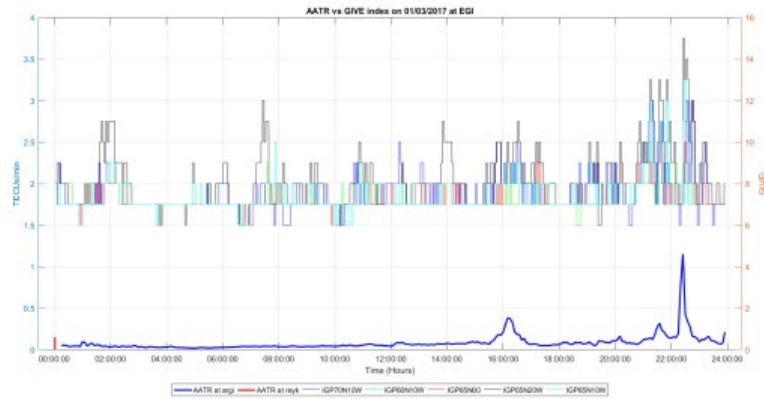


Figure 80. Temporal evolution of GIVE indices at IGPs surrounding assessed RIMS and AATR at IGS stations on DOY 60.

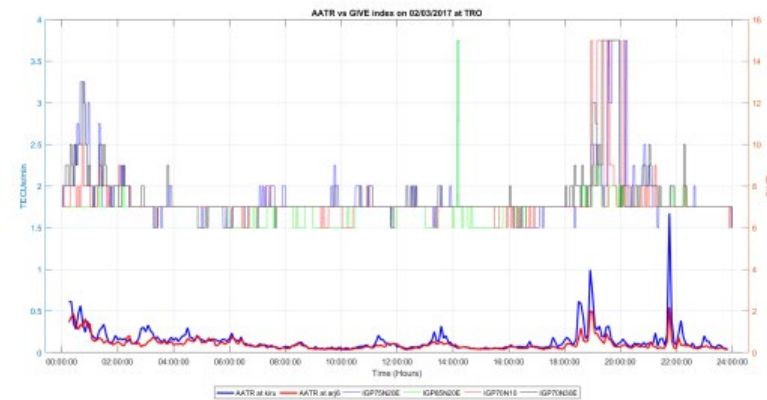
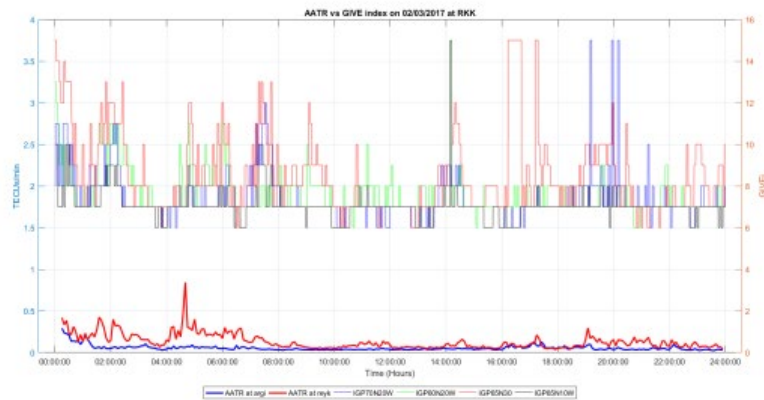
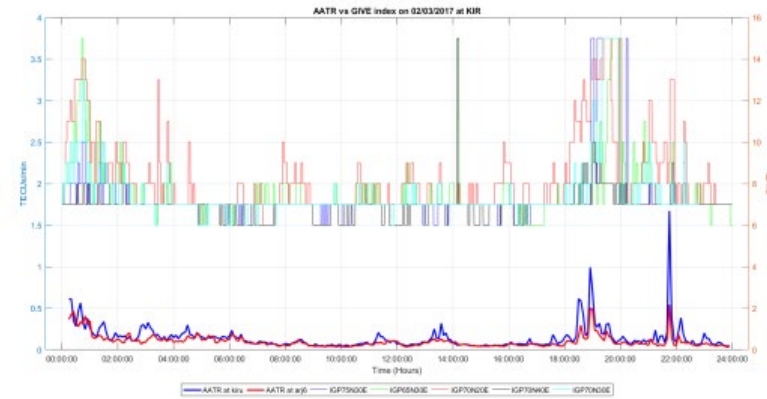
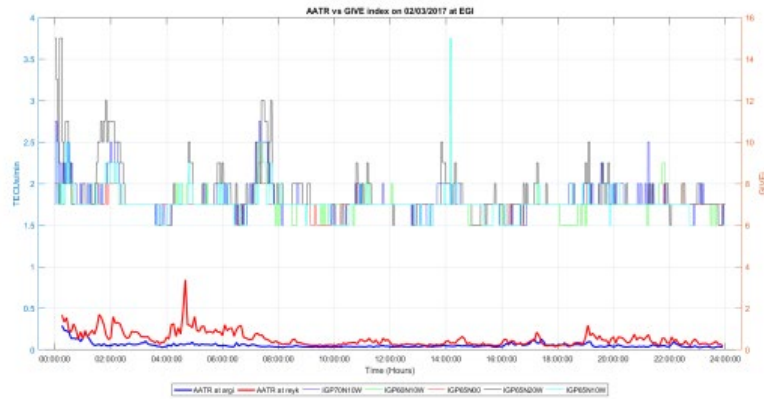


Figure . Temporal evolution of GIVE indices at IGPs surrounding assessed RIMS and AATR at IGS stations on DOY 61.

A.3 DOY 86 and 87

On 27/03/2017 high geomagnetic activity has been observed within all day impacting North part of EGNOS Service Area. High increase in AATR values by the end of day is well correlated with the increase in xPL values. Increase in GIVE indicators is well seen with high spikes of AATR values indicating impact in performance. In addition, maintenance activities performed in the asset located in the North West of ECAC area could increase both, the APV-I availability degradation and the increase of GIVE values.

On 28/03/2017 the geomagnetic activity followed degrading the performance of EGNOS in North part of Service Area. In the graphs below the high spikes of AATR values are present in correlation with increase of xPL values as well as increase in GIVE indicators.

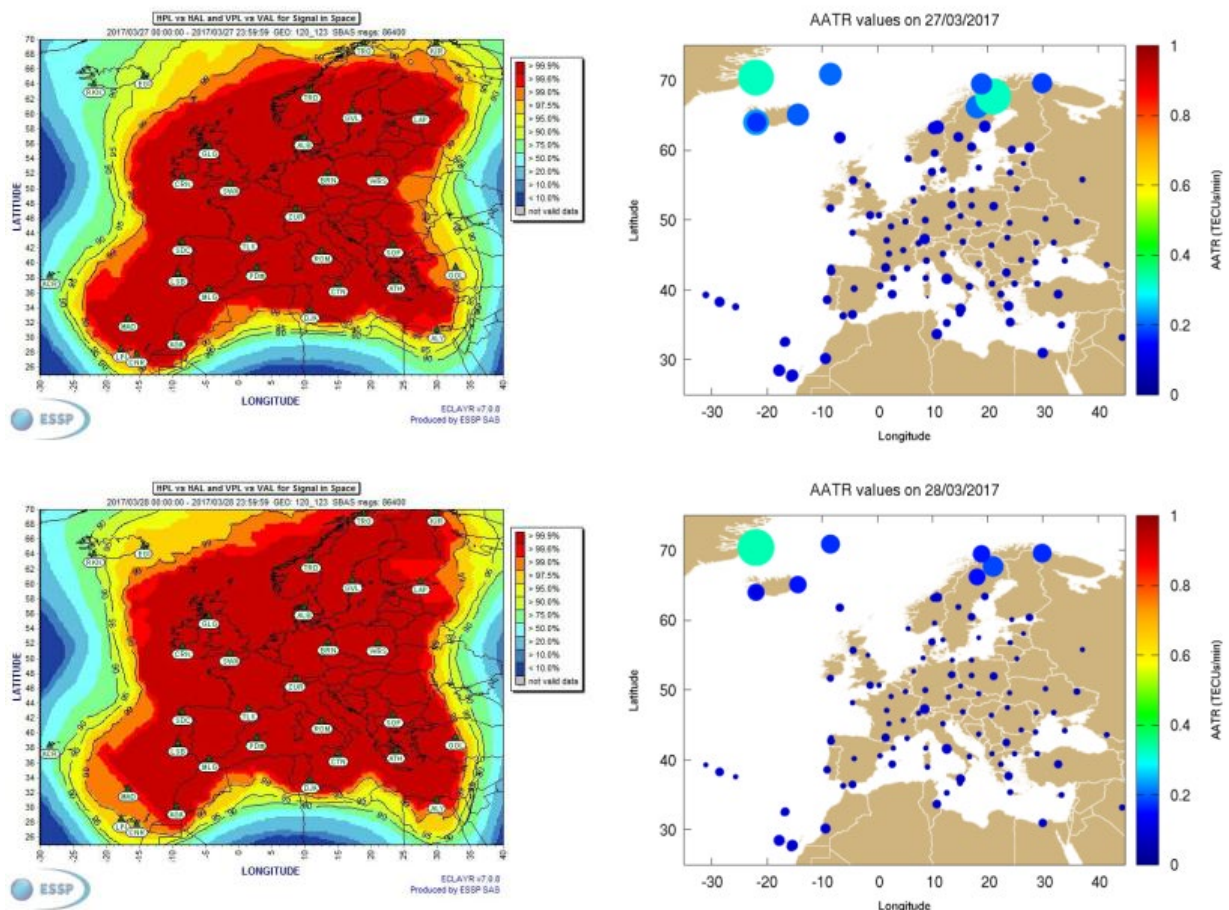


Figure 81. EGNOS APV-I availability maps and AATR daily mean values at IGS stations on DOY 86 and 87.

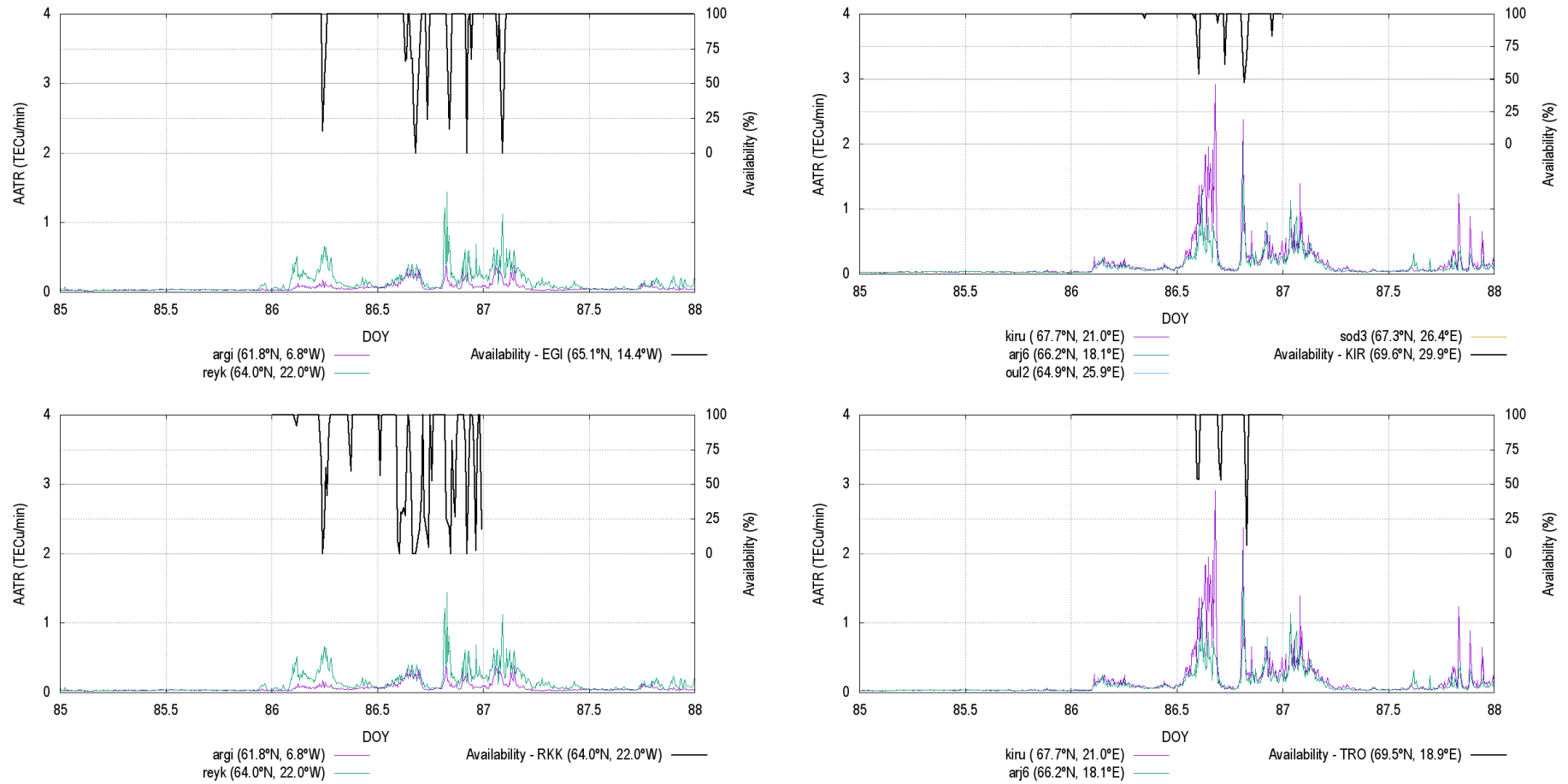


Figure 82. APV-I availability for assessed RIMS and AATR values at IGS station on DOY 86 and 87.

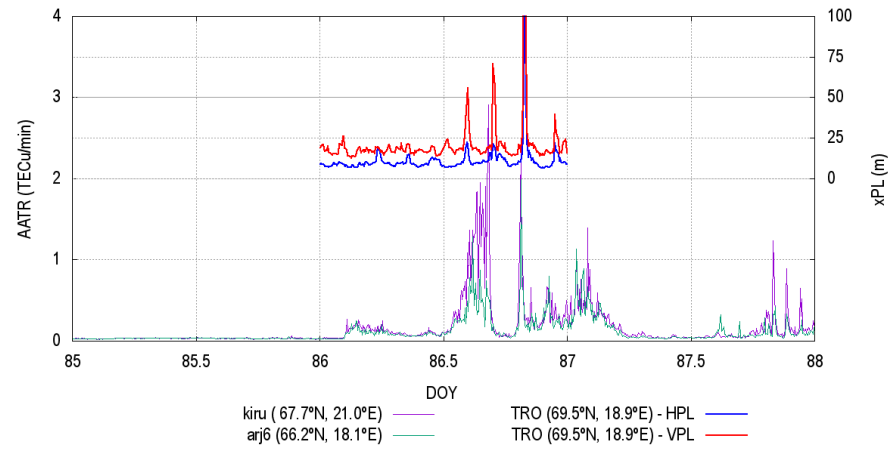
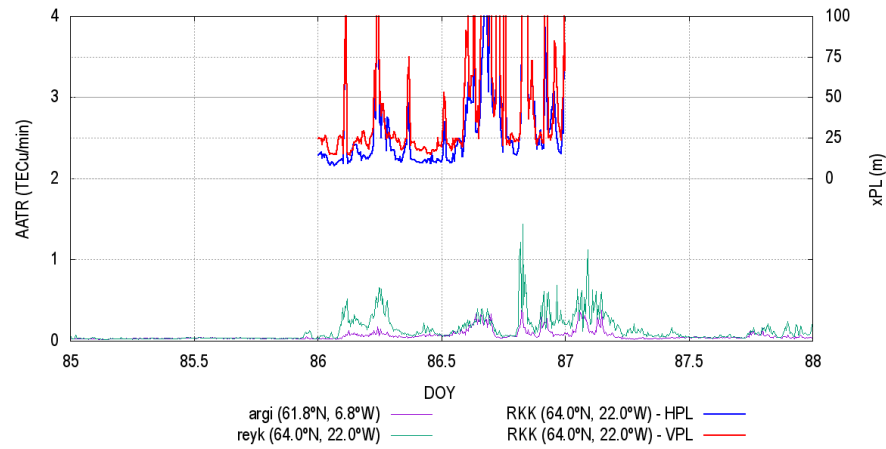
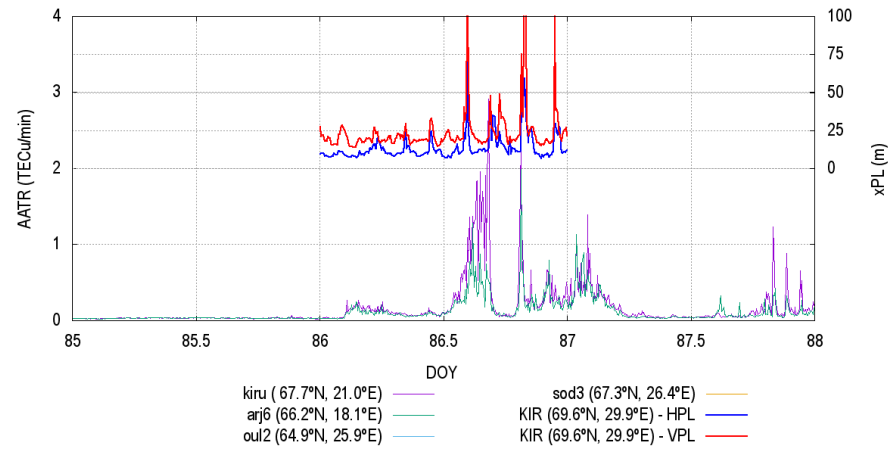
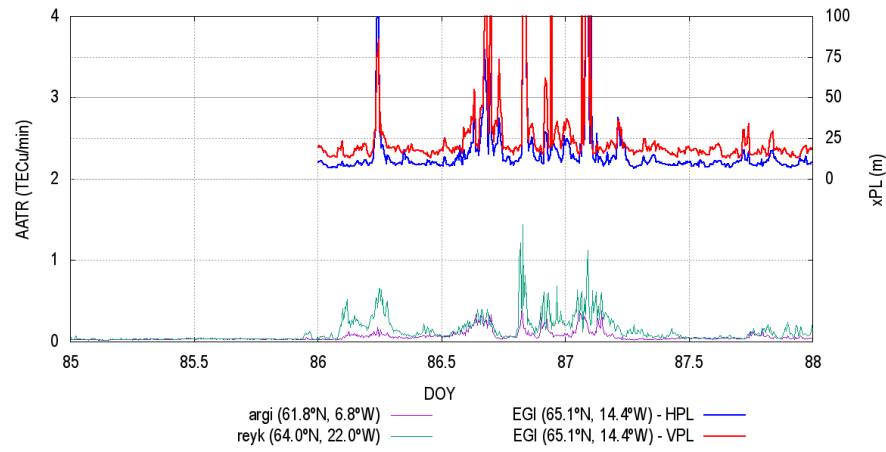


Figure 83. HPL and VPL variation for assessed RIMS and AATR values at IGS station on DOY 86 and 87.

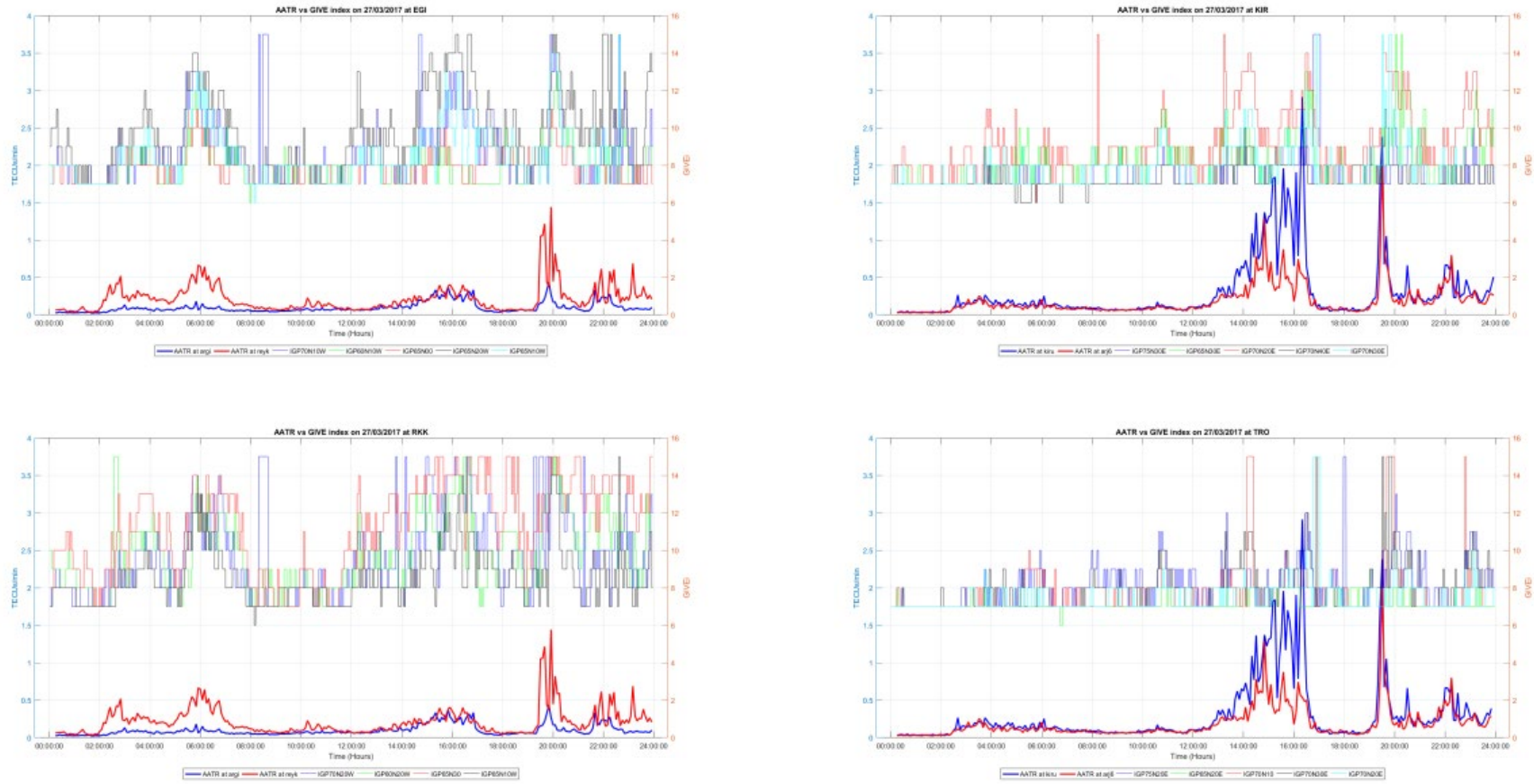


Figure 84. Temporal evolution of GIVE indices at IGPs surrounding assessed RIMS and AATR at IGS stations on DOY 86.

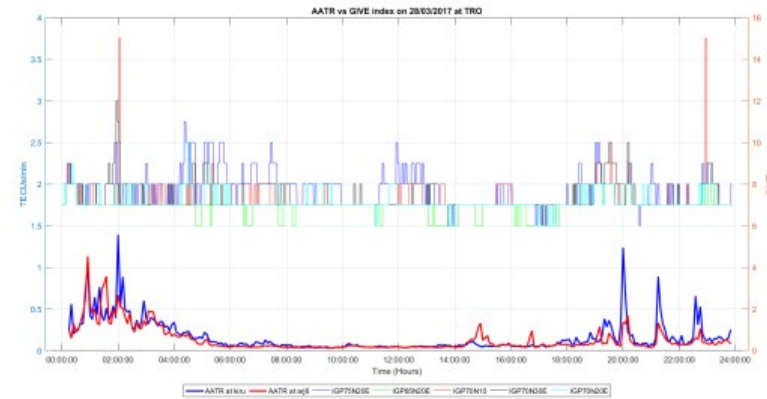
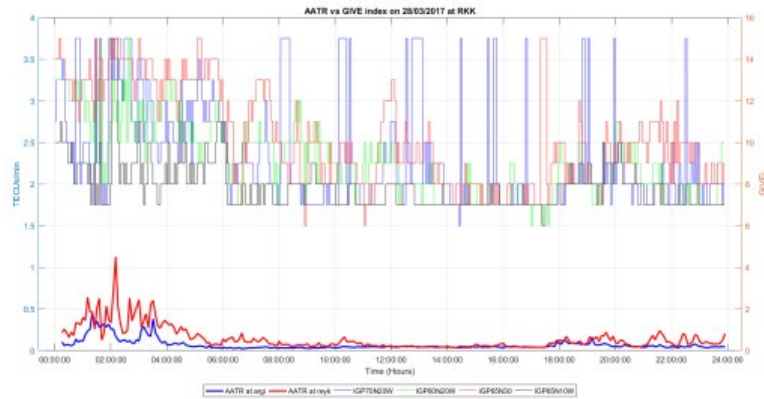
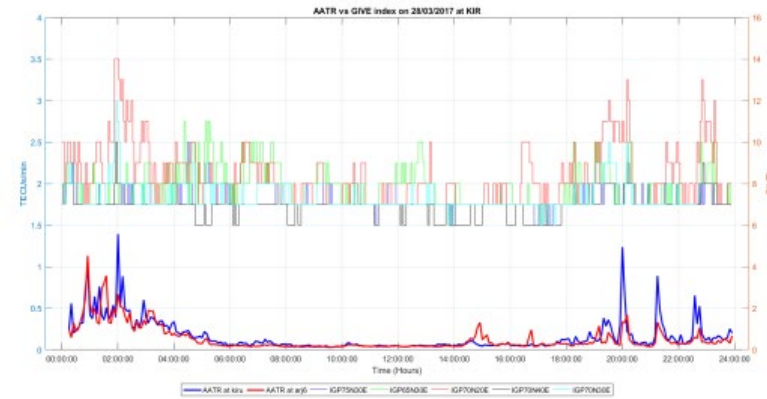
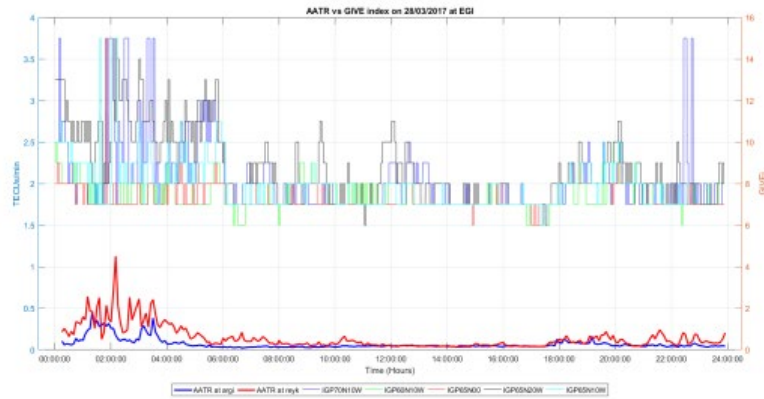


Figure 85. Temporal evolution of GIVE indices at IGPs surrounding assessed RIMS and AATR at IGS stations on DOY 87.

A.4 DOY 110 and 113

On 20/04/2017 high geomagnetic activity has been observed within whole day impacting Northern part of EGNOS Service Area. High spikes of AATR values are well correlated with increase in xPL values. Those parameters are also well correlated with increase in GIVE indicators at the begging of the day.

On 23/04/2017 high geomagnetic activity has been observed at the beginning of the day which impacted Northern part of EGNOS service. High spikes of AATR values have been observed which are well correlated with increase of xPL values. High values of GIVE indicator have been observed with correlation of high spikes of AATR values. In addition, the degradation observed in the North East part of EGNOS Service Area was impacted by additional reasons not linked to ionospheric activity.

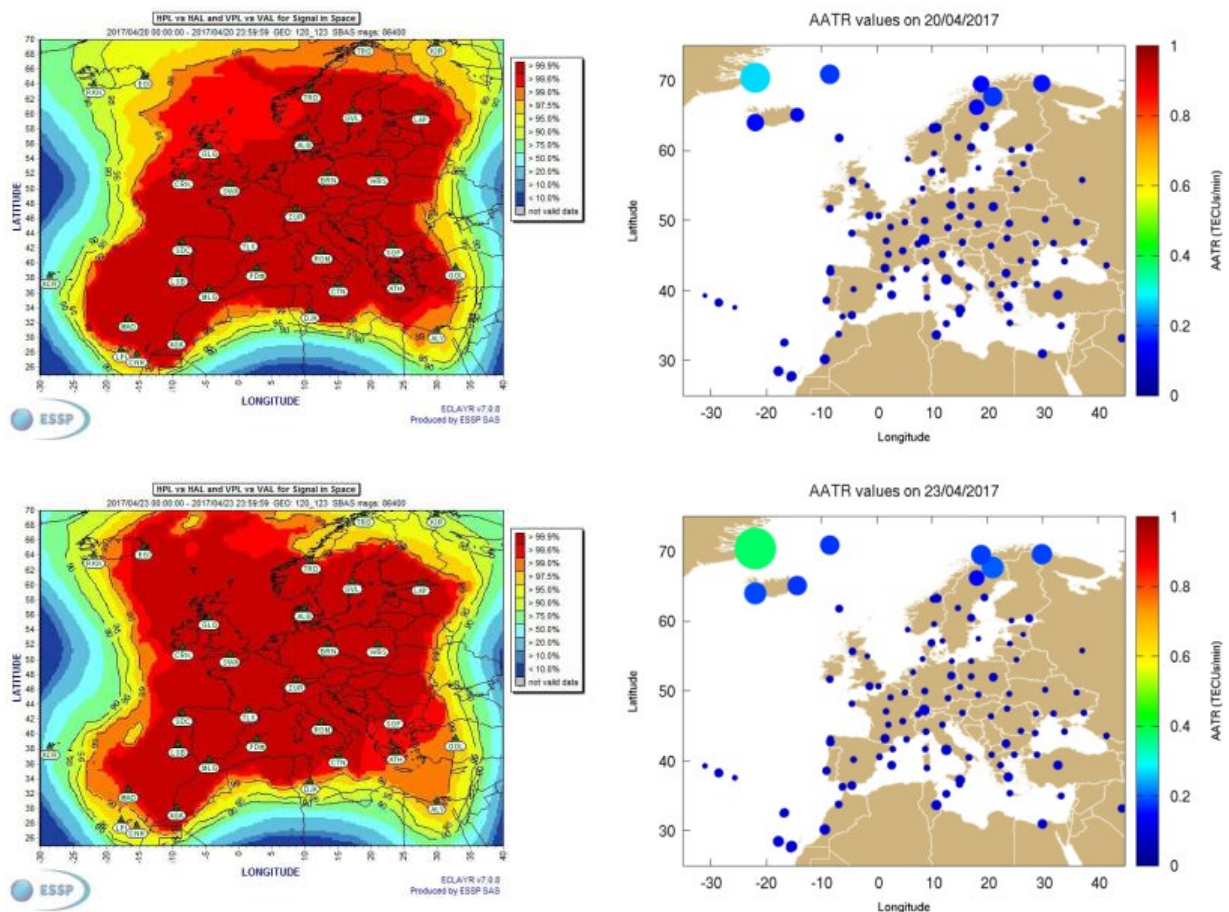


Figure 86. EGNOS APV-I availability maps and AATR daily mean values at IGS stations on DOY 110 and 113.

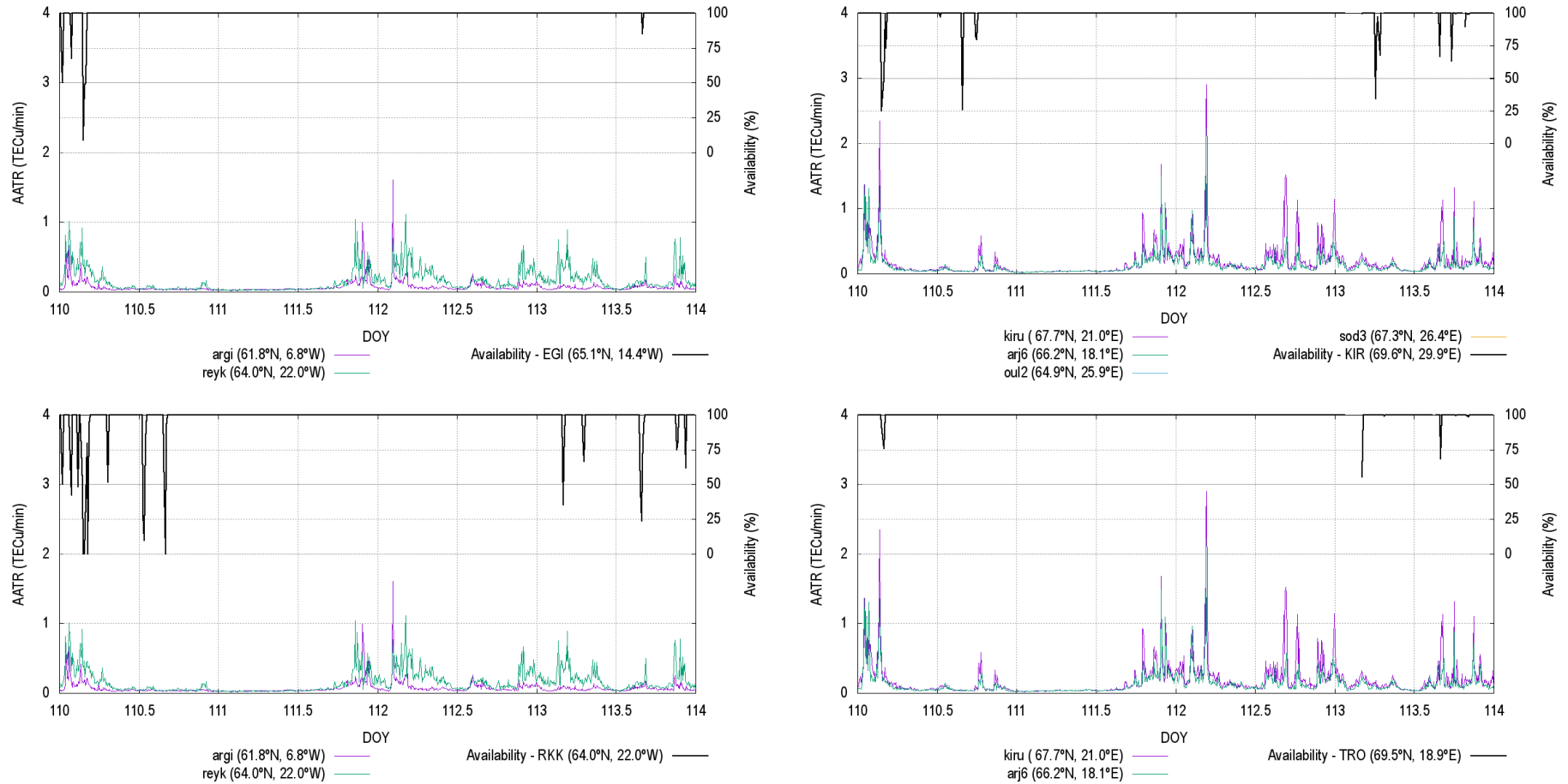


Figure 87. APV-I availability for assessed RIMS and AATR values at IGS station on DOY 110 and 113.

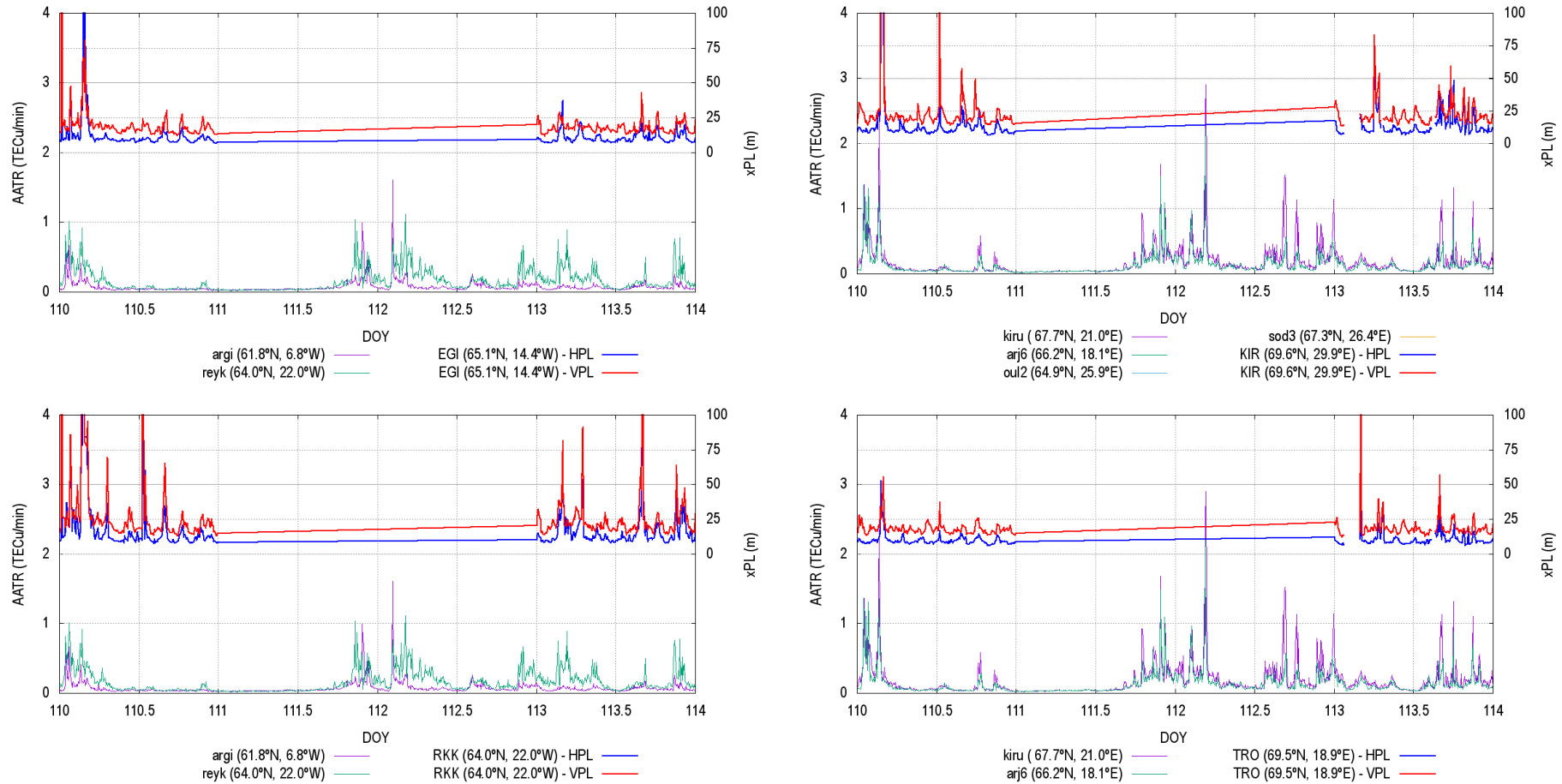


Figure 88. HPL and VPL variation for assessed RIMS and AATR values at IGS station on DOY 110 and 113.

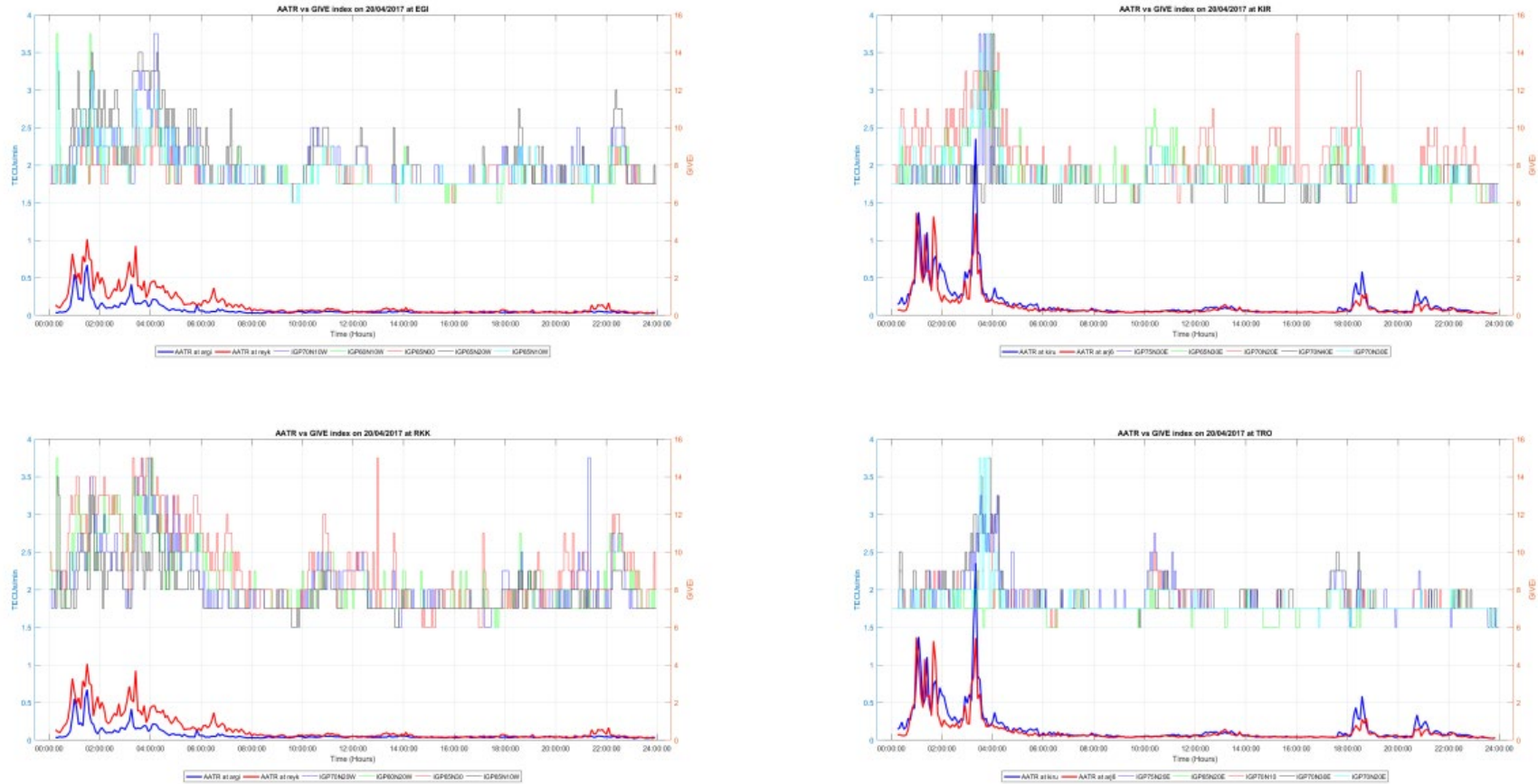


Figure 89. Temporal evolution of GIVE indices at IGPs surrounding assessed RIMS and AATR at IGS stations on DOY 110.



Figure 90. Temporal evolution of GIVE indices at IGPs surrounding assessed RIMS and AATR at IGS stations on DOY 113.

A.5 DOY 139 and 140

On 19/05/2017 high geomagnetic activity has been observed by the end of the day. On the graphs presented below, it is observed a decrease in EGNOS performance in the Northern part of Service Area with correlation of high spikes of AATR values. The decrease in performance (increase of xPL values) is enhanced by an additional event which is not linked with ionospheric activity. The high values of GIVE indicator are observed during all day long with increase of AATR values by the end of the day which is induced by ionospheric activity.

On 20/05/2017 high geomagnetic activity has been observed within all day which increased the values of AATR and decreased the EGNOS performance. In addition to geomagnetic activity, an additional event (not linked to the ionospheric activity) has increased underperformance of EGNOS in the North West part of Service Area.

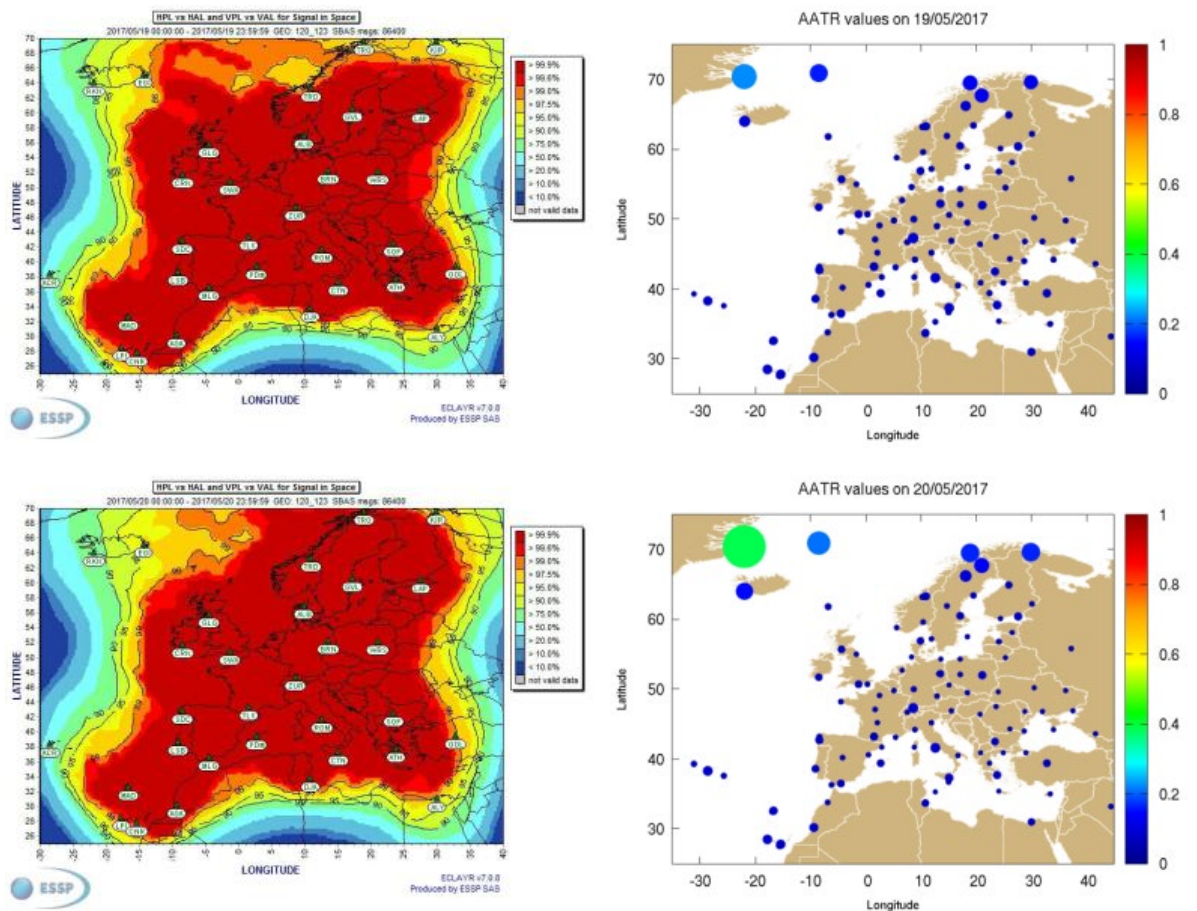


Figure 91. EGNOS APV-I availability maps and AATR daily mean values at IGS stations on DOY 139 and 140.

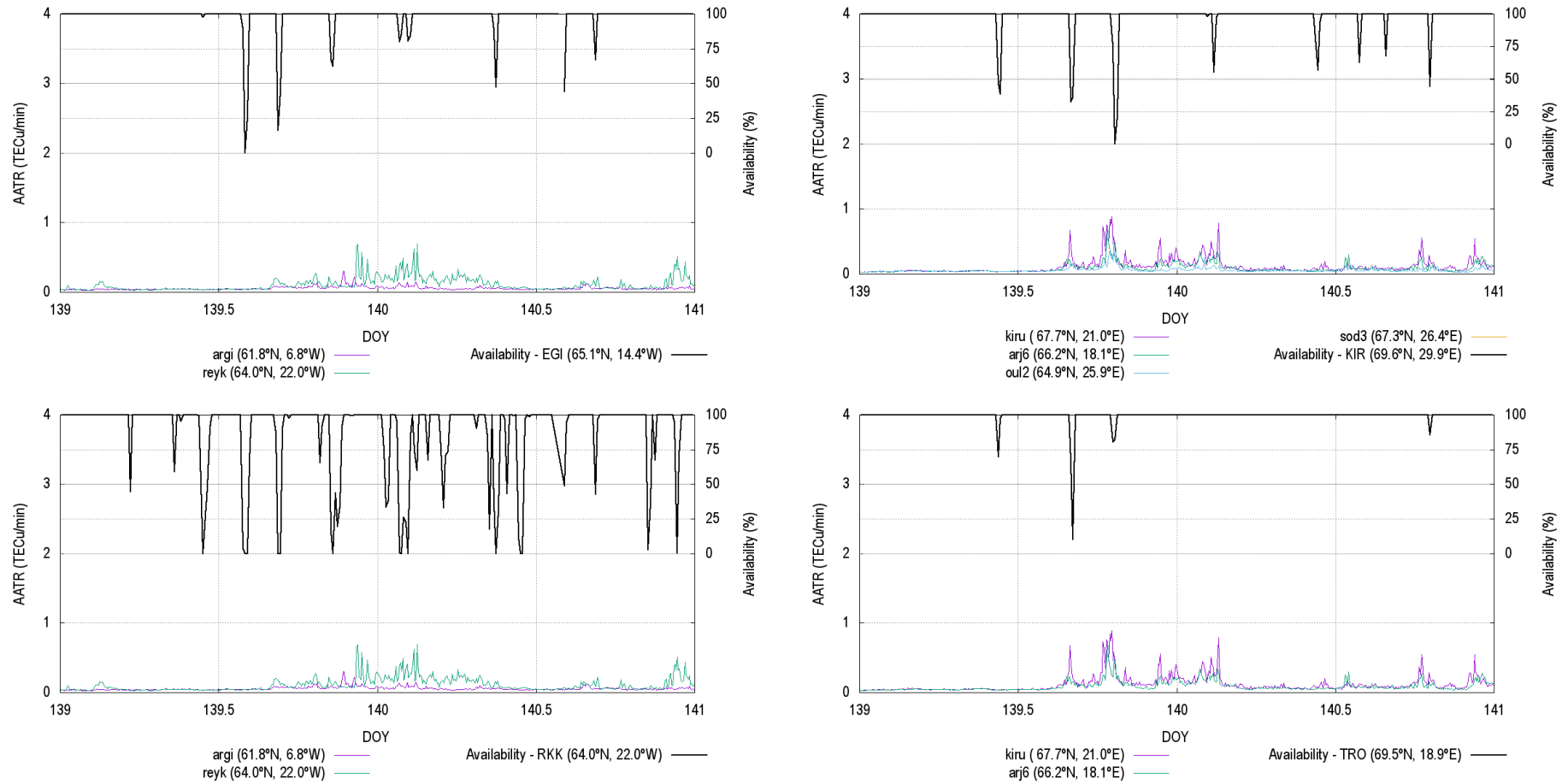


Figure 92. APV-I availability for assessed RIMS and AATR values at IGS station on DOY 139 and 140.

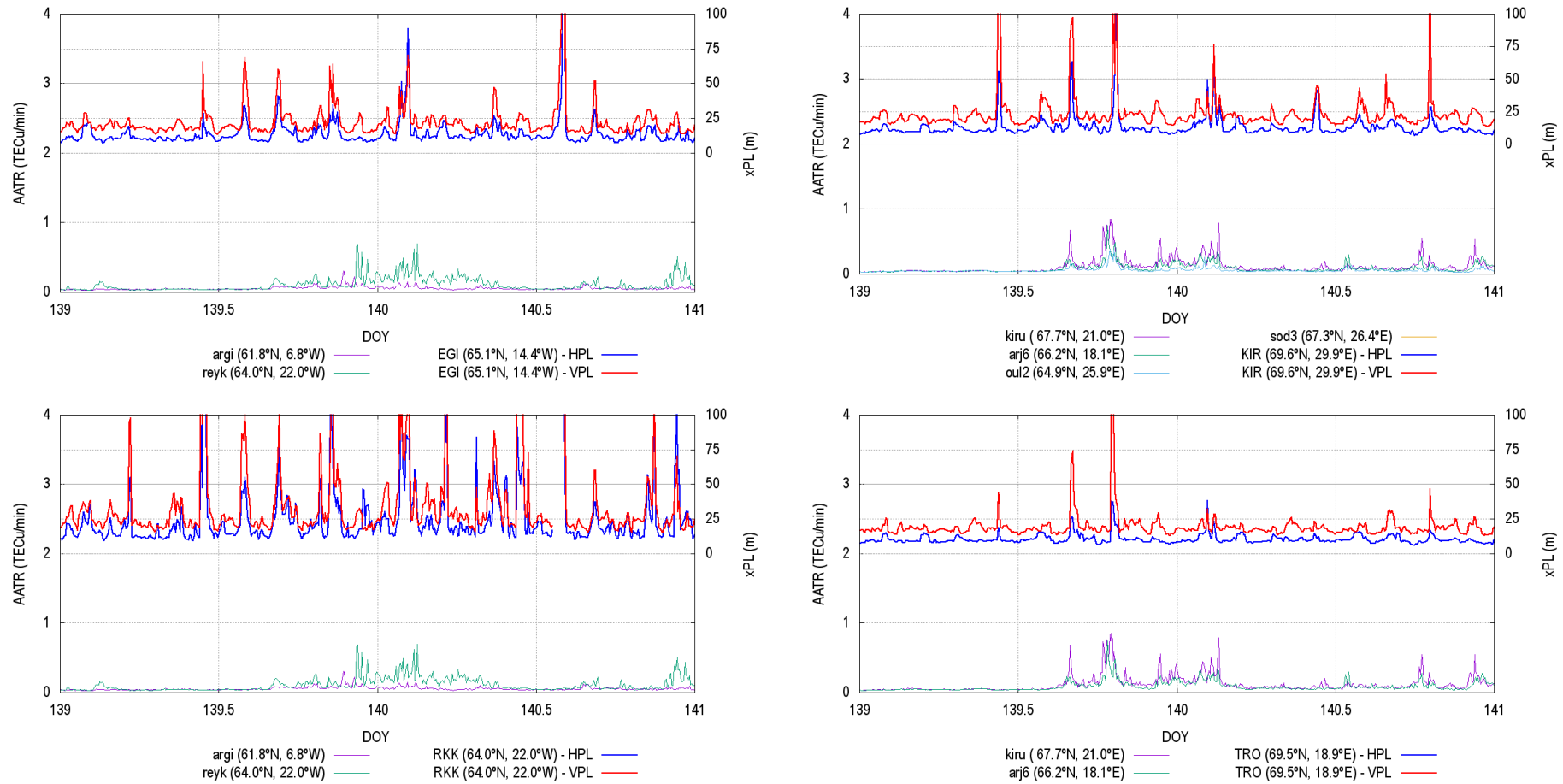


Figure 93. HPL and VPL variation for assessed RIMS and AATR values at IGS station on DOY 139 and 140.

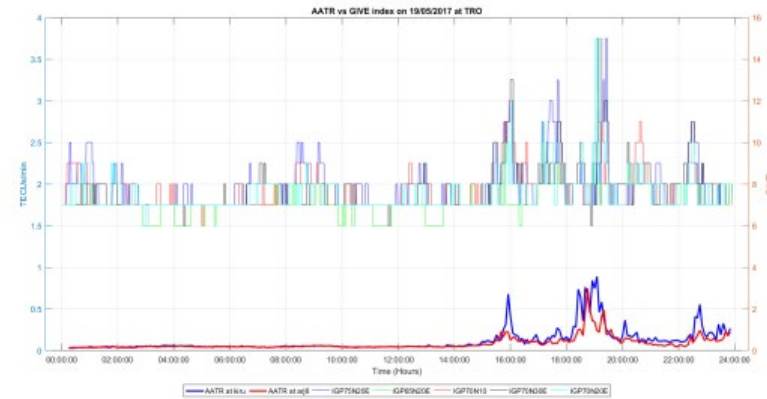
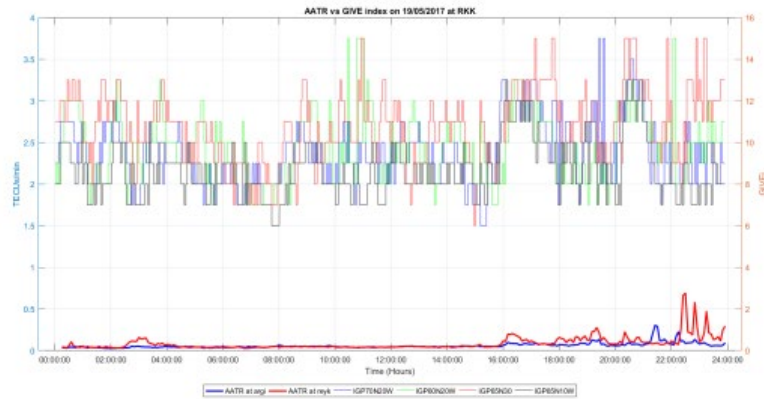
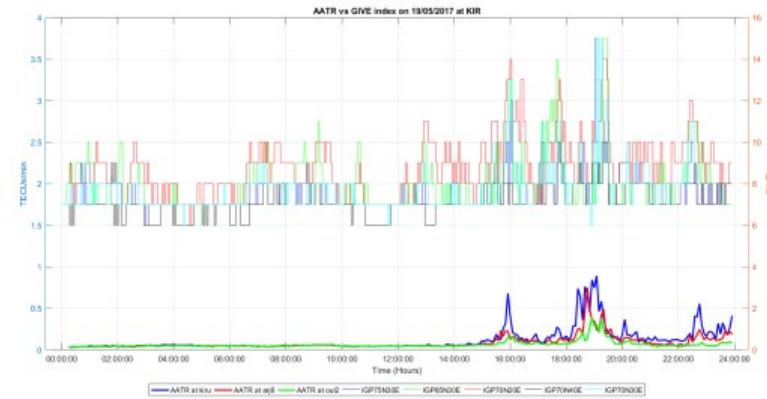
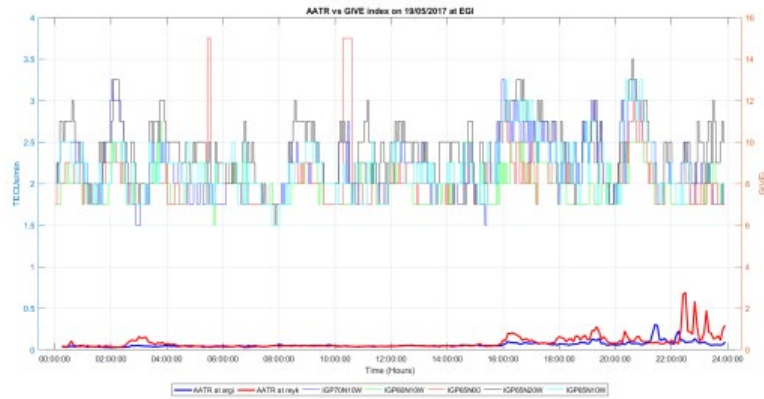


Figure 94. Temporal evolution of GIVE indices at IGPs surrounding assessed RIMS and AATR at IGS stations on DOY 139.

FIGURE NOT AVAILABLE

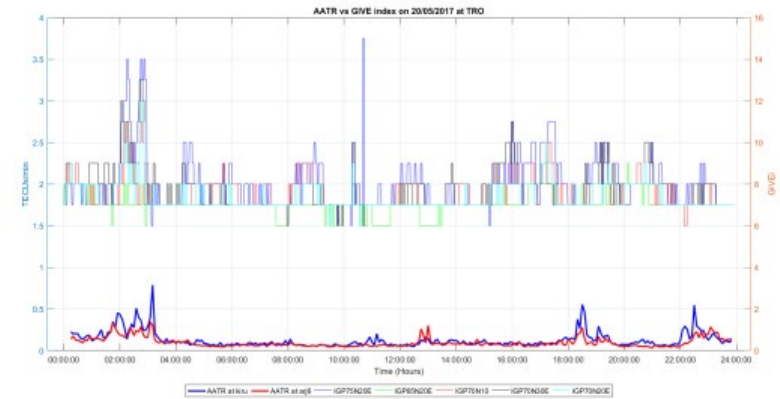
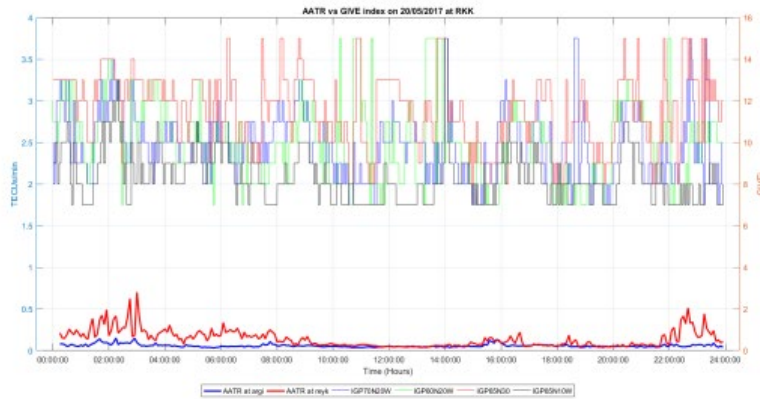
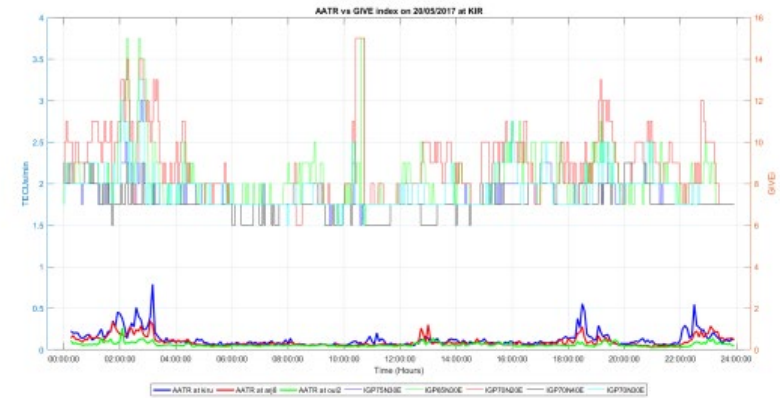


Figure 95. Temporal evolution of GIVE indices at IGPs surrounding assessed RIMS and AATR at IGS stations on DOY 140.

A.6 DOY 148

On 28/05/2017 very strong geomagnetic activity has been observed at the beginning of the day which had a strong impact in the North part of EGNOS Service Area. High spikes of AATR values are observed with significant impact decreasing performance at xPL level. It is also seen a strong correlation of high GIVE indicators at the beginning of the day with a high spikes of AATR values.

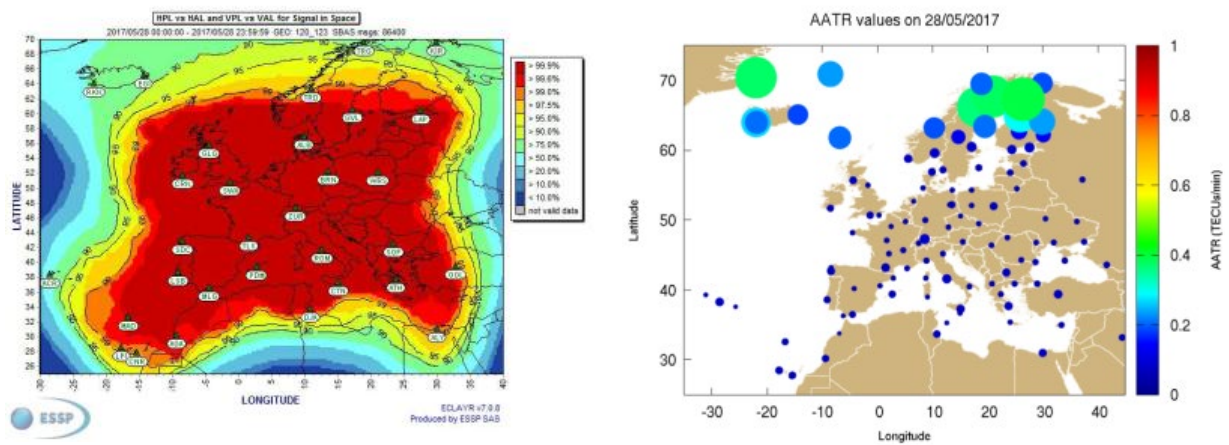


Figure 96. EGNOS APV-I availability maps and AATR daily mean values at IGS stations on DOY 148.

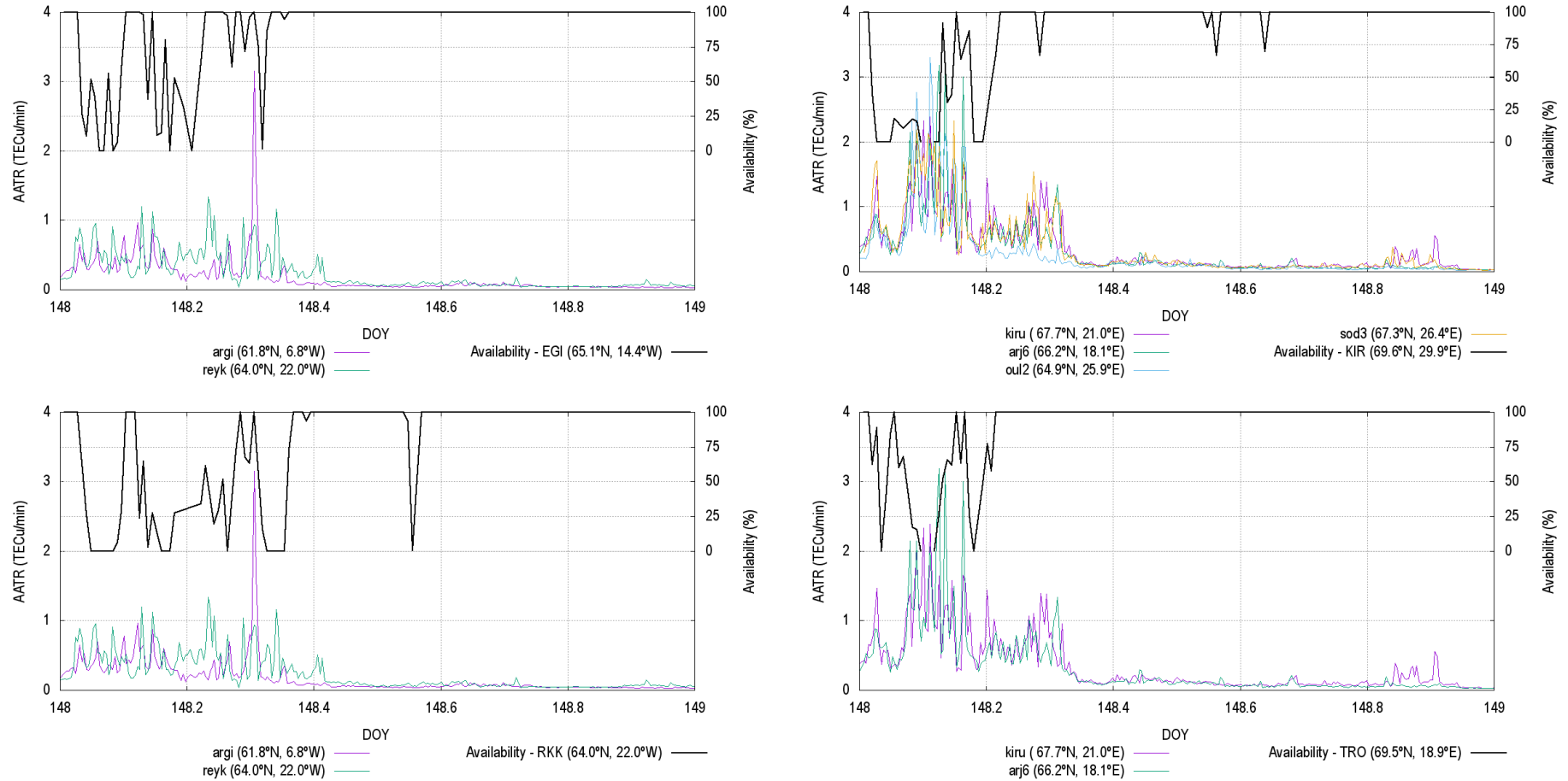


Figure 97. APV-I availability for assessed RIMS and AATR values at IGS station on DOY 140.

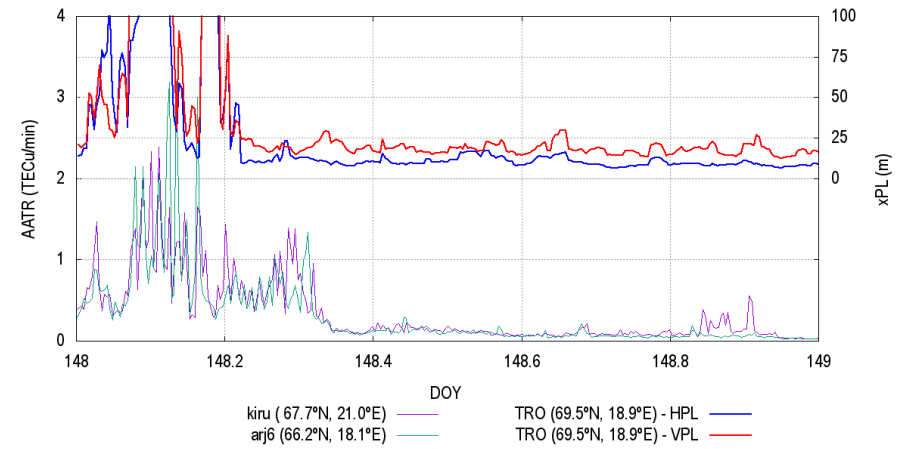
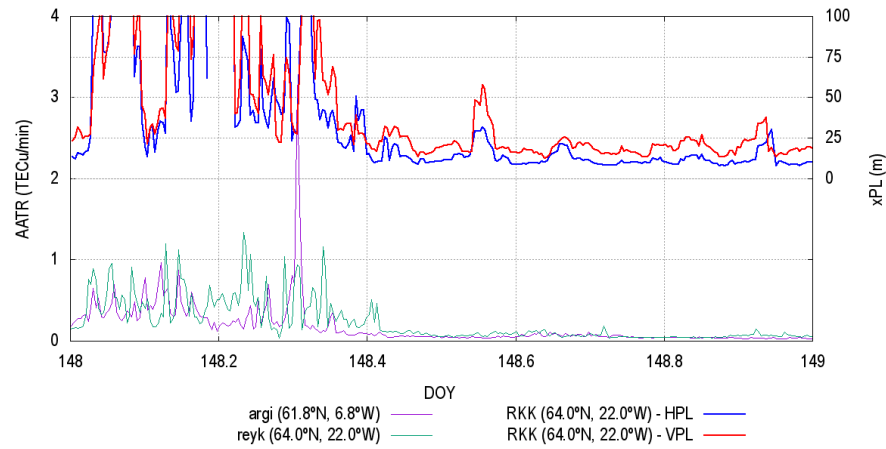
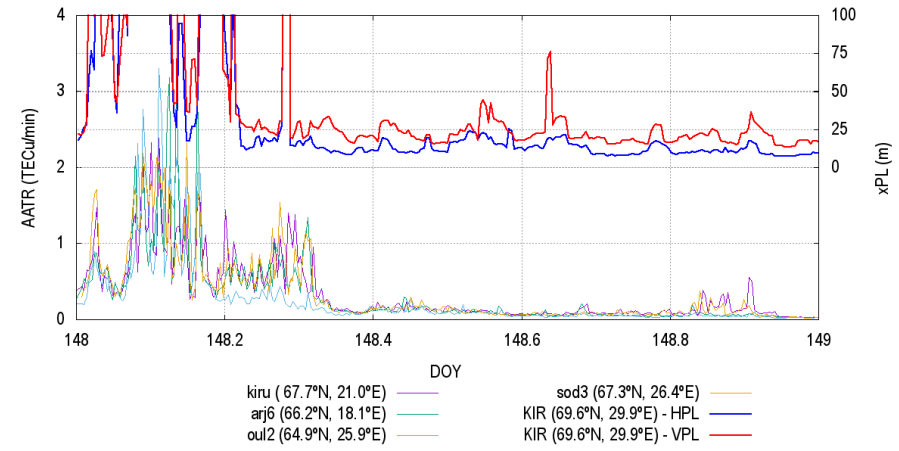
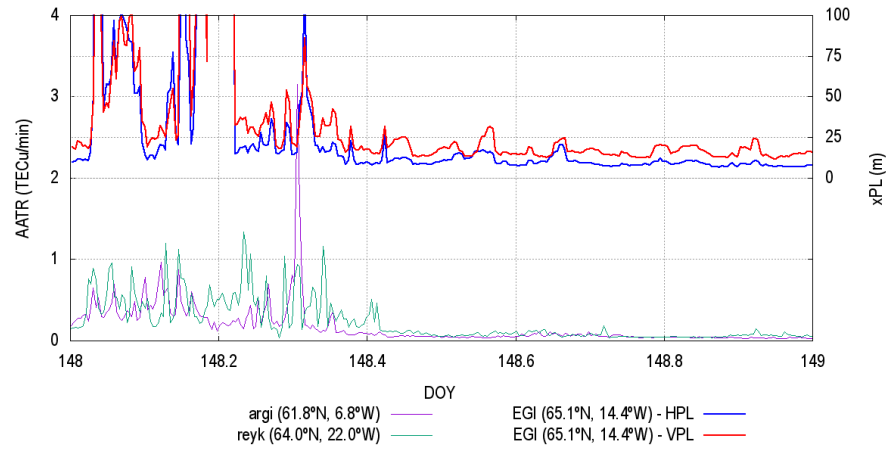


Figure 98. HPL and VPL variation for assessed RIMS and AATR values at IGS station on DOY 148.

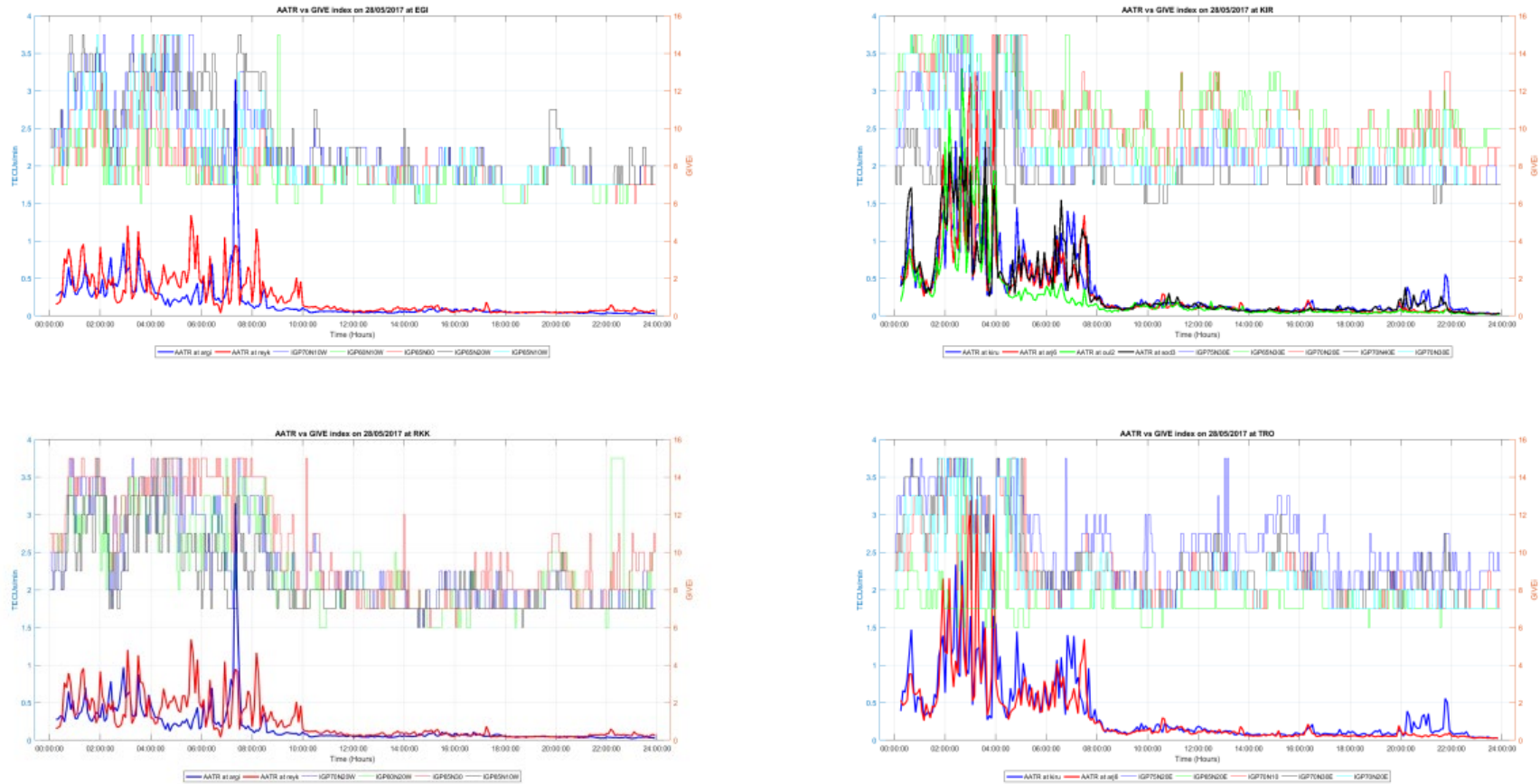


Figure 99. Temporal evolution of GIVE indices at IGPs surrounding assessed RIMS and AATR at IGS stations on DOY 148.

A.7 DOY 197

On 16/07/2017 geomagnetic impact has been present especially in the second part of the day degrading EGNOS performance in the North part of Service Area. The strong correlation between high values of AATR and decrease in availability is seen in the graph below. The high values of GIVE indices have been observed in correlation of AATR high spikes.

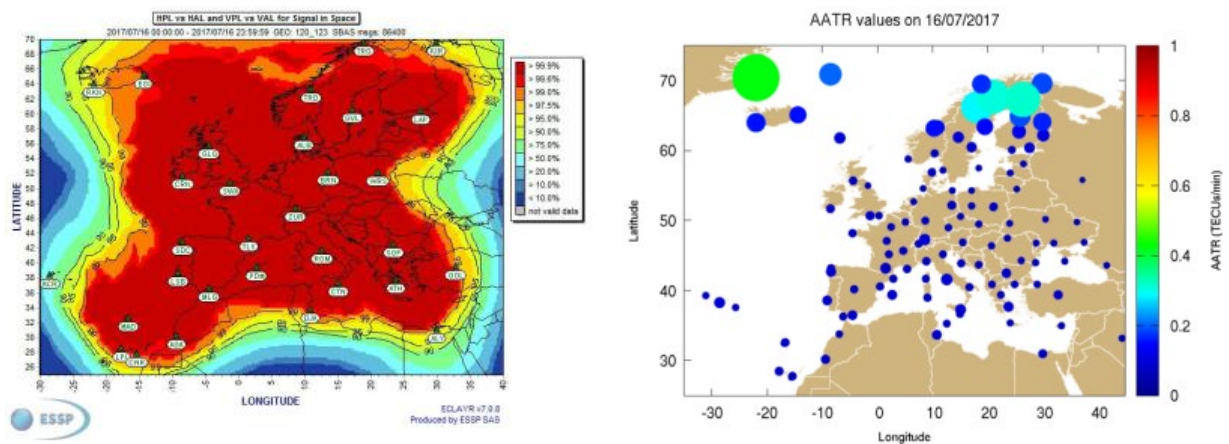


Figure 100. EGNOS APV-I availability maps and AATR daily mean values at IGS stations on DOY 197.

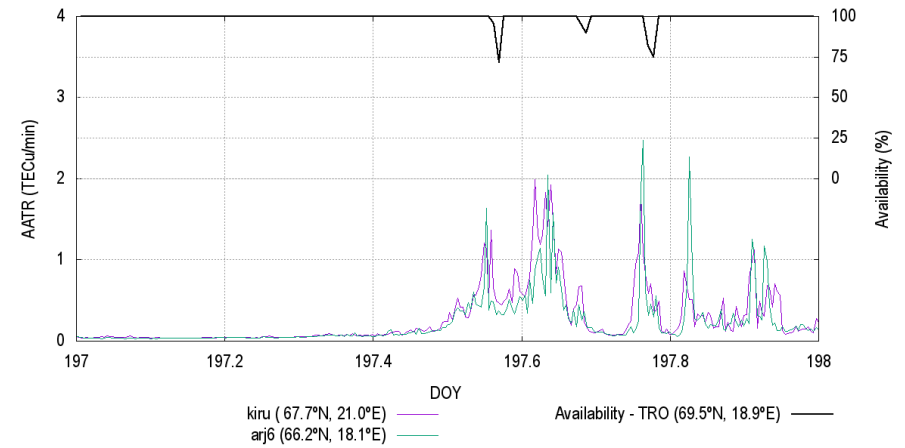
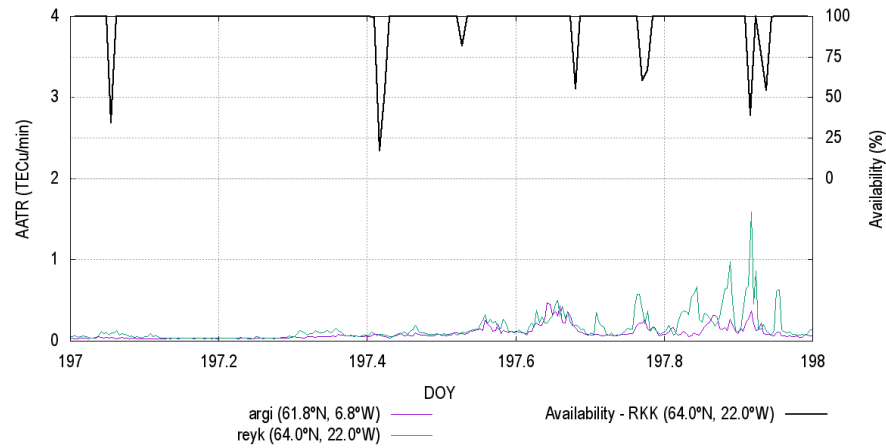
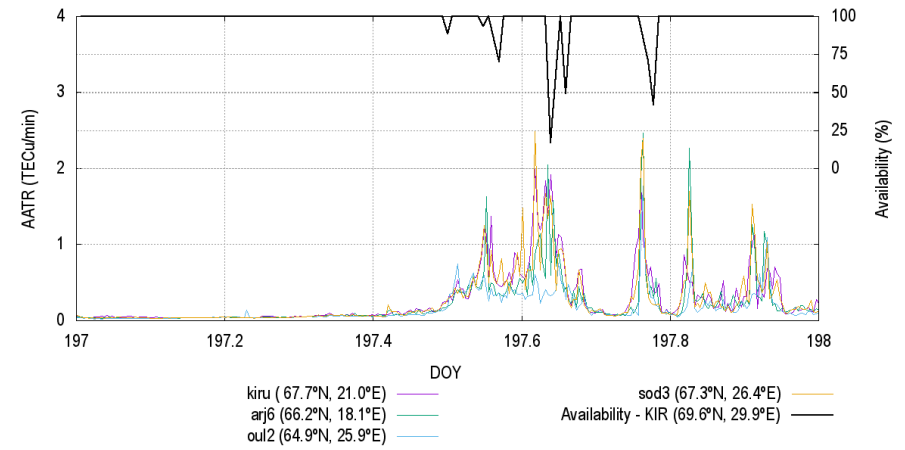
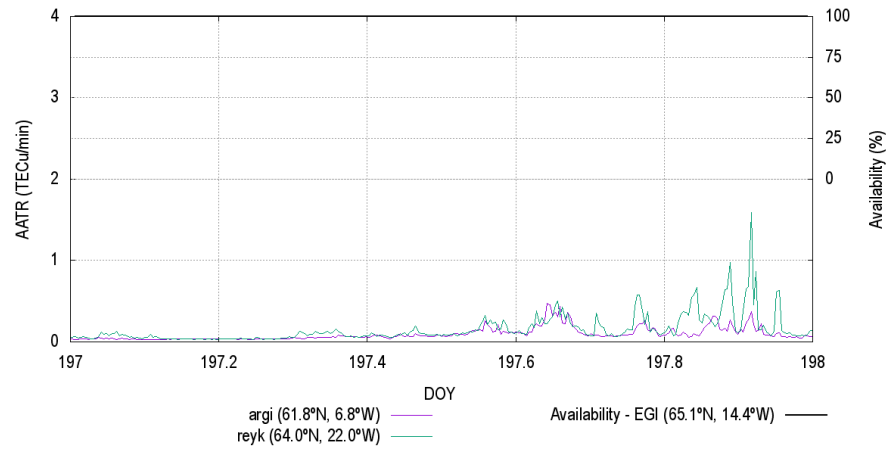
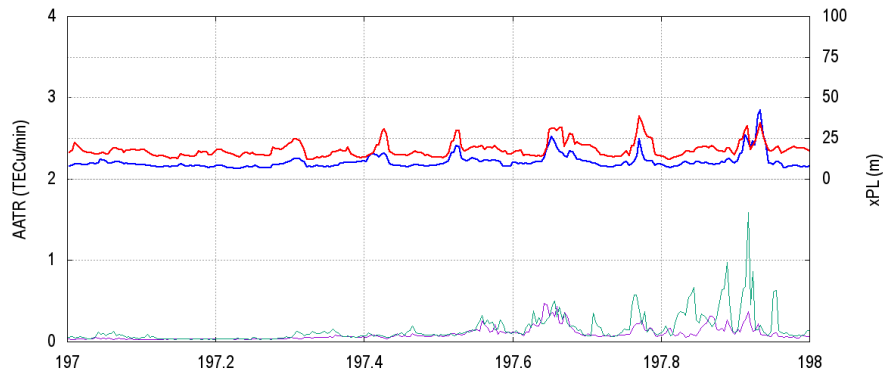
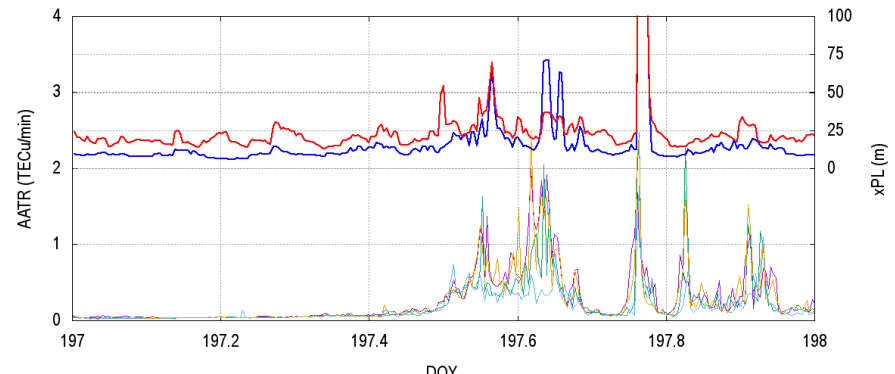


Figure 101. APV-I availability for assessed RIMS and AATR values at IGS station on DOY 197.



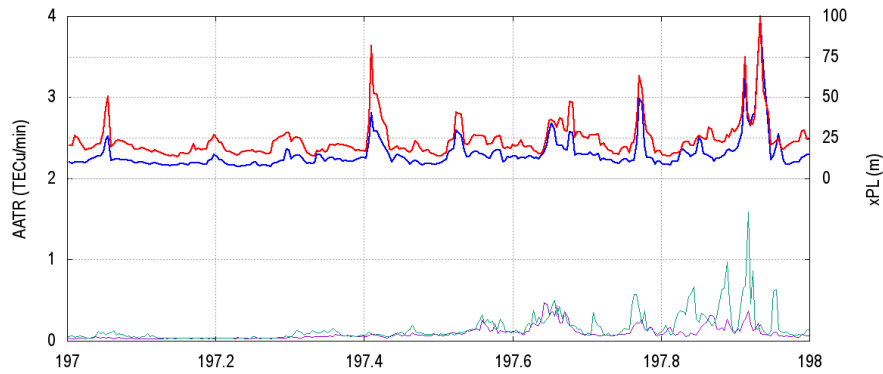
DOY

argi (61.8°N, 6.8°W)	reyk (64.0°N, 22.0°W)	EGI (65.1°N, 14.4°W) - HPL	EGI (65.1°N, 14.4°W) - VPL
----------------------	-----------------------	----------------------------	----------------------------



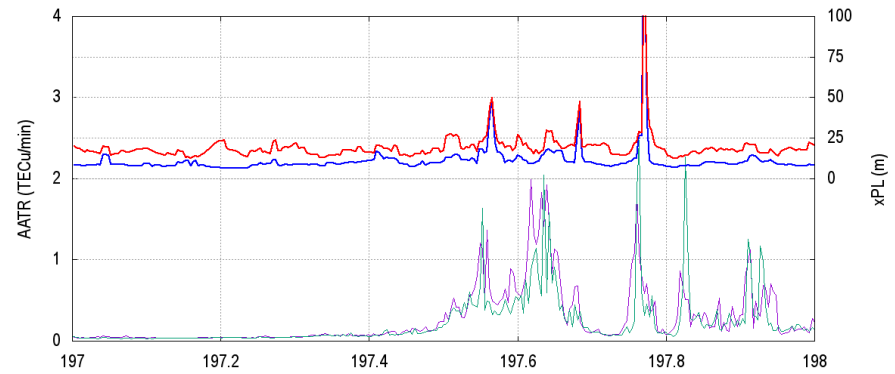
DOY

kiru (67.7°N, 21.0°E)	arj6 (66.2°N, 18.1°E)	oul2 (64.9°N, 25.9°E)	sod3 (67.3°N, 26.4°E)	KIR (69.6°N, 29.9°E) - HPL	KIR (69.6°N, 29.9°E) - VPL
-----------------------	-----------------------	-----------------------	-----------------------	----------------------------	----------------------------



DOY

argi (61.8°N, 6.8°W)	reyk (64.0°N, 22.0°W)	RKK (64.0°N, 22.0°W) - HPL	RKK (64.0°N, 22.0°W) - VPL
----------------------	-----------------------	----------------------------	----------------------------



DOY

kiru (67.7°N, 21.0°E)	arj6 (66.2°N, 18.1°E)	TRO (69.5°N, 18.9°E) - HPL	TRO (69.5°N, 18.9°E) - VPL
-----------------------	-----------------------	----------------------------	----------------------------

Figure 102. HPL and VPL variation for assessed RIMS and AATR values at IGS station on DOY 197.

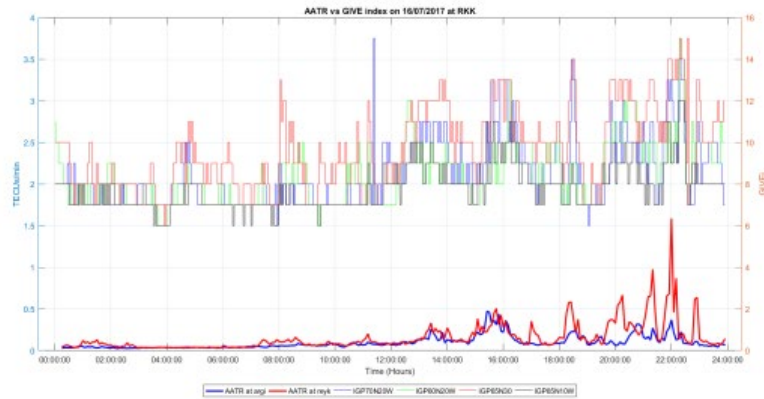
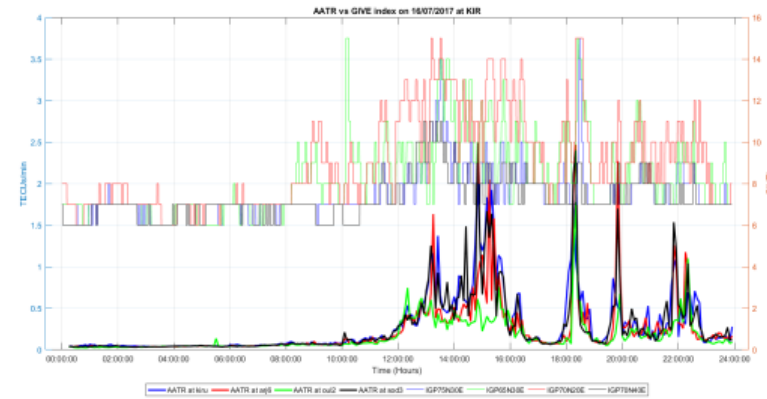
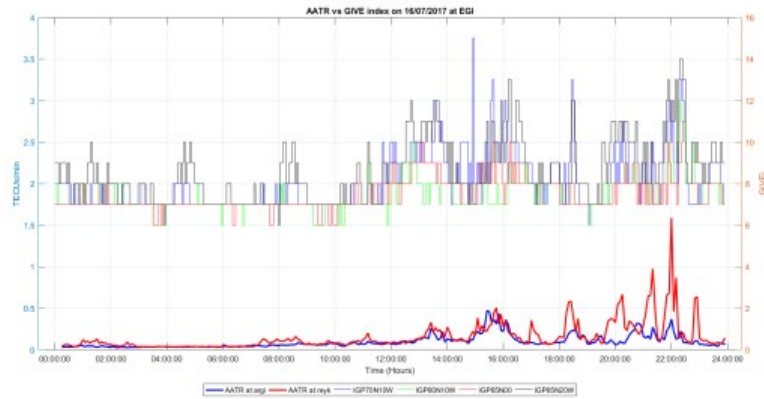


Figure 103. Temporal evolution of GIVE indices at IGPs surrounding assessed RIMS and AATR at IGS stations on DOY 197.

A.8 DOY 234 and 235

On 22/08/2017 geomagnetic activity was observed at the beginning and by the end of the day which had slight impact in EGNOS performance in the North part of Service Area. Spikes of AATR values are observed with correlation to increase of xPL values. The correlation of spikes present in AATR distribution is observed with increase of GIVE indicators.

On 23/08/2017 geomagnetic storm was observed with impact on EGNOS performance in the North part of Service Area by the end of the day. The spikes of AATR values with correlation of high values of xPLs were seen. The increase of GIVE indicators has been observed with correlation of increase of AATR values.

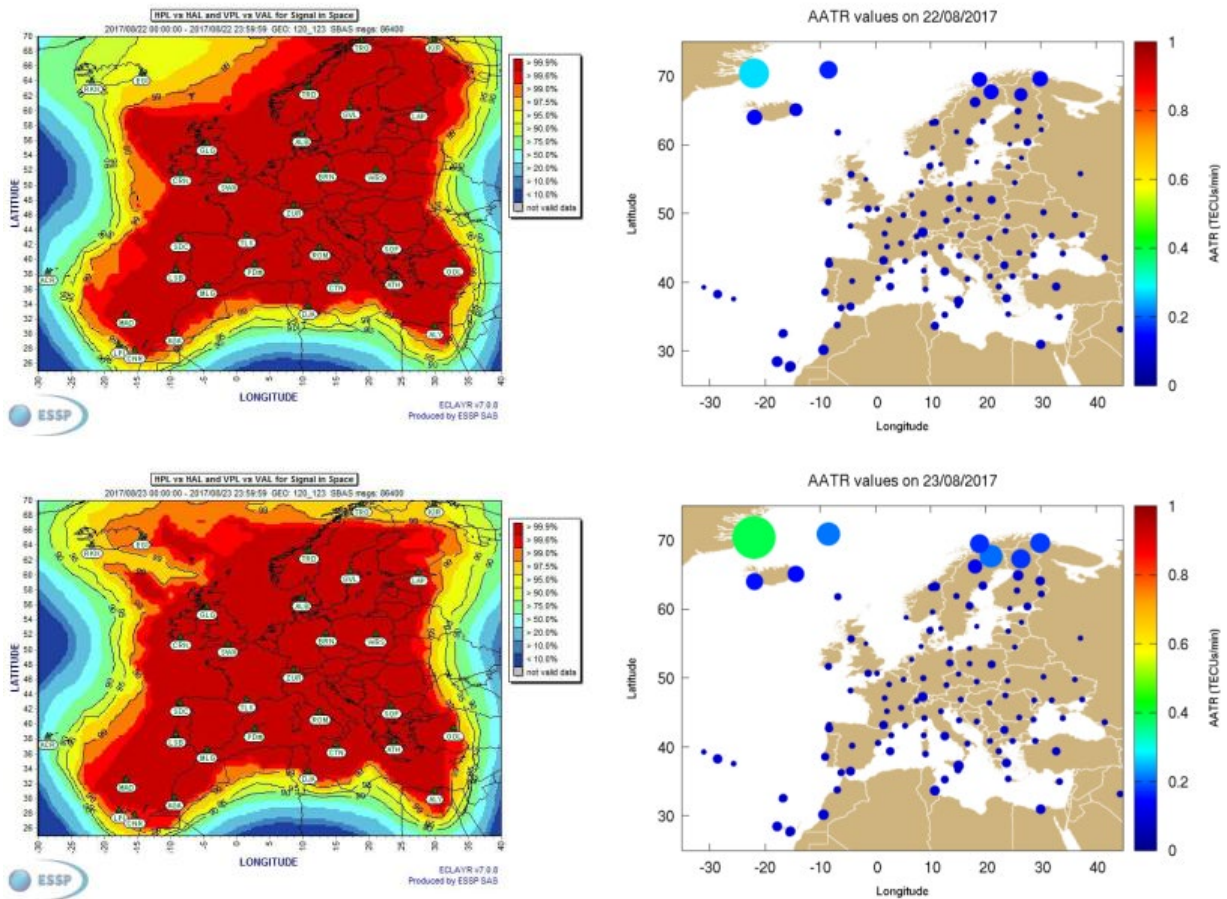


Figure 104. EGNOS APV-I availability maps and AATR daily mean values at IGS stations on DOY 234 and 235.

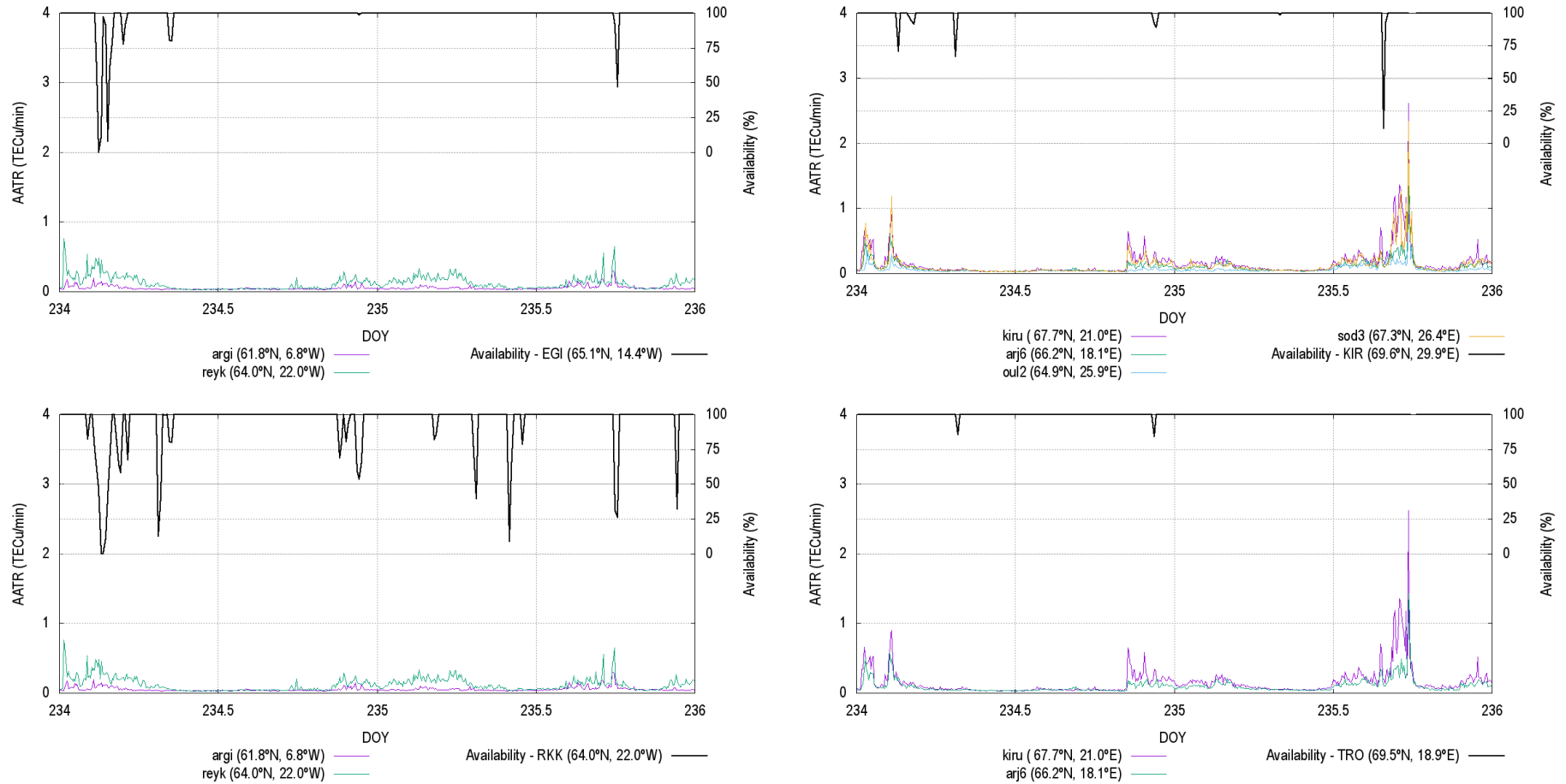


Figure 105. APV-I availability for assessed RIMS and AATR values at IGS station on DOY 234 and 235.

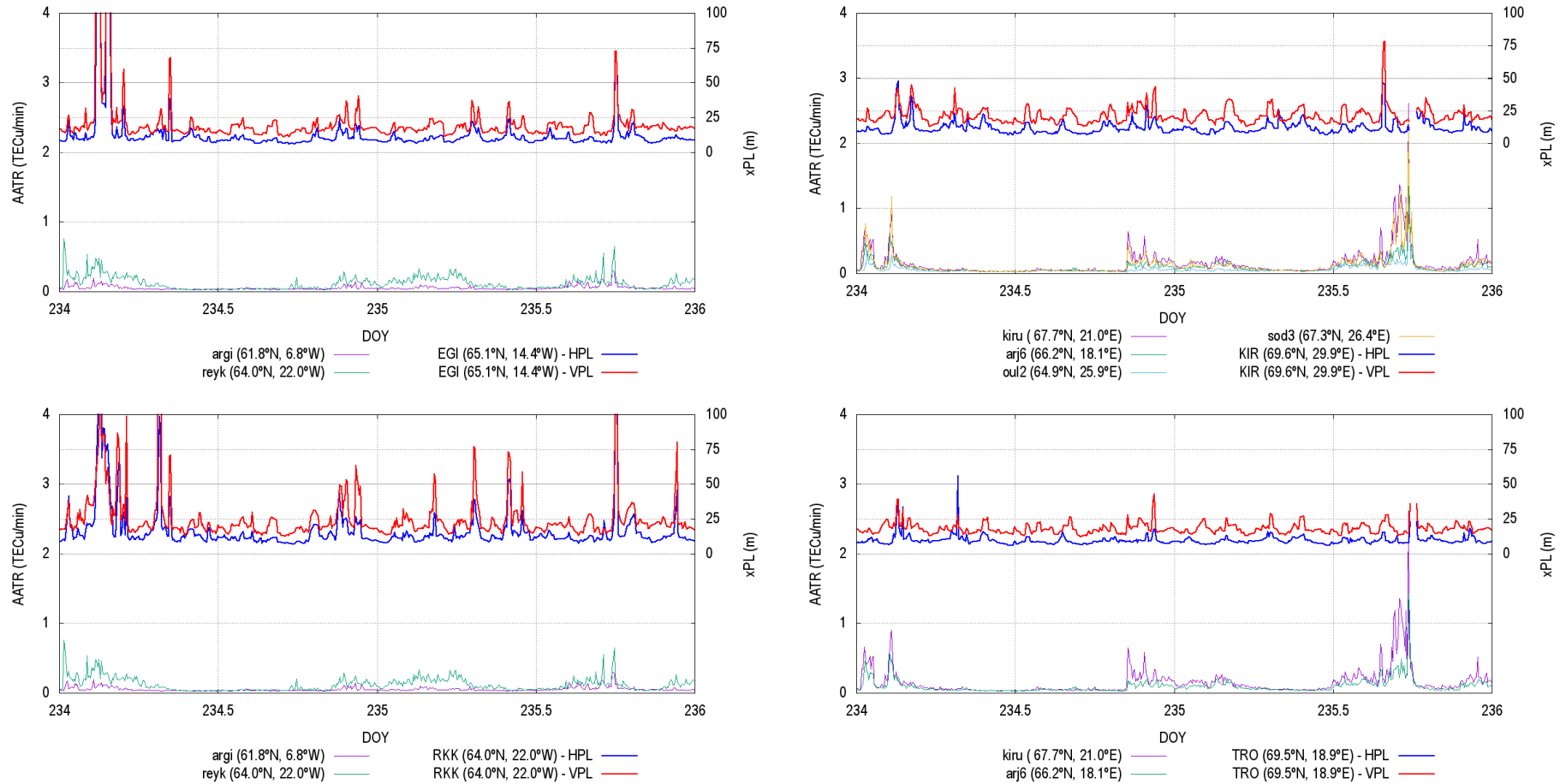


Figure 106. HPL and VPL variation for assessed RIMS and AATR values at IGS station on DOY 234 and 235.

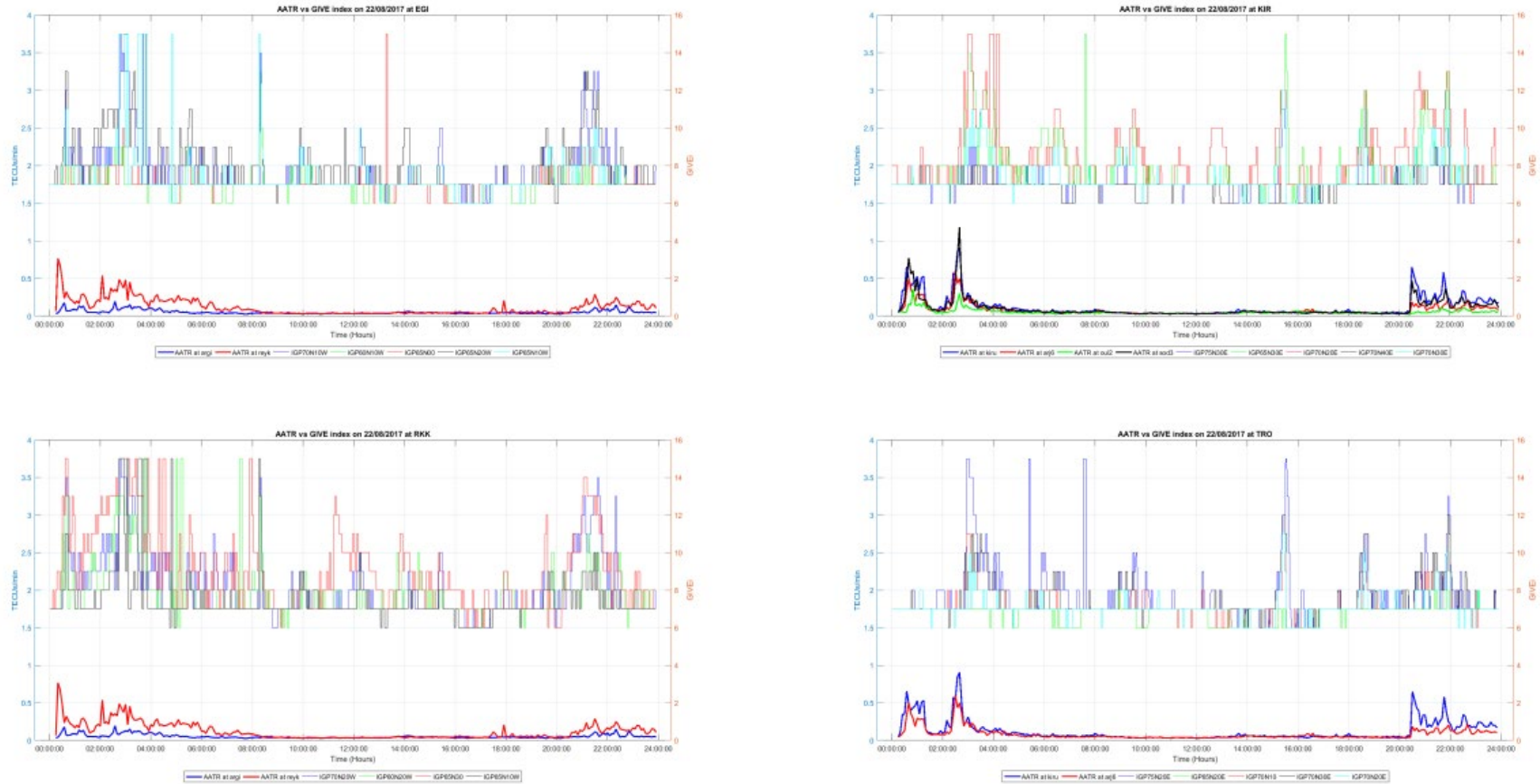


Figure 107. Temporal evolution of GIVE indices at IGP stations surrounding assessed RIMS and AATR at IGS stations on DOY 234.

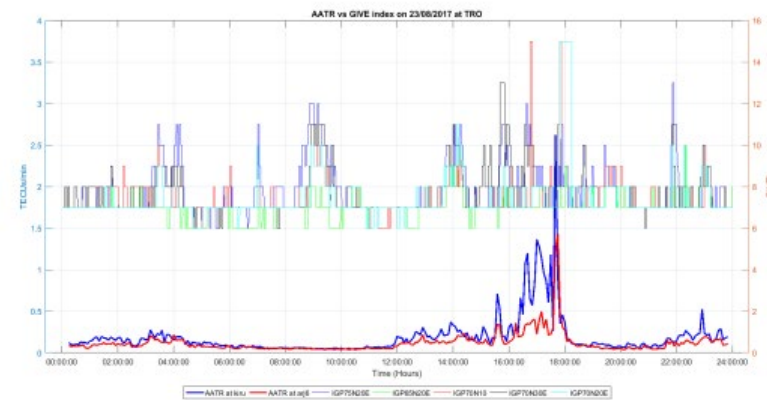
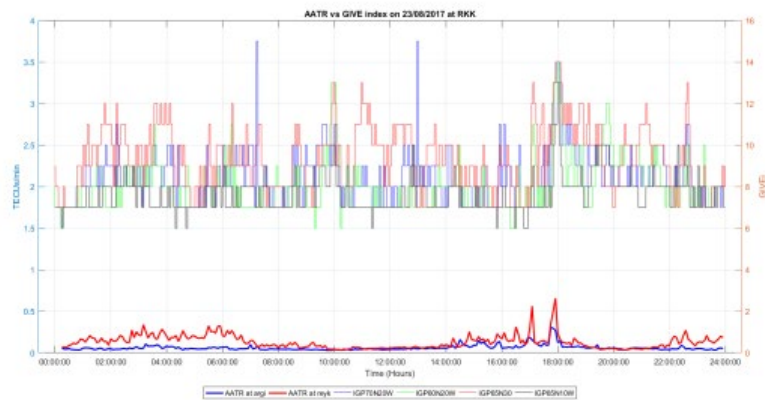
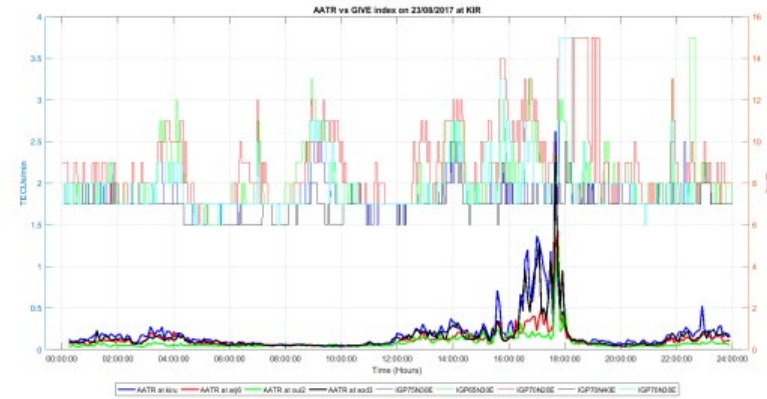
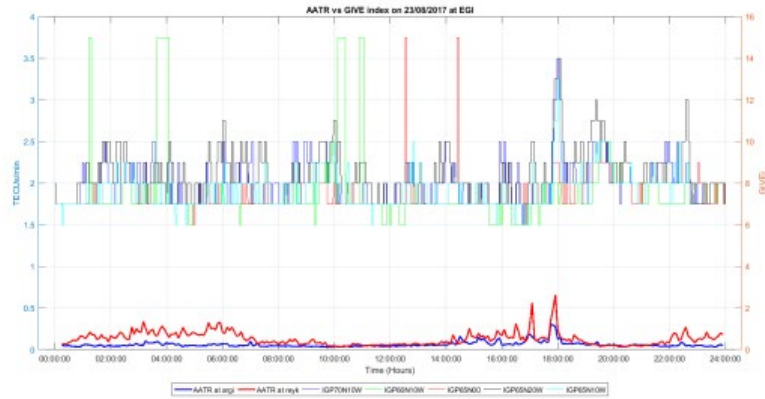


Figure 108. Temporal evolution of GIVE indices at IGPs surrounding assessed RIMS and AATR at IGS stations on DOY 235.

A.9 DOY 255 to 259

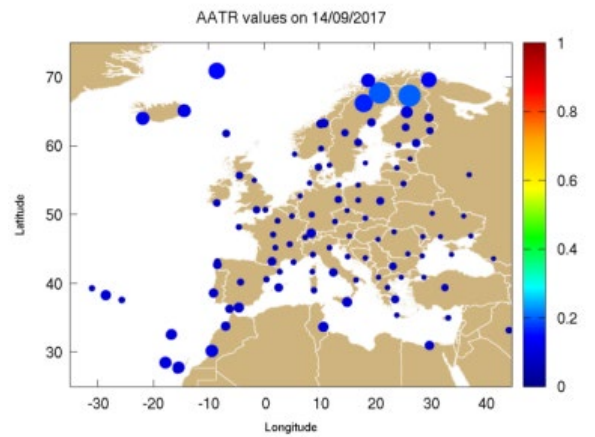
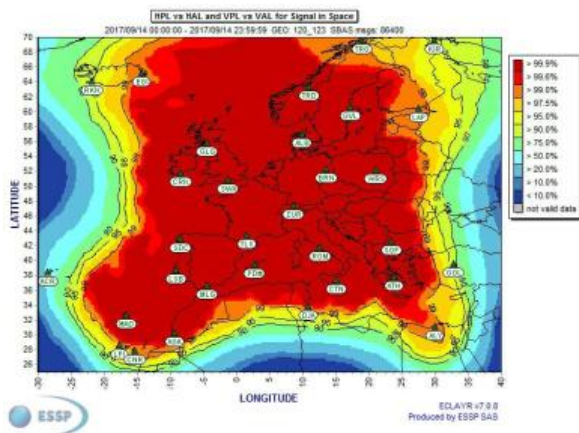
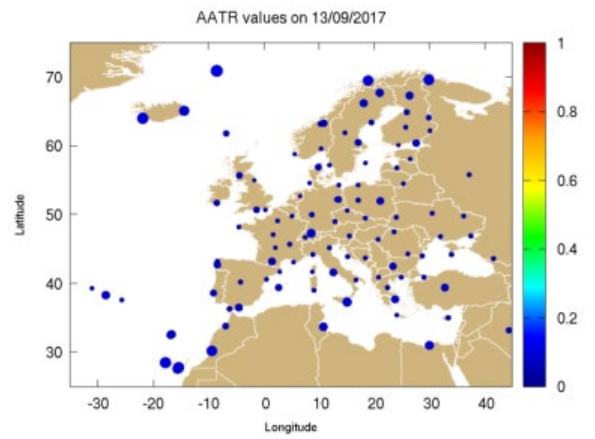
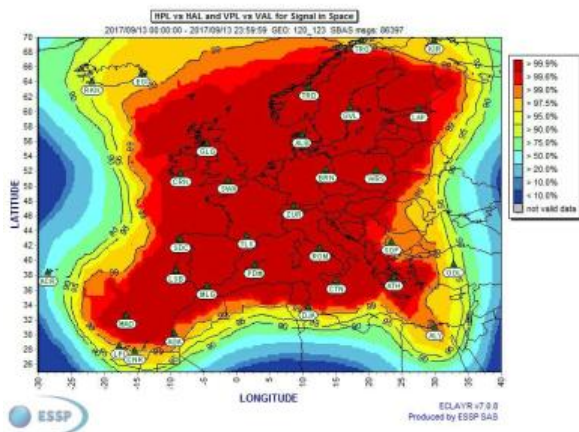
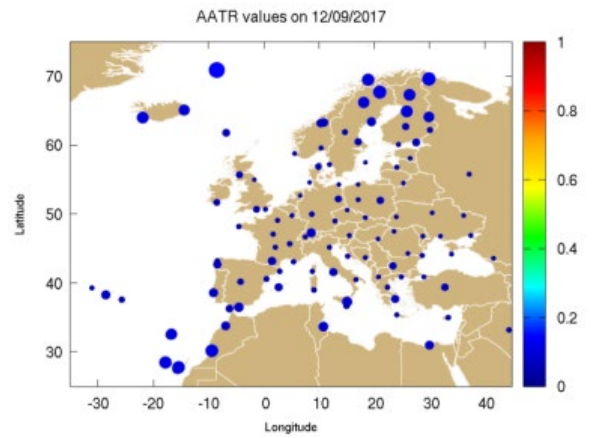
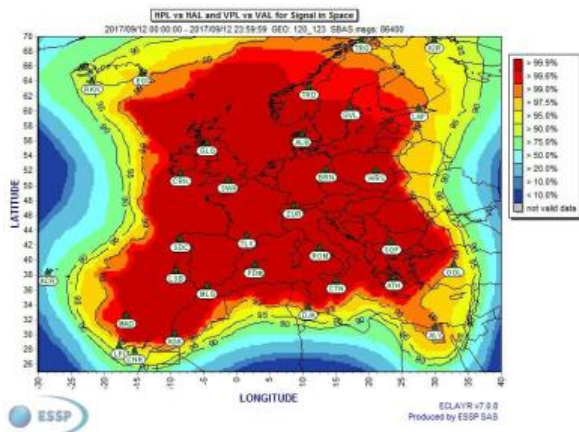
On 12/09/2017 geomagnetic activity has been observed by the end of the day decreasing EGNOS performance. It is observed high spikes of AATR values and increase in xPL values. In addition the high increase of GIVE indicators have been observed with increase of AATR values by the end of the day. The degradation observed in EGNOS performance in the beginning of the day has no link with ionospheric activity.

On 13/09/2017 geomagnetic activity has been present at the beginning of the day degrading EGNOS performance in the North part of Service Area. The increase in AATR values are well correlated with increase of xPL values. The GIVE indicators have been estimated at high values at the beginning of the day with present spikes of AATR values. Presence of additional degradation in EGNOS availability performance is caused by other source.

On 14/09/2017 geomagnetic activity has been observed by the end of the day degrading EGNOS performance in the North part of Service Area. High spikes of AATR values are present at the end of the day with increase in xPL values. The increase in GIVE indicators are present by the end of the day correlated well with increase of AATR values.

On 15/09/2017 geomagnetic activity has been observed at the beginning and at the end of the day impacting EGNOS performance. The AATR high spikes are present at the beginning and end of the day with increased values of xPLs. The high GIVE indicators are also well correlated with high spikes of AATR values at the same time as other parameters.

On 16/09/2017 geomagnetic activity has been observed especially at the beginning of the day degrading EGNOS performance in the North part of Service Area. The high spikes of AATR values are present at the beginning of the day and well correlated with increased values of xPL values. The increase of GIVE indicators is presented and correlated with high spikes of AATR values.



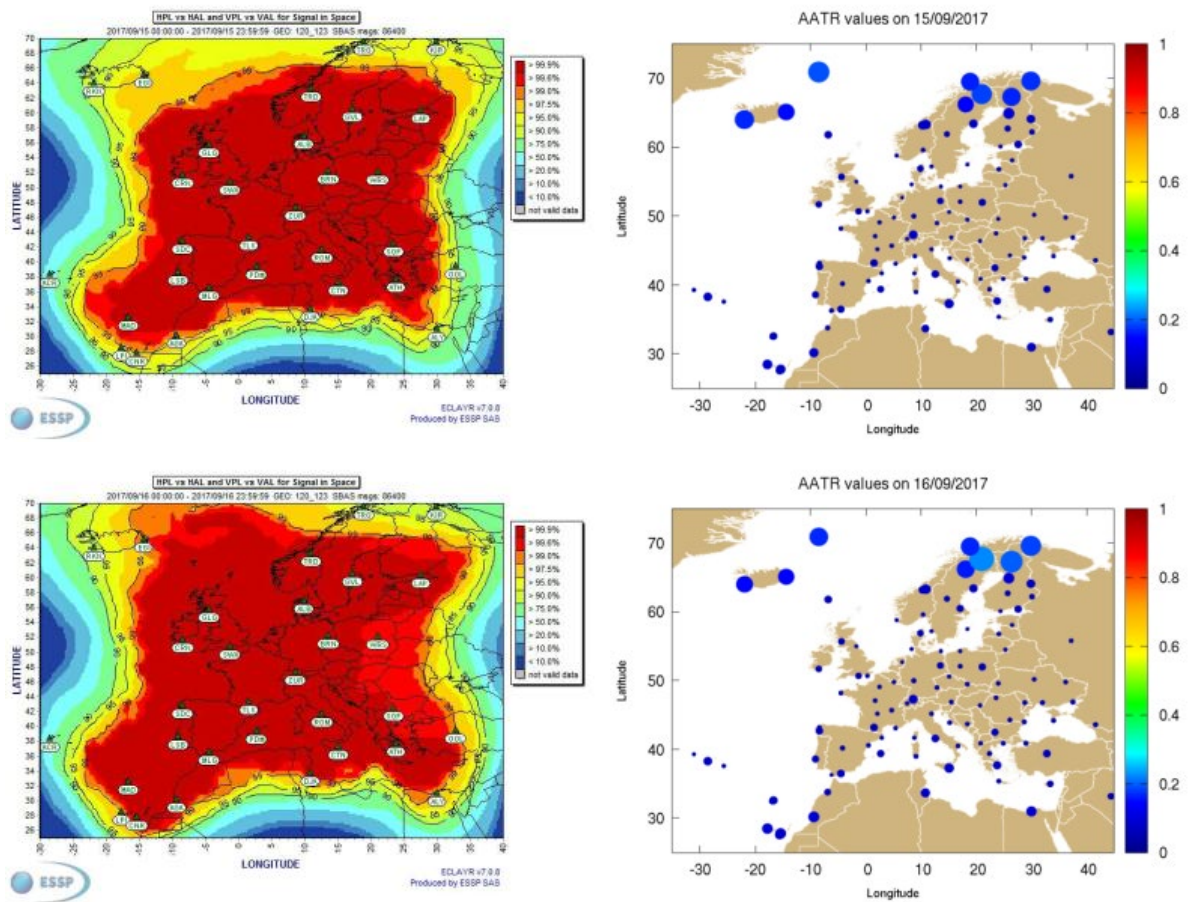


Figure 109. EGNOS APV-I availability maps and AATR daily mean values at IGS stations from DOY 255 to 259.

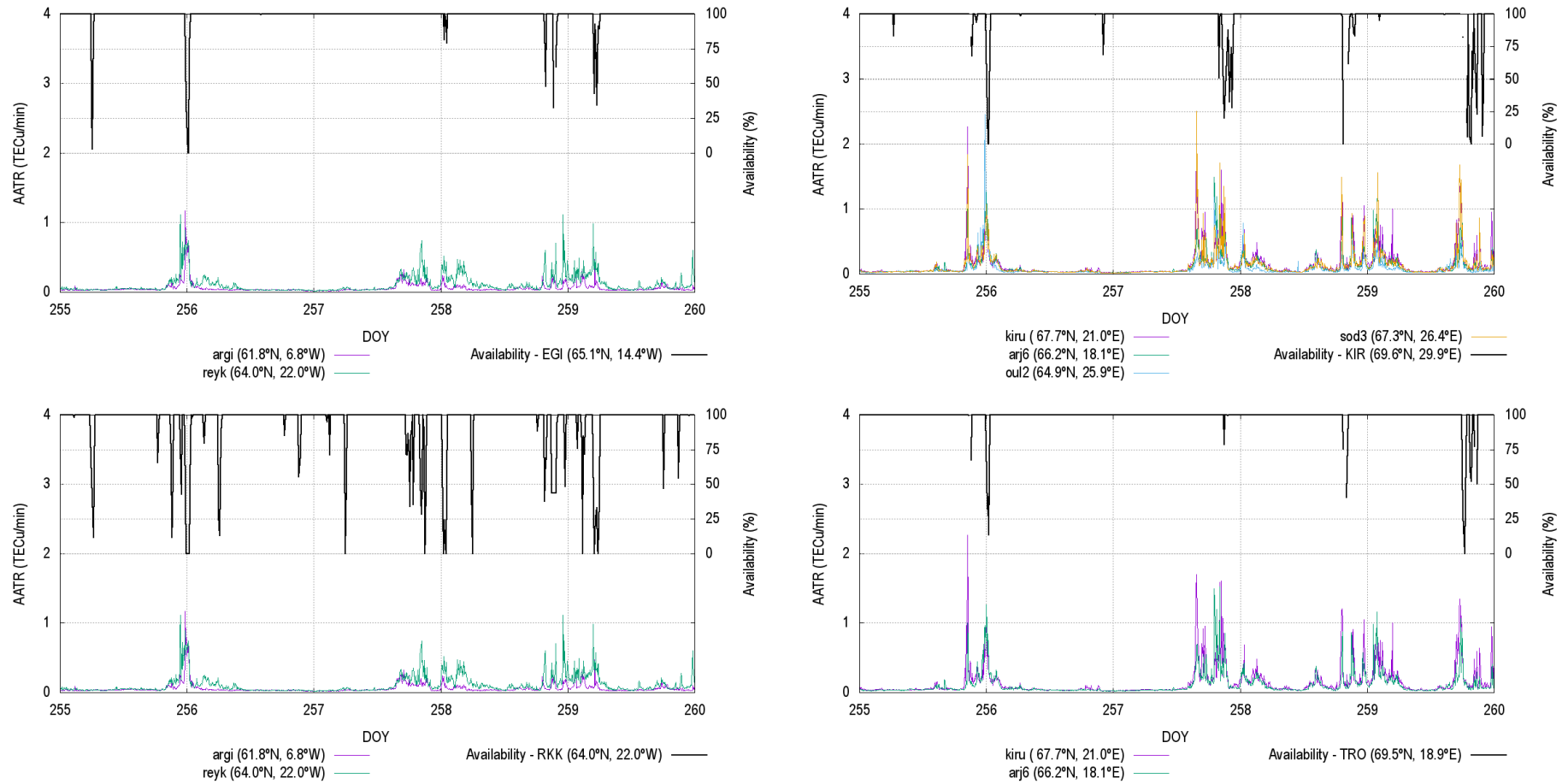


Figure 110. APV-I availability for assessed RIMS and AATR values at IGS station from DOY 255 to 259.

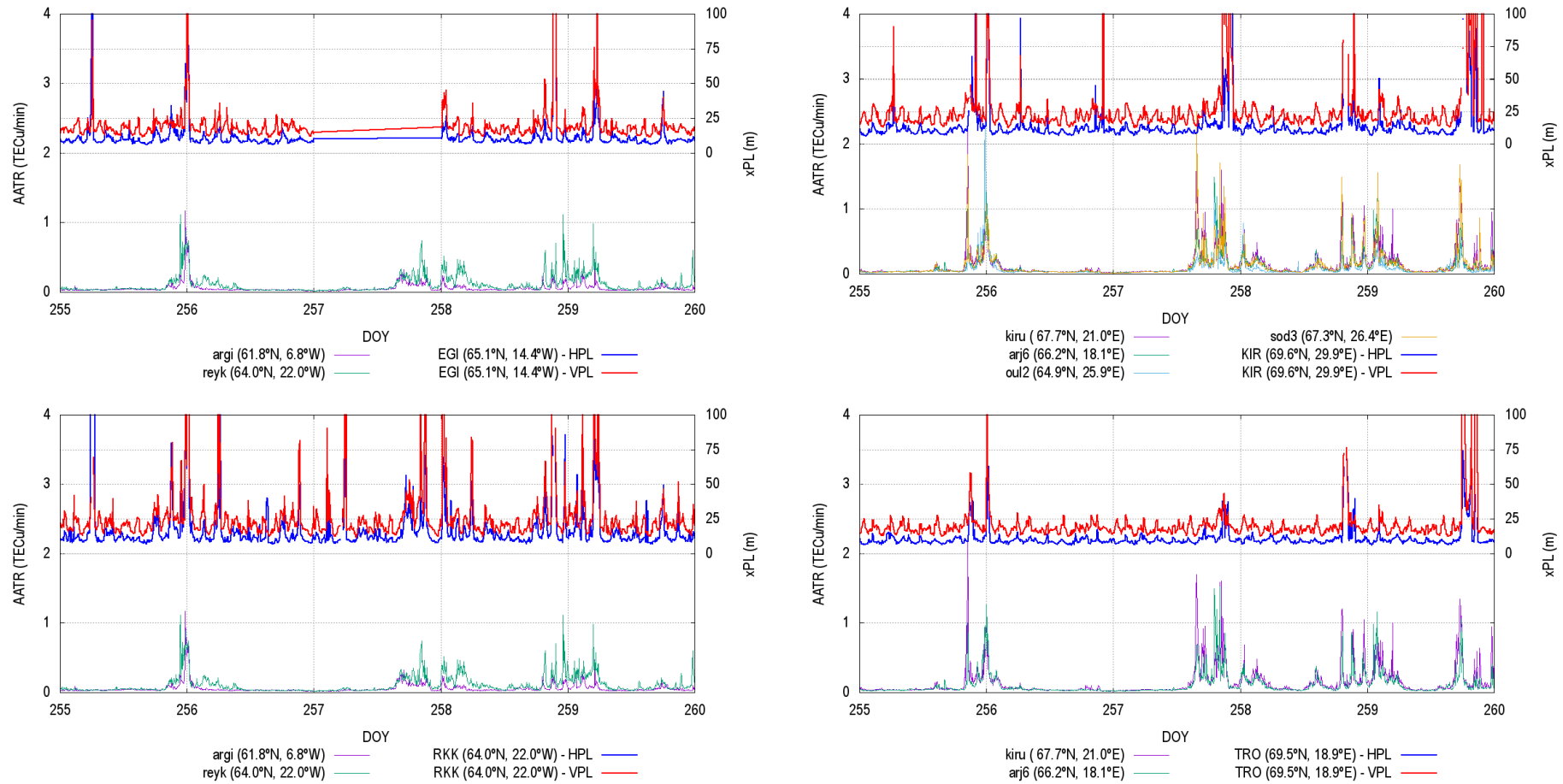


Figure 111. HPL and VPL variation for assessed RIMS and AATR values at IGS station from DOY 255 to 259.

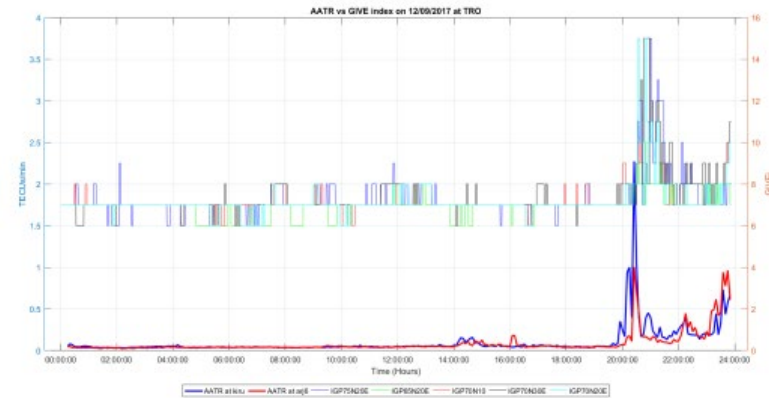
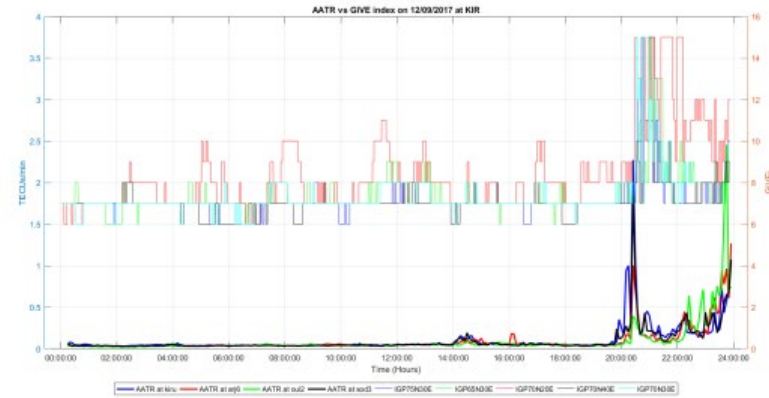


Figure 112. Temporal evolution of GIVE indices at IGP's surrounding assessed RIMS and AATR at IGS stations on DOY 255.

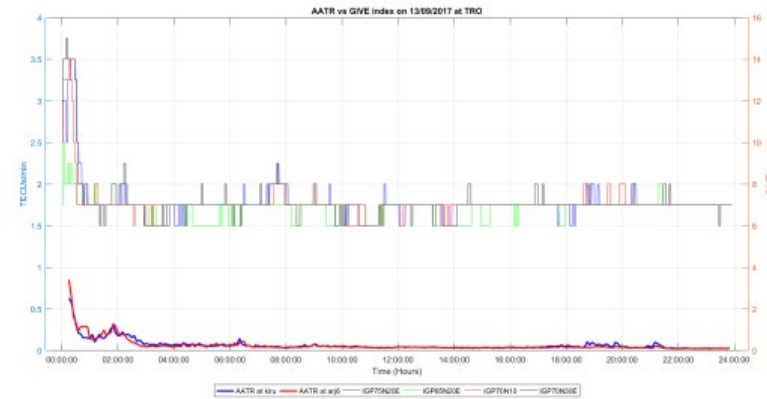
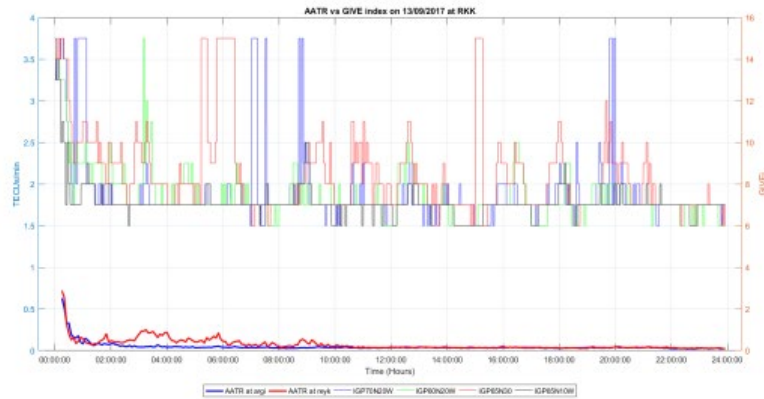
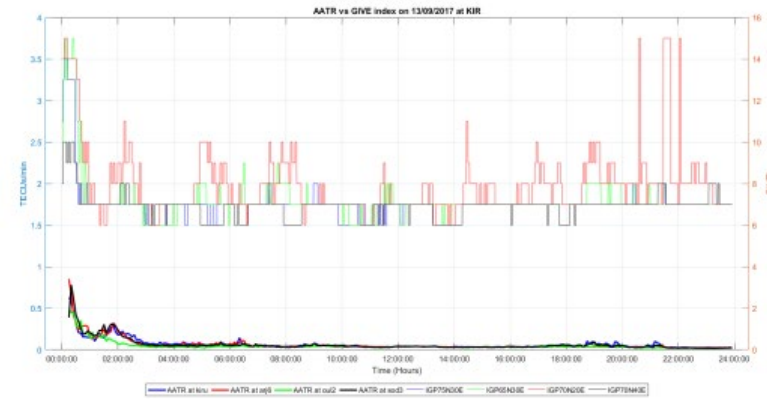
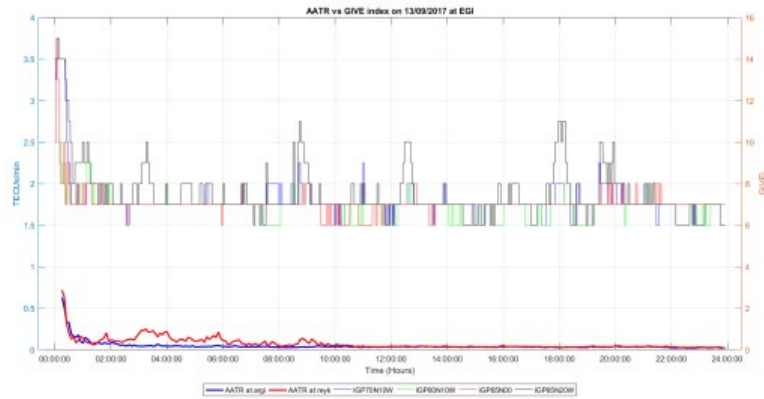


Figure 113. Temporal evolution of GIVE indices at IGPs surrounding assessed RIMS and AATR at IGS stations on DOY 256.

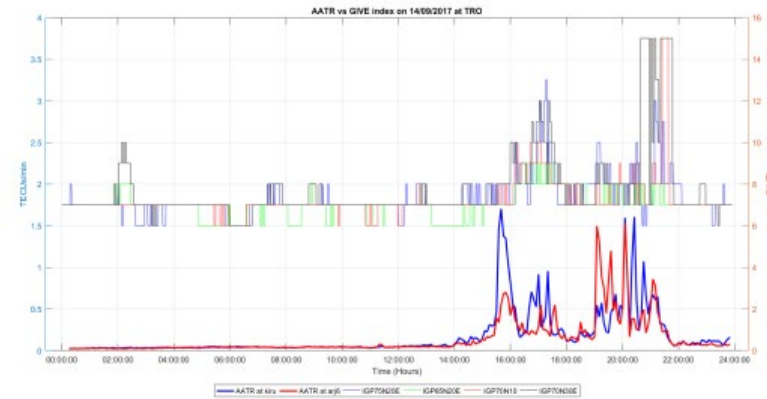
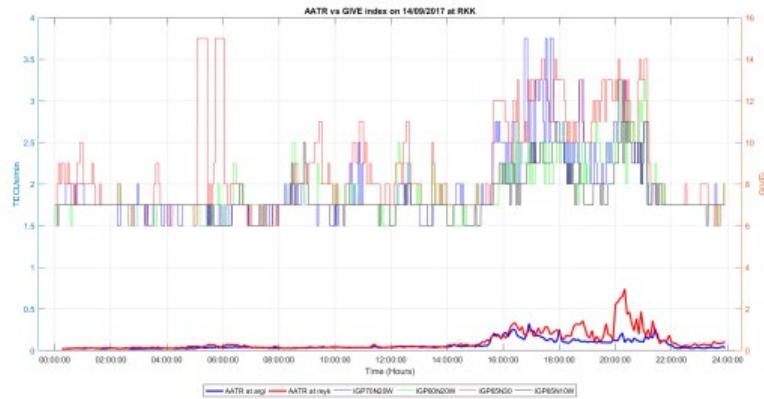
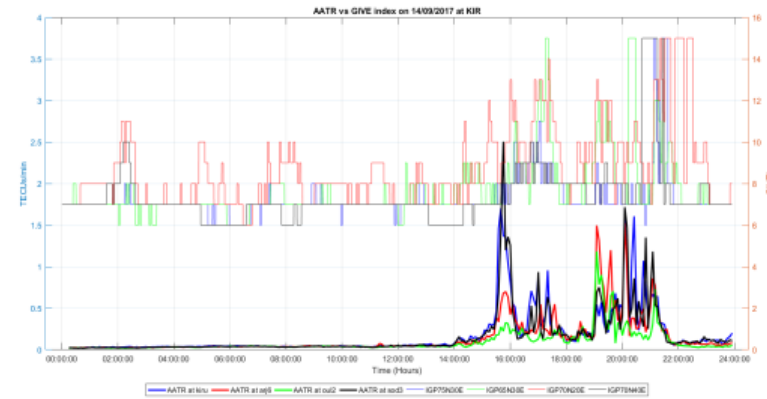
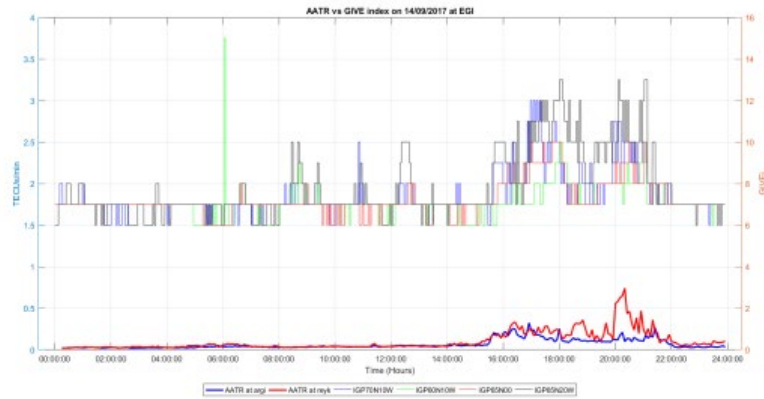


Figure 114. Temporal evolution of GIVE indices at IGPs surrounding assessed RIMS and AATR at IGS stations on DOY 257.

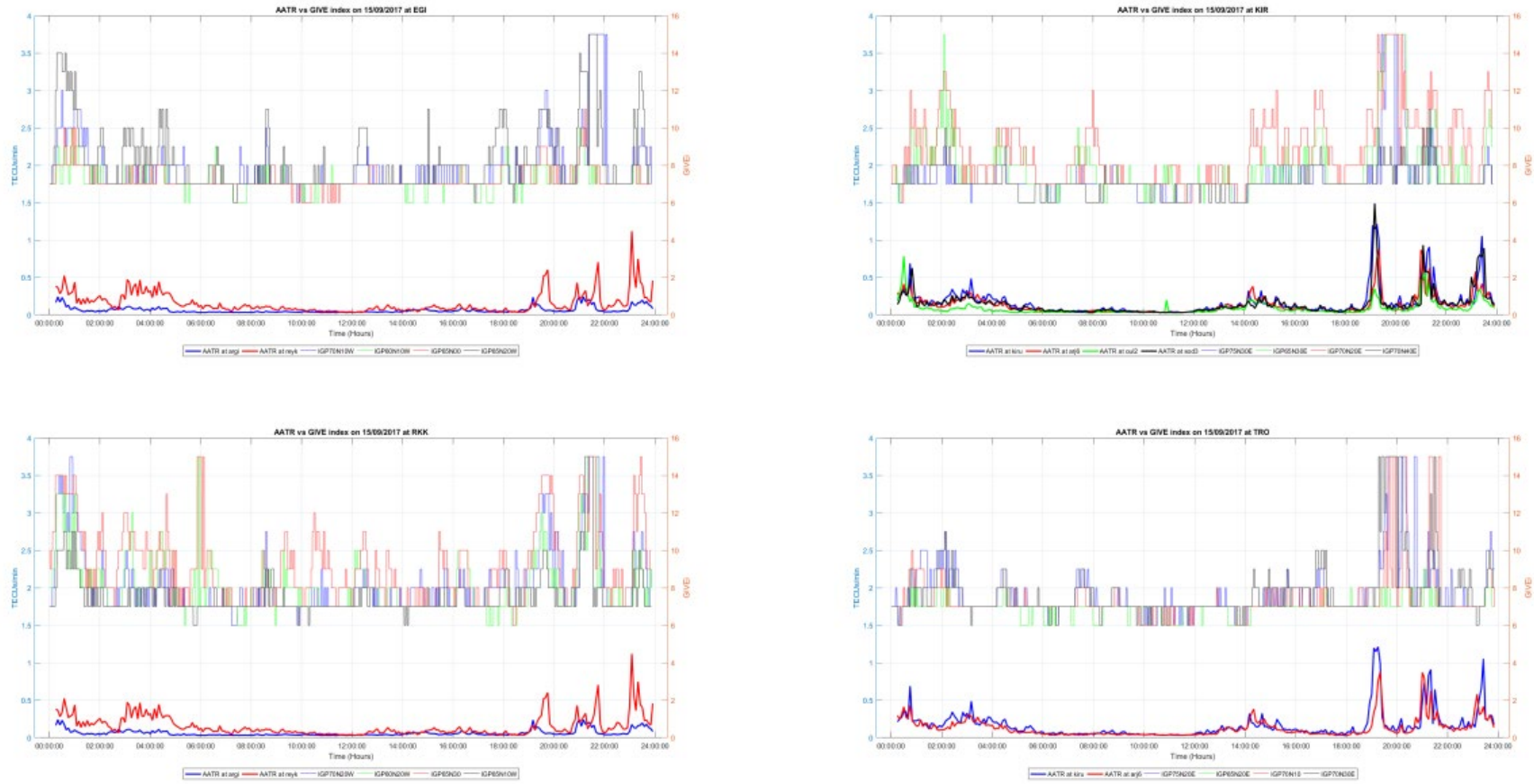


Figure 115. Temporal evolution of GIVE indices at IGP stations surrounding assessed RIMS and AATR at IGS stations on DOY 258.

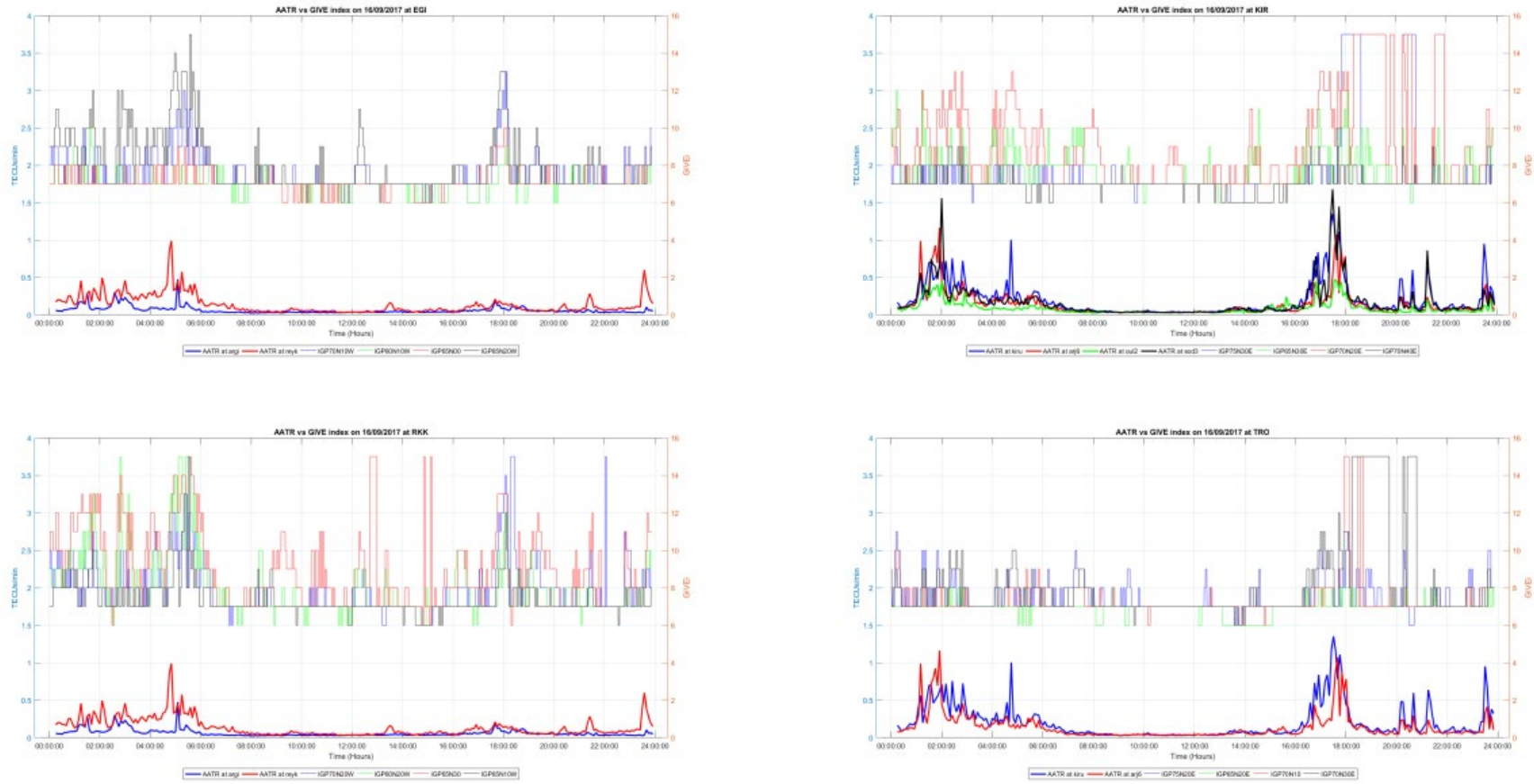


Figure 116. Temporal evolution of GIVE indices at IGP stations surrounding assessed RIMS and AATR at IGS stations on DOY 259.

A.10 DOY 270 and 271

On 27/09/2017 geomagnetic activity has been present at the end of the day impacting EGNOS performance in the North part of Service Area. The increase of xPL values is present in correlation with high spikes of AATR values. The increase in GIVE indicators is well correlated with increase in AATR values by the end of the day.

On 28/09/2017 geomagnetic activity has been present at the beginning and end of the day impacting EGNOS performance in the North part of Service Area. The increase of xPL values is well correlated with high spikes of AATR values. The increase of GIVE indicators is present at the beginning and end of the day with well correlated spikes of AATR values present at approximately the same time.

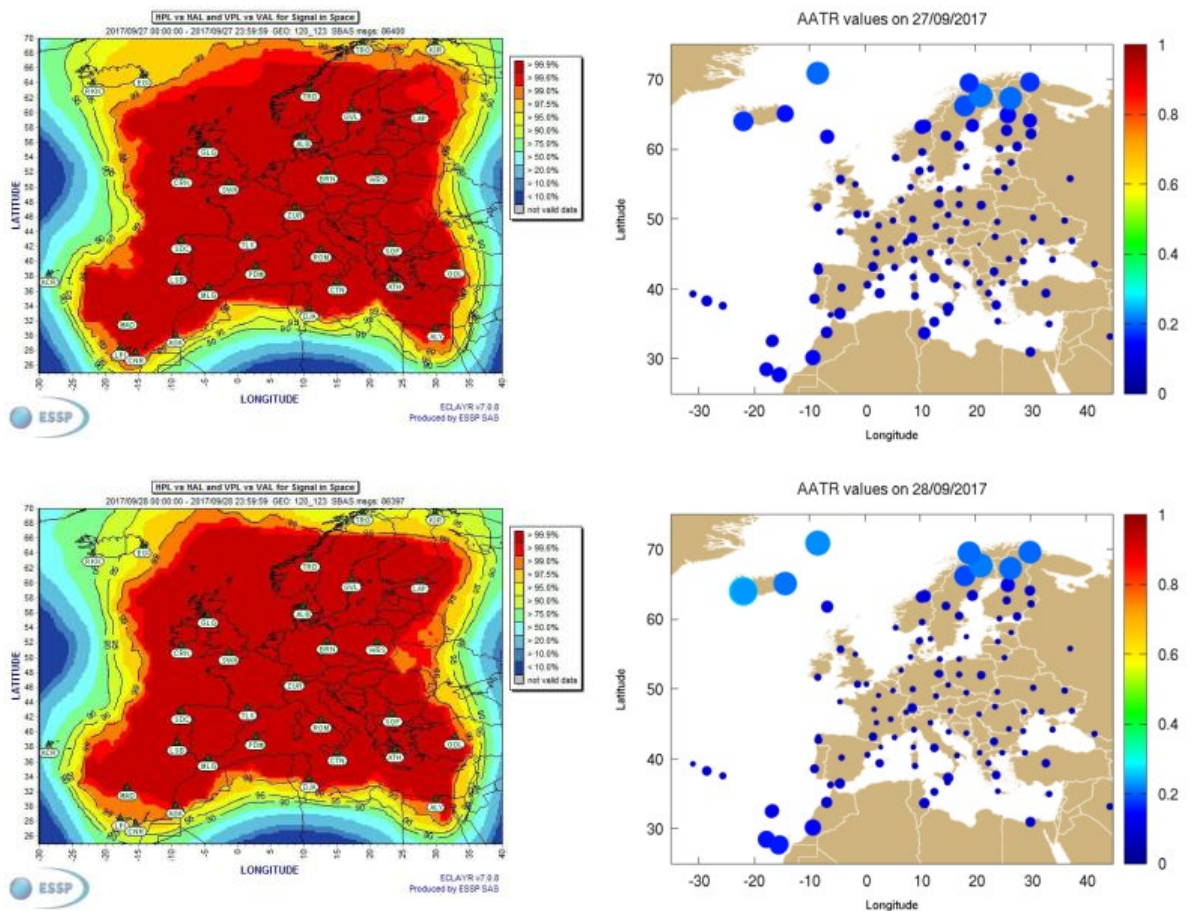


Figure 117. EGNOS APV-I availability maps and AATR daily mean values at IGS stations on DOY 270 and 271.

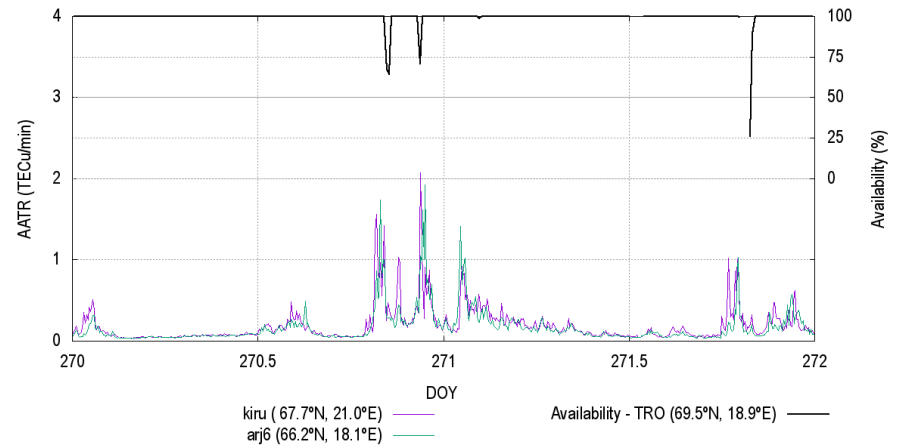
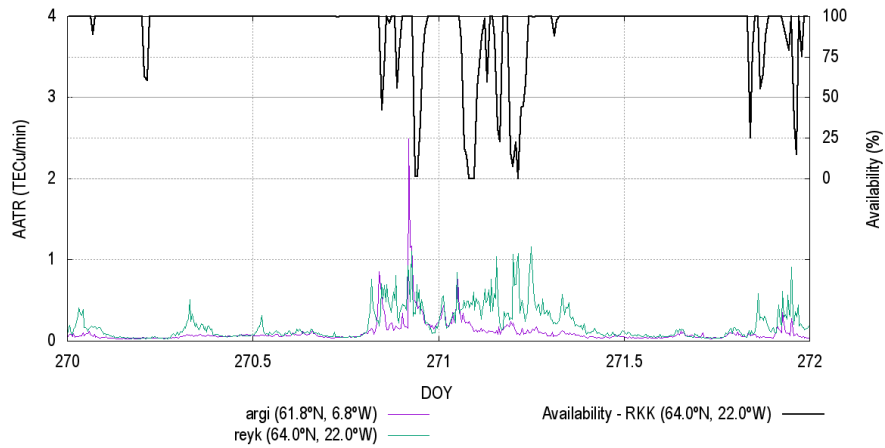
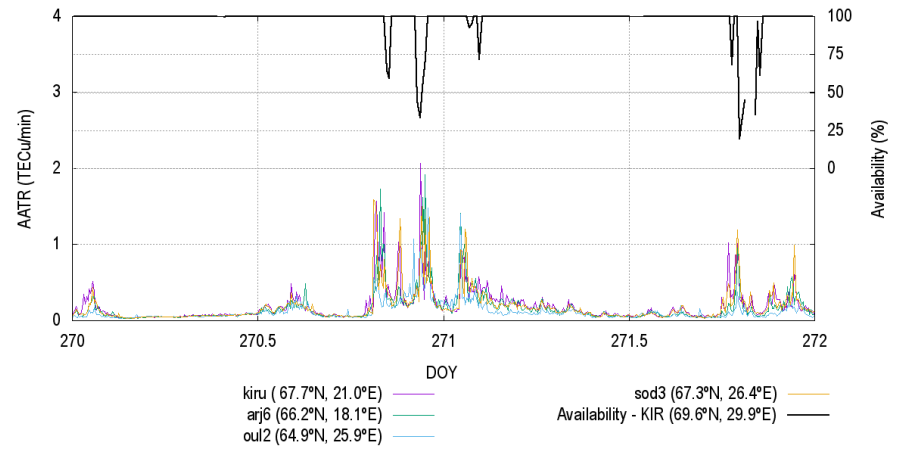
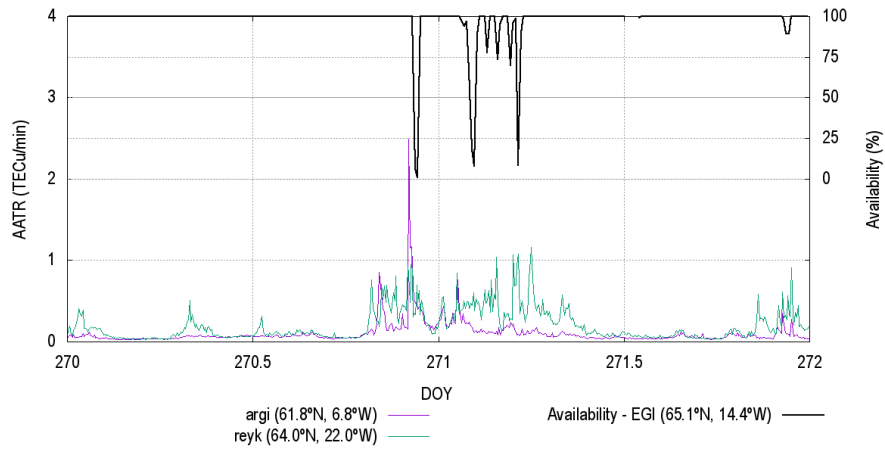


Figure 118. APV-I availability for assessed RIMS and AATR values at IGS station on DOY 270 and 271.

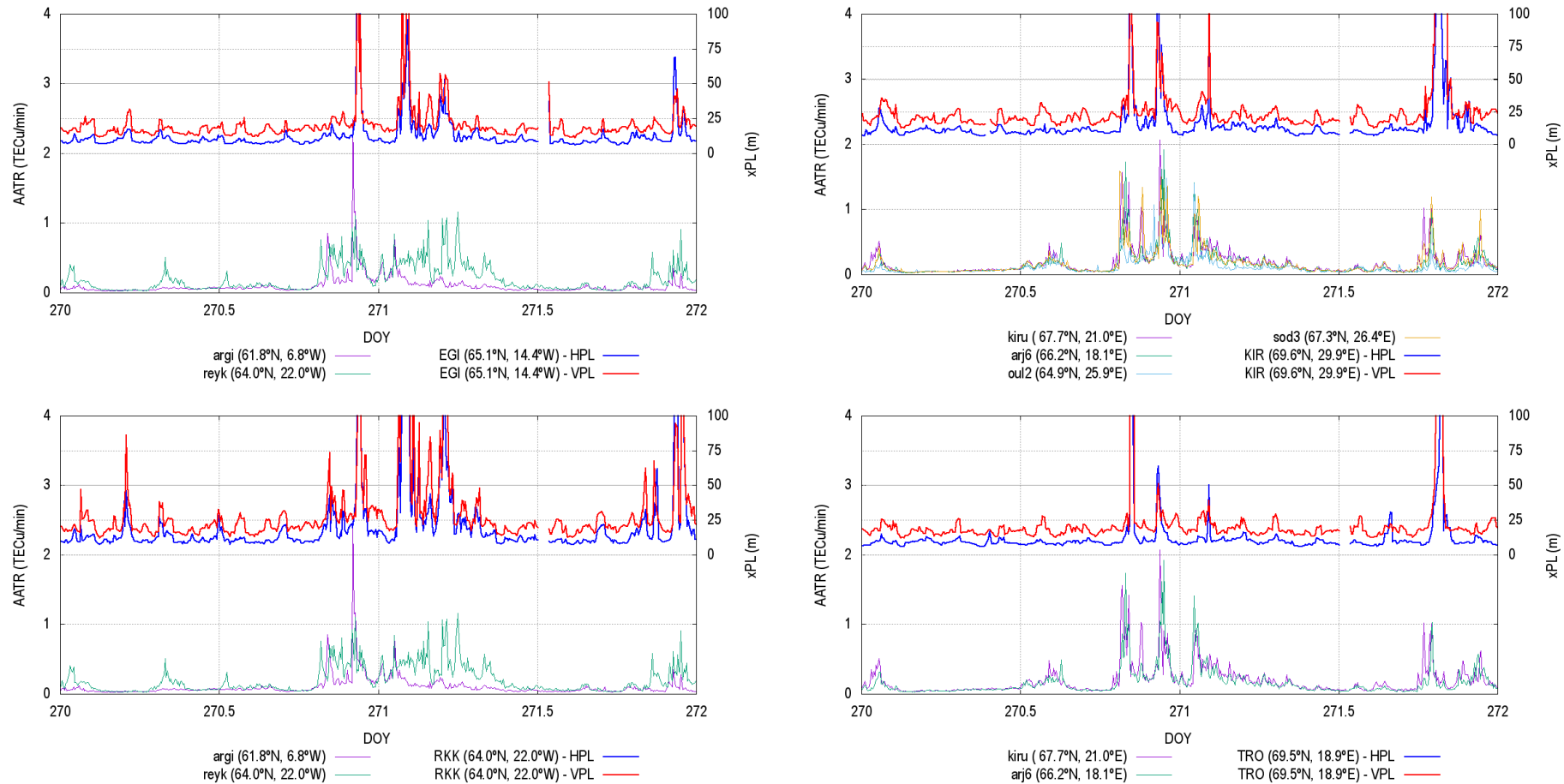


Figure 119. HPL and VPL variation for assessed RIMS and AATR values at IGS station on DOY 270 and 271.

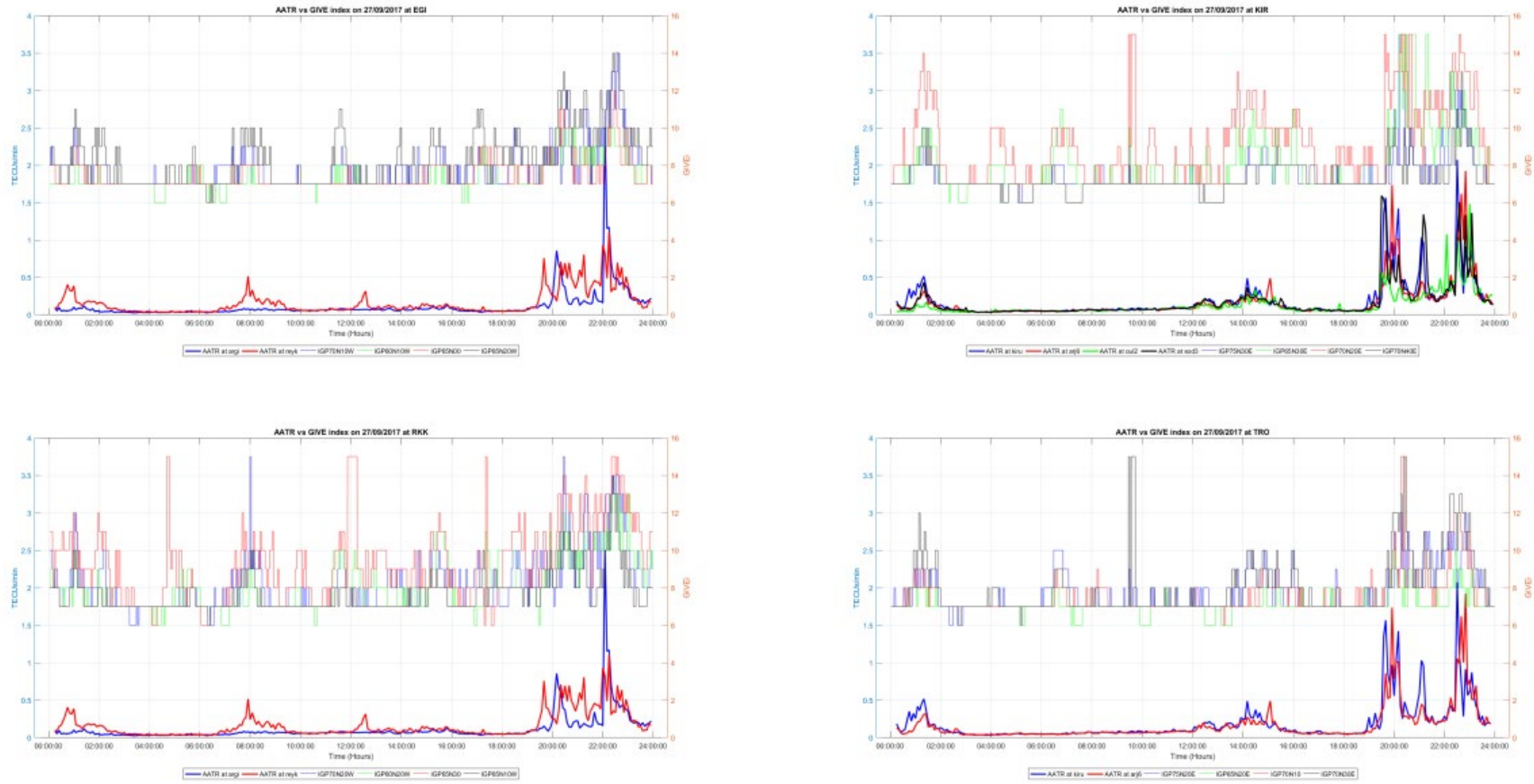


Figure 120. Temporal evolution of GIVE indices at IGP stations surrounding assessed RIMS and AATR at IGS stations on DOY 270.

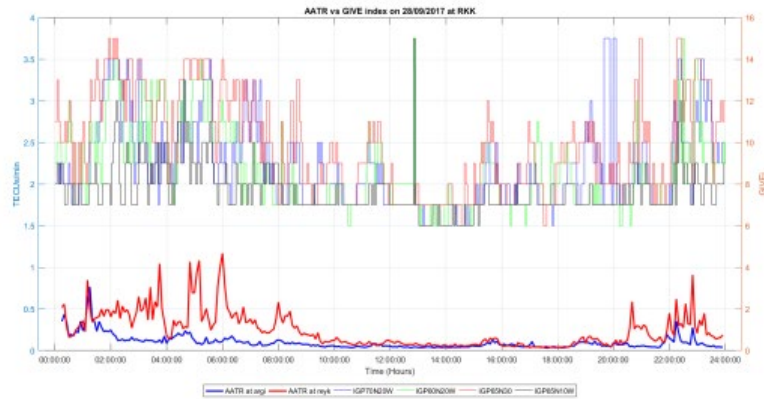
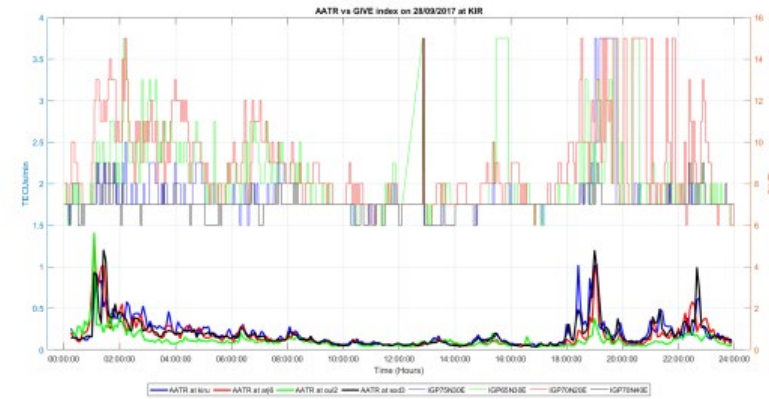
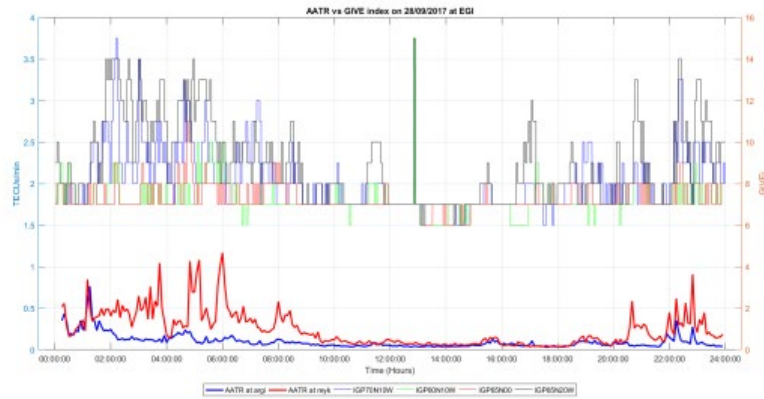


Figure 121. Temporal evolution of GIVE indices at IGPs surrounding assessed RIMS and AATR at IGS stations on DOY 271.

A.11 DOY 285 and 286

On 12/10/2017 geomagnetic activity has been observed at the beginning and end of the day which degraded Northwest part of EGNOS Service Area. The high values of xPL are correlated with high values of AATR. The increase in GIVE indicator is present with high values of AATR at the beginning and end of the day.

On 13/10/2017 geomagnetic activity has been observed especially in the second part of the day impacting EGNOS performance in North part of Service Area. High values of xPL are well correlated with high values of AATR. Also, GIVE indicators were estimated to high values in the second part of the day where high spikes of AATR values were observed.

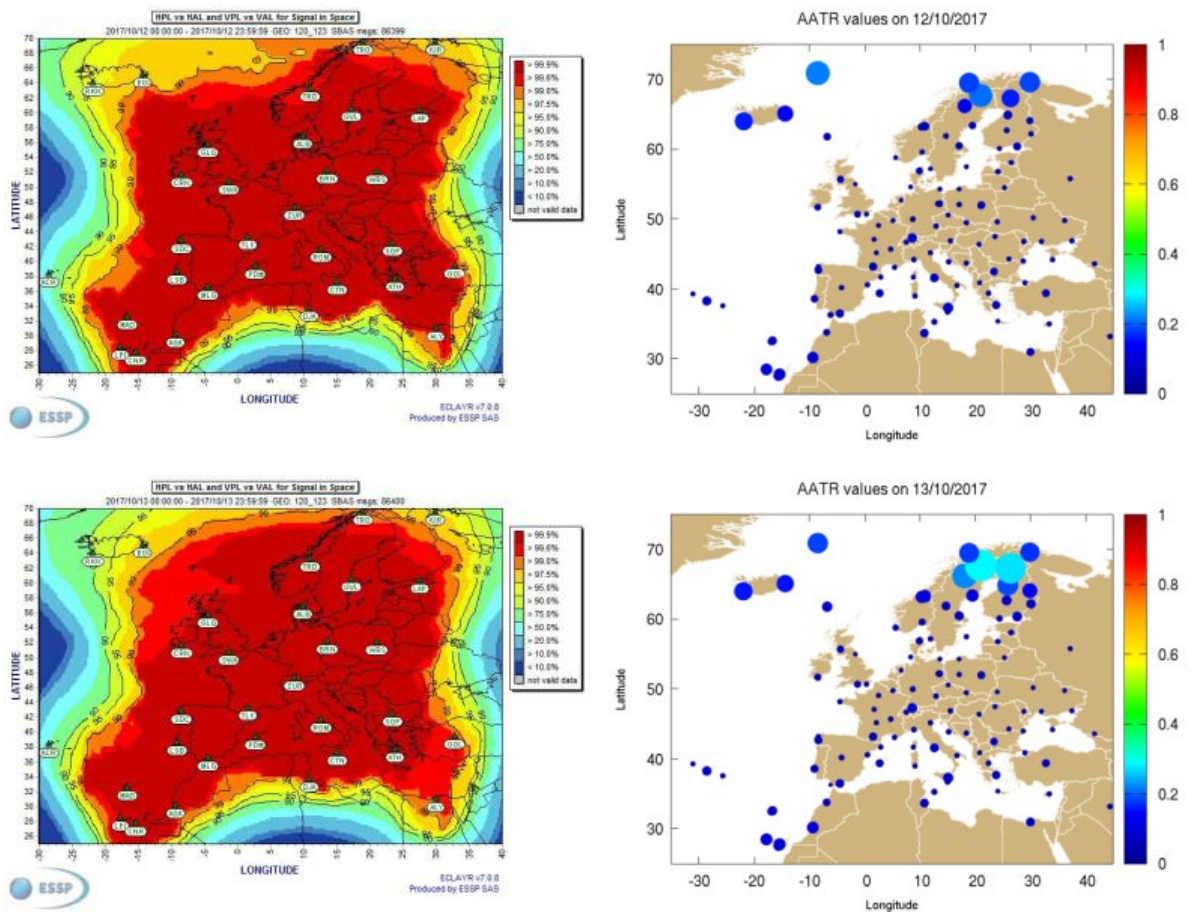


Figure 122. EGNOS APV-I availability maps and AATR daily mean values at IGS stations on DOY 285 and 286.

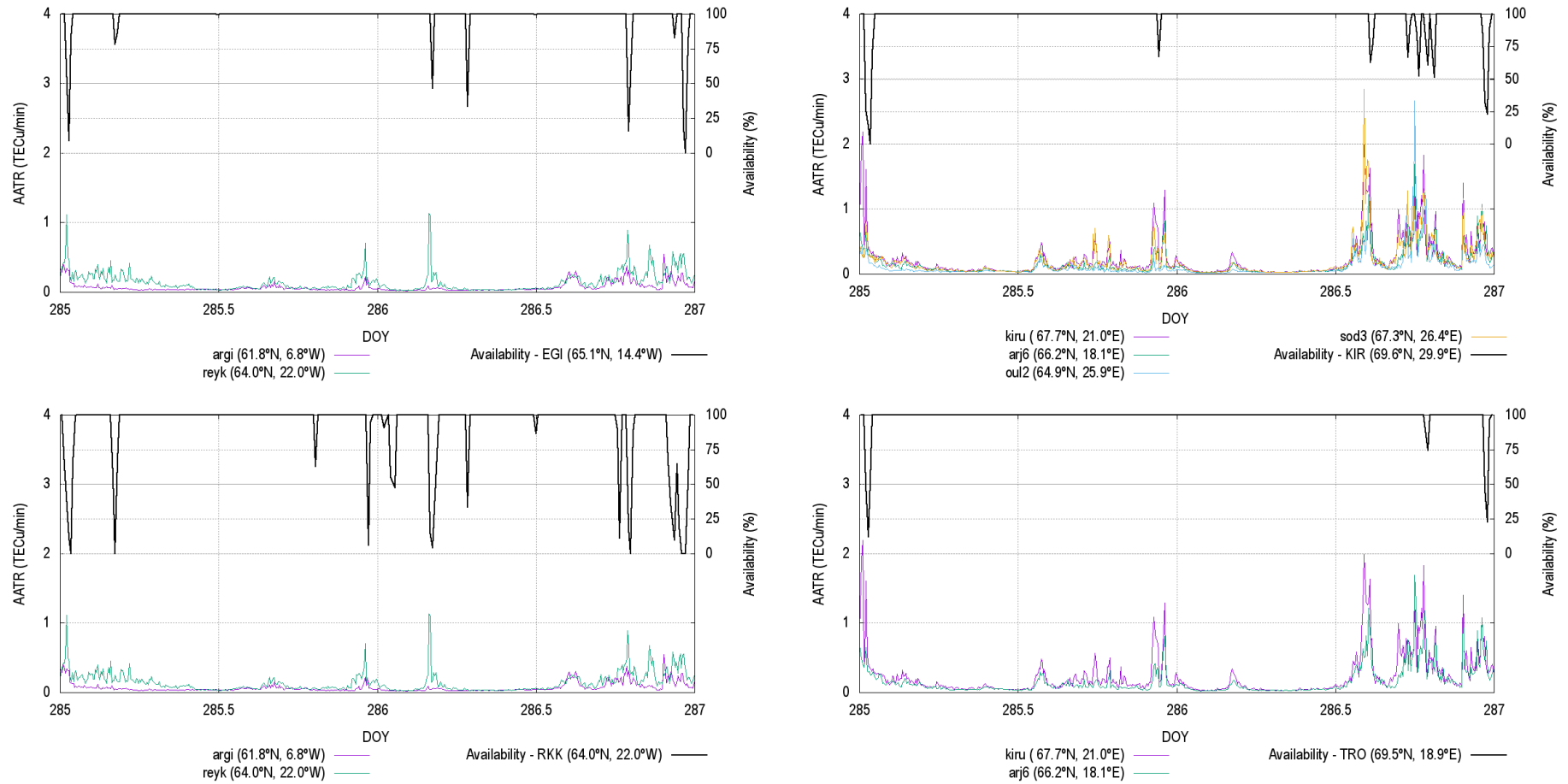


Figure 123. APV-I availability for assessed RIMS and AATR values at IGS station on DOY 285 and 286.

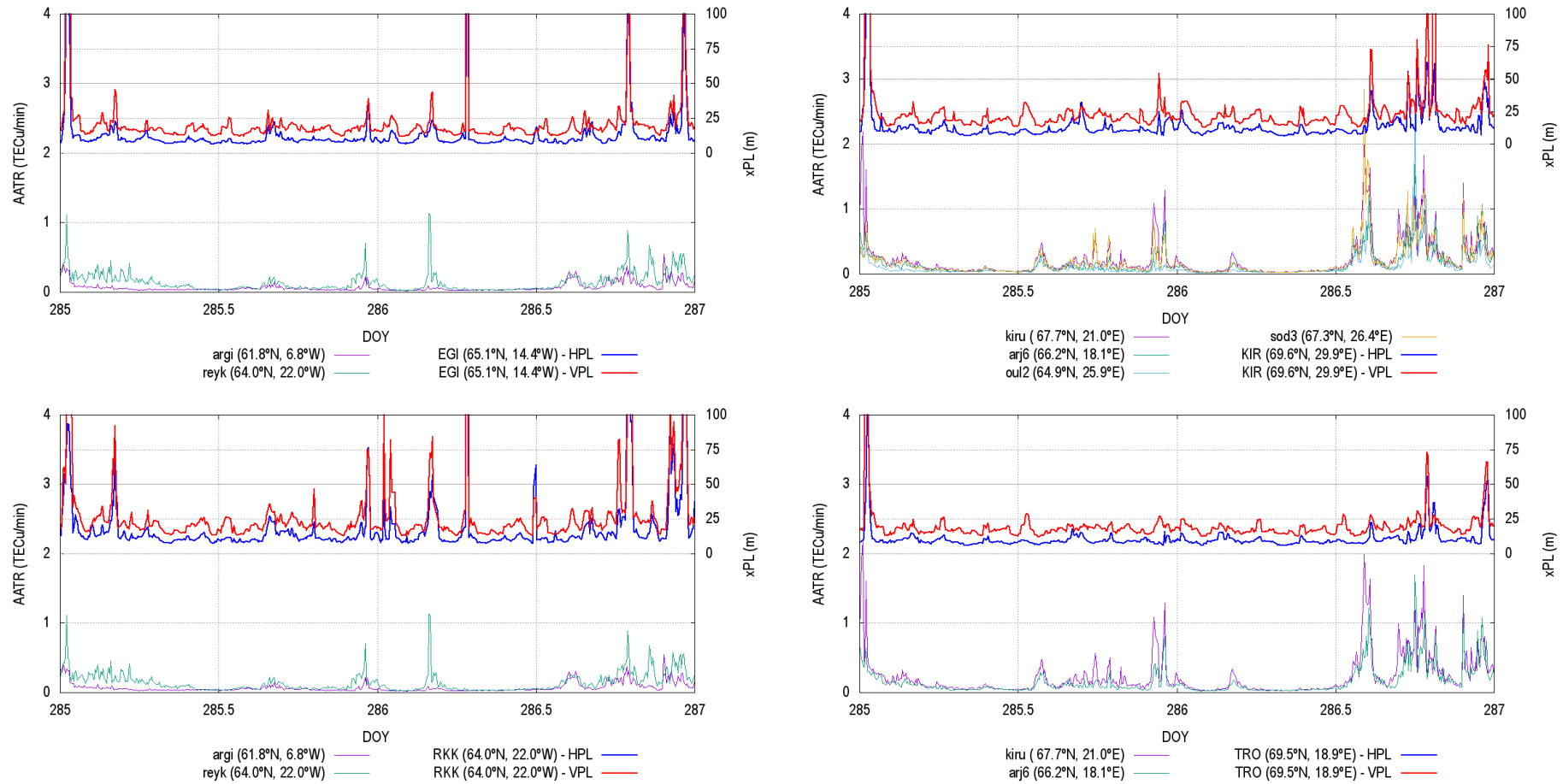


Figure 124. HPL and VPL variation for assessed RIMS and AATR values at IGS station on DOY 285 and 286.

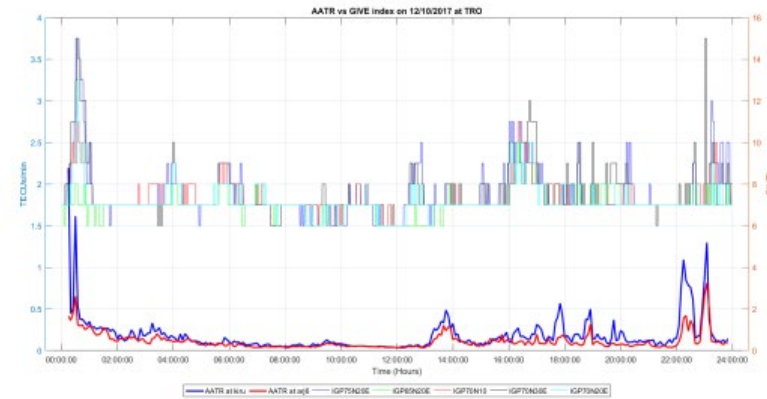
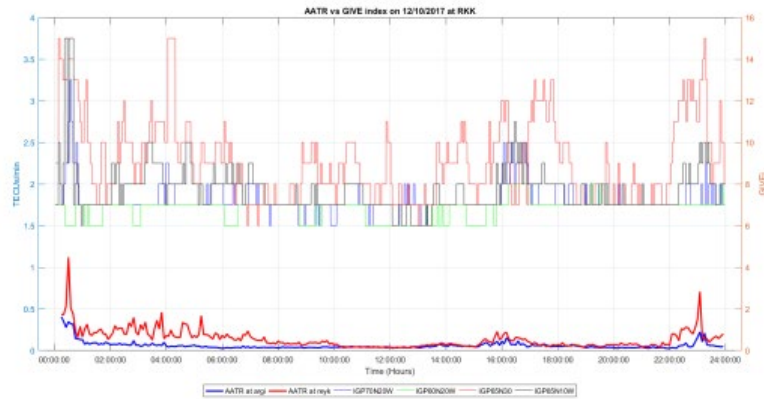
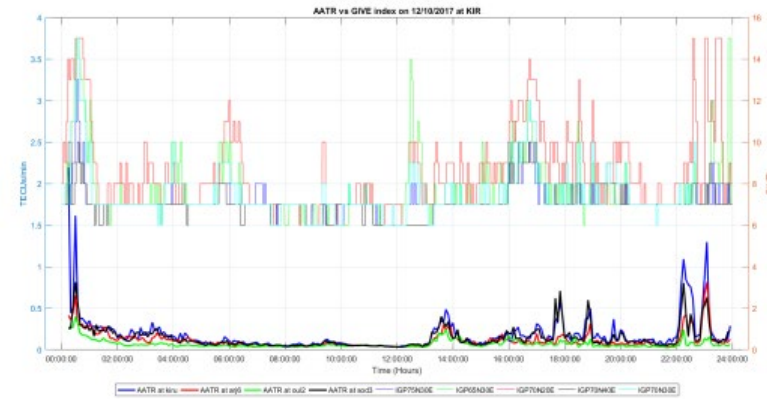
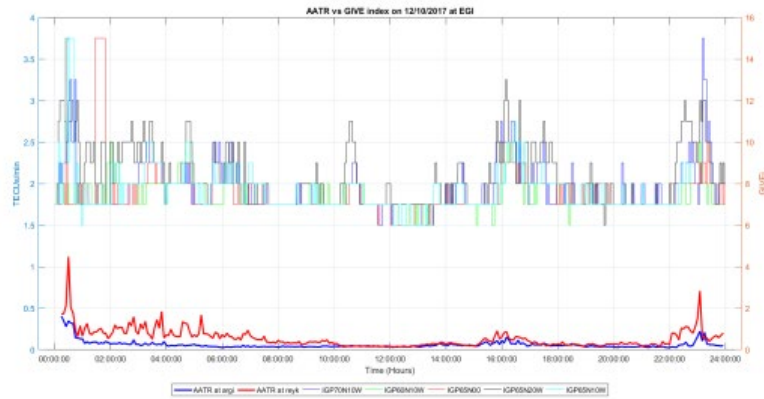


Figure 125. Temporal evolution of GIVE indices at IGP's surrounding assessed RIMS and AATR at IGS stations on DOY 285.

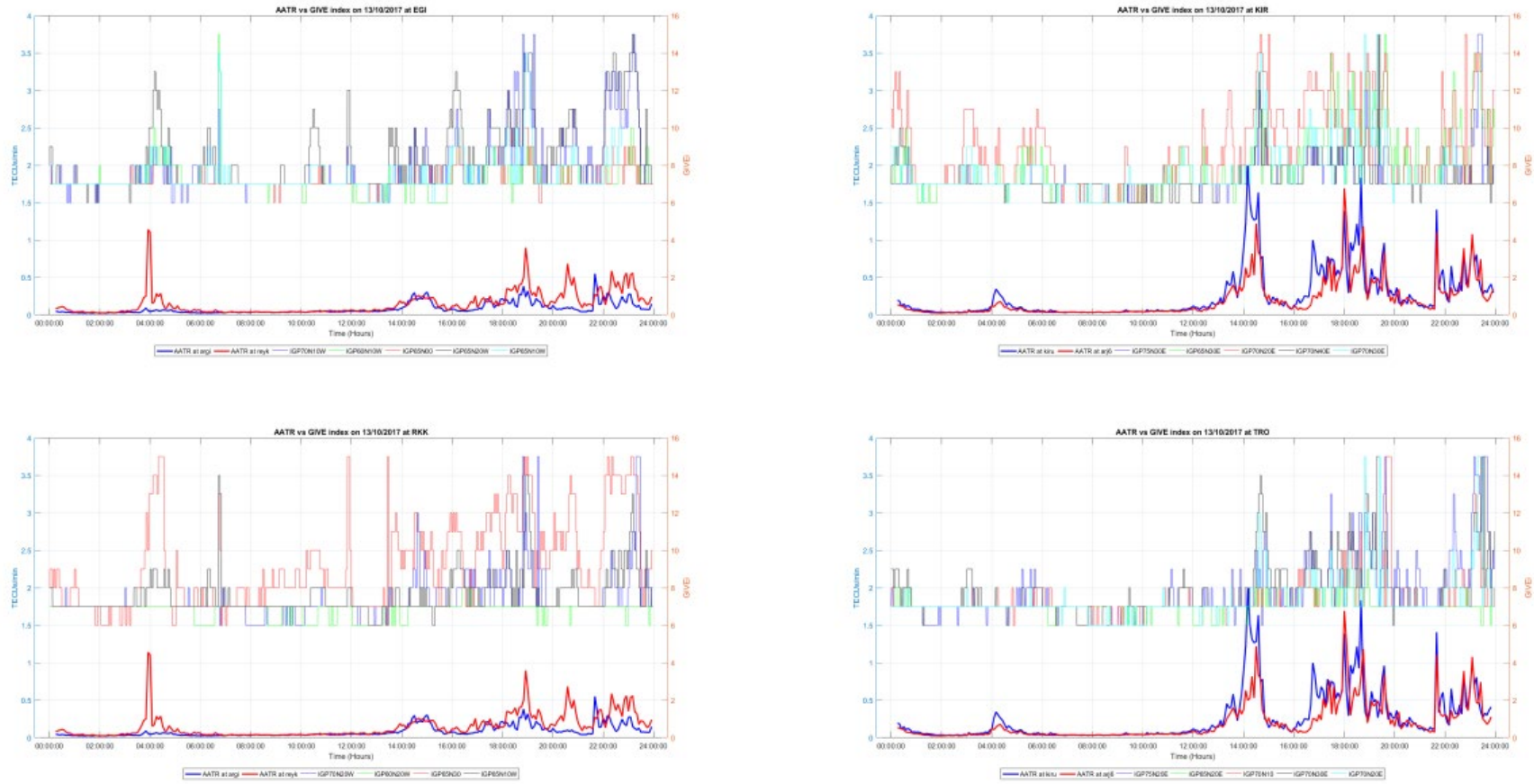


Figure 126. Temporal evolution of GIVE indices at IGPs surrounding assessed RIMS and AATR at IGS stations on DOY 286.

A.12 DOY 311 and 312

On 07/11/2017 geomagnetic activity has been observed at the end of the day impacting EGNOS performance in North part of Service Area. Increase in xPL values is very well correlated with high spikes of AATR values. The increase of GIVE indicators is observed by the end of the day and well correlated with increase in AATR values.

On 08/11/2017 geomagnetic activity has been observed at the beginning of the day and late afternoon impacting EGNOS performance in the North part of Service Area. An increase in xPL values has been observed at the beginning of the day and late afternoon together with high spikes of AATR values. The increase in GIVE indicators estimated in the North part of Service Area has been also correlated with high AATR values.

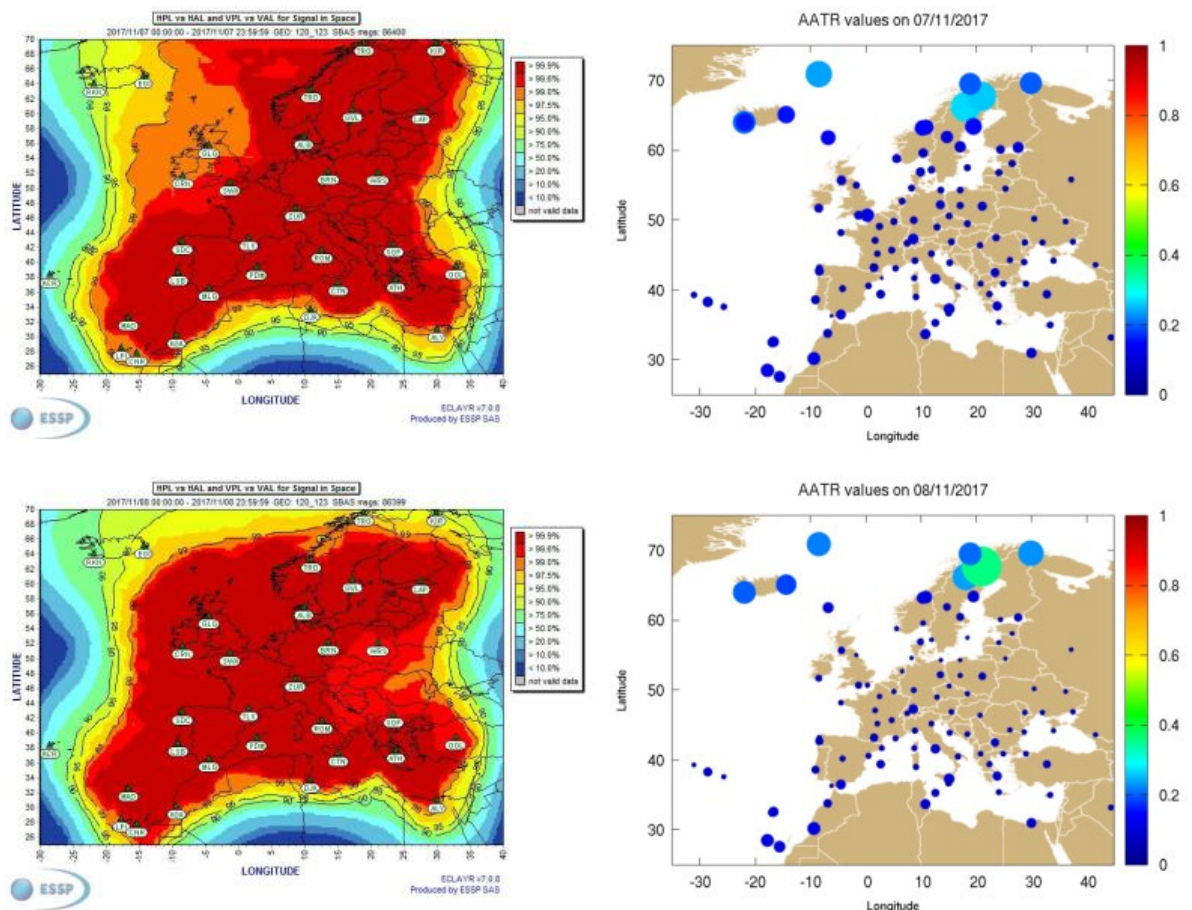


Figure 127. EGNOS APV-I availability maps and AATR daily mean values at IGS stations on DOY 311 and 312.

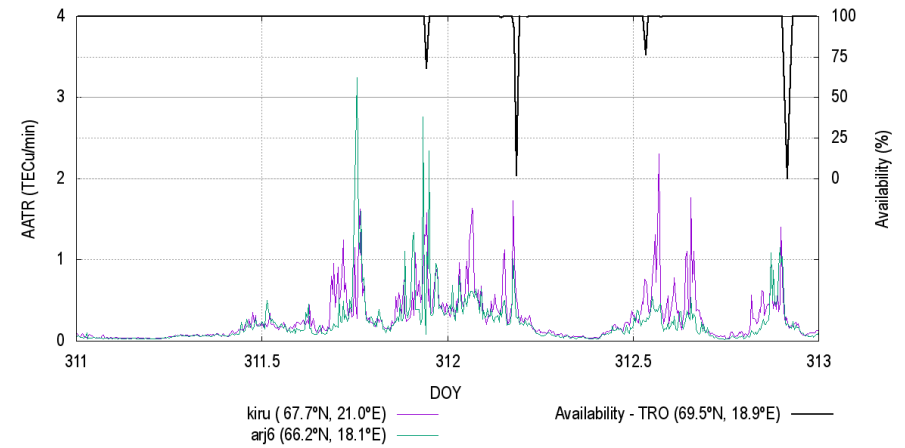
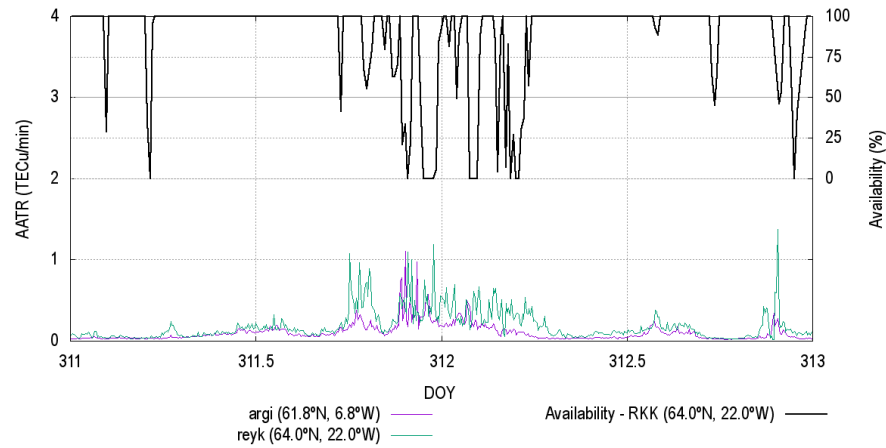
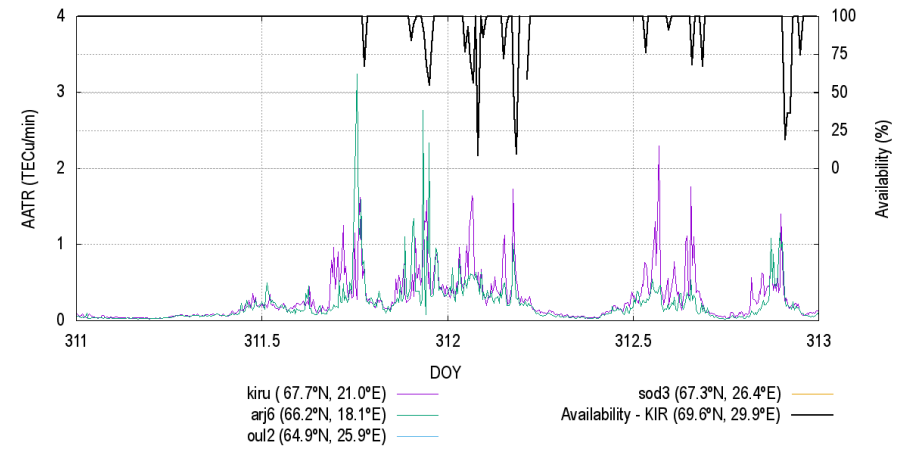
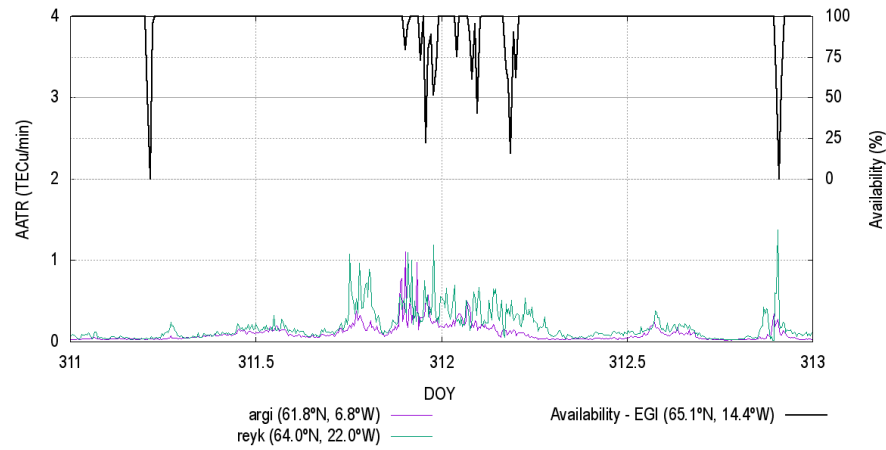


Figure 128. APV-I availability for assessed RIMS and AATR values at IGS station on DOY 311 and 312.

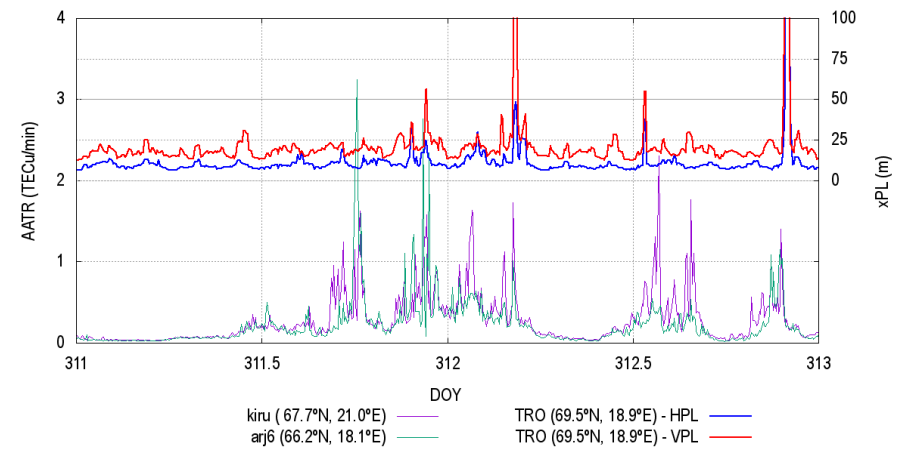
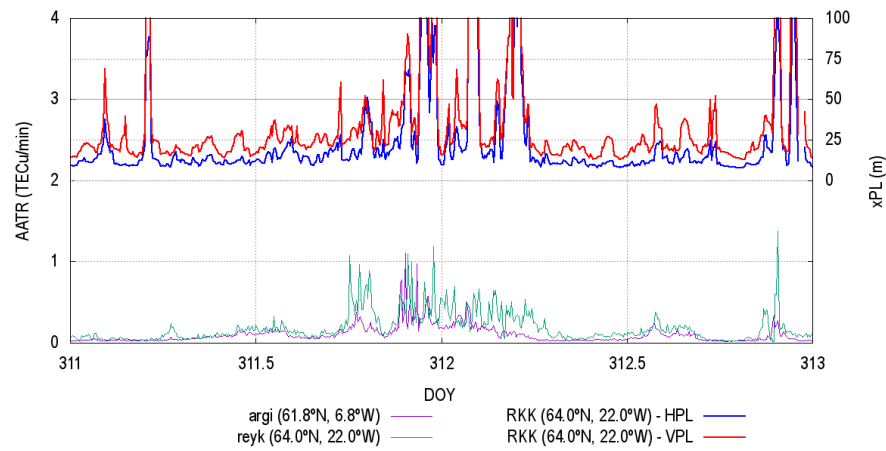
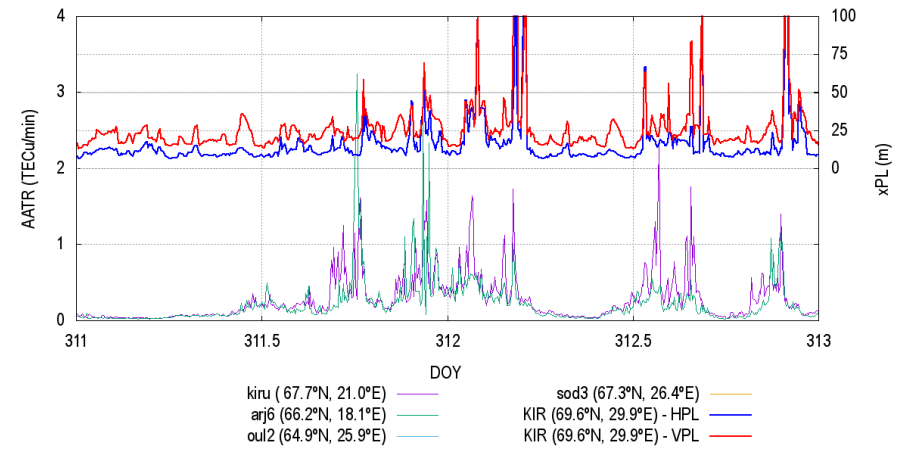
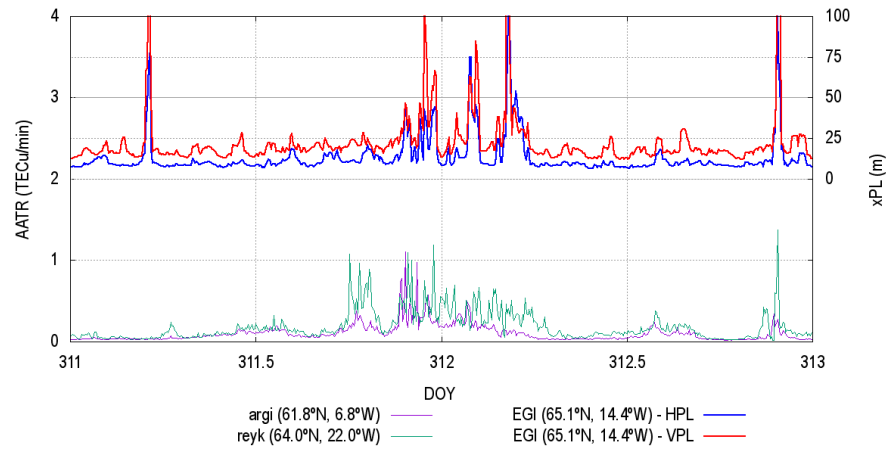


Figure 129. HPL and VPL variation for assessed RIMS and AATR values at IGS station on DOY 311 and 312.

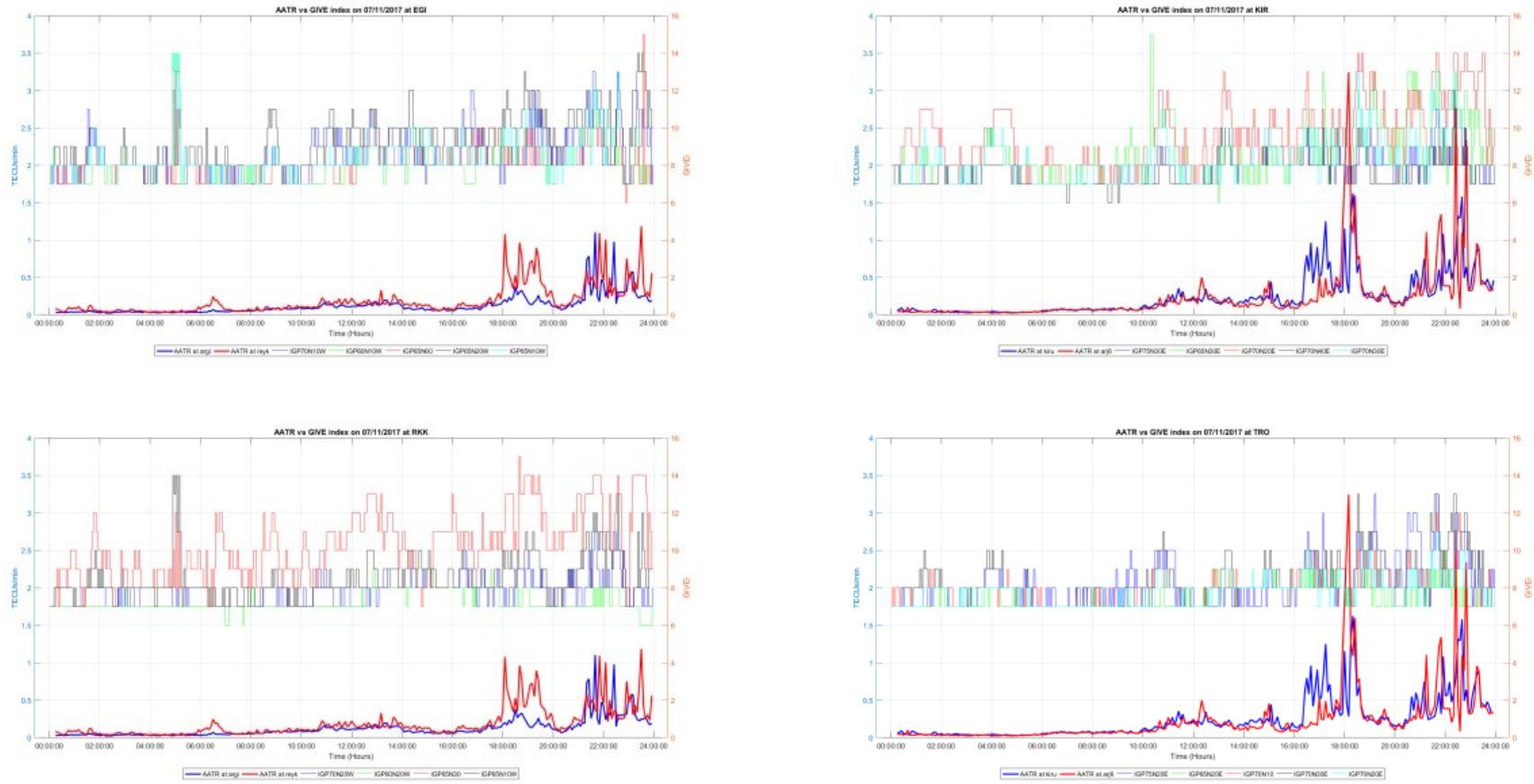


Figure 130. Temporal evolution of GIVE indices at IGP's surrounding assessed RIMS and AATR at IGS stations on DOY 311.

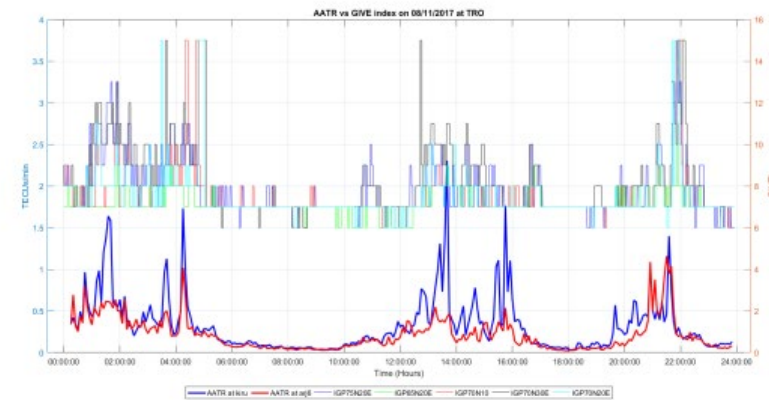
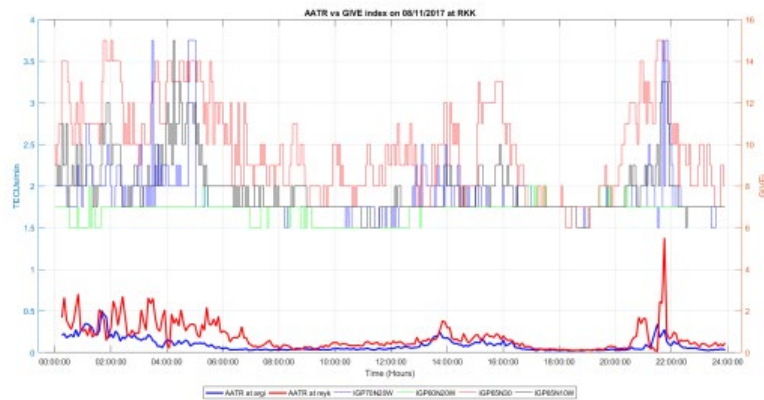
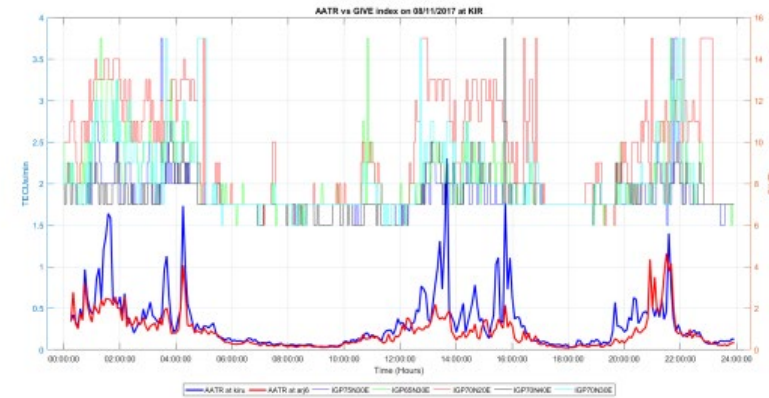
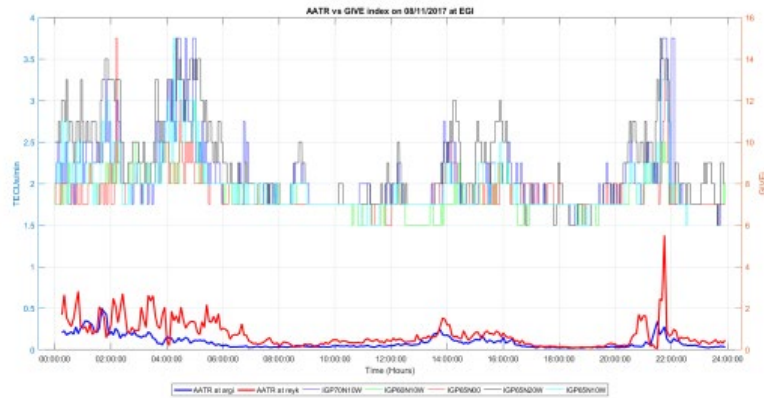


Figure 131. Temporal evolution of GIVE indices at IGPs surrounding assessed RIMS and AATR at IGS stations on DOY 312.

A.13 DOY 328

On 24/11/2017 geomagnetic activity has been observed with slight impact on EGNOS performance in the North part of Service Area. The degradation has been observed at the beginning and end of the day where high xPLs values have been observed when AATR values increased. The GIVE indicators also presented high values at the beginning and end of the day which are well correlated with AATR values.

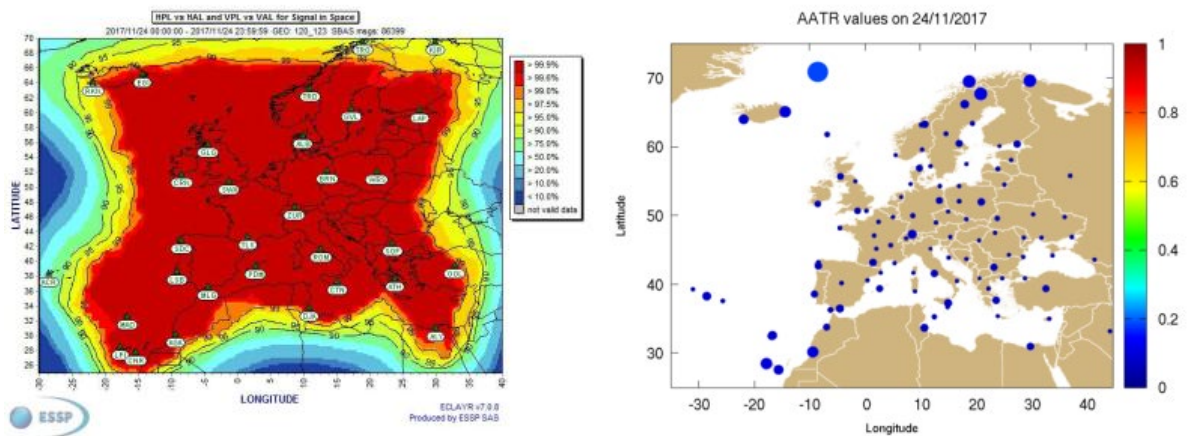


Figure 132. EGNOS APV-I availability maps and AATR daily mean values at IGS stations on DOY 328.

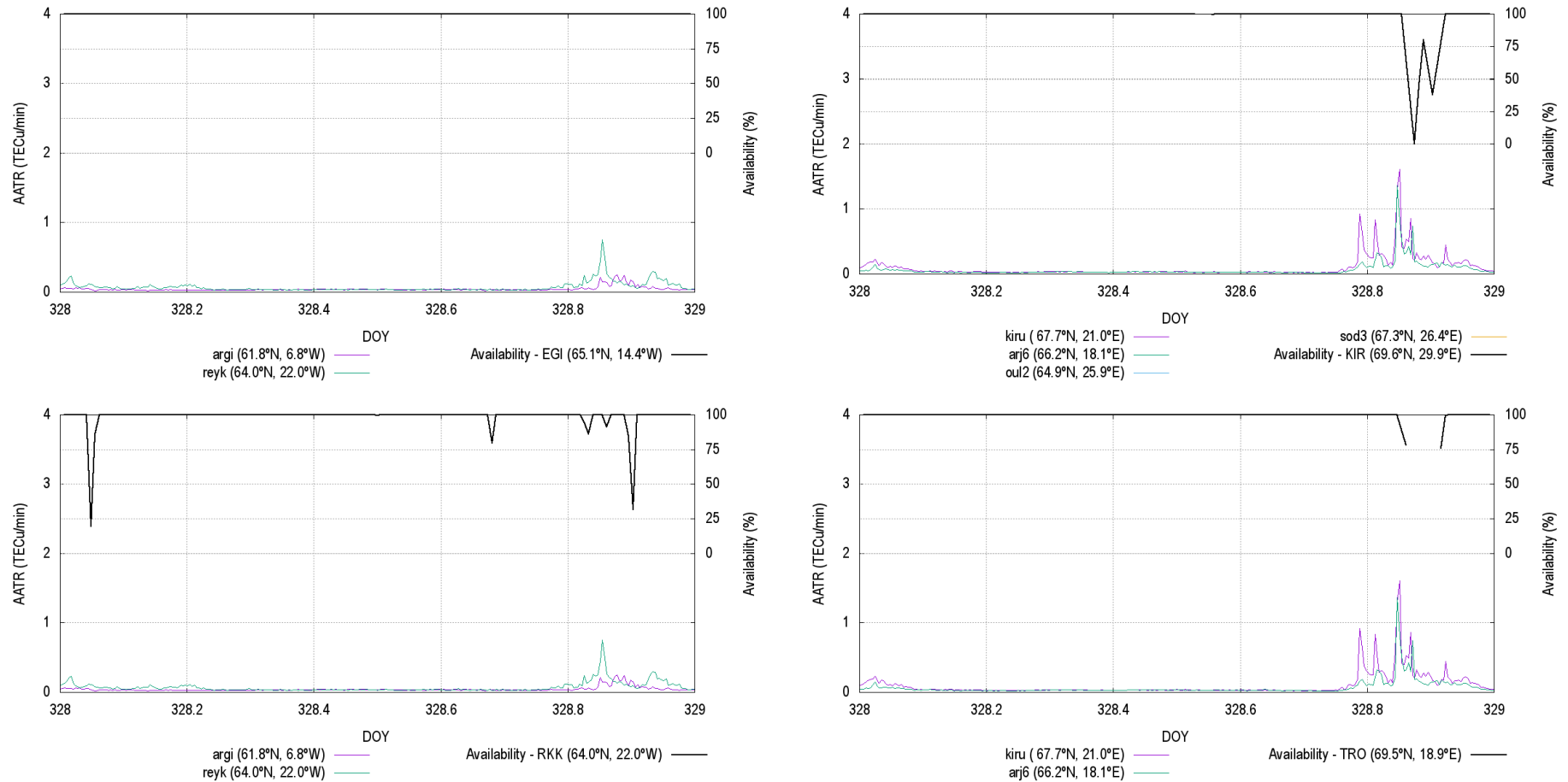


Figure 133. APV-I availability for assessed RIMS and AATR values at IGS station on DOY 328.

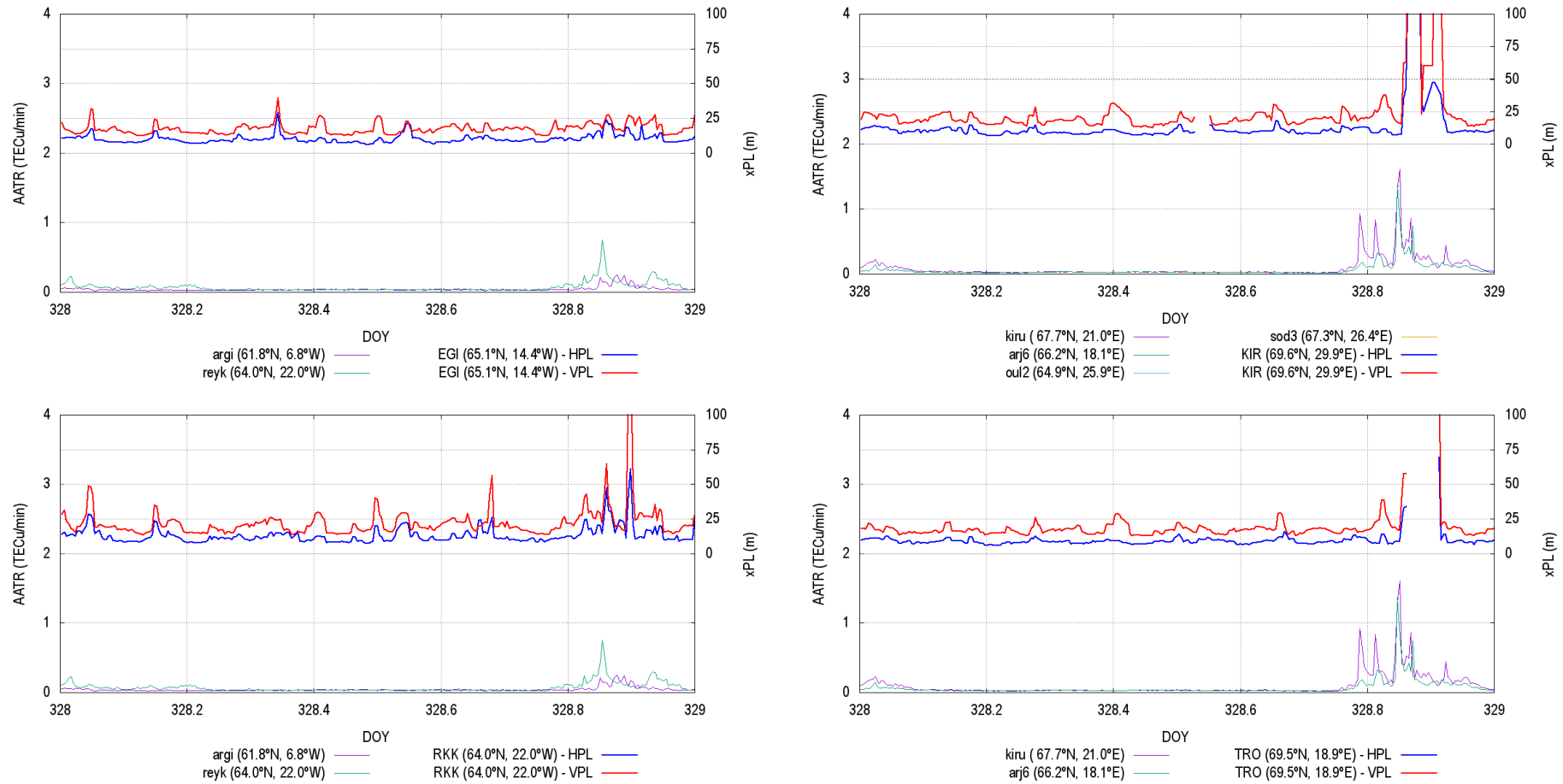


Figure 134. HPL and VPL variation for assessed RIMS and AATR values at IGS station on DOY 328.

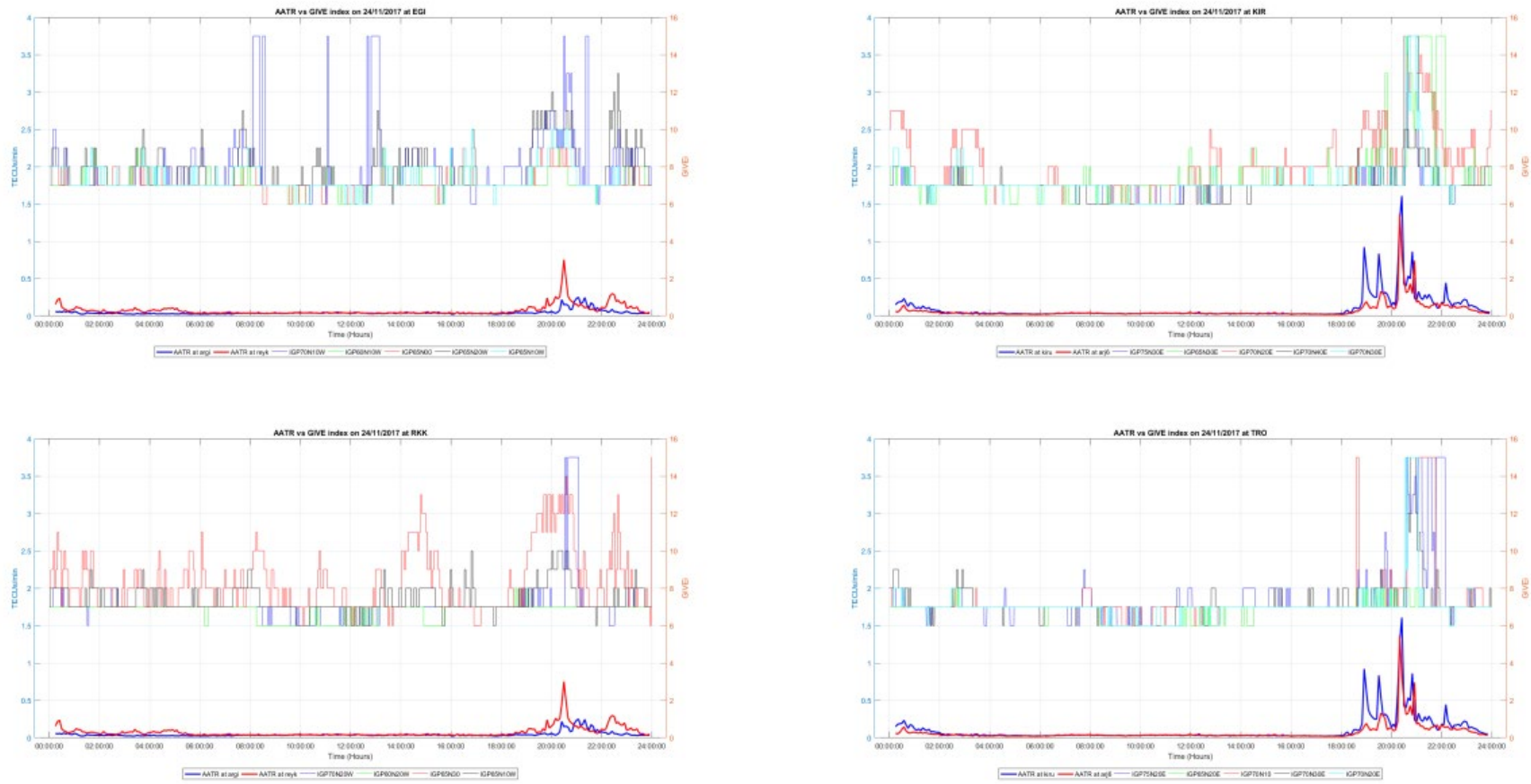


Figure 135. Temporal evolution of GIVE indices at IGPs surrounding assessed RIMS and AATR at IGS stations on DOY 328.

A.14 DOY 346

On 12/12/2017 geomagnetic activity has been observed in the second part of the day impacting EGNOS performance in the North part of Service Area. The increased values of xPLs are well correlated with the presence of high values of AATR in the second part of the day. The increased estimation of GIVE indicators present at the end of the day is well correlated with presence of high values of AATR. In the first part of the day, the AATR values were not present as the ionospheric activity was not present hence not impacting the EGNOS performance. Thus, other cause than ionospheric activity impacted EGNOS performance.

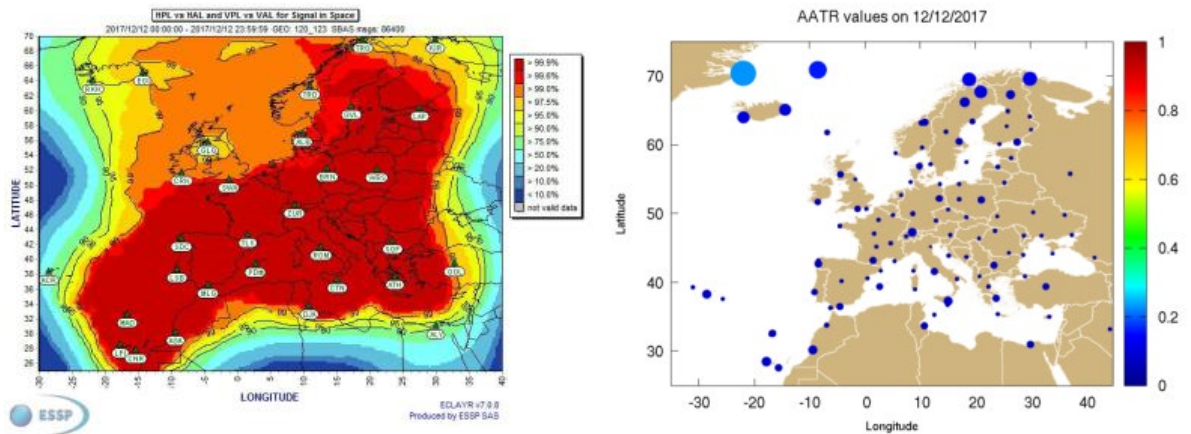


Figure 136. EGNOS APV-I availability maps and AATR daily mean values at IGS stations on DOY 346.

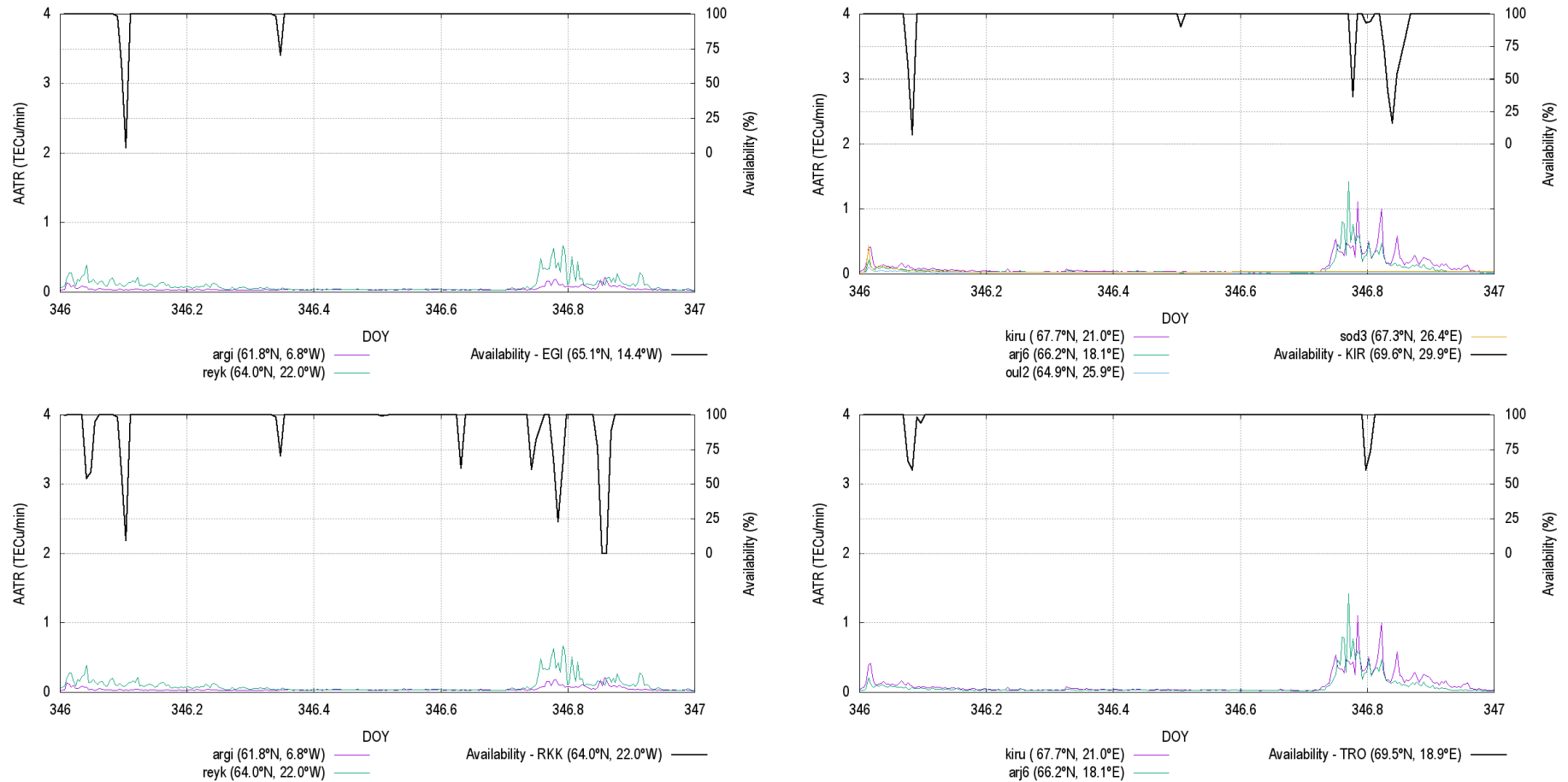


Figure 137. APV-I availability for assessed RIMS and AATR values at IGS station on DOY 346.

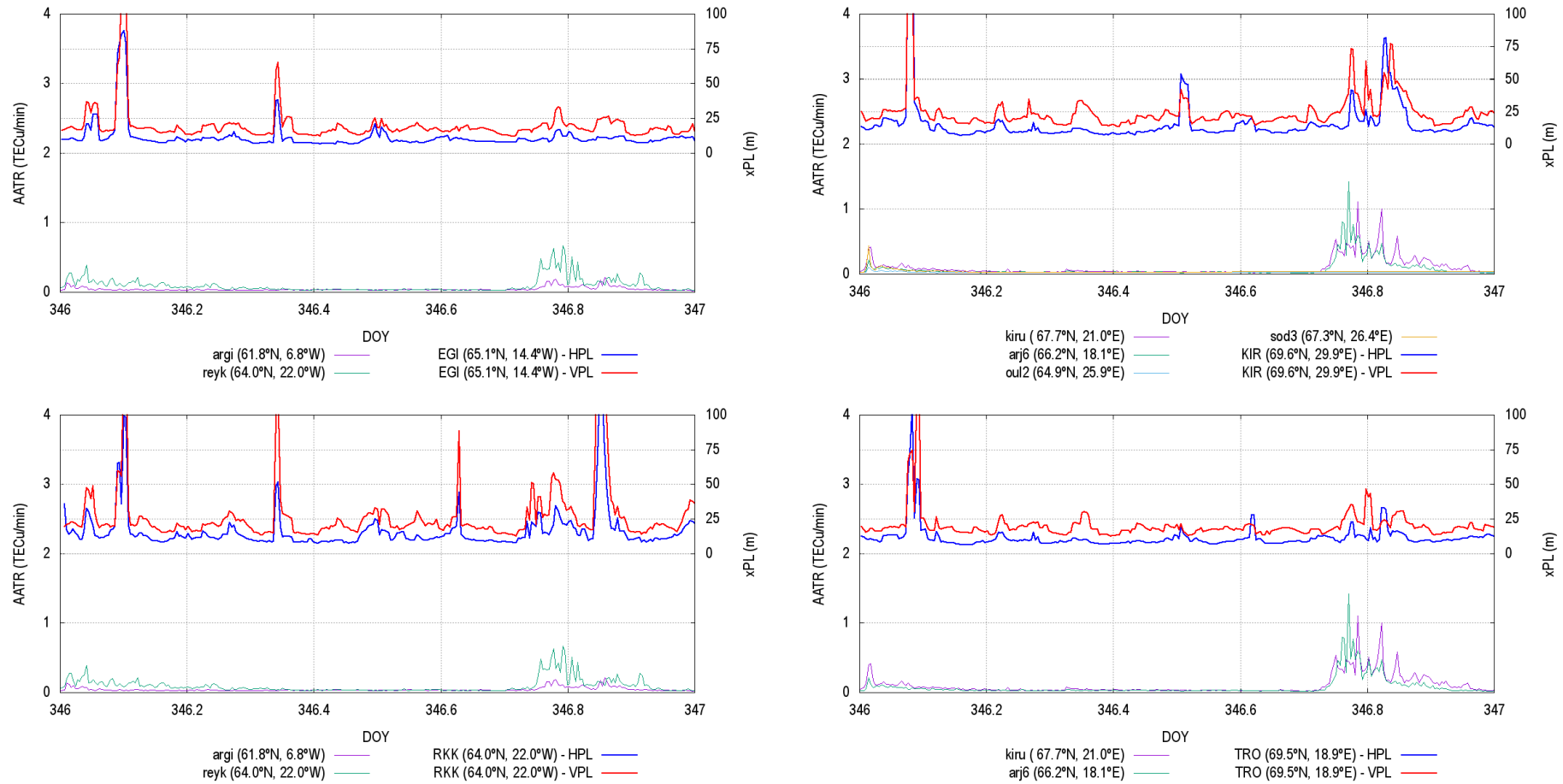


Figure 138. HPL and VPL variation for assessed RIMS and AATR values at IGS station on DOY 346.

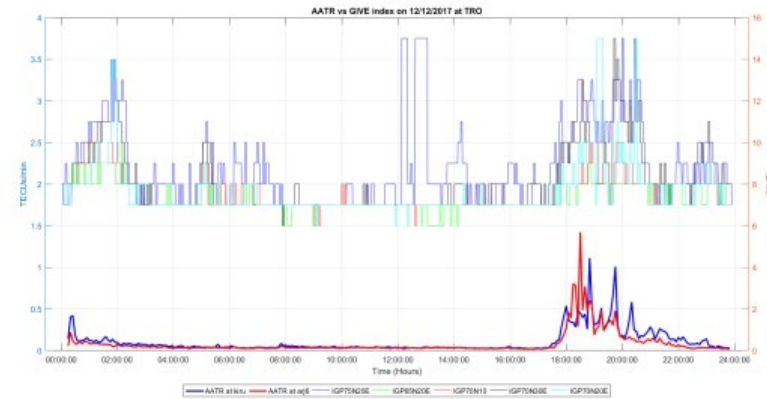
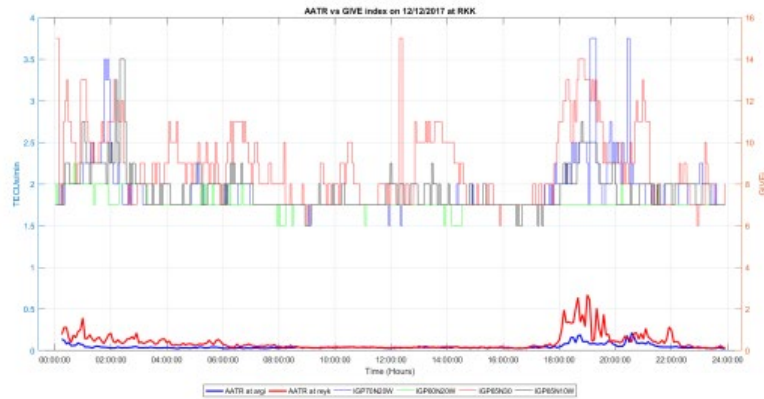
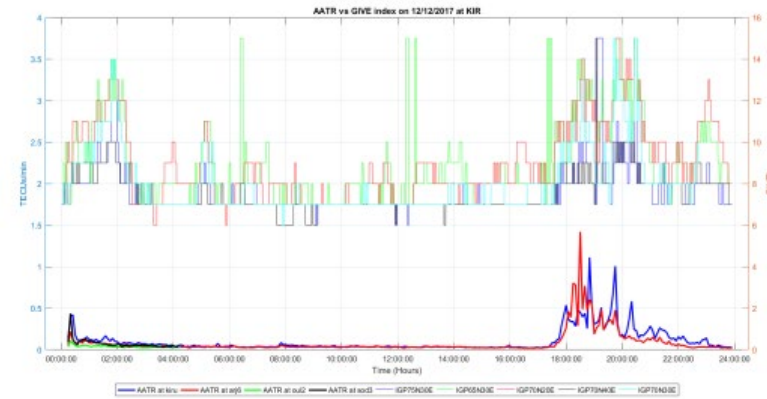
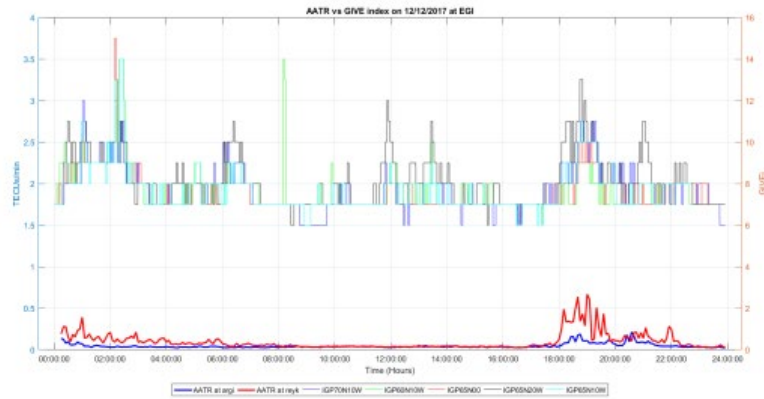


Figure 139. Temporal evolution of GIVE indices at IGPs surrounding assessed RIMS and AATR at IGS stations on DOY 346.

A.15 DOY 351

On 17/12/2017 geomagnetic activity has been observed in the second part of the day impacting EGNOS performance in the North part of Service Area. Increase in xPLs values is observed with increase in AATR values. High values of GIVE indicators are observed with a presence of spikes of AATR values in the second part of the day. Underperformance observed in the first part of the day in the North part of Service Area is not linked with ionospheric activities.

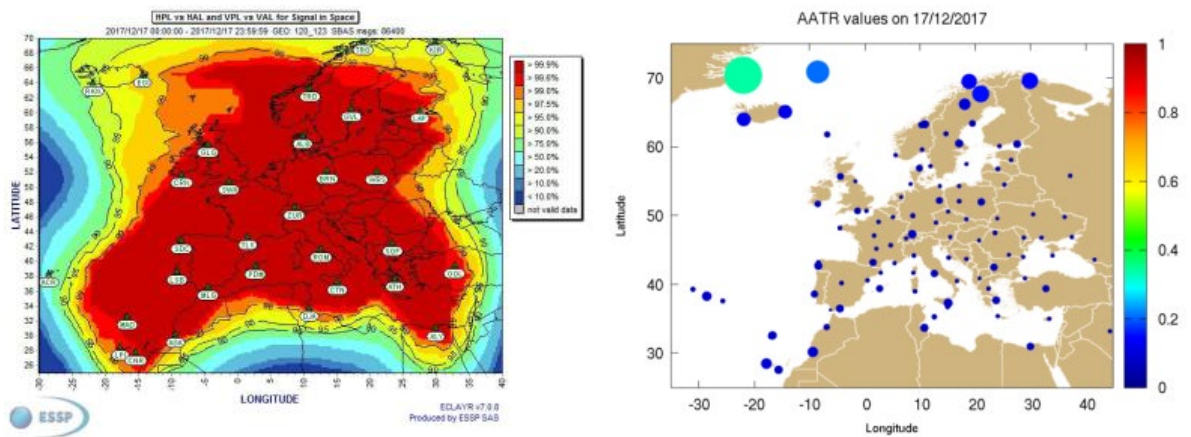


Figure 140. EGNOS APV-I availability maps and AATR daily mean values at IGS stations on DOY 351.

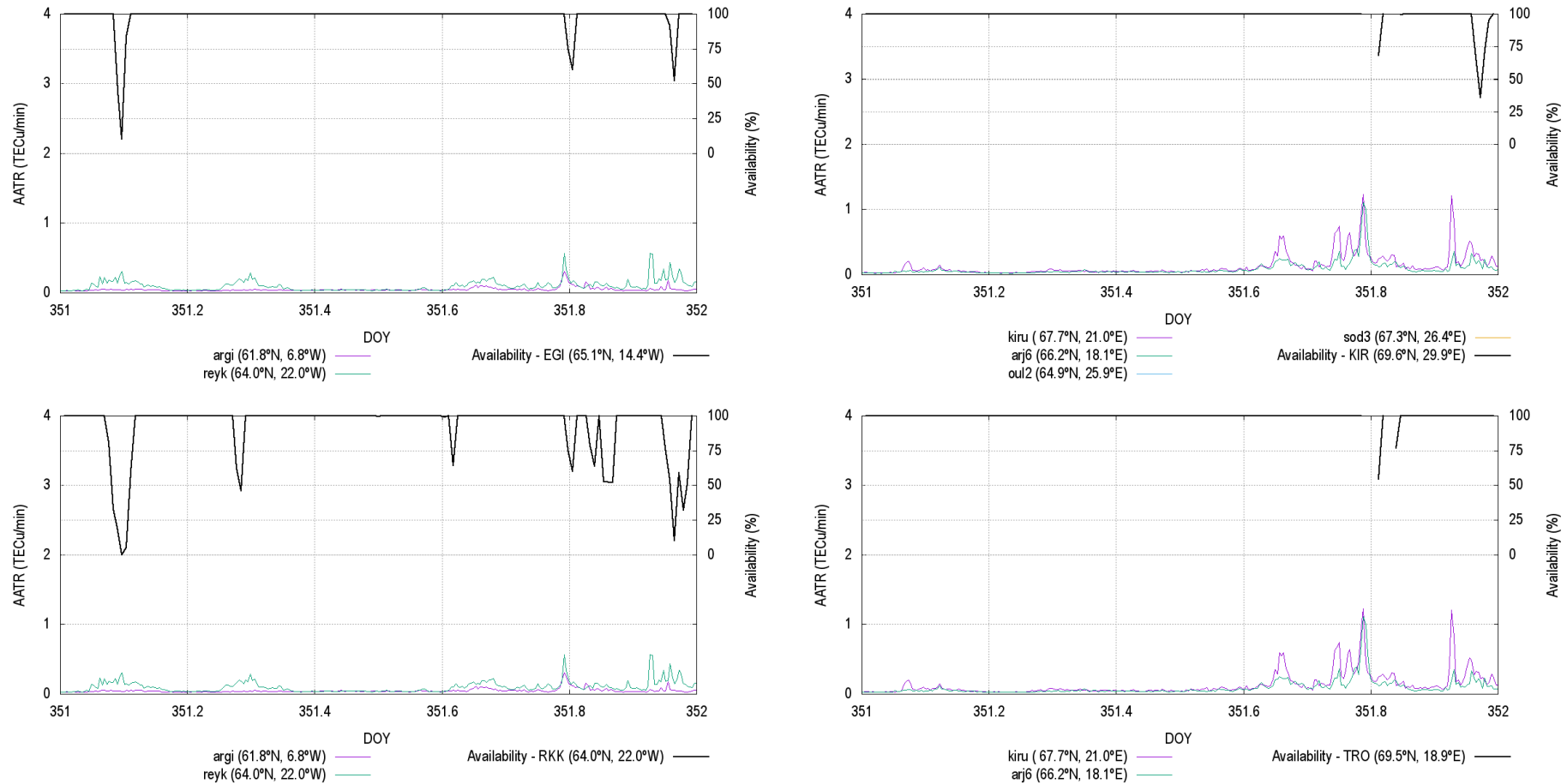


Figure 141. APV-I availability for assessed RIMS and AATR values at IGS station on DOY 351.

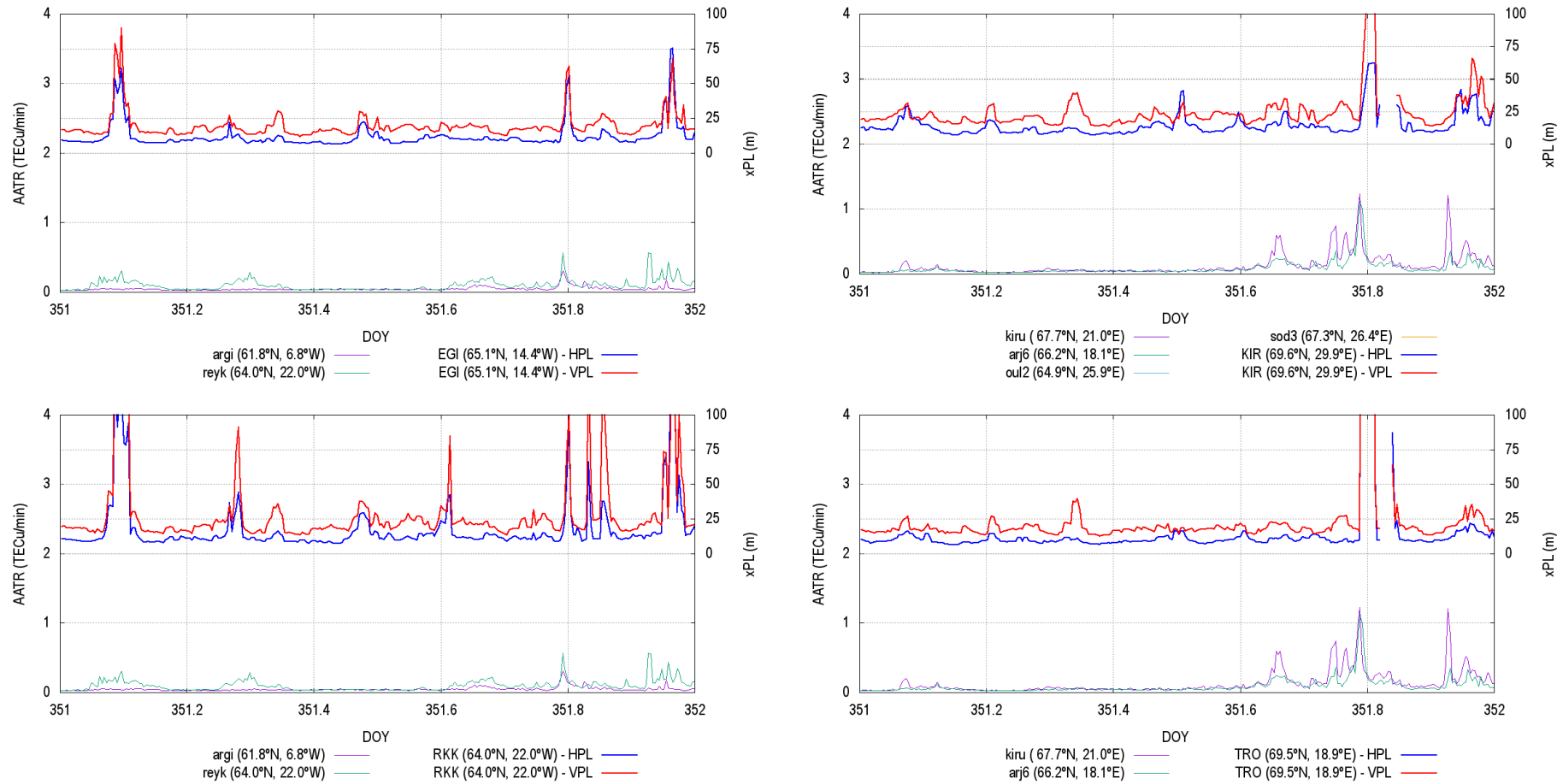


Figure 142. HPL and VPL variation for assessed RIMS and AATR values at IGS station on DOY 351.

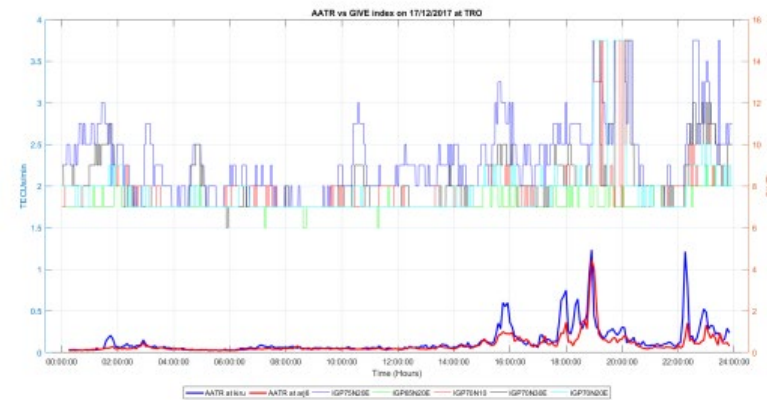
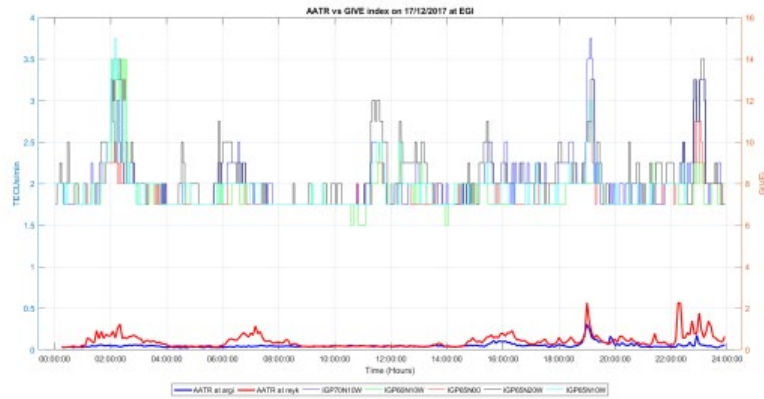


Figure 143. Temporal evolution of GIVE indices at IGP's surrounding assessed RIMS and AATR at IGS stations on DOY 351.

A.16 DOY 360

On 26/12/2017 geomagnetic activity has been observed at the beginning and end of the day impacting EGNOS performance in the North part of Service Area. Increase in xPLs values are seen at these periods with increased values of AATR. The increased values of GIVE indicators are well correlated with increased values of AATR at the beginning and end of the day.

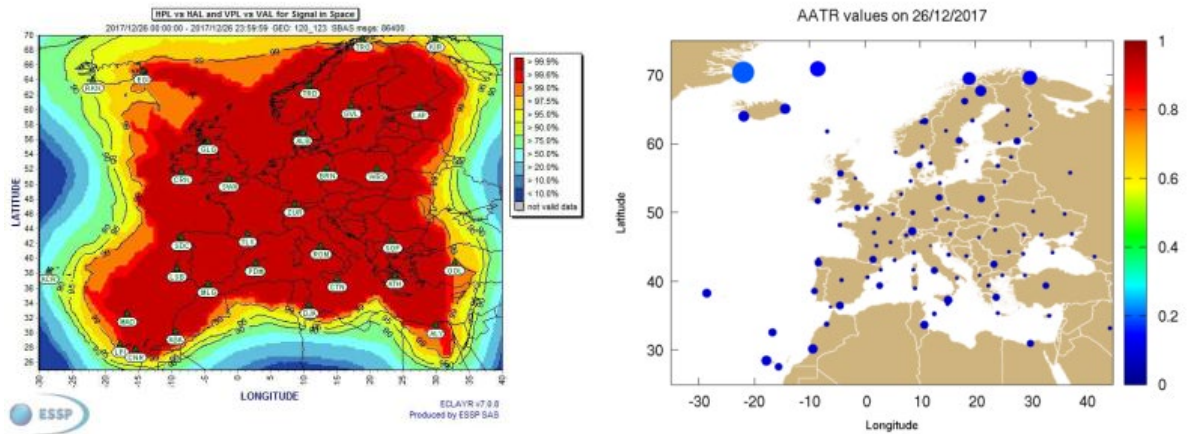


Figure 144. EGNOS APV-I availability maps and AATR daily mean values at IGS stations on DOY 360.

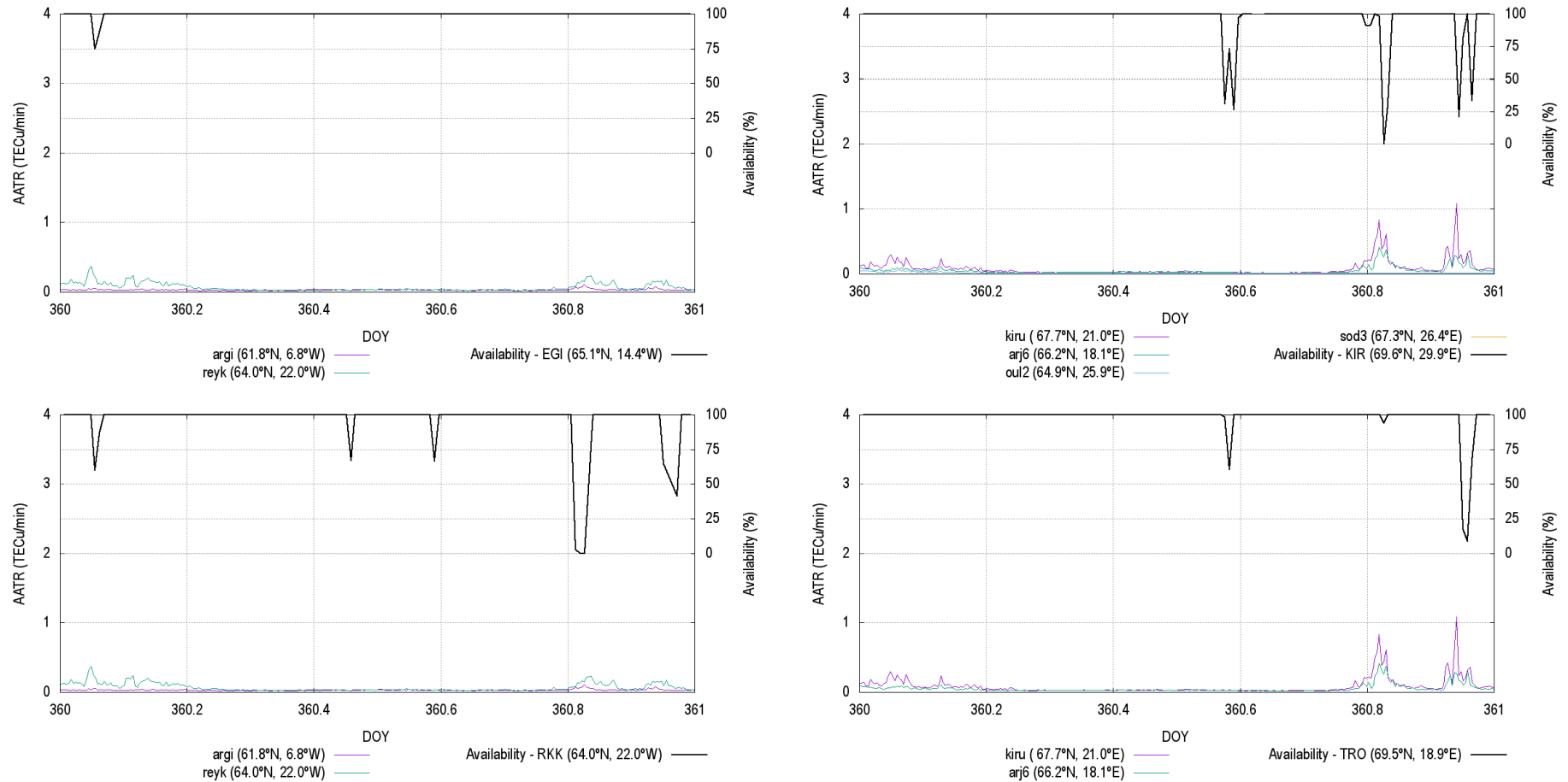


Figure 145. APV-I availability for assessed RIMS and AATR values at IGS station on DOY 360.

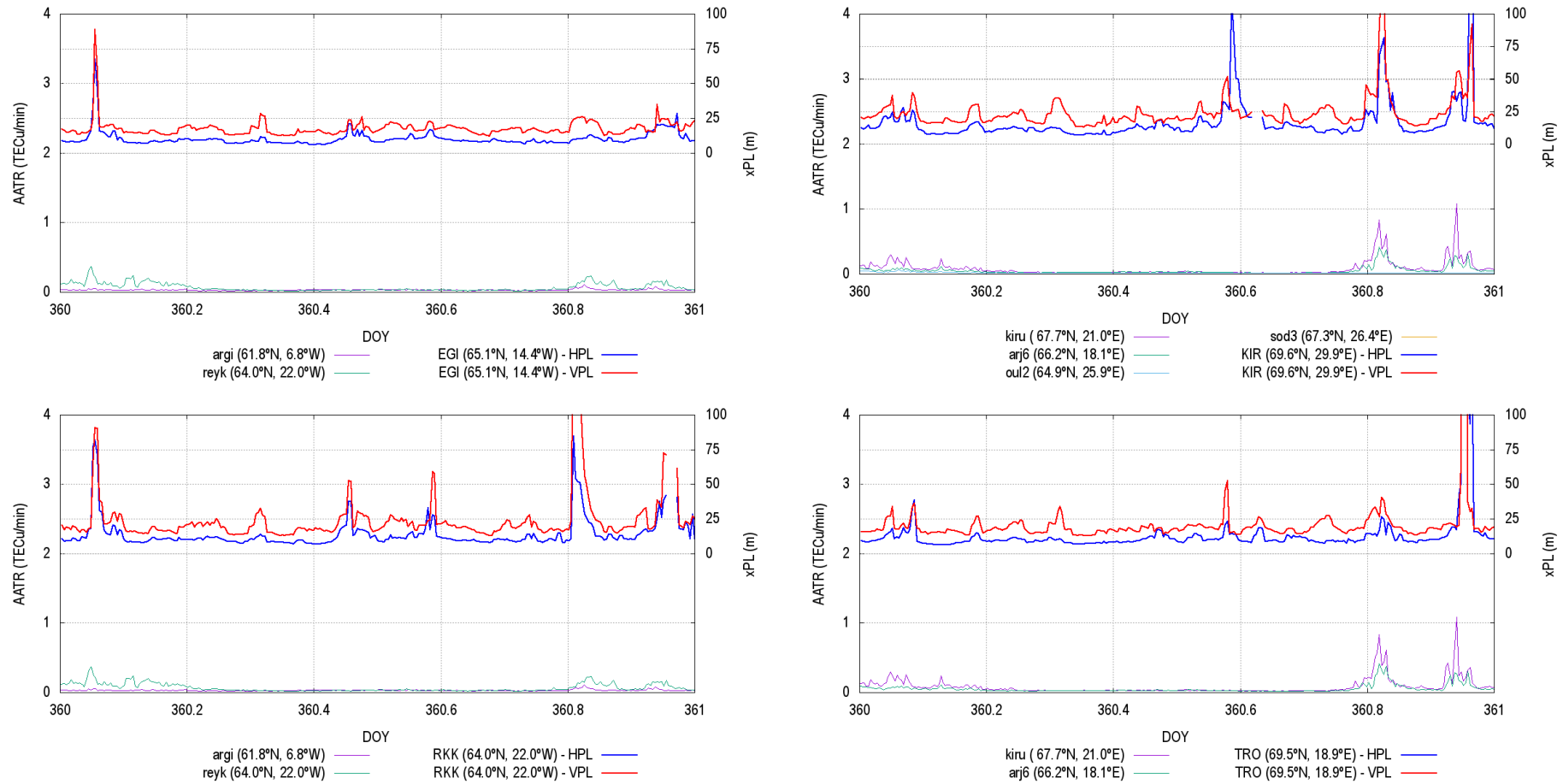


Figure 146. HPL and VPL variation for assessed RIMS and AATR values at IGS station on DOY 360.

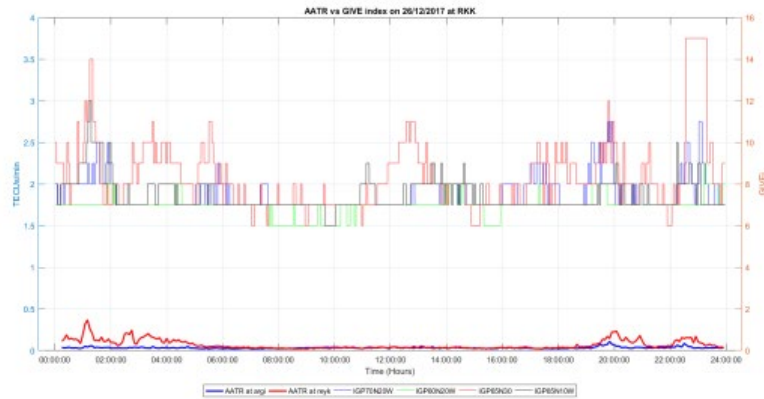
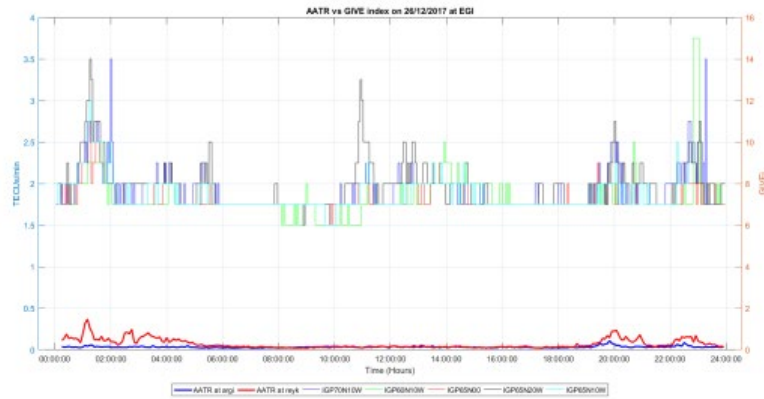


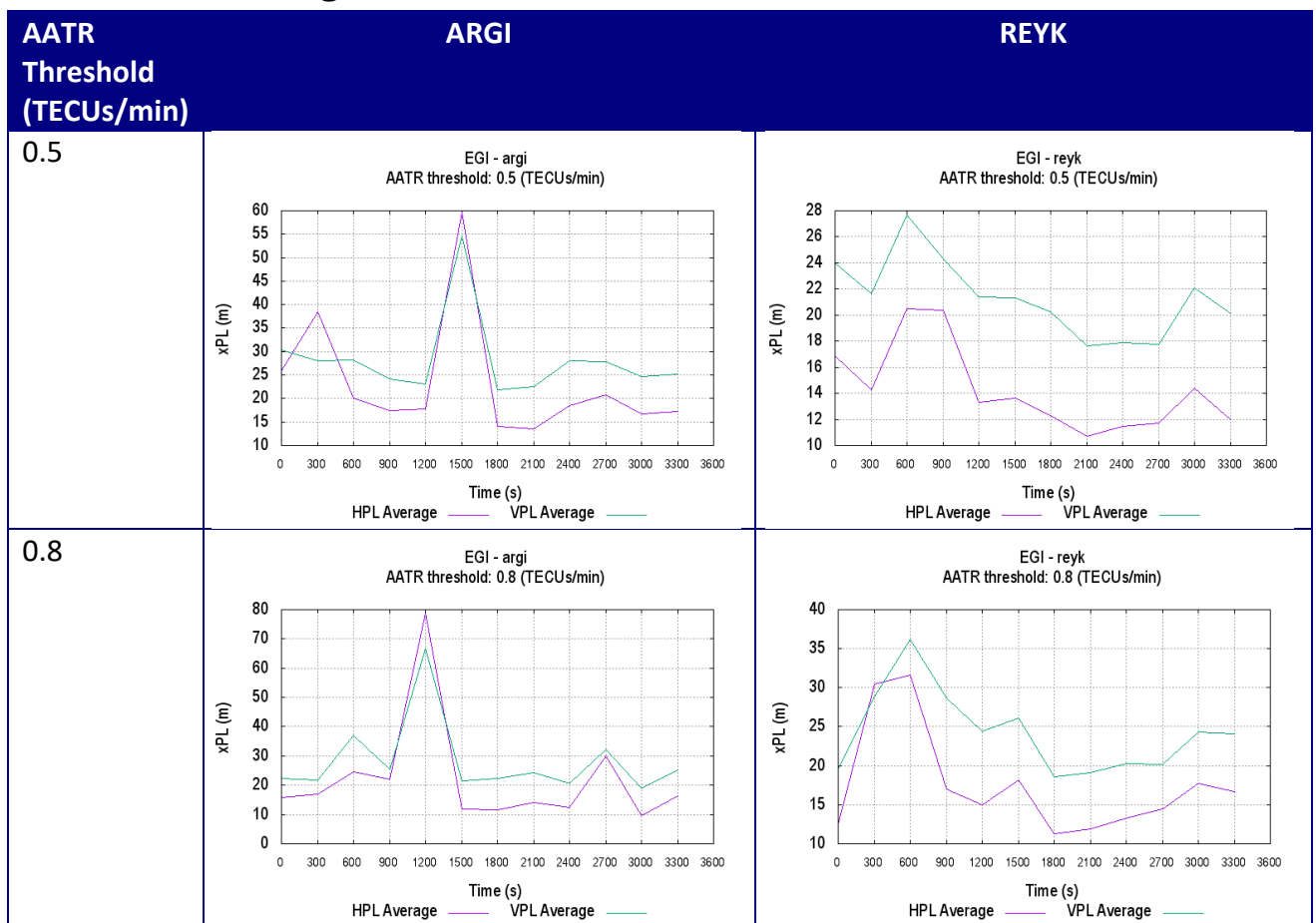
Figure 147. Temporal evolution of GIVE indices at IGP's surrounding assessed RIMS and AATR at IGS stations on DOY 360.

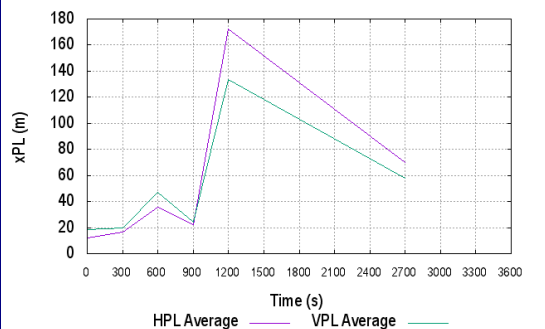
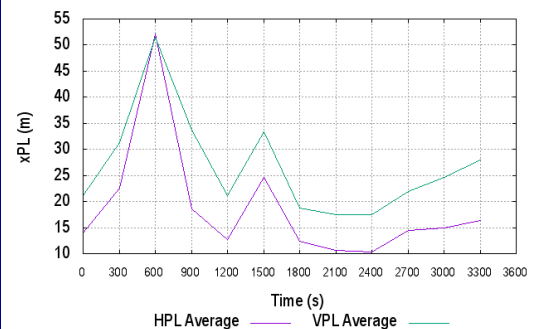
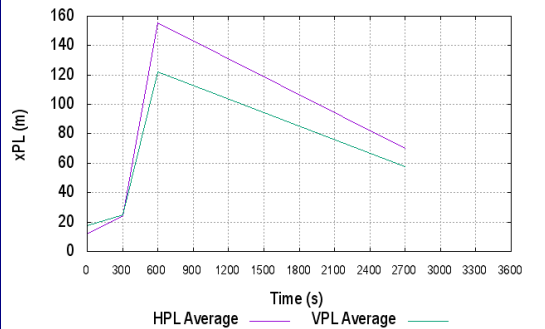
Annex B AATR Scenarios Figures

This annex presents the average value of the Horizontal and Vertical Protection Levels obtained in each RIMS against the time after the AATR threshold has been exceeded in the IGS station.

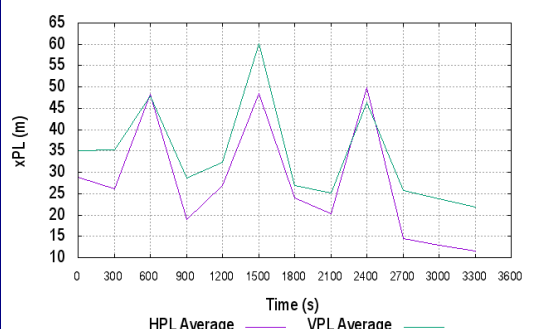
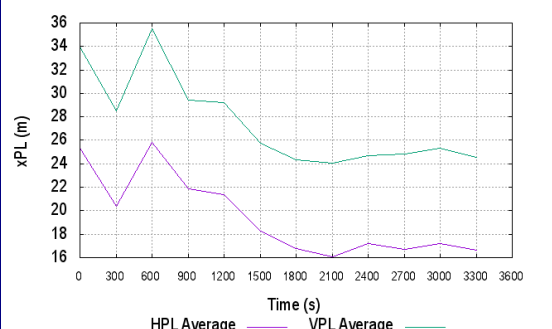
Some plots present some peaks in the xPL values. The criterion used for the selection of the offset is the selection of both HPL and VPL increase. If one of the PL increases before the other one, the later values was selected. In case one of the PL does not present a clear increase, the greatest increase of the other one is selected.

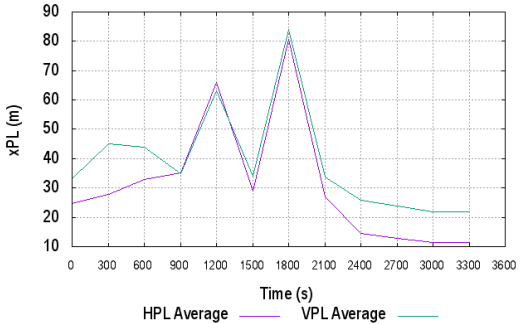
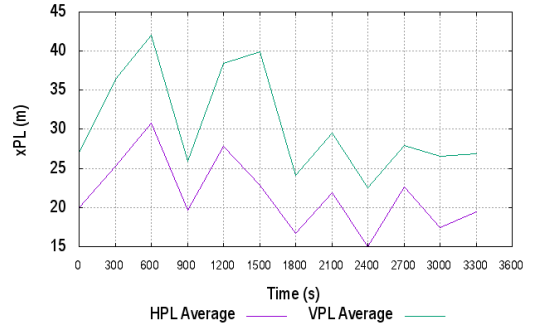
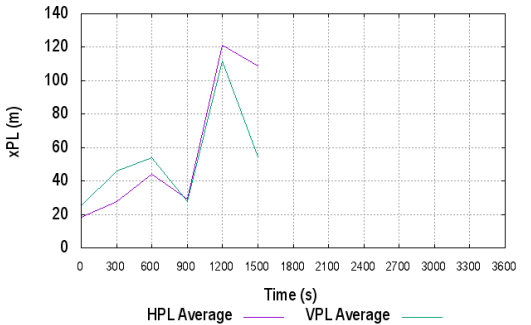
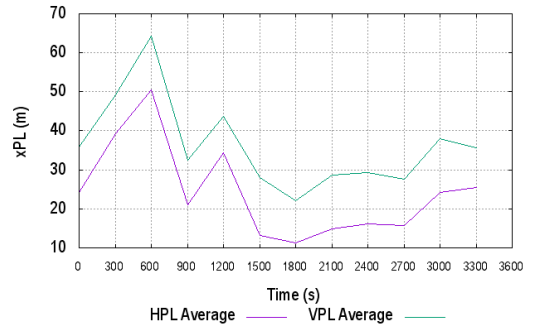
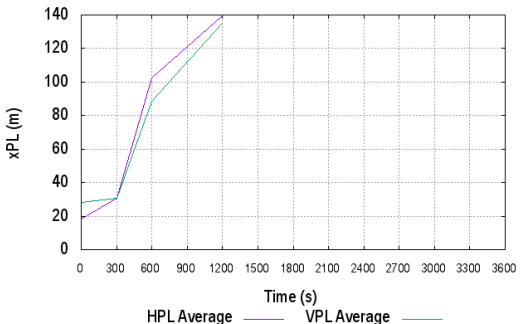
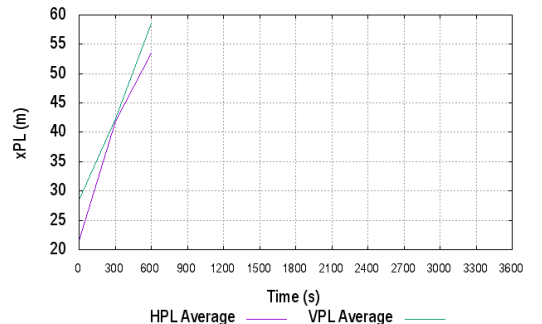
B.1 RIMS EGI average xPL values



AATR Threshold (TECUs/min)	ARGI	REYK
1.0	<p>EGI - argi AATR threshold: 1.0 (TECUs/min)</p> 	<p>EGI - reyk AATR threshold: 1.0 (TECUs/min)</p> 
1.2	<p>EGI - argi AATR threshold: 1.2 (TECUs/min)</p> 	

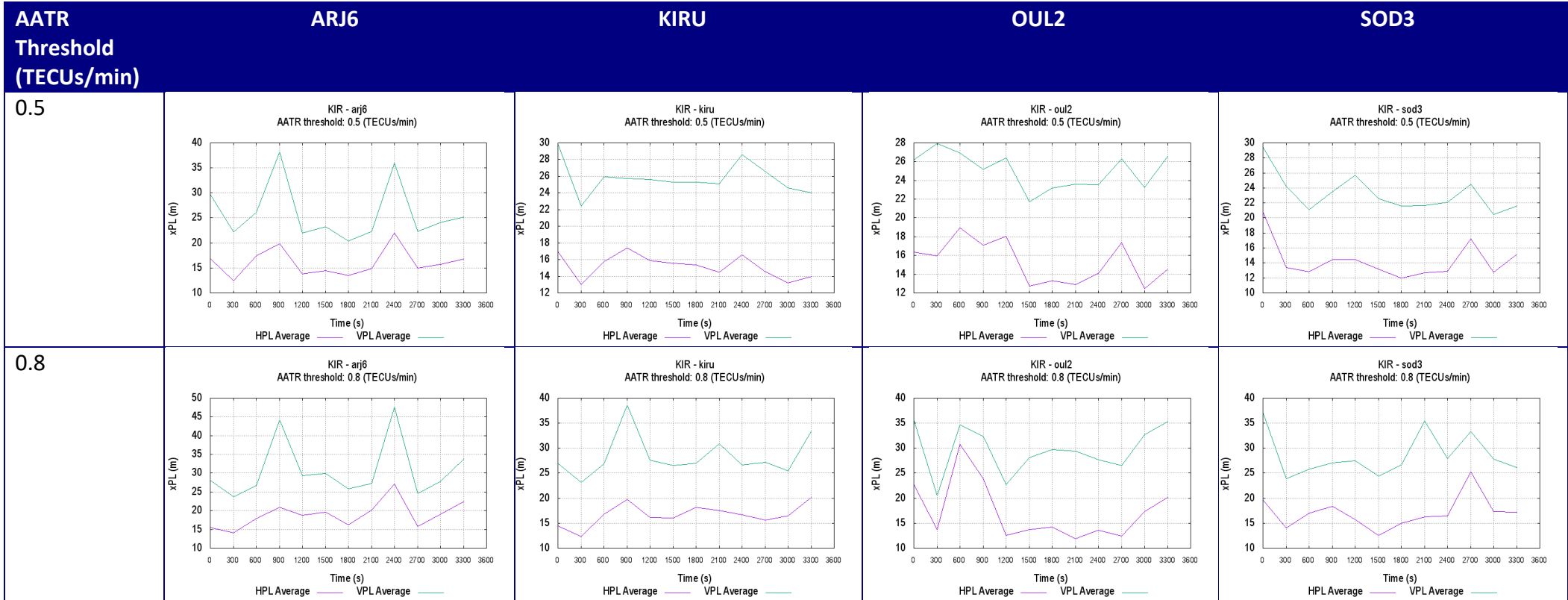
B.2 RIMS RKK average xPL values

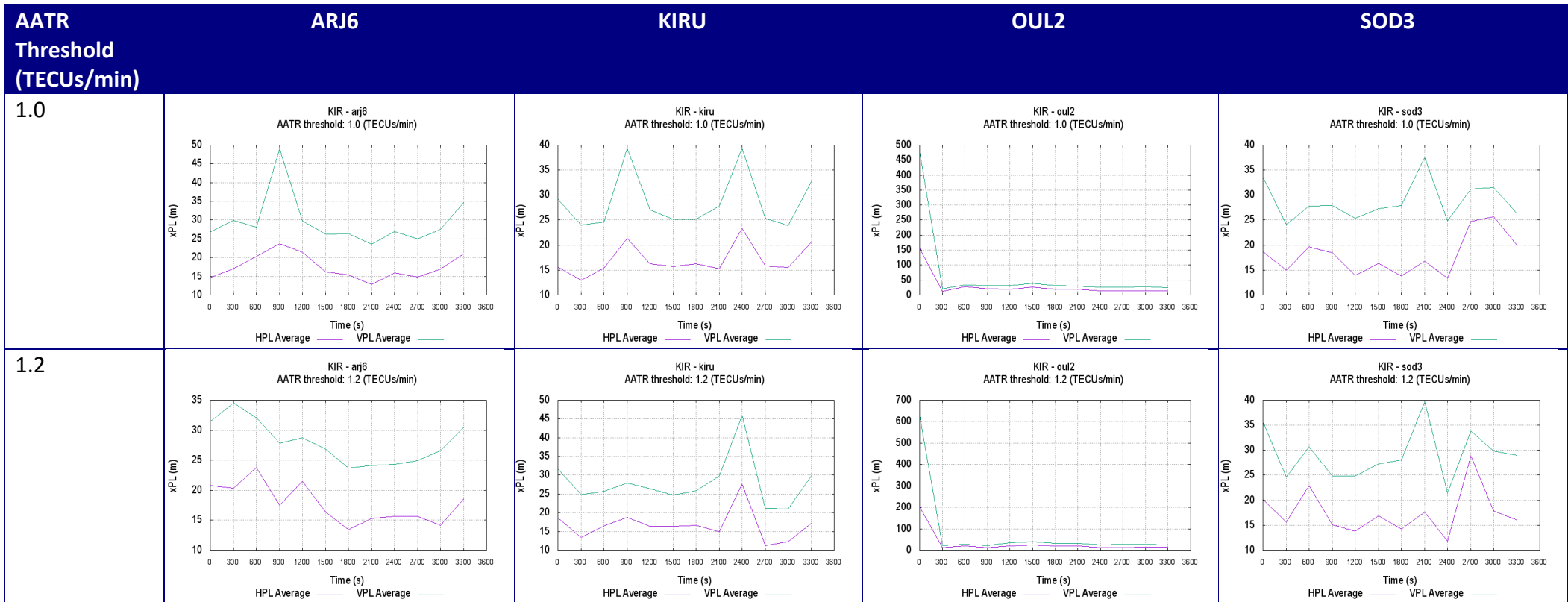
AATR Threshold (TECUs/min)	ARGI	REYK
0.5	<p>RKK - argi AATR threshold: 0.5 (TECUs/min)</p> 	<p>RKK - reyk AATR threshold: 0.5 (TECUs/min)</p> 

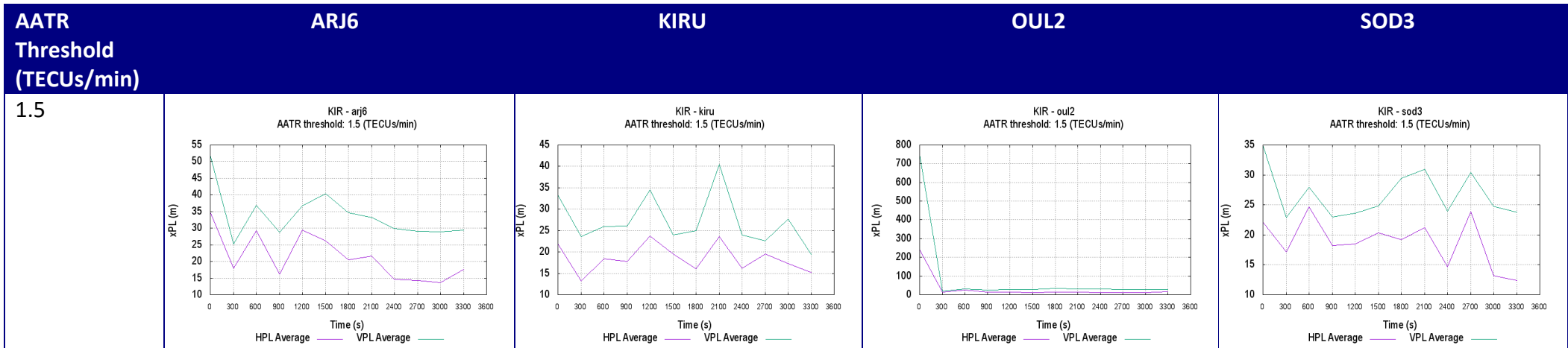
AATR Threshold (TECUs/min)	ARGI	REYK
0.8	<p>RKK - argi AATR threshold: 0.8 (TECUs/min)</p> 	<p>RKK - reyk AATR threshold: 0.8 (TECUs/min)</p> 
1.0	<p>RKK - argi AATR threshold: 1.0 (TECUs/min)</p> 	<p>RKK - reyk AATR threshold: 1.0 (TECUs/min)</p> 
1.2	<p>RKK - argi AATR threshold: 1.2 (TECUs/min)</p> 	<p>RKK - reyk AATR threshold: 1.2 (TECUs/min)</p> 



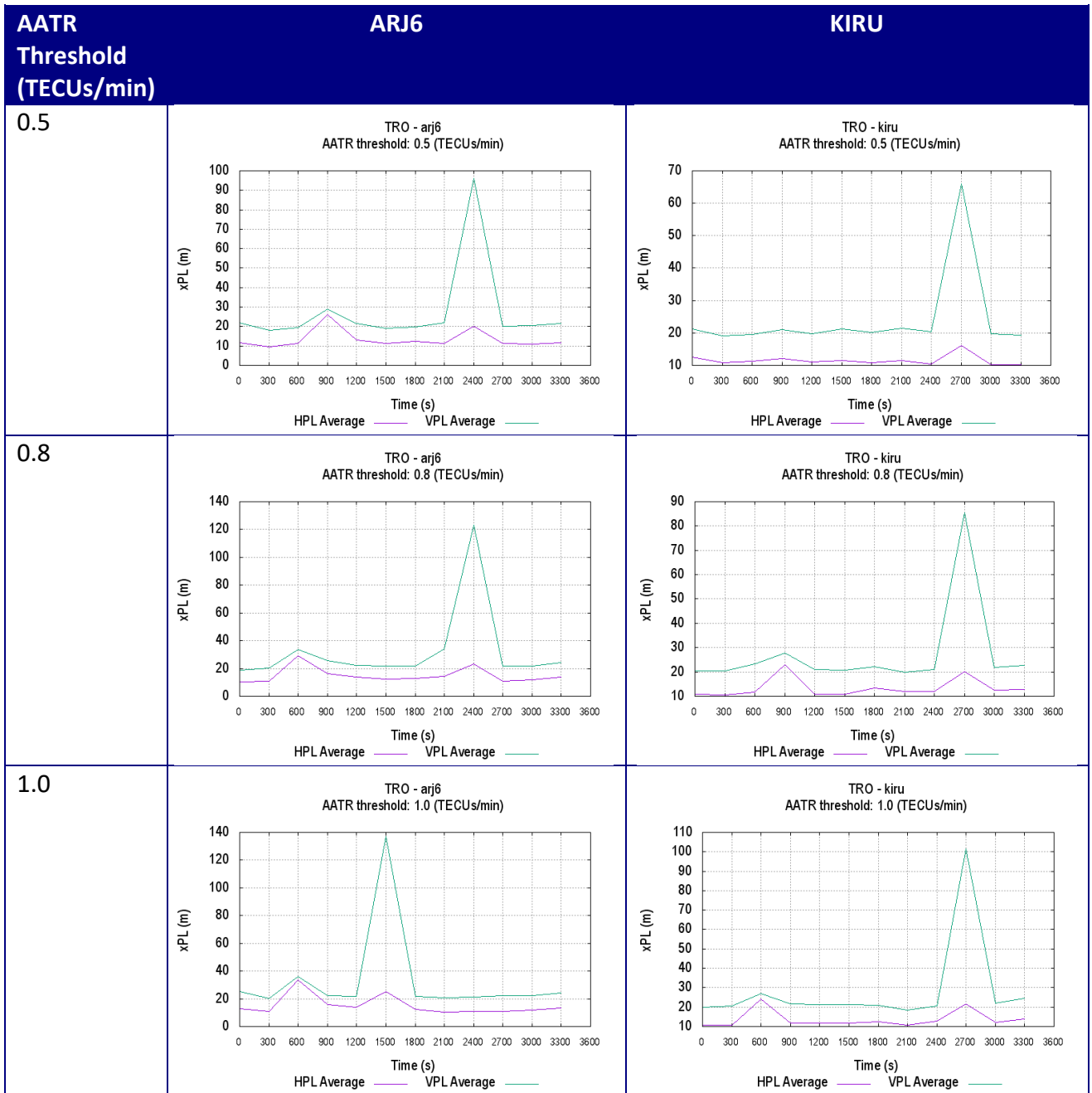
B.3 RIMS KIR average xPL values

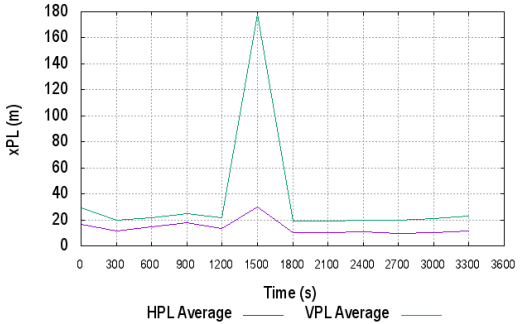
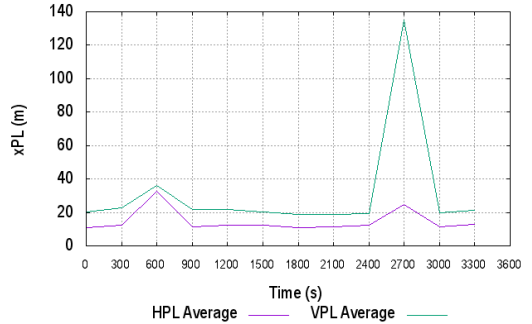
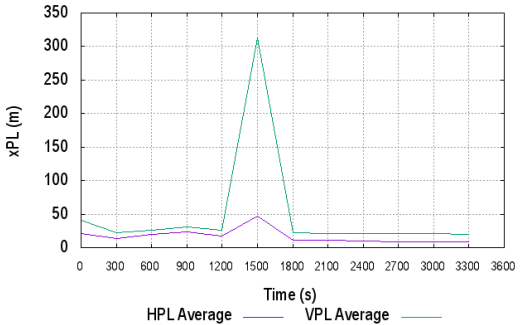
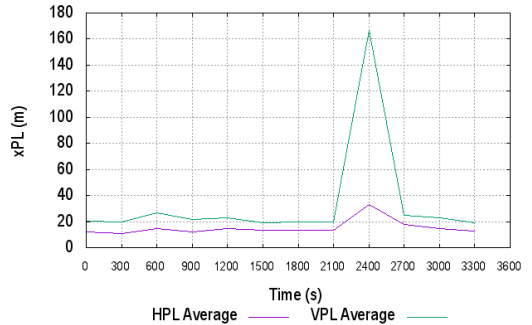






B.4 RIMS TRO average xPL values



AATR Threshold (TECUs/min)	ARJ6	KIRU
1.2	<p>TRO - arj6 AATR threshold: 1.2 (TECUs/min)</p> 	<p>TRO - kiru AATR threshold: 1.2 (TECUs/min)</p> 
1.5	<p>TRO - arj6 AATR threshold: 1.5 (TECUs/min)</p> 	<p>TRO - kiru AATR threshold: 1.5 (TECUs/min)</p> 

Annex C: Network Stations' Distances

	Station name	Station name	Distance (km)
1	lleï	ebre	90.2106
2	avel	ebre	119.783
3	esco	ebre	211.878
4	sorg	ebre	180.651
5	reus	ebre	68.8556
6	bell	ebre	115.29
7	sona	ebre	155.78
8	garr	ebre	130.518
9	lliv	ebre	221.596
10	plan	ebre	142.003
11	sbar	ebre	190.697
12	mare	ebre	180.93
13	beud	ebre	242.07
14	case	ebre	233.79
15	creu	ebre	288.336
16	avel	lleï	30.8266
17	esco	lleï	122.329
18	sorg	lleï	93.9704
19	reus	lleï	69.9504
20	bell	lleï	67.1749
21	sona	lleï	86.4795
22	garr	lleï	116.273
23	lliv	lleï	147.939
24	plan	lleï	118.427
5	sbar	lleï	136.827
26	mare	lleï	153.713
27	beud	lleï	185.971
28	case	lleï	194.022
29	creu	lleï	238.077
30	esco	avel	92.1043
31	sorg	avel	63.2299

32	reus	avel	86.4029
33	bell	avel	62.5405
34	sona	avel	64.7394
35	garr	avel	117.008
36	lliv	avel	120.817
37	plan	avel	115.143
38	sbar	avel	118.614
39	mare	avel	145.554
40	beud	avel	164.688
41	case	avel	178.788
42	creu	avel	217.704
43	sorg	esco	37.7276
44	reus	esco	170.011
45	bell	esco	126.524
46	sona	esco	89.785
47	garr	esco	173.949
48	lliv	esco	85.3177
49	plan	esco	164.545
50	sbar	esco	126.669
51	mare	esco	176.957
52	beud	esco	148.052
53	case	esco	182.81
54	creu	esco	196.813
55	reus	sorg	133.839
56	bell	sorg	88.913
57	sona	sorg	53.0191
58	garr	sorg	136.561
59	lliv	sorg	70.1187
60	plan	sorg	127.691
61	sbar	sorg	96.5814
62	mare	sorg	143.124
63	beud	sorg	127.913
64	case	sorg	156.344

65	<i>creu</i>	<i>sorg</i>	180.006
66	<i>bell</i>	<i>reus</i>	51.5357
67	<i>sona</i>	<i>reus</i>	95.8422
68	<i>garr</i>	<i>reus</i>	63.9867
69	<i>lliv</i>	<i>reus</i>	159.953
70	<i>plan</i>	<i>reus</i>	73.9094
71	<i>sbar</i>	<i>reus</i>	123.027
72	<i>mare</i>	<i>reus</i>	113.182
73	<i>beud</i>	<i>reus</i>	174.013
74	<i>case</i>	<i>reus</i>	165.106
75	<i>creu</i>	<i>reus</i>	219.519
76	<i>sona</i>	<i>bell</i>	44.6609
77	<i>garr</i>	<i>bell</i>	54.7539
78	<i>lliv</i>	<i>bell</i>	108.481
79	<i>plan</i>	<i>bell</i>	52.8893
80	<i>sbar</i>	<i>bell</i>	76.9293
81	<i>mare</i>	<i>bell</i>	86.5575
82	<i>beud</i>	<i>bell</i>	128.418
83	<i>case</i>	<i>bell</i>	128.948
84	<i>creu</i>	<i>bell</i>	177.711
85	<i>garr</i>	<i>sona</i>	84.4355
86	<i>lliv</i>	<i>sona</i>	65.8244
87	<i>plan</i>	<i>sona</i>	74.7872
88	<i>sbar</i>	<i>sona</i>	54.5107
89	<i>mare</i>	<i>sona</i>	92.0764
90	<i>beud</i>	<i>sona</i>	100.215
91	<i>case</i>	<i>sona</i>	115.715
92	<i>creu</i>	<i>sona</i>	153.056
93	<i>lliv</i>	<i>garr</i>	131.751
94	<i>plan</i>	<i>garr</i>	15.2248
95	<i>sbar</i>	<i>garr</i>	79.3528
96	<i>mare</i>	<i>garr</i>	50.7652
97	<i>beud</i>	<i>garr</i>	124.29
98	<i>case</i>	<i>garr</i>	105.415
99	<i>creu</i>	<i>garr</i>	162.96

100	<i>lliv</i>	<i>plan</i>	117.718
101	<i>sbar</i>	<i>plan</i>	64.3034
102	<i>mare</i>	<i>plan</i>	39.318
103	<i>beud</i>	<i>plan</i>	109.187
104	<i>case</i>	<i>plan</i>	92.1972
105	<i>creu</i>	<i>plan</i>	148.906
106	<i>lliv</i>	<i>sbar</i>	57.7701
107	<i>mare</i>	<i>sbar</i>	54.6385
108	<i>beud</i>	<i>sbar</i>	51.5476
109	<i>case</i>	<i>sbar</i>	61.5029
110	<i>creu</i>	<i>sbar</i>	101.581
111	<i>lliv</i>	<i>mare</i>	112.213
112	<i>beud</i>	<i>mare</i>	83.2324
113	<i>case</i>	<i>mare</i>	55.4976
114	<i>creu</i>	<i>mare</i>	114.258
115	<i>lliv</i>	<i>beud</i>	62.9505
116	<i>case</i>	<i>beud</i>	45.5251
117	<i>creu</i>	<i>beud</i>	53.2503
118	<i>lliv</i>	<i>case</i>	101.455
119	<i>creu</i>	<i>case</i>	59.1966
120	<i>lliv</i>	<i>creu</i>	111.965



END OF DOCUMENT